DISSERTATION

submitted to the

Combined Faculty of Mathematics, Engineering and Natural Sciences

of Heidelberg University, Germany

for the degree of

Doctor of Natural Sciences

Put forward by

Janine Hempfling

born in: Ludwigsburg

Oral examination: 10th July 2024

Optimization of CONUS+ Detectors and the Search for Neutrino Electromagnetic Properties

Referees: Prof. Dr. Dr. h.c. Manfred Lindner
JProf. Dr. Loredana Gastaldo

Abstract

The search for coherent elastic neutrino nucleus scattering is currently among the most popular experimental investigations in neutrino physics. One of the leading reactor experiments is the CONUS experiment, located at 17 m distance to the 3.9 GW_{th} reactor core of the Brokdorf nuclear power plant in Germany. The four high-purity germanium detectors, enclosed by a compact shield, collected data in five runs from May 2018 to December 2022. After the stopped operation of the Brokdorf reactor, the optimized experiment was relocated to the Swiss nuclear power plant in Leibstadt. This thesis deals with the search for beyond standard model physics, as well as with the optimization for the future operation of CONUS+ with improved detector understanding and technological progress. In the first part of the thesis, a full analysis on neutrino electromagnetic properties was conducted using new data of the last two runs combined with Run-1 and Run-2 data. Here, an upper limit on the neutrino magnetic moment of $\mu_\nu < 5.18 \cdot 10^{-11} \mu_B$ at 90% C.L. was obtained, while the neutrino millicharge analysis yielded an upper limit of $|q_\nu| < 1.76 \cdot 10^{-12} e_0$. Furthermore, a pulse-shape simulation for the CONUS detectors was set up for future detector and background studies. In the last part of the thesis, the optimized detectors for CONUS+ were characterized and tested. Here, an excellent energy resolution and detection efficiency performance was observed with an unprecedented energy threshold of around 150 eV.

Zusammenfassung

Die Suche nach kohärenter Neutrino-Kern-Streuung ist zur Zeit eines der gefragtesten Forschungsgebiete in der Neutrinophysik. Eines der führenden Reaktorexperimente ist das CONUS-Experiment, das sich in einer Entfernung von 17 m vom 3.9 GW_{th} Reaktorkern des Kernkraftwerkes Brokdorf in Deutschland befindet. In fünf Messkampagnen von Mai 2018 bis Dezember 2022 haben die vier hochreinen Germanium Detektoren in einer kompakten Abschirmung Daten genommen. Nach der Einstellung des Reaktorbetriebs in Brokdorf zog das verbesserte Experiment an den schweizer Kernreaktor in Leibstadt um. Die vorliegende Arbeit beschäftigt sich mit der Suche nach Physik jenseits des Standardmodells und mit der Optimierung für den zukünftigen Betrieb von CONUS+. Im ersten Teil wurden die neuesten Daten aus den letzten beiden Messkampagnen und Daten aus Run-1 und Run-2 auf die elektromagnetischen Eigenschaften der Neutrinos untersucht. Daraus wurde eine obere Grenze für das magnetische Moment des Neutrinos von $\mu_\nu < 5.18 \cdot 10^{-11} \mu_B$ (90% Konfidenz-Intvall) und für die Milliladung von $|q_\nu| < 1.76 \cdot 10^{-12} e_0$ abgeleitet. Darüber hinaus wurde eine Pulsform-Simulation für die CONUS Detektoren aufgesetzt mit der zukünftige Detektor- und Untergrund-Studien durchgeführt werden können. Im letzten Teil dieser Arbeit wurden die optimierten Detektoren für CONUS+ charakterisiert und getestet. Dabei wurde eine exzellente Energieauflösung und Detektionseffizienz mit einer überragenden Energieschwelle von etwa 150 eV ermittelt.

Contents

1. Introduction

Neutrinos are one of the most abundant particles in the Universe, but due to their rare interactions, the experimental study of their properties has been a big challenge. Since the first postulation of the neutrino by W. Pauli in 1930 [1] a lot of effort was made to shed light on this elusive particle. The standard model (SM) of particle physics predicts the neutrino as a massless particle. With the evidence of neutrino oscillations by the Super-Kamiokande [2] and SNO [3] experiments, a discrepancy between the anticipated massless neutrino in the SM and the observed neutrino behavior arose, as transitions between the different neutrino flavors hint for a non-vanishing rest mass of the neutrino. At this point, it became apparent that the SM is not sufficient and that it needs more to describe the nature of neutrinos. With this discovery, the age of beyond standard model (BSM) searches in neutrino physics has begun. But besides that, the detailed investigation of SM processes will help to nail down the nature of the neutrino, which has been done in many experiments since the discovery of the neutrino by F. Reines and C. L. Cowan [4]. One of these SM processes is the coherent elastic neutrino nucleus scattering (CEνNS). In CEνNS a neutrino scatters off an entire nucleus through a weak interaction. For a long time, it was not possible to observe this process despite it having the highest interaction probability of all neutrino interactions. The reason for this are the tiny nuclear recoils as only observables of the scattering process, making it hard to be detected. With progressing detector technologies, the detection of the CEνNS process became tangible, and many experiments have been planned and partly set up to measure this neutrino scattering.
One of these experiments is the CONUS experiment, which aims to measure CEνNS at a nuclear reactor. From Mai 2018 to December 2022, it was operated at the nuclear reactor of Brokdorf in Germany. Several layers of lead and polyethylene surround the four high-purity germanium detectors to shield against external background. In five measurement campaigns data were collected to set world-best upper limits on CEνNS. Besides the CEνNS analysis, it is also possible to investigate BSM physics with CONUS. One of the most popular pending issues is the question of whether the neutrino possesses some electromagnetic properties induced by the presence of a small neutrino mass. Here, a possible neutrino magnetic moment and neutrino millicharge are of special interest. With the CONUS data it is also feasible to search

for these neutrino characteristics and competitive upper limits have been set already using data of the first two data collection periods.
With the stopped operation of the Brokdorf nuclear power plant, the physics program for the CONUS experiment has not been completed. A lot of effort was put into moving the whole experimental setup to the nuclear reactor of Leibstadt in Switzerland. In the course of the relocation of the experiment, several improvements were made regarding the setup and the detectors to increase the sensitivity of the new experiment CONUS+.

The work presented in this thesis has been carried out in the context of the CONUS and CONUS+ experiments and deals with the whole spectrum of experimental work, from a comprehensive data analysis regarding the BSM part of neutrino physics to the future of the experiment. The focus of this thesis is on three different parts of CONUS/CONUS+, including the analysis of already measured, but not yet analyzed, data of the CONUS experiment, the improvement of detector and background understanding, and the characterization of detector performance for CONUS+ at the Leibstadt reactor.
Chapter 2 deals with a detailed description of the CONUS experiment and the theoretical foundations of the main physics goal of CEνNS. Here, also results regarding the neutrino electromagnetic properties of the first two short experimental data-taking runs are summarized.
With the additional high exposure of Run-4 and Run-5, the sensitivity for the BSM physics search increased. For this reason, a likelihood analysis with respect to neutrino electromagnetic properties, more precisely the neutrino magnetic moment and the neutrino millicharge, is conducted in this work, which is explained in detail in Chapter 3. The theoretical description of an effective neutrino magnetic moment and millicharge in the context of elastic neutrino electron scattering is described, as well as the basics of statistical data analysis with hypothesis tests and the maximum likelihood method. Before conducting the analysis, the measured CONUS data have to be selected based on stability criteria and datasets have to be prepared for the next step. The full analysis is then performed with an already available data analysis framework, which is also explained in this chapter. Finally, the results on neutrino magnetic moment and neutrino millicharge, using data from the latest two runs, as well as a combined result with the data of Run-1 and Run-2 are presented.
For the future data collection in CONUS+, there are several ways of further improving the sensitivity of the experiment for SM and BSM physics searches. One path towards this is an improved understanding of background and detectors. With the study of detector signals, background events can be categorized and rejected. For the theoretical study of the signal-like and background events, a pulse-shape simulation for the CONUS experiment is set up in Chapter 4. Here, the mechanism of particle detection in the CONUS detectors, as well as the resulting signal pulses are illustrated. For the pulse-shape simulation, an open-source simulation package is adjusted to the need of CONUS and validated by comparing it to the measured

data.
Another way to improve the sensitivity of the experiment is to improve the detector performance. With the move from Brokdorf to Leibstadt, the CONUS detectors were optimized at Mirion Lingolsheim regarding detection threshold and efficiency. In Chapter 5, a rough overview of the new experimental site for CONUS+ and the improvements on the experimental setup are given, followed by a detailed description of the motivation for the upgrade and the detector optimization steps. Before deployment of the full experimental setup to the Leibstadt reactor, the optimized detectors are characterized and the detector performance is monitored extensively. Here, special care is taken on the energy resolution and the trigger-efficiency of the detectors, as they both affect the energy threshold of the detectors.
Finally, a summary of the work conducted in this thesis is given in Chapter 6, as well as a brief outlook on the future measurement campaign of CONUS+.

2. CONUS and the Search for Coherent Elastic Neutrino Nucleus Scattering

With the search for the standard model neutrino interaction of coherent elastic neutrino nucleus scattering the era of human-sized detectors in neutrino physics has begun. In contrast to large neutrino experiments as Super-Kamiokande [5] or Borexino [6], with experimental setups matching the size of a house and a volume of several thousands of m^3, CEνNS detectors are only a small fraction of this size. The reason for this surprising advantage is the unusual high cross-section of the interaction, explained in Section 2.1. One of the most successful CEνNS experiments is the CONUS (COherent elastic Neutrino nUcleus Scattering) experiment operated by the Max-Planck Institut für Kernphysik (MPIK) at a nuclear reactor. It aims for the detection of CEνNS using reactor $\overline{\nu_e}$ at shallow depth. During the five years of runtime, the CONUS experiment set standards for this kind of experiment and also made a lot of progress in the search for CEνNS at nuclear reactors as world best upper limits on coherent scattering. Besides the search for CEνNS, the experiment also allows for different other channels as beyond standard model searches, which are part of this work.
In the following, the initial purpose of the experiment, the search for coherent elastic neutrino nucleus scattering, is explained as well as all prerequisites for such a measurement. In Section 2.2 an overview of the CONUS experiment and a summary of all so far achieved physical results are given.

2.1. Coherent Elastic Neutrino Nucleus Scattering

The standard model process of coherent elastic neutrino nucleus scattering was theoretically described for the first time by Daniel Z. Freedman in 1974 [7]. In this neutral current (NC) elastic scattering, low-energy neutrinos interact with the entire nucleus coherently. As this interaction process is mediated by a Z^0-boson exchange, CEνNS is insensitive to the neutrino flavor, and therefore, the scattering cross section is

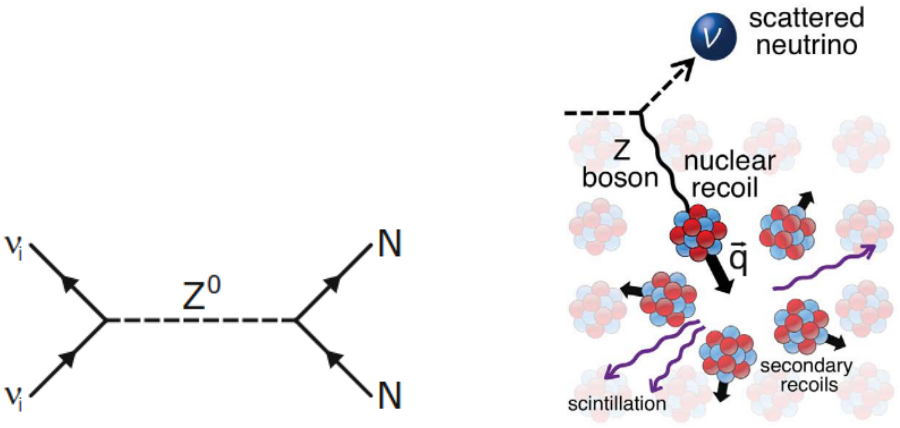

(a) (b)

Figure 2.1.: a) Feynman diagram of the CEνNS process. ν_i denotes (anti-)neutrinos of arbitrary flavor, and N denotes the target nucleus. The incoming neutrino scatters off the nucleus exchanging a neutral Z^0-boson. From [8].
b) Schematic principle of CEνNS. A low energy neutrino coherently scatters off a nucleus while momentum exchange ($\vec{q}$) is sufficiently small and $qR \lesssim 1$. During scattering a neutral Z-boson is exchanged. The only visible outcome of this interaction is a low-energy nuclear recoil. In scintillating materials secondary recoils can be detected. From [9].

identical for all neutrino flavors. The Feynman diagram and a schematic illustration of the process are shown in Figure 2.1, where an incoming neutrino of arbitrary flavor scatters off the whole nucleus. The SM prediction of the CEνNS cross section [10, 11] is given by

$$\frac{d\sigma}{dT_{\mathrm{coh}}} = \frac{G_{\mathrm{F}}^2 M}{2\pi}\left[(G_{\mathrm{V}}+G_{\mathrm{A}})^2 + (G_{\mathrm{V}}-G_{\mathrm{A}})^2\left(1-\frac{T}{E_\nu}\right)^2 - (G_{\mathrm{V}}^2 - G_{\mathrm{A}}^2)\frac{MT}{E_\nu^2}\right] \tag{2.1}$$

with

$$G_{\mathrm{V}} = (g_{\mathrm{V}}^{\mathrm{p}} Z + g_{\mathrm{V}}^{\mathrm{n}} N) F_{\mathrm{nucl}}^{\mathrm{V}}(q^2), \tag{2.2}$$

$$G_{\mathrm{A}} = (g_{\mathrm{A}}^{\mathrm{p}}(Z_+ - Z_-) + g_{\mathrm{A}}^{\mathrm{n}}(N_+ - N_-)) F_{\mathrm{nucl}}^{\mathrm{A}}(q^2). \tag{2.3}$$

Here, G_{F} is the Fermi constant, M the mass of the nucleus, T the recoil energy and E_ν is the neutrino energy. Furthermore, $g_{\mathrm{V}}^{\mathrm{p,n}}$, $g_{\mathrm{A}}^{\mathrm{p,n}}$ are the factors for SM vector- and axial-vector couplings for protons (p) and neutrons (n), Z and N are the proton and neutron numbers with $\pm$ referring to the number of spin up and spin down nucleons and $F^{\mathrm{V,A}}$ are the nuclear form factors dependent on the momentum transfer q. Often, the vector contribution dominates over the axial contribution, as axial

contributions are small due to the dependence on unpaired nucleons, or zero for spin-zero nuclei. Hence they can be neglected and assuming $T \ll E_\nu$, the cross section is then approximately given by [10]

$$\frac{d\sigma}{dT_{\text{coh}}} \sim \frac{G_{\text{F}}^2 M}{2\pi} \frac{Q_{\text{W}}^2}{4} F^2(q) \left(2 - \frac{MT}{E_\nu^2}\right), \tag{2.4}$$

with the weak nuclear charge

$$Q_{\text{W}} = N - (1 - 4\sin^2\theta_{\text{W}})Z. \tag{2.5}$$

Since the weak mixing angle $\sin^2\theta_{\text{W}} = 0.223$ [12] is close to 1/4 the contribution from proton coupling can be neglected in a first-order approximation compared to the neutron contribution [8] and Equation 2.4 simplifies to

$$\frac{d\sigma}{dT_{\text{coh}}} \sim \frac{G_{\text{F}}^2 M}{2\pi} \frac{N^2}{4} F^2(q) \left(2 - \frac{MT}{E_\nu^2}\right). \tag{2.6}$$

The point-like form factor $F(q)$ represents the distribution of protons and neutrons in the nucleus [7]. If the momentum transfer q is small enough or almost negligible, the condition of coherence $qR \lesssim 1$ [13], with $R = A^{1/3} \cdot 1.2\,\text{fm}$ [8] the radius of the nucleus and A the mass number, is fulfilled at low neutrino energies. Hence the nuclear form factor can be normalized to $F(0) = 1$. If the energy of the scattering neutrino gets higher, the limit of vanishing momentum transfer $q \to 0$ is not valid anymore as the effective de Broglie wavelength h/q reaches the size of the nucleus. Here, the nucleus interacts as a collection of the individual nucleons [8]. Therefore the form factor can no longer approximated with 1. The coherency condition and, thus, the characteristics of the form factor play a big role in the choice of the experimental realization for a CEνNS measurement. This will be discussed in detail in Chapter 2.1.1.

Equation 2.6 implies that CEνNS is mainly sensitive to the neutron distribution in the nucleus and the cross section scales with a N^2 dependence. This dependence leads to an enhanced cross section compared to other neutrino interactions as inverse beta decay (IBD) [14] or elastic anti-neutrino electron scattering (EνeS) [15] by several orders of magnitude and is shown in Figure 2.2 a) for a Ge target. Hence a heavy nucleus with a high neutron number is ideal for a large CEνNS cross section. On the other side the maximum recoil energy T_{max} of the nucleus is given by [16]

$$T_{\text{max}}(E_\nu) = \frac{2E_\nu^2}{M + 2E_\nu}. \tag{2.7}$$

It can be seen that the maximum recoil energy is inversely proportional to the mass of the nucleus if $E_\nu \ll M$. With the mass of the nucleus proportional to A, this leads to a trade-off between a high neutron number for the N^2 dependence of the

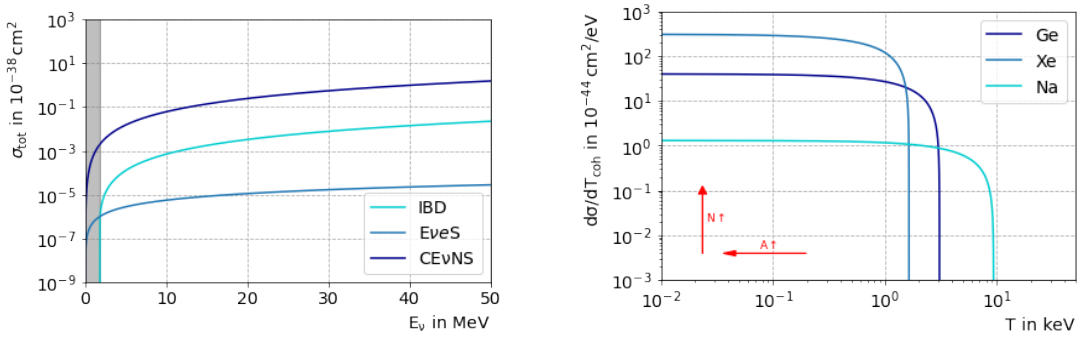

(a) (b)

Figure 2.2.: a) Total cross sections for CEνNS in Ge (dark blue), elastic anti-neutrino electron scattering (EνeS, blue), and inverse beta decay (IBD, cyan). The detection threshold for IBD is marked in grey. The CEνNS cross section is enhanced by several orders of magnitude compared to the other interactions due to the N^2 dependence of the target nucleus.
b) Differential CEνNS cross section for different target nuclei at a neutrino energy of 10 MeV. With increasing neutron number N of the target nucleus the cross section increases. At the same time, the maximum recoil energy decreases with the mass of the target A.

cross section and a low neutron number, and therefore a lighter nucleus for higher recoil energies. From these considerations, it becomes clear that a medium mass nucleus is ideal for a CEνNS detection. Here, for example, Germanium (Ge) is a good candidate as a target material with medium proton number Z=32 and neutron number N=38-44, depending on the isotope. This trade-off situation can be seen in Figure 2.2 b). Here, the differential CEνNS cross section for different target nuclei is shown. The N^2 dependence of the cross section leads to a higher cross section for heavier nuclei, whereas at the same time, the nuclear recoil energy scales with $1/A$, leading to a lower cut-off for heavy nuclei.

2.1.1. Neutrino Sources

Various possible neutrino sources are known, from artificial to astronomical sources, but for a CEνNS detection, several requirements to the source must be fulfilled. As discussed before low-energy neutrinos are necessary due to the coherency condition, which restricts the process to neutrino energies of below $E_\nu \sim 30$ MeV [13]. As for several low energy detection techniques as germanium detectors the detection threshold is a limiting factor, the nuclear recoil energy, given by Equation 2.7, has to be maximized, which implies not too small neutrino energies. Furthermore, intense neutrino fluxes are required to increase the number of expected events. For better background suppression, it is also favorable to have a time period when the source is switched off. These requirements are met in two artificial neutrino sources: stopped

pion beams and reactors.
At stopped pion beams, also called pion-decay at rest ($\pi-$DAR) sources, a source produces a pion beam through proton collisions with nuclei. These pions are stopped at a target and will decay according to

$$\begin{aligned} \pi^+ \rightarrow & \mu^+ + \nu_\mu \\ & \hookrightarrow e^+ + \overline{\nu}_\mu + \nu_e \end{aligned} \tag{2.8}$$

releasing a mono-energetic muon neutrino with an energy of 30 MeV [17]. Subsequently, the μ^+ will decay into e^+, $\overline{\nu}_\mu$ and ν_e. The maximum neutrino energy of a $\pi-$DAR source is given by

$$E_\nu^{\max} = \frac{m_\mu}{2} \tag{2.9}$$

with m_μ the muon mass [17]. This results in a maximum neutrino energy of $\sim$ 53 MeV with the consequence that the nuclear form factor can no longer be assumed to be 1 for these high energies. For background suppression, a beneficial characteristic of the $\pi-$DAR source, the pulsed emission of neutrinos, is used. The steady contribution from environmental and cosmic-ray-induced radiation can, therefore, be reduced by approximately three to four orders of magnitude [8]. At the Spallation Neutron Source (SNS) at Oak Ridge National Laboratory the CEνNS process was measured for the first time by the COHERENT experiment in 2017 [9]. For this evidence several detector techniques with different target materials were used, for example a CsI[Na] scintillator crystal.
In contrast to the emission of mixed neutrino flavors at a $\pi-$DAR source a nuclear reactor only emits electron anti-neutrinos by the beta-decay of the fission isotopes with energies below 10 MeV. The energy spectrum of the reactor neutrinos is shown in Figure 2.3. The majority of the emitted neutrinos are $\lesssim$ 1 MeV leading to the simplification that the nuclear form factor can be assumed to be 1. Due to the dependence on the energy threshold of the detector, the neutrino energies contributing strongest to the measurable CEνNS events can be higher.
Usually once a year a nuclear reactor is shut off for maintenance reasons. In this time, background data can be collected, helping to discriminate not-reactor-correlated background. Experimental evidence for fully coherent neutrino nucleus scattering at a reactor is still lacking.

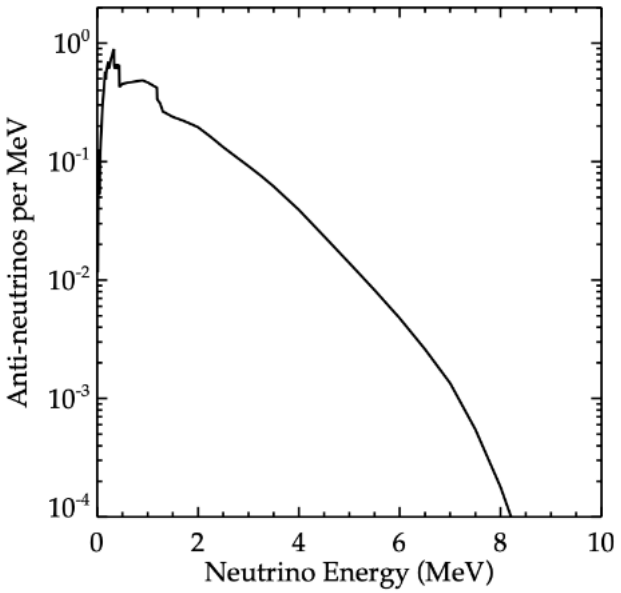

Figure 2.3.: Electron anti-neutrino spectrum of a nuclear reactor. From [17].

2.1.2. Experimental Requirements and Challenges

Although CEνNS is an SM process and yields the highest cross section of all neutrino interactions, it took over 40 years from the theoretical prediction to the experimental evidence. This time delay is caused by different experimental challenges, which make the process hard to detect. The only observable outcome of the neutrino scattering is a tiny recoil of the hit nucleus. Considering a Ge-target at a reactor with a 10 MeV neutrino, a maximum recoil energy of $T_{\mathrm{max}} \approx 3\,\mathrm{keV_{nr}}$[1], according to Equation 2.7, is expected. In addition, depending on the detector technology and material, the measured signal can be different from the actual nuclear recoil energy produced by the scattered neutrino, which is called quenching. A short summary of the quenching effect in germanium is given in Section 2.2.3. With an already small maximum recoil energy in germanium, the observable energy is due to the quenching even smaller. Therefore in HPGe detectors sub-keV energy signals are expected demanding for very low energy detection thresholds.
To maximize the number of expected CEνNS events a high neutrino flux is required. For this reason, the experiments are placed as close as possible to the neutrino source. This involves a position at shallow depth. Thus, compared to other neutrino experiments located deep underground, the background suppression is demanding, while a stable and very low background level is necessary for a CEνNS detection. The background components have to be known precisely to be suppressed systematically.

[1] $\mathrm{eV_{nr}}$ refers to the nuclear recoil energy, whereas $\mathrm{eV_{ee}}$ refers to the actual measured electron equivalent energy in the detector

For this purpose, data has to be collected also in the absence of the source, as stated in Chapter 2.1.1, and is then compared to data with a neutrino source to extract a CEνNS signal.
To sum it up, intense neutrino fluxes, very low and stable background levels, and very low detection thresholds are necessary for a successful CEνNS measurement.
At the moment several experiments to measure coherent elastic neutrino nucleus scattering, both at π-DAR sources or at reactors are running, as COHERENT [10], CONNIE [18] and νGEN [19] or are in preparation, as NUCLEUS [20] and Ricochet [21]. Among the reactor experiments, the CONUS experiment is the most promising experiment using semiconductor detectors, which will be discussed in this thesis.

2.2. The CONUS Experiment

With all the above-described prerequisites and difficulties, experiments meeting these requirements have to be specially designed to measure the process of CEνNS successfully at a reactor. The CONUS experiment was set up in 2018 at a commercial nuclear power plant in Germany and was operated there for five years until the end of 2022. In this time data from five data-taking runs was collected and world best limits on CEνNS at reactors and competitive limits on beyond standard model physics were achieved.
In the following, the experimental site inside the reactor containment and the setup of the experiment are explained in detail, whereas the so-far achieved results and the future of the CONUS experiment are discussed in Section 2.2.3 and Section 2.2.4.

2.2.1. Experimental Site

The CONUS experiment was located at the nuclear power plant of Brokdorf (KBR) in Germany. The single-unit pressurized water reactor, operated by Preussen Elektra GmbH [22], provided a maximum thermal power of $3.9\,\mathrm{GW_{th}}$ until it shut down at the end of 2021. The CONUS experimental setup was located inside room A-408 at a distance of 17.1 m from the reactor core resulting in a high anti-neutrino flux of $2.3 \cdot 10^{13}\,\mathrm{cm^{-2}s^{-1}}$ at maximum thermal power. With the position of the experimental site directly below the spent fuel storage pool an overburden of $10 - 45\,\mathrm{m}$ of water equivalent (m w.e.) depending on the solid angle, resulting in an average depth of 24 m w.e. [23], was given. The position of the CONUS experiment inside the nuclear power plant is sketched in Figure 2.4. The location of room A-408 inside the safety containment of KBR but outside the innermost biological shield surrounding the reactor core offers accessibility at any time. In contrast, setting up an experiment inside a nuclear power plant yields a lot of challenges. For safety reasons, no cryogenic liquids are allowed, and the used material has to fulfill special requirements. Furthermore, no remote control is possible, and the setup has to be robust against earthquakes. Finally, reactor-correlated background and unstable environmental conditions, such as temperature and radon in the ambient air, have to be taken into account.

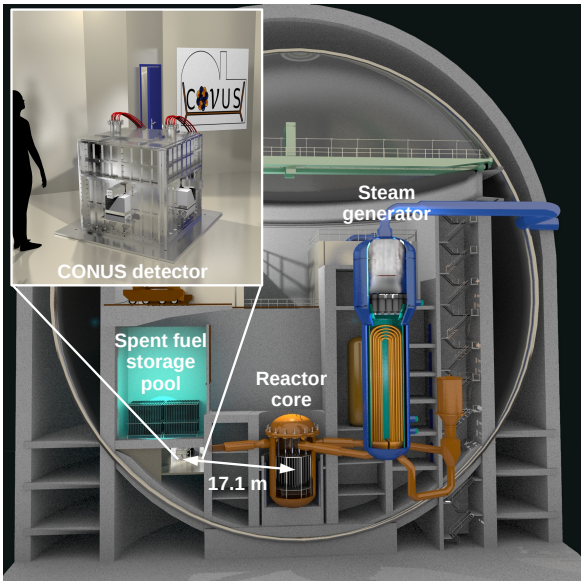

Figure 2.4.: Position of the CONUS setup in the nuclear power plant of Brokdorf. The detector is located below the spent fuel storage pool at a distance of 17.1 m to the reactor core. The enlarged image shows the detector inside A-408. From [24].

2.2.2. Detector and Shield Setup

For the measurement of a potential CEνNS signal a very low detection threshold and a very low background is required. Both requirements are realized in the CONUS setup as special care was taken during the selection of the materials used. For the entire setup, very low background components were identified, selected, and used for the production of the detectors and the shielding.
With roughly 1 m side length and a volume of only 1.63 m^3 [24] the experimental setup is extremely compact. The CONUS experiment consists of four p-type point contact high purity germanium (HPGe) detectors (further details on the detectors and the measurement principle are discussed in Chapter 4.1) embedded in an elaborated shield. Developments in the production techniques and the operation of HPGe detectors during the last decades achieved steadily lower thresholds and better detectors. With a large crystal mass of 1 kg each and a pulser resolution of $< 85\,eV_{ee}$ resulting in a low energy threshold of below $300\,eV_{ee}$[25] the HPGe detectors are suitable to observe CEνNS at reactor site. For the CONUS detectors, ultra-low noise and a very low intrinsic background contamination were achieved. The germanium crystals are cooled down to an operation temperature of ~ 80 K by a maintenance-free electrical cryocooler, driven by a pulse-tube, as no cryogenic liquids are allowed in the reactor containment. The electrical cryocooler CP5-plus is controlled by an external controller. The overall HPGe detector design is depicted in Figure 2.5. The detector crystals are located in the detector endcap, which is made of copper, and are connected to the cryostat by a coldfinger. The cryostat arms are elongated due

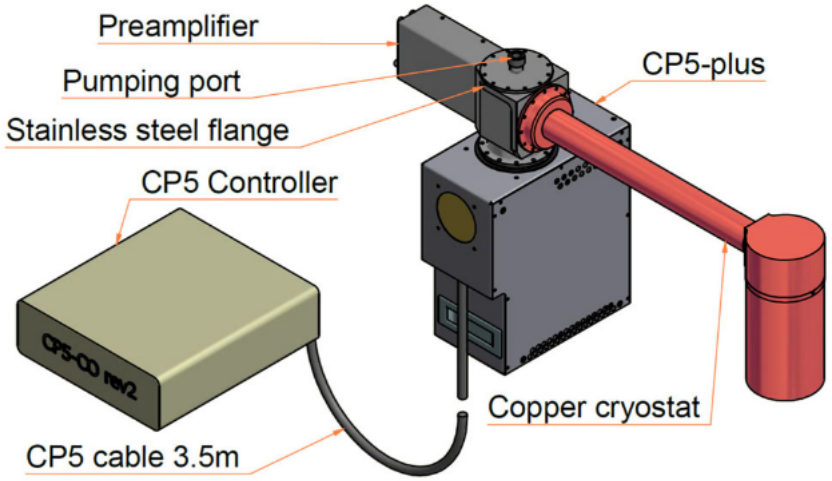

Figure 2.5.: Design of the CONUS detectors. The HPGe crystal is located inside the copper cryostat endcap. The diode is cooled by an electrical cryocooler (CP5-plus) which is controlled by an external controller. From [25].

to the boundary conditions given by the thickness of the shield design. The signals from the crystal are amplified by a preamplifier, which has an additional test input. With a function generator, hereinafter referred to as pulser, artificial test signals can be injected through the input to test the process chain of the preamplifier as the resolution.
In addition to the four detectors enclosed in the shielding at KBR, which are named CONUS-1 to CONUS-4 (or C1 to C4), a fifth detector identically in construction called CONUS-5 (C5) is available for research and development at MPIK.
The CONUS shield consists of an onion-like structure of several materials to guarantee the best shielding against cosmic, environmental, and reactor-correlated background. In total 11 tons of low background materials are used to achieve the best possible background level. The design for shallow depth application is based on the shield design of the GIOVE detector [26] developed at MPIK, which is used for material screening. To shield against external γ radiation five layers of lead (Pb) with increasing radiopurity towards the detector chamber are used, therefore a total thickness of 25 cm of lead is included in the shield. The innermost Pb-layer is made of radiopure lead partially from the Freiburg Minster with a small mean ^{210}Pb contamination of $< 1\,\mathrm{Bq\ kg^{-1}}$ [27]. The decision for lead was made due to a stronger self-absorption resulting in a lower intensity of the residual muon-induced bremsstrahlung continuum at low energies compared to copper (Cu), which is advantageous for a CEνNS detection. To shield effectively against neutrons additional layers made of pure polyethylene (PE) and borated PE, which will moderate and capture the neutrons, are installed. The (B)-doped PE is placed closer to the detector center to shield neutrons that are created by muons in the Pb of the detector

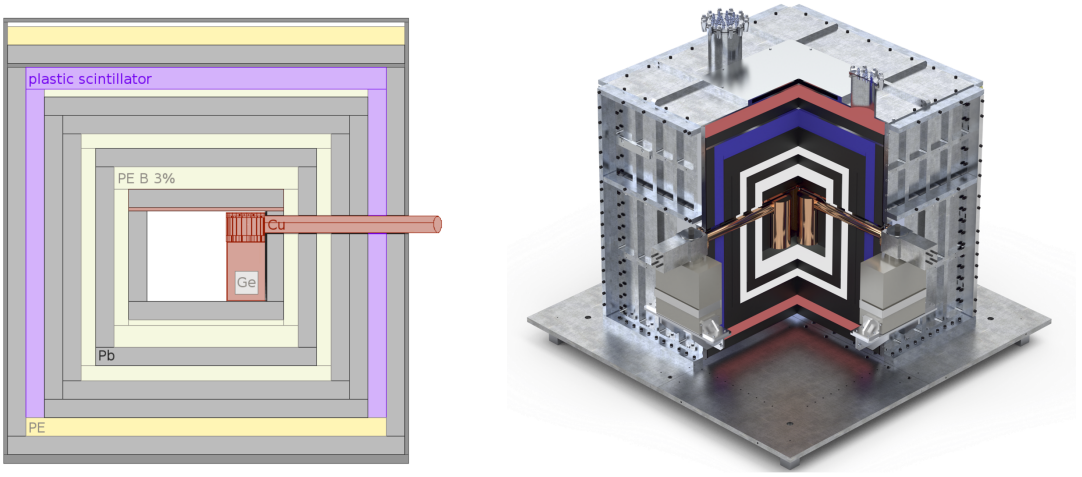

(a) (b)

Figure 2.6.: a) Side view of the CONUS shield with one detector. Displayed are the different layers of Pb (grey), PE (yellow), borated PE (light yellow), and the plastic scintillator (purple). From [28]. b) Exterior view of the CONUS setup. Here, the steel cage for earthquake safety and two detectors with cryostat are visible. From [23].

or by the reactor. To reject events induced by muons originating from cosmic rays an active muon-veto is implemented. For this purpose, a layer of plastic scintillator equipped with photomultiplier tubes (PMTs) is installed. This system allows the rejection of $\sim$ 97% of the prompt muon-induced signals in the detector. The whole setup is enclosed by a steel frame to meet the safety regulations of the nuclear power plant, especially earthquake safety, and to reduce the radon (Rn) diffusion from the outside to the inner detector chamber. For this purpose, the whole shield is flushed with air from bottles to prevent radon from entering the shield. The bottled air was stored for at least three weeks to guarantee the full decay of the Rn. All components of the CONUS shield design and the whole CONUS setup are illustrated in Figure 2.6. Here, the onion-like structure is visible with the detectors in the inner chamber. With this elaborated shield a background reduction of several orders of magnitude is achievable, depicted in Figure 2.7. The black spectrum corresponds to a measurement with CONUS-1 at KBR without shield. The background level is strongly reduced by the passive shield which is shown in the red spectrum. Finally, by applying the muon-veto (blue spectrum) a low background level of $\sim$ 10 counts $\mathrm{kg}^{-1}\mathrm{d}^{-1}\mathrm{keV}^{-1}$ in the region of interest (ROI) for the CEνNS signal is achieved.

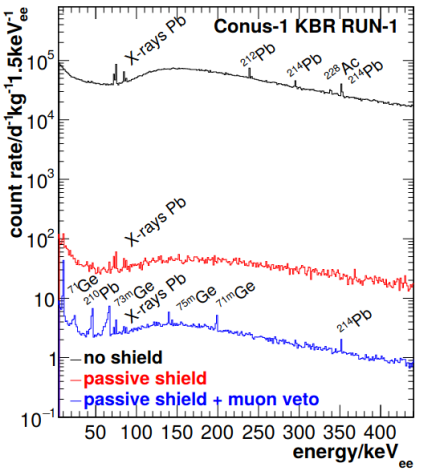

Figure 2.7.: Background suppression capability of the CONUS shield. The black line corresponds to the measured spectrum at KBR without any shielding. Only with the passive shield of Pb and PE (red line) the count rate is reduced by many orders of magnitude. Equipped with the active muon veto (blue line) another order of magnitude in reduction is achieved. From [27].

2.2.3. Results

The CONUS experiment collected data in five physics runs during the time between 2018 and 2022. Each physics run contains data collected when the reactor was running (reactor ON time) and also data during outages of the reactor (reactor OFF time) to constrain the background. Additionally, the full background of the experiment was modeled properly [27]. After each run the experimental stability conditions were improved. For Run-1 to Run-4, the integrated multichannel analyzer LYNX [29] was used. This data acquisition system (DAQ) was supplemented in Run-5 by the digital multichannel analyzer module V1782 by CAEN [30] as it offers the possibility of recording detector pulses and the choice of the triggering algorithm. Also lowering the energy threshold was possible down to 210 eV [31]. To achieve this low threshold, the environmental stability was improved, as well as further background suppression due to pulse-shape discrimination. With the data recorded during the single runs, several results regarding CEνNS and BSM physics were obtained, which are summarized in the following.

Constraints on CEνNS with Run-1 and Run-2 Data

Beginning of 2021 the CONUS experiment published the first results on CEνNS. With the analysis of 248.7 kg d reactor ON data and 58.8 kg d reactor OFF data, collected in the first two runs of the experiment between 2018 and 2019, the best limit on CEνNS in the fully coherent regime was obtained from reactor antineutrinos. The analysis was conducted in the energy ROI of $0.3 - 1$ keV. As discussed in

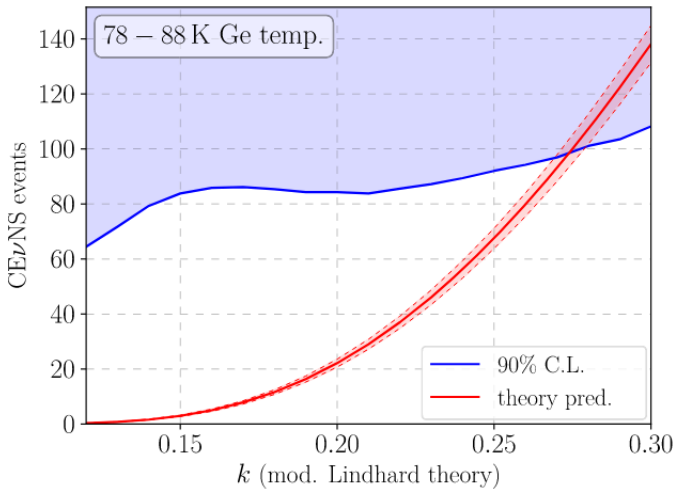

Figure 2.8.: The 90 % C.L. upper limit (blue) on the CEνNS counts measured by CONUS with data of Run-1 and Run-2. The predicted count rate is shown in red. Both curves are plotted as a function of the quenching parameter k. From [23].

Chapter 2.1.2, the ionization quenching factor QF plays a non-negligible role in CEνNS detection. Details about the quenching factor are given in the section about the quenching factor measurement below. As QF was not measured properly for the low energies for germanium at this time, the quenching parameter k was not fixed for the analysis, and therefore, the results are presented in dependence of this parameter shown in Figure 2.8. The blue line indicates the k-parameter dependent limit obtained by the analysis of the CONUS data at 90% C.L., whereas the red line indicates the expected amount of CEνNS event also in dependence of k. As no CEνNS signal was found a quenching parameter above 0.27 could be excluded.
To get reliable results for future analyses, the ionization quenching factor in Ge was measured extensively also for nuclear recoil energies in the keV range [32], which is discussed in detail in the following. The k-parameter was measured to be $k = 0.164 \pm 0.004$. With the fixed k-parameter the world-best limit can be specified to $< 0.4\,\mathrm{cts\ kg^{-1}d^{-1}}$, 17 times higher than the predicted value [33].

Constraints on BSM Physics and Neutrino Electromagnetic Properties with Run-1 and Run-2 Data

Furthermore, the CONUS Collaboration set new limits on BSM processes, including non-standard interactions (NSI) in the neutrino-quark sector, light mediators [24] and neutrino electromagnetic properties [34]. For tensor NSIs, a world best limit was set, constraining the scale of corresponding new physics to above 360 GeV, while for scalar and vector mediators competitive limits were obtained [24]. For the constraints on neutrino electromagnetic properties as the neutrino magnetic moment, CONUS data was analyzed for neutrino electron scattering. A slightly extended dataset of 689.1 kg d reactor ON and 131.0 kg d reactor OFF data with an ROI of $2 - 8$ keV was used to determine an upper limit on the effective neutrino magnetic moment of $\mu_\nu < 7.5 \cdot 10^{-11} \mu_B$ at 90 % confidence level. From this magnetic moment limit an upper bound on the neutrino millicharge of $|q_\nu| < 3.3 \cdot 10^{-12} e_0$ was derived [34]. With the accumulated exposure of the latest datasets Run-4 and Run-5, a combined analysis on neutrino electromagnetic properties is conducted in this work and will be discussed in Chapter 3.

Measurement of the Germanium Ionization Quenching Factor

The quenching factor of germanium plays a major role in the signal prediction, as well as in the data analysis of HPGe detectors.
In some materials a part of the incoming recoil energy is only partially converted into ionization energy. The residual part is converted to phonons, vibrations of the crystal lattice. The material and energy-dependent ionization quenching factor QF is defined as the ratio of the observable ionization energy E_{ee} and the deposited nuclear recoil energy E_{nr}

$$QF = \frac{E_{\text{ee}}}{E_{\text{nr}}}. \tag{2.10}$$

Theoretical predictions for the quenching factor are made by the Lindhard theory [35, 36]. Here, the energy dependence of the ionization quenching factor is described by a single free parameter k, and the observable ionization energy is given by [32]

$$E_{\text{ee}} = QF \cdot E_{\text{nr}} = \frac{kg(\epsilon)}{1 + kg(\epsilon)} \cdot E_{\text{nr}} \tag{2.11}$$

with $\epsilon = 11.5 \cdot Z^{-7/3} \cdot E_{\text{nr}}$ and $g(\epsilon) = 3\epsilon^{0.15} + 0.7\epsilon^{0.6} + \epsilon$.
The germanium quenching factor was measured extensively in the nuclear recoil energy range above 10 keV but for low recoil energies, which are the case for a CEνNS measurement at a reactor, there are only measurements with large uncertainties. Also, there are tensions between the different measurements and with the underlying theory. For this reason, the CONUS collaboration performed in cooperation with the Physikalisch-Technische Bundesanstalt (PTB) a model-independent direct

measurement of the ionization quenching factor in germanium [32]. An HPGe detector as an active target was placed in a neutron beam. Scattered neutrons were then detected in coincidence by liquid scintillator detectors in an array surrounding the germanium detector. With the measurement very low nuclear recoils in the range between $0.4\,\mathrm{keV_{nr}}$ and $6.3\,\mathrm{keV_{nr}}$ were probed. Within an extensive analysis of this data, a quenching parameter of $k = 0.164 \pm 0.004$ was found with the result of a quenching factor compatible with the Lindhard theory.

Constraints on CEνNS with Run-5 Data

Also with the data of the last run at KBR a result on CEνNS was obtained. In Run-5, data was collected between May 2021 and December 2022, where almost a full year of reactor OFF data is available due to the shutdown of nuclear reactors in Germany at the end of 2021. Regarding the environmental parameters, Run-5 is the most stable run of CONUS, but OFF data had to be excluded due to a broken AC and, thus, unstable temperatures at the end of the run. As the noise rate of the detector is highly correlated to the room temperature periods with high ambient temperature had to be excluded. More details about the cuts applied also on the CEνNS dataset can be found in Chapter 3.3.1. For the analysis, data obtained by the CAEN DAQ was used, resulting in a total exposure of 426 kg d reactor ON data and 272 kg d reactor OFF data. With this data and a detector threshold of 210 eV a new upper limit of $< 0.34\,\mathrm{cts\ kg^{-1}\ d^{-1}}$ is obtained, which is less than a factor of 2 away from the prediction [31]. Compared to the previous result, which was 17 times higher than the SM prediction, it was possible to improve the constraints on CEνNS by an order of magnitude. Within the analysis also other quenching model descriptions were tested, which are in tension with the Lindhard model, leading to the exclusion of one description.

2.2.4. Future of the CONUS Experiment

With the ending operation of the KBR reactor at the end of 2021, the gain of further neutrino data for CONUS is stopped. For this reason, the successor experiment CONUS+ has been planned and realized. CONUS+ will take data at a new reactor in Leibstadt in Switzerland with optimized detectors and improved stability. More information on the CONUS+ experiment and a detailed study about the upgraded detectors are given in Chapter 5. With the optimized and improved experiment, it will be possible to lower the threshold below 200 eV, which will enhance the probability of not only obtaining a better limit but actually measuring the CEνNS signal. The dependence of the CEνNS signal expectation on the detection threshold is depicted in Figure 2.9. Here, the expected CEνNS events are computed in dependence of the energy threshold and detector mass for an experiment similar to CONUS with a distance of 20 m to the $3.6\,\mathrm{GW_{th}}$ reactor core. With a threshold of 150 eV a signal strength of around 2000 CEνNS events per year is expected, which is almost an order of magnitude more than with the Run-5 threshold of 210 keV.

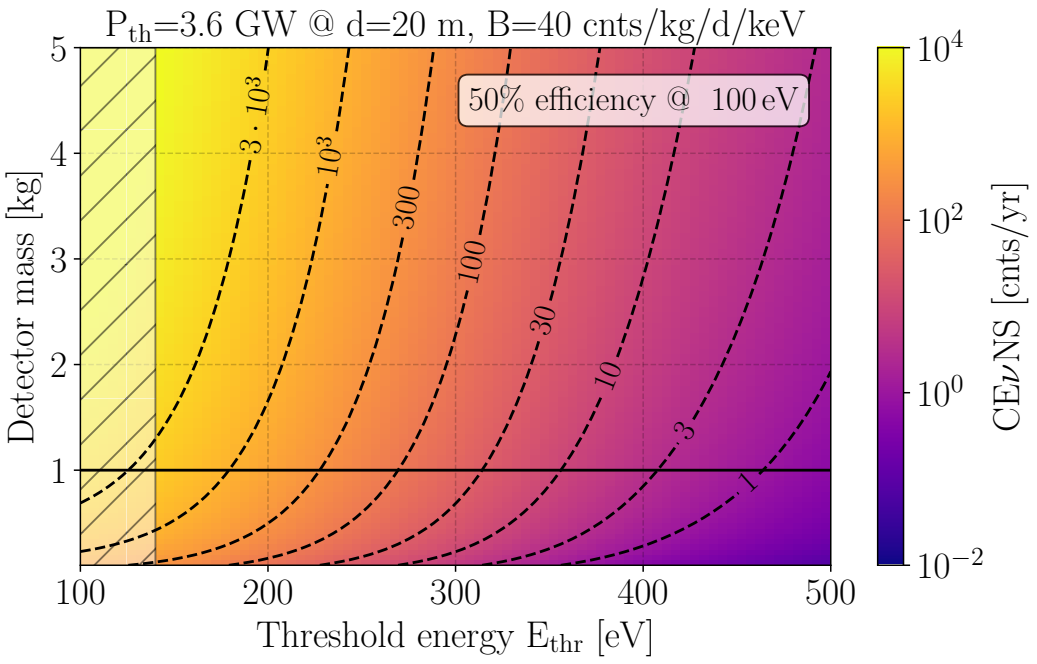

Figure 2.9.: CEνNS signal expectation in dependence of energy threshold and detector mass. For the sensitivity study a distance to the reactor of 20 m, a background level of 40 cts/kg/d/keV and a thermal reactor power of 3.6 GW$_{th}$ are assumed, as well as a detection efficiency of 50% at 100 eV. From [37].

But besides that, the already measured data of the five CONUS runs will still provide new results, for example, on BSM physics. The results obtained in a combined analysis of all runs regarding the neutrino electromagnetic properties are presented in Chapter 3.

3. Search for Neutrino Electromagnetic Properties

Besides the main design goal, the measurement of the CEνNS process, the CONUS experiment is also capable of searching for other SM and BSM interactions. As briefly mentioned in the previous chapter also a focus on neutrino electromagnetic properties, in particular on the determination of upper limits on the neutrino magnetic dipole moment (NMM) and its millicharge (NMC), was set. The newly available datasets of Run-4 and Run-5 collected between 2020 and 2023 provide a new opportunity to restrict the parameter space of these neutrino properties. For this reason, a statistical analysis is performed on the new data to investigate the neutrino magnetic moment and the millicharge, which is the topic of the present chapter. After a theoretical introduction of the neutrino electromagnetic properties in Section 3.1, the fundamentals of statistical data analysis are discussed in Section 3.2. This knowledge allows analyzing the acquired datasets for a magnetic moment and a millicharge of the neutrino, which is covered in Section 3.3. Herein, the preparation of datasets, as well as the applied analysis framework, are described. Finally, the results on neutrino electromagnetic properties, especially upper limits on the neutrino magnetic dipole moment and its millicharge, are discussed and can be found in Section 3.3.3.

3.1. Neutrino Electromagnetic Properties

In the SM the neutrino is a massless and only left-handed particle. The electric charge of the neutrino is zero, and therefore, no electromagnetic interactions are possible. A magnetic moment would require a coupling of a left-handed state with a right-handed state [38]. As the SM does not contain any right-handed neutrinos, neutrino magnetic moments do not exist. With the discovery of neutrino oscillations, which hint towards a small neutrino mass, it became obvious that the current SM is incomplete. To account for the non-zero neutrino masses the SM has to be extended. In a minimal extension of the SM with right-handed neutrinos incorporating their mass and mixing, the neutrino gains electromagnetic properties through loop processes [39, 40], which allow direct electromagnetic interaction with electromagnetic

fields and other particles [41]. The experimental search for these properties offers a direct connection to fundamental particle physics as Dirac and Majorana neutrinos can be distinguished by the different characteristics of their electromagnetic properties [39].
The most studied electromagnetic properties of the neutrino are the electric and magnetic dipole moments [39], which are summarized in the following. Some extended models also allow for a non-zero neutrino electric millicharge which is discussed in Section 3.1.4. The following summary is based on [39, 41, 42, 43].

3.1.1. Neutrino Electric and Magnetic Dipole Moments

The electric and magnetic dipole moments of the neutrino in the minimal extension of the SM are highly dependent on its fermionic nature. Therefore, the predictions for Dirac and Majorana neutrinos differ from each other. For both, the moments are calculated by loop diagrams with an initial fermion, a final fermion and a photon shown in Figure 3.1.
For Dirac neutrinos the electric dipole moment $\epsilon^{\mathrm{D}}_{kj}$ and the magnetic dipole moment μ^{D}_{kj} are given by

$$\mu^{\mathrm{D}}_{kj} \simeq \frac{3e_0 G_{\mathrm{F}}}{16\sqrt{2}\pi^2}(m_k + m_j)\left(\delta_{kj} - \frac{1}{2}\sum_{l=e,\mu,\tau} U^*_{lk}U_{lj}\frac{m_l^2}{m_W^2}\right), \tag{3.1}$$

$$i\epsilon^{\mathrm{D}}_{kj} \simeq \frac{3e_0 G_{\mathrm{F}}}{16\sqrt{2}\pi^2}(m_k - m_j)\left(\delta_{kj} - \frac{1}{2}\sum_{l=e,\mu,\tau} U^*_{lk}U_{lj}\frac{m_l^2}{m_W^2}\right), \tag{3.2}$$

with the neutrino masses m_k and m_j, the charged-lepton masses m_l with $l = e, \mu, \tau$, G_{F} the Fermi coupling constant, m_W the mass of the W-boson, the charge of the electron e_0 and the mixing matrix U. For the diagonal elements, if $k = j$, the electric dipole moment is zero and the magnetic dipole moment simplifies to

$$\mu^{\mathrm{D}}_{kk} \simeq \frac{3e_0 G_{\mathrm{F}} m_k}{8\sqrt{2}\pi^2} = 3.2 \cdot 10^{-19}\left(\frac{m_k}{\mathrm{eV}}\right)\mu_{\mathrm{B}}, \tag{3.3}$$

with $\mu_{\mathrm{B}} = \frac{e_0}{2m_{\mathrm{e}}}$ being the Bohr magneton [44]. Therefore, the magnetic dipole moment is independent of the mixing matrix and of the values of the charged-lepton masses at leading order in small ratios of m_l^2/m_W^2. With the existing constraints on the neutrino masses in the eV-range [38], the values of the magnetic dipole moment are expected to be very small. However, in different models beyond the minimally extended SM, the magnetic dipole moment can be much larger (for example [45] and [46]).
For the neutrino transition dipole moments ($k \neq j$), which are relevant to the neutrino radiative decay $\nu_k \to \nu_j + \gamma$ [44], the electric and magnetic dipole moments

are given by

$$\begin{aligned}\mu_{kj}^{\mathrm{D}} &\simeq -\frac{3e_0 G_{\mathrm{F}}}{32\sqrt{2}\pi^2}(m_k + m_j)\sum_{l=e,\mu,\tau} U_{lk}^* U_{lj}\frac{m_l^2}{m_W^2} \\ &\simeq -3.9\cdot 10^{-23}\mu_{\mathrm{B}}\left(\frac{m_k + m_j}{\mathrm{eV}}\right)\sum_{l=e,\mu,\tau} U_{lk}^* U_{lj}\frac{m_l^2}{m_\tau^2},\end{aligned} \tag{3.4}$$

$$\begin{aligned}i\epsilon_{kj}^{\mathrm{D}} &\simeq -\frac{3e_0 G_{\mathrm{F}}}{32\sqrt{2}\pi^2}(m_k - m_j)\sum_{l=e,\mu,\tau} U_{lk}^* U_{lj}\frac{m_l^2}{m_W^2} \\ &\simeq -3.9\cdot 10^{-23}\mu_{\mathrm{B}}\left(\frac{m_k - m_j}{\mathrm{eV}}\right)\sum_{l=e,\mu,\tau} U_{lk}^* U_{lj}\frac{m_l^2}{m_\tau^2}\end{aligned} \tag{3.5}$$

with m_τ the mass of the τ as $m_l^2/m_W^2 \leq m_\tau^2/m_W^2 \simeq 5\cdot 10^{-4}$. It becomes obvious that the transition magnetic dipole moment is suppressed with respect to the diagonal moment.

For Majorana neutrinos, which are their own antiparticles, only the transition electric and magnetic dipole moments exist as the diagonal moments are forbidden. The Majorana transition electric and magnetic dipole moments are given by

$$\mu_{kj}^{\mathrm{M}} \simeq -\frac{3ie_0 G_{\mathrm{F}}}{16\sqrt{2}\pi^2}(m_k + m_j)\sum_{l=e,\mu,\tau} \mathrm{Im}[U_{lk}^* U_{lj}]\frac{m_l^2}{m_W^2}, \tag{3.6}$$

$$\epsilon_{kj}^{\mathrm{M}} \simeq \frac{3ie_0 G_{\mathrm{F}}}{16\sqrt{2}\pi^2}(m_k - m_j)\sum_{l=e,\mu,\tau} \mathrm{Re}[U_{lk}^* U_{lj}]\frac{m_l^2}{m_W^2}. \tag{3.7}$$

Here, the comparison to the Dirac case is difficult as the mixing matrices are different for Majorana neutrinos due to additional phases. If charge and parity are conserved (CP conservation) two cases are possible. If ν_k and ν_j have the same phase the dipole moments are given by

$$\mu_{kj}^{\mathrm{M}} = 0, \tag{3.8}$$

$$\epsilon_{kj}^{\mathrm{M}} = 2\epsilon_{kj}^{\mathrm{D}}. \tag{3.9}$$

For opposite phases the Majorana transition dipole moments are

$$\mu_{kj}^{\mathrm{M}} = 2\mu_{kj}^{\mathrm{D}}, \tag{3.10}$$

$$\epsilon_{kj}^{\mathrm{M}} = 0. \tag{3.11}$$

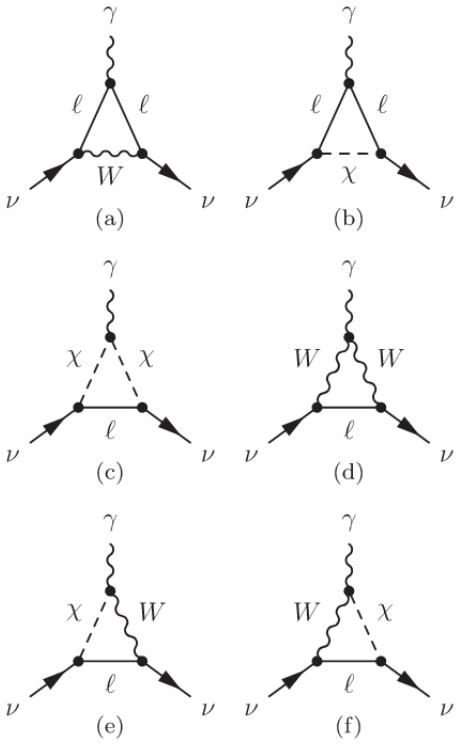

Figure 3.1.: Feynman diagrams for electromagnetic neutrino interaction in minimal extended standard model with right-handed neutrinos. Here, χ is an unphysical charged scalar boson. From [39].

3.1.2. Magnetic Moment in the Context of Elastic Neutrino Electron Scattering

The experimental measurement of elastic (anti-)neutrino electron scattering provides a good method to investigate the electromagnetic properties of the neutrino. For this purpose, solar, accelerator, or reactor neutrinos can be used. The following summary will be focused on reactor antineutrinos as in the case of CONUS, while generalization to other neutrino flavors is straightforward. For the elastic interaction of an electron antineutrino with an electron at rest in the laboratory frame

$$\overline{\nu}_\mathrm{e} + e^- \rightarrow \overline{\nu}_\mathrm{e} + e^- \tag{3.12}$$

the kinetic recoil energy of the electron T is constrained by

$$T \leq \frac{2E_\nu^2}{2E_\nu + m_\mathrm{e}}, \tag{3.13}$$

with E_ν the energy of the neutrino and m_e the mass of the electron. The cross section of the neutrino scattering on a free electron in the presence of electromagnetic

neutrino interactions is given by the sum of the SM weak and electromagnetic (EM) interactions

$$\frac{d\sigma}{dT} = \left(\frac{d\sigma}{dT}\right)_{\mathrm{SM}} + \left(\frac{d\sigma}{dT}\right)_{\mathrm{EM}}. \tag{3.14}$$

Here, the SM contribution of EνeS is

$$\left(\frac{d\sigma}{dT}\right)_{\mathrm{SM}} = \frac{G_{\mathrm{F}}^2 m_{\mathrm{e}}}{2\pi}\left[(g_{\mathrm{V}}+g_{\mathrm{A}})^2 + (g_{\mathrm{V}}-g_{\mathrm{A}})^2\left(1-\frac{T}{E_\nu}\right)^2 + (g_{\mathrm{A}}^2-g_{\mathrm{V}}^2)\frac{m_{\mathrm{e}}T}{E_\nu^2}\right] \tag{3.15}$$

with the coupling constants $g_{\mathrm{V}} = 2\sin^2(\theta_{\mathrm{W}}) + \frac{1}{2}$ and $g_{\mathrm{A}} = -\frac{1}{2}$ for electron antineutrinos. The coupling terms for electron neutrino and other flavors can be found in [39]. For $E_\nu \gg T$ this simplifies to

$$\left(\frac{d\sigma}{dT}\right)_{\mathrm{SM}} = \frac{G_{\mathrm{F}}^2 m_{\mathrm{e}}}{2\pi}(1+4\sin^2\theta_{\mathrm{W}}+8\sin^2\theta_{\mathrm{W}})\left[1+\mathcal{O}\left(\frac{T}{E_\nu}\right)\right]. \tag{3.16}$$

For $\left(\frac{d\sigma}{dT}\right)_{\mathrm{EM}}$ all possible electromagnetic neutrino interactions as a neutrino millicharge can contribute, but here the focus is only on the impact of the magnetic moment. The magnetic moment contribution to the cross section is given by

$$\left(\frac{d\sigma}{dT}\right)_{\mu_\nu} = \frac{\pi\alpha^2}{m_{\mathrm{e}}^2}\left(\frac{1}{T}-\frac{1}{E_\nu}\right)\left(\frac{\mu_\nu}{\mu_{\mathrm{B}}}\right)^2 \tag{3.17}$$

with α the fine-structure constant and μ_ν the effective magnetic moment, which is discussed in the following Section 3.1.3. With $E_\nu \gg T$ Equation 3.17 simplifies to

$$\left(\frac{d\sigma}{dT}\right)_{\mu_\nu} \approx \frac{\pi\alpha^2}{m_{\mathrm{e}}^2 T}\left(\frac{\mu_\nu}{\mu_{\mathrm{B}}}\right)^2. \tag{3.18}$$

Hence, the cross section is inversely dependent on the recoil energy of the electron. In an experiment, the existence of a neutrino magnetic moment will manifest itself in an excess of events over those predicted by SM processes and background. Due to the $1/T$-dependence of the cross section smaller magnetic moments can be probed by lowering the threshold of the experiment. The sensitivity of an experiment to the neutrino magnetic moment can be estimated by comparing Equation 3.16 and Equation 3.18 and yields

$$\mu_\nu^2 \leq \frac{G_{\mathrm{F}}^2 m_{\mathrm{e}}^3 T}{2\pi^2\alpha^2}(1+4\sin^2\theta_{\mathrm{W}}+8\sin^2\theta_{\mathrm{W}})\mu_{\mathrm{B}}^2. \tag{3.19}$$

3.1.3. Effective Magnetic Moment

In CONUS and any other neutrino experiment, the neutrino is created as a superposition of neutrino mass eigenstates. This initial superposition is again distorted by subsequent oscillations from the source to the detector. For this reason, the experimentally measured magnetic moment is not the pure theoretically predicted magnetic moment. The so-called effective magnetic moment takes into account neutrino mixing and oscillations during the distance between the detector and the source. In the following chapters, the effective neutrino magnetic moment is simply referred to as the neutrino magnetic moment. The effective magnetic moment of an antineutrino of various flavor $l = e, \mu, \tau$ measured at a distance L from the neutrino source is given by

$$\mu^2_{\overline{\nu}_l}(L, E_\nu) = \sum_j \left| \sum_k U^*_{lk} e^{\frac{i\Delta m^2_{kj} L}{2E_\nu}} (\mu_{jk} - i\epsilon_{jk}) \right|^2 . \tag{3.20}$$

As in the case of reactor experiments, the distance between source and detector is very short and therefore $\Delta m^2 L/2E_\nu \ll 1$, the effective magnetic moment can be simplified by to the effective short-baseline magnetic moment

$$\mu^2_{\nu_l}(L, E_\nu) \simeq \sum_j \left| \sum_k U^*_{lk} (\mu_{jk} - i\epsilon_{jk}) \right|^2 , \tag{3.21}$$

which is the same for neutrinos and antineutrinos. In this case, the effective magnetic moment is independent of neutrino energy and distance.
For the effective magnetic moment, several experimental limits exist up to now. The strongest limit from experimental side is obtained by the XENONnT experiment with a neutrino effective magnetic moment of $\mu_\nu \leq 6.4 \cdot 10^{-12} \mu_B$ [47]. Among the reactor experiments, the GEMMA experiment obtained the best limit with a value of $\mu_\nu \leq 2.9 \cdot 10^{-11} \mu_B$ [48, 49]. Limits on the neutrino magnetic moment can not only be set by experiments but also bounds can be derived by astrophysical observations. The strongest bound from astrophysics is obtained by observed properties as mass and brightness of globular cluster stars and yields $\mu_\nu \leq 3 \cdot 10^{-12} \mu_B$ [50]. Therefore, with the current sensitivity of the experiments and also from observations in astrophysics, it is only possible to set limits orders of magnitude above the expected values of the neutrino magnetic moment. Also, a determination between Dirac or Majorana nature is problematic as with the effective magnetic moment diagonal and transition magnetic moments are not distinguishable.
Using data from the first two physics runs Run-1 and Run-2, the CONUS experiment obtained an upper limit on the neutrino effective magnetic moment of $\mu_\nu < 7.5 \cdot 10^{-11} \mu_B$ at 90% C.L. [43, 34], which is in the range of typical reactor experiments.

3.1.4. Neutrino Electric Millicharge

Besides the introduction of a magnetic moment also a tiny charge of the neutrino is possible. Values of these neutrino millicharges are constrained from the neutrality of the hydrogen atom to $q_\nu \leq 10^{-21} e_0$ with e the electron charge. As the magnetic moment, the neutrino millicharge can be investigated using elastic neutrino electron scattering. Here, the cross section due to a millicharged neutrino is given by

$$\left(\frac{d\sigma}{dT}\right)_{\mathrm{q}_\nu} \approx \frac{2\pi\alpha}{m_\mathrm{e} T^2} q_\nu^2 \tag{3.22}$$

which adds up to the SM cross section. In contrast to the effective magnetic moment, the cross section of the millicharge contribution is inversely proportional to the squared recoil energy. By calculating the ratio between magnetic moment component and charge component of the cross section

$$R = \frac{\left(\frac{d\sigma}{dT}\right)_{\mathrm{q}_\nu}}{\left(\frac{d\sigma}{dT}\right)_{\mu_\nu}} = \frac{2m_\mathrm{e}}{T} \frac{(\frac{q_\nu}{e_0})^2}{(\frac{\mu_\nu}{\mu_\mathrm{B}})^2} \tag{3.23}$$

it is possible to obtain a bound on q_ν by demanding $R \leq 1$. The limit on the neutrino millicharge assuming only a limit on the neutrino magnetic moment can then be approximated by

$$q_\nu^2 \leq \frac{T}{2m_\mathrm{e}} \left(\frac{\mu_\nu}{\mu_\mathrm{B}}\right)^2 e_0^2. \tag{3.24}$$

Also for the neutrino millicharge, bounds were set by experiments and astrophysical observations. The strictest constraint among all experiments investigating the neutrino millicharge is set by the LZ experiment with a value of $|q_\nu| < 2.24 \cdot 10^{-13} e_0$ [51].[1] Again here, the GEMMA experiment holds the lowest upper limit among reactor neutrino experiments with a value of $|q_\nu| < 1.5 \cdot 10^{-12} e_0$ [53],[2] whereas the most stringent astrophysical constraint from a BSM prediction during supernova explosions, where the angular velocity of a star shifts due to neutrinos escaping the star, is $|q_\nu| < 1.3 \cdot 10^{-19} e_0$ [54].
The upper limit on the neutrino millicharge obtained by the CONUS experiment using Run-1 and Run-2 data and using the upper limit on the effective neutrino magnetic moment via Equation 3.24 yields $|q_\nu| < 3.3 \cdot 10^{-12} e_0$ [43, 34], which is also

[1] An even lower limit of $|q_\nu| < 1.5 \cdot 10^{-13} e_0$ was obtained by [52] in an independent analysis using the same LZ data, but regarding to [51] the combined uncertainty of background rates is underestimated in this result.

[2] The limit of $|q_\nu| < 1.5 \cdot 10^{-12} e_0$ is obtained by a rough estimation of the GEMMA NMM limit with Equation 3.24 according to [53]. A full data analysis of the GEMMA data, comparable to the analysis conducted in this work, yields an upper limit on the NMC of $|q_\nu| < 2.7 \cdot 10^{-12} e_0$ [53].

in the range of upper limits obtained by reactor experiments.

3.2. Basics of Statistical Data Analysis

In modern particle physics, the outcome of an experiment is often related to fluctuating variables. Therefore the physical result is often obtained by statistical data analysis. Also for the determination of the neutrino's magnetic moment and the millicharge in this work, a statistical data analysis is conducted. Here, some basic knowledge about statistical data analysis is summarized to follow the investigation of this work. The following section is based on [55, 56, 57, 58, 59, 43].
Often a theory gives a model for the probability that predicts the distribution of the experimental observables. Some of these parameters are unknown and are called parameters of interest. The goal of an experimental data analysis is the determination of these unknown parameters $\vec{\theta} = (\theta_1, ..., \theta_m)$ of some probability distribution. Therefore, an estimated value $\hat{\theta}$ and the corresponding uncertainty $\delta\theta$ is obtained from the data with $\theta = \hat{\theta} \pm \delta\theta$. Additional unknown parameters, such as the detector response, called the nuisance parameters are determined together with the parameters of interest. Moreover, often, there is the question of whether a new signal is present in the measured dataset of an experiment. This can be inferred from a hypothesis test.

3.2.1. Probability Density Functions

Assuming an experiment with a single continuous random variable x as an outcome, the probability of observing a value within an interval $[x, x + dx]$ is given by the probability density function (PDF) $f(x; \vec{\theta})$

$$\text{probability to observe } x \text{ in } [x, x + dx] = f(x; \vec{\theta})dx. \tag{3.25}$$

In this case, the PDF is normalized as

$$\int f(x)dx = 1. \tag{3.26}$$

If the measurement of the random variable x is repeated n times with $\vec{x} = (x_1, ..., x_n)$ the probability is given by the joint PDF

$$\text{probability to observe } x_i \text{ in } [x_i, x_i + dx_i] \text{ for all } i = \prod_{i=1}^{n} f(x_i, \vec{\theta})dx_i. \tag{3.27}$$

3.2.2. Hypothesis Tests

For a given dataset, there is the question if the observed data is in agreement with the predicted probabilities. To quantify the compatibility between two or more hypotheses based on this data a hypothesis test is conducted. The tested hypothesis is called null hypothesis H_0 and it is compared to at least one alternative Hypothesis H_1 to draw a statement about H_0. Measured variables $\vec{x} = (x_1, ..., x_n)$ in a data sample are randomly distributed according to a PDF $f(\vec{x})$ which is different under the hypotheses H_0 and H_1:

$$f(\vec{x}) = f(\vec{x}|H_0), \tag{3.28}$$
$$f(\vec{x}) = f(\vec{x}|H_1). \tag{3.29}$$

To determine whether the observed data sample better agrees with H_0 or H_1 a function of the measured variables is constructed. This test statistic $t(\vec{x})$ summarizes the information contained in the data and can be the original data values as well as it can also be multidimensional $\vec{t} = (t_1, ..., t_m)$ with lower dimension than $\vec{x}$. For each hypothesis also a PDF for the test statistic is given as $g(t|H_0)$ and $g(t|H_1)$.
To accept or reject a hypothesis based on the test statistic, a critical region is defined such that the probability for t to be observed in this region, under the assumption of H_0 to be correct, is given by the significance level α. The critical region is confined by the selection criterion t_{cut} where H_0 is accepted if $t < t_{\text{cut}}$. The significance level and therefore the probability of rejecting H_0, even if it is true, is then given by

$$\alpha = \int_{t_{\text{cut}}}^{\infty} g(t|H_0)dt. \tag{3.30}$$

If the hypothesis H_0 is accepted but the alternative hypothesis H_1 is true, the probability is given by

$$\beta = \int_{-\infty}^{t_{\text{cut}}} g(t|H_1)dt, \tag{3.31}$$

with $1-\beta$ the power of the test to discriminate against H_1. The probability densities of the test statistic under two hypotheses H_0 and H_1, the critical region, and the acceptance condition of H_0 are shown in Figure 3.2.
For a multidimensional test statistic, the definition of a critical region is difficult. For this case, the Neyman-Pearson lemma states that for a fixed α the acceptance region with the highest power $1 - \beta$ is the region of $\vec{t}$-space with

$$\frac{g(\vec{t}|H_0)}{g(\vec{t}|H_1)} > c \tag{3.32}$$

with c a constant determined by the desired level of significance α.

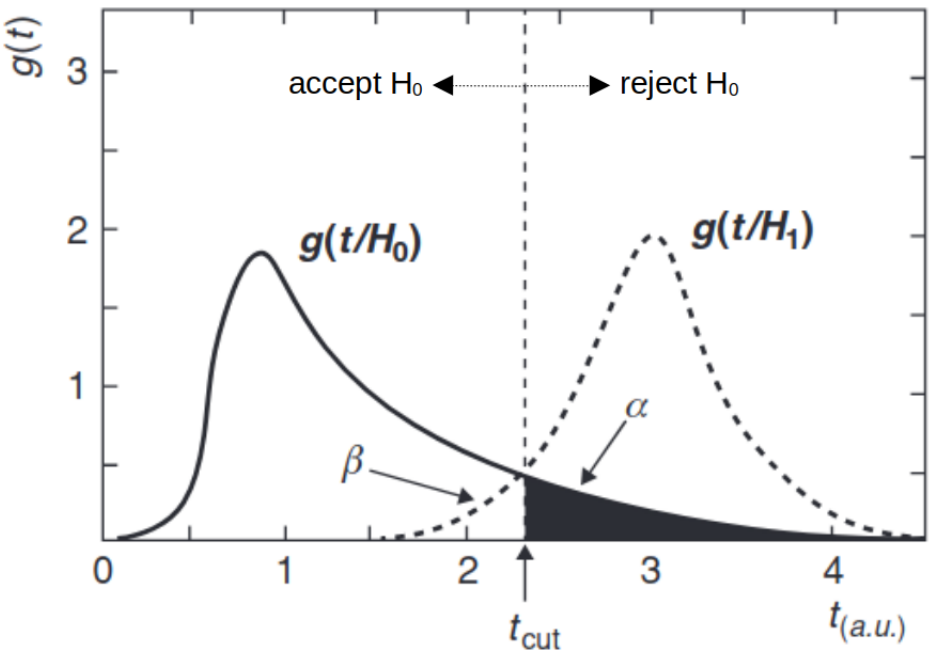

Figure 3.2.: Probability densities $g(t)$ for the test statistic t for H_0 and H_1. The null hypothesis H_0 is accepted if t is not in the critical region at $t > t_{\text{cut}}$. Modified figure taken from [59].

3.2.3. Maximum Likelihood Method

A frequent method to find an estimate for unknown parameters on a data sample is the maximum likelihood method (ML). Here, a likelihood function is constructed out of a combined probability distribution, and subsequently, the parameter set maximizing the likelihood function is determined. The likelihood function returns the value of the PDF, which is evaluated on the observed data sample, for given values of the unknown parameters and is given by

$$L(\vec{\theta}) = \prod_{i=1}^{n} f(x_i; \vec{\theta}). \tag{3.33}$$

For simplification and more stable computation of the ML function often the double negative logarithm is constructed

$$-2 \log L(x_i; \vec{\theta}) = -2 \sum_{i=1}^{n} \log f(x_i; \vec{\theta}) \tag{3.34}$$

and the estimators are found by determining the minimum of the ML function by

$$-\frac{\partial \log L(x_i;\vec{\theta})}{\partial \theta_k}\bigg|_{\hat{\theta}_k} = 0 \qquad \text{for } k = 1, ..., m. \tag{3.35}$$

If the number of observations n itself is a random variable according to a Poisson distribution with a mean value v, the likelihood function is composed of the Poisson probability for n and Equation 3.33. This extended likelihood function is then given by

$$L(v,\vec{\theta}) = \frac{v^n}{n!}e^{-v}\prod_{i=1}^{n} f(x_i;\vec{\theta}) = \frac{e^{-v}}{n!}\prod_{i=1}^{n} v f(x_i;\vec{\theta}). \tag{3.36}$$

The logarithm of the likelihood function yields

$$\log L(v,\vec{\theta}) = -v + n\log v - \log n! + \sum_{i=1}^{n}\log f(x_i;\vec{\theta}), \tag{3.37}$$

where the constant term $-\log n!$ can be neglected during the minimization process. For large data samples, it gets more complex to add the likelihood functions for each single observation. Therefore it is more efficient to analyze the data in a histogram where the individual observations are collected in N bins. All events of a bin are assumed to have roughly the same likelihood, and the number of entries in each bin is compared with the parameter-dependent prediction. The number of entries n_i in bin i follows a multinomial distribution and the expectation of events $\vec{v} = v_1, ..., v_N$ in bin i is given by

$$v_i(\vec{\theta}) = n\int_{x_i^{\min}}^{x_i^{\max}} f(x;\vec{\theta})dx \tag{3.38}$$

with n the total number of observations and $x_i^{\max}/x_i^{\min}$ the bin edges. Thus, the joint PDF is given by

$$f(\vec{n};\vec{v}) = \frac{n!}{n_1!...n_N!}\left(\frac{v_1}{n}\right)^{n_1}...\left(\frac{v_N}{n}\right)^{n_N} \tag{3.39}$$

and the binned likelihood function simplifies to

$$\log L(\vec{\theta}) = \sum_{i=1}^{N} n_i \log v_i(\vec{\theta}). \tag{3.40}$$

When the number of entries in each bin is small compared to the total number of events a Poisson distribution can be assumed and the joint PDF is given by

$$f(\vec{n};\vec{v}) = \prod_{i=1}^{N} \frac{v_i^{n_i}}{n_i!} e^{-v_i} \tag{3.41}$$

resulting in the extended binned likelihood function

$$\log L(v;\vec{\theta}) = -v + \sum_{i=1}^{N} n_i \log v_i(v;\vec{\theta}) \tag{3.42}$$

with $v = \sum_{i=1}^{N} v_i$ the mean of the Poisson distribution.

3.2.4. Likelihood Ratio Test

As stated by the Neyman-Pearson lemma the ratio of the test statistics PDF can provide a good discrimination between hypotheses. The test statistic given by the ratio of the likelihood functions

$$\lambda(\vec{x}) = \frac{L(\vec{x}|H_1)}{L(\vec{x}|H_0)} \tag{3.43}$$

can also be computed for the Poisson distributed case of binned data following Equation 3.41 and yields

$$\lambda = \frac{L(\vec{n}|\vec{v})}{L(\vec{n}\vec{n})} = \frac{f(\vec{n};\vec{v})}{f(\vec{n};\vec{n})} = e^{n-v} \prod_{i=1}^{N} \left(\frac{v_i}{n_i}\right)^{n_i}. \tag{3.44}$$

For the negative logarithm, the likelihood ratio is then given by

$$-2\log\lambda = 2\sum_{i=1}^{N}(v_i - n_i + n_i \log n_i - n_i \log v_i) \sim \chi^2 \tag{3.45}$$

which follows a χ^2 distribution according to Wilk's theorem if H_0 and H_1 are nested hypotheses where H_0 is a subset of H_1. Here, the degrees of freedom of the χ^2 distribution are equal to the difference in parameter set dimensions of the different hypotheses. The χ^2 relation is only true for a two-sided test where the parameter of interest can also be negative. For a one-sided test, which means that the parameter of interest can be infinitesimally small or even zero but not negative, the logarithmic likelihood ratio follows $\frac{1}{2}\delta + \frac{1}{2}\chi^2$ [60], with the δ-distribution accounting for the ignored negative region.
In the presence of an additional nuisance parameter μ, it is recommended to compute the profile likelihood ratio. Here, the independence of the test statistic's PDF from the nuisance parameter is approximately given. For the profile likelihood ratio the likelihood function with fixed θ and best-fit values of the maximizing nuisance

parameters $\hat{\hat{\mu}}$ is used. Using that, the ratio with the likelihood function maximized by the best-fit parameter values $\hat{\theta}$ and $\hat{\mu}$ is calculated

$$\lambda(\theta) = \frac{L(\vec{x}; \theta, \hat{\hat{\mu}})}{L(\vec{x}; \hat{\theta}, \hat{\mu})}. \tag{3.46}$$

This expression can be generalized for several nuisance parameters $\vec{\mu}$ and parameters of interest $\vec{\theta}$.
The test statistic can be modified depending on the purpose of the analysis. One case is the discovery of a positive signal with the test statistic

$$q_0 = \begin{cases} -2\log\lambda(0), & \hat{\theta} \geq 0 \\ 0, & \hat{\theta} < 0 \end{cases} \tag{3.47}$$

and the other case is the determination of an upper limit with

$$q_\theta = \begin{cases} -2\log\lambda(\theta), & \hat{\theta} \leq \theta \\ 0, & \hat{\theta} > \theta \end{cases} . \tag{3.48}$$

Here, $\lambda(0)$ is the profile likelihood ratio with $\theta = 0$.

3.2.5. P-Values and Upper Limit

For a test statistic, the p-value gives the probability of the test statistic value being greater or equal to the observed one. For data following a Gaussian distribution, it is a random variable uniformly distributed between 0 and 1 for H_0. The p-values for a profile likelihood ratio test with $q_{\text{obs}} = -2\log\lambda(\vec{\theta})$ are given according to [60] by

$$p = \int_{q_{\text{obs}}}^{\infty} \chi^2(q) dq. \tag{3.49}$$

To exclude values of a parameter of interest the p-value has to be below a certain level, for which the desired significance α usually is used. The value is then excluded at the confidence level (CL) of $1 - \alpha$.
If, in the analysis for a certain signal over the background, the obtained value is not significantly different from zero, an upper limit on the parameter can be calculated. To obtain an upper limit, the p-value has to be smaller than α, and the upper limit is determined at the point where the p-value is equal to α.

3.3. Neutrino Electromagnetic Properties Analysis of CONUS Data

With all the theoretical prerequisites discussed above the actual data can be investigated. With the available datasets a likelihood analysis to determine the electromagnetic properties of the neutrino is conducted. Here, the parameters are fitted by a maximum likelihood approach, and afterwards a likelihood ratio test is conducted to determine upper limits. In the following, the data collection periods and the dataset preparation are explained. The NMM and NMC investigations are performed with the help of an already available data analysis framework which is explained in detail in Section 3.3.2. In Section 3.3.3 the final results of this analysis on neutrino magnetic moment and millicharge are stated and discussed.

3.3.1. Dataset Preparation

For the following analysis of the neutrino's magnetic moment and millicharge new data of the last two experimental runs of the CONUS experiment, i.e. Run-4 and Run-5, is investigated. Additionally, the datasets of Run-1 and Run-2 used in previous investigations [34, 23, 24] are used. The respective data collection periods for Run-4 and Run-5 and also the corresponding thermal reactor power are sketched in Figure 3.3. For this analysis only data measured with the Canberra LYNX Digital Signal Analyzer DAQ are used. For each run, data are obtained with running reactor for a sufficiently long time period, hereinafter referred to as reactor ON. Also data measured during the outages of the reactor, hereinafter referred to as reactor OFF, are available. Before the data collection period of Run-4 the leakage test of the reactor building in September 2019 was performed. For the leakage test overpressure was generated in the containment building of KBR to test the reactor safety. To avoid any harm to the evacuated detectors, they were filled with gaseous argon to prevent the copper cryostats from imploding. After the leakage test the vacuum of the detectors was restored. For unknown reasons, this procedure changed the noise and background characteristics of the detectors, requiring the change of the diode temperatures to counteract the impact of the leakage test [61]. More information on the additional background induced by the leakage test can be found in [31]. After an optimization phase in the first half of the year, Run-4 started in September 2020. During Run-4, reactor OFF data of roughly one month was collected. In the last run of the CONUS experiment a new DAQ system (see Chapter 2.2) was installed. For the data collection, both DAQ systems were used in parallel. Run-5 started in May 2021, and reactor ON data were collected until the reactor shut down at the end of 2021, followed by a very long reactor OFF data collection period of roughly one year. Thus, Run-5 exhibits the largest exposure for both, reactor ON and OFF periods, and is the most stable run in environmental and detector conditions due to an improved setup. In Run-5, the LYNX connection of CONUS-3 was used to monitor the radon content inside the shield, and therefore, no data from this detector is

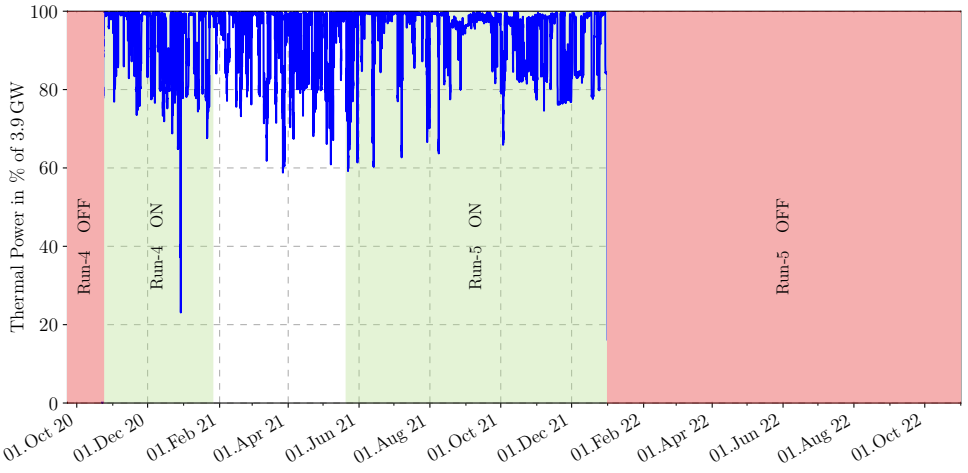

Figure 3.3.: Data collection periods of the CONUS experiment of Run-4 and Run-5 used for the NMM analysis as well as the corresponding reactor power. Periods with a running reactor are marked in green, and periods with the reactor shut down are marked in red. The blue line is indicating the thermal reactor power in % of the maximum reactor power of 3.9 GW_{th}. Figure prepared with the help of T. Rink.

available for analysis. In the OFF period the LYNX connection of CONUS-2 crashed and it was impossible to restore it. Therefore, only 43 kg d of data is available for CONUS-2 during reactor OFF. The final exposure of ON and OFF datasets for all runs are summarized in Table 3.1, where the exposure is given after data selection due to stability criteria and applying all relevant data cuts which are explained in the following sections. In all runs ^{228}Th-calibrations and measurements with a test-pulse injection are carried out regularly to monitor the stability of the data-taking. For the measured energy spectra a self-calibration with the available activation lines of the germanium was performed by W. Maneschg.
In the following, the available data of the two new runs is checked for quality and selected by stability. As the ROI for the NMM analysis is chosen to be within $[2, 20]\,keV_{ee}$ the focus on the selection is on this energy interval. Compared to the previous analysis of neutrino electromagnetic properties the energy range is extended due to an increased measuring interval by optimized settings before Run-4.
In the CAEN dataset for the CEνNS analysis of Run-5 a new background component was discovered, which is only present in reactor ON data [31]. This additional ON component is likely due to different muon veto efficiencies in reactor ON and OFF periods, as its origin is related to muon-induced background events. This background is assumed to be created by high energetic ^{16}N gamma radiation originating from the reactor and can be modeled by the muon-induced Monte Carlo spectrum. More information on the additional ON component can be found in [31]. During the Run-5 data preparation in the course of this work, it turned out that the additional

Table 3.1.: Final exposure of Run-4 and Run-5. The exposures are given after applying all data cuts and the final selection of datasets.

Run	Detector	Reactor ON in kg d	Reactor OFF in kg d
Run-4	CONUS-1	69.46	21.15
Run-4	CONUS-2	56.92	21.86
Run-4	CONUS-3	69.32	21.30
Run-4	CONUS-4	69.42	27.53
Run-5	CONUS-1	215.26	286.10
Run-5	CONUS-2	214.60	43.77
Run-5	CONUS-4	202.61	271.86
Total	-	897.59	693.57

ON component is also present in the LYNX data. Therefore, this component also has to be included in the background description for the analysis.

Quality Cuts on Data

In the data processing routine of the CONUS experiment, two important cuts are applied to the data. The first cut is the so-called Time-Difference-Distribution (TDD) cut. It is used to remove noise events based on the difference in timing of the events. For this purpose, the time difference between two events Δt starting from a certain energy threshold is calculated. An example of the TDD is shown in Figure 3.4 for CONUS-1 in the reactor ON period of Run-5. The corresponding time period is roughly two weeks. It becomes visible that the TDD can be classified into three regions. The region of physical distributed events above $\Delta t = 10^{-1.5}$ s, the region of intermediate events from $\Delta t = 10^{-1.5}$ s to $\Delta t = 10^{-4.6}$ s, containing events produced by microphonic noise, and the region of fast events below $\Delta t = 10^{-4.6}$ s, produced by wrong energy reconstruction of the LYNX DAQ system, also called spurious events. To apply the cut to the data, the lowest energy threshold still separating the physical events from the others is determined and the data are cut below this threshold. The cut thresholds for Run-4 and Run-5 of all detectors are displayed in Table 3.2. More information on the TDD cut can be found in [61, 25]. To make sure that the TDD cut is not affecting events in the ROI the spectra with and without TDD cut are compared. Exemplary, the spectra for ON and OFF in Run-5 for CONUS-1 are shown in Figure 3.5. The spectra for the other detectors and runs can be found in Appendix A. As visible, the TDD cut is affecting the spectrum only slightly or not at all proving the approach.
The second cut is the Noise-Temperature-Correlation (NTC) cut. The noise rate of the CONUS detectors is highly correlated to the cryocooler power consumption and, therefore, to the ambient room temperature [25]. As for an energy spectrum analysis, a stable and reliable event rate is crucial, time periods with unstable or

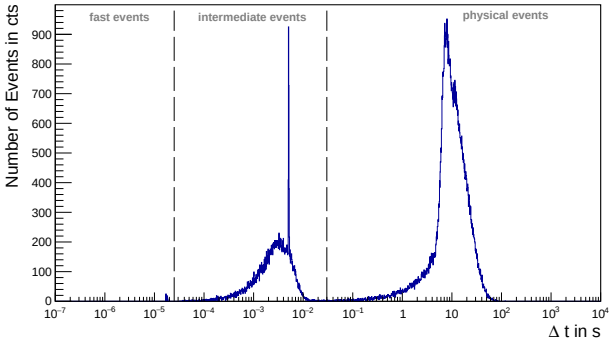

(a)

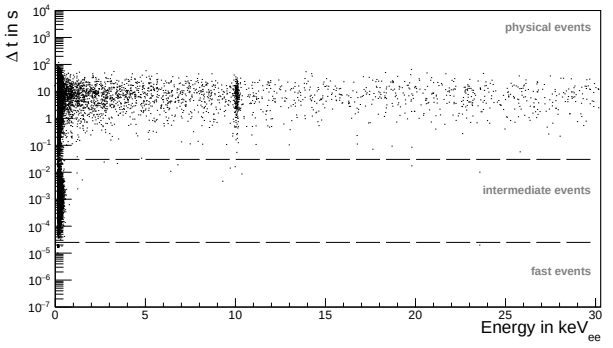

(b)

Figure 3.4.: Example Time-Difference-Distribution for Run-5 for the CONUS-1 detector during reactor ON with a cut threshold of 180 channels. Here, a time period of roughly two weeks is used. In (a), the number of events is plotted against the time difference to the next event Δt, whereas the Time-Difference-Distribution as a function of energy is shown in (b). Three populations corresponding to physical events, intermediate/microphonic events, and fast/spurious events are separated by the dotted lines at $\Delta t = 10^{-1.5}$ s and $\Delta t = 10^{-4.6}$ s.

high event rates in the ROI are rejected. This is especially important for Run-5 OFF data as the room temperature was instable due to a broken air conditioning, resulting in high fluctuating event rates of the detectors. Exemplary, the event rate over time for the CONUS-1 detector in Run-5 is shown in Figure 3.6 (a) for the whole low energy range up to 30 keV and in (b) for $2 - 20$ keV. Time periods with unusually high rate are not excluded in the plots. Similar plots for the other detectors in Run-5, as well as for Run-4 can be found in Appendix B. More information on the NTC cut can be found in [61, 25].

Table 3.2.: Time-Difference-Distribution cut thresholds for Run-4 and Run-5 for all detectors. The thresholds depend on DAQ settings and the detector.

Run	Detector	Cut threshold in channels
Run-4	CONUS-1	431
Run-4	CONUS-2	520
Run-4	CONUS-3	489
Run-4	CONUS-4	430
Run-5	CONUS-1	180
Run-5	CONUS-2	170
Run-5	CONUS-4	140

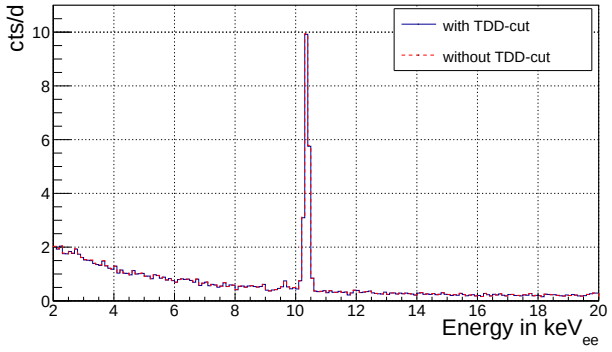

(a)

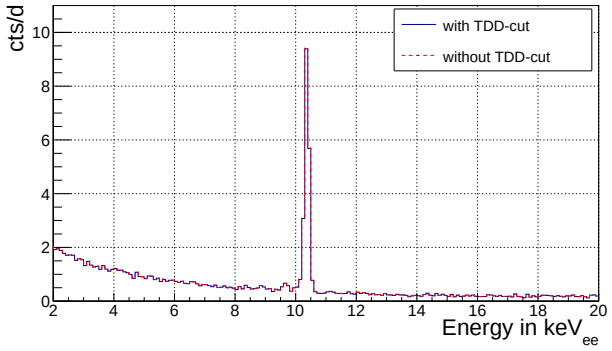

(b)

Figure 3.5.: TDD cut impact on ON (a) and OFF (b) spectra for Run-5 for the CONUS-1 detector in the region $[2, 20]\text{keV}_{\text{ee}}$. The spectrum with applied TDD cut (solid blue) matches the spectrum without TDD cut (dashed red) very well.

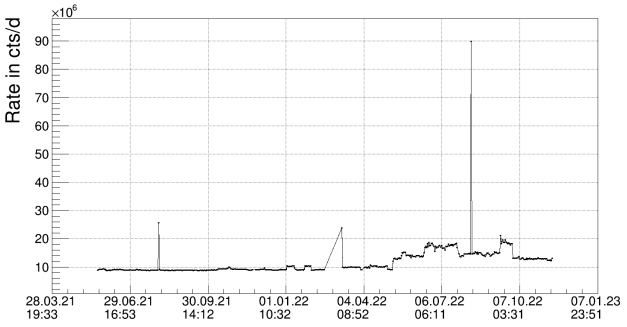

(a)

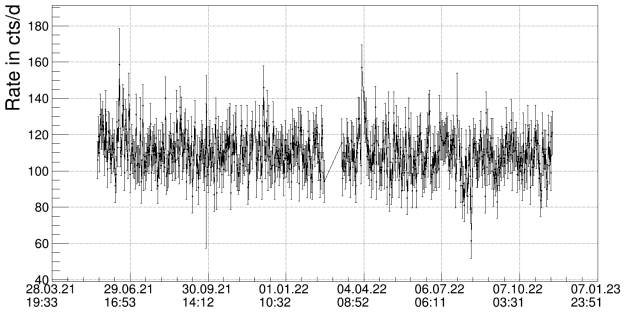

(b)

Figure 3.6.: Count rate evolution of CONUS-1 during Run-5. The full low energy range from $[0, 30]$ keV (a) is subject to strong fluctuations due to noise variations while the region of interest for the electromagnetic properties analysis of $[2, 20]$ keV is much more stable. The rate evolution is plotted before the stability cuts.

Further Treatment of Data

For the data preparation, not only the two cuts are applied, but also different other parameters are taken into account. Periods with a high count rate in the high energy spectra up to 450 keV, especially background produced by the ^{222}Rn decay chain, are excluded from the datasets. As the radon flushing system was improved after the first runs, there is no background produced by radon inside the shielding in the Run-4 and Run-5 data. Furthermore, the stability of the energy scale is considered. For this purpose, the position and resolution of the 10.4 keV line of the germanium and the 238 keV line of the regularly conducted ^{228}Th-calibrations are monitored. Examples for Run-5 are given in Figure 3.7 for the 10.4 keV line and in Figure 3.8 for the Thorium line. The stability of the resolution and respective peak position is given for both cases, indicating that no data have to be excluded from this point of view. Also here, similar plots for the other detectors in Run-5 as well as for Run-4 can be found in Appendix B. As last data selection criterion energy spectra with unusual artifacts, as they can be produced by wrong energy identification of the

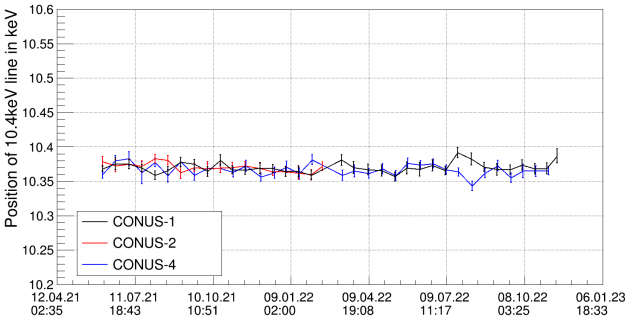

(a)

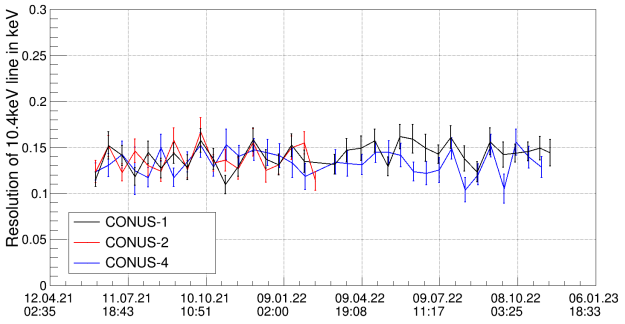

(b)

Figure 3.7.: Evolution of the 10.4 keV line during Run-5 for CONUS-1 (black), CONUS-2 (red) and CONUS-4 (blue). The position (a) and the resolution (b) of the cosmogenic activation line are constant over the whole Run-5.

DAQ, are excluded.
With this procedure, the datasets for Run-4 and Run-5 are fixed, and the exposure given in Table 3.1 is gained.

3.3.2. CONUS Data Analysis Framework

The NMM and NMC analysis of the CONUS data presented in this work is conducted with the CONUS data analysis framework developed by T. Rink and T. Hugle. The implementation is described in [43] and in [34].
For the analysis an extended binned likelihood assuming a Poisson distribution is used. Here, the reactor ON and OFF data are fitted simultaneously where the ON data is treated as a combination of signal and background and the OFF data as background only. The NMM or NMC signals are respectively included in the fit of the reactor ON datasets as signal parameters whereas the fit of the reactor OFF datasets provides additional information on the nuisance parameters and the background. The nuisance parameters, such as detector-related input and background normalization, are included in the likelihood function via Gaussian pull terms. In the following the incorporated nuisance parameters and the background description

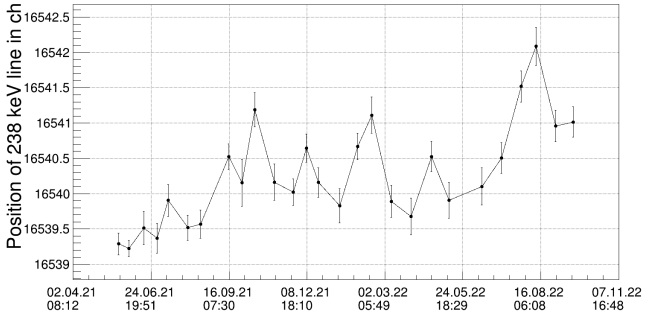

(a)

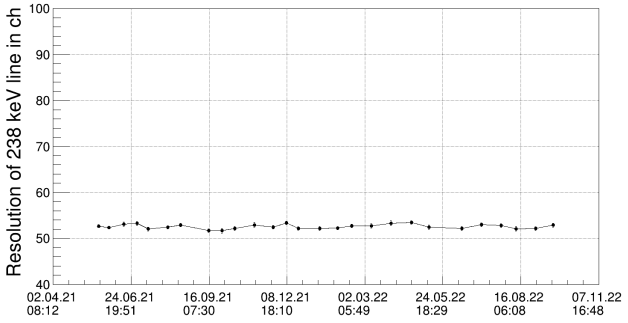

(b)

Figure 3.8.: Evolution of the 238 keV line by ^{228}Th-calibrations for CONUS-1 during Run-5. The evolution of the peak position is depicted in (a) while the resolution is shown in (b).

are covered in detail.

Background Model and Nuisance Parameters

The background description of the CONUS experiment was developed by J. Hakenmüller [61, 27] by Monte Carlo simulations of the individual background components. During the course of this work, the simulations were evaluated for the corresponding detectors and run times of Run-4 and Run-5, and input spectra for the analysis code were produced. For the analysis, the background model is then multiplied with the corresponding detection efficiency and the normalization b_{mc}, which are fitted as nuisance parameters. The uncertainties of the background description are assumed to be negligible [43].
Due to the leakage test described in Section 3.3.1, the background increased for all detectors with different strengths. Since this background is not part of the background model, it has to be included in the analysis as an additional component, from now on referred to as leakage component. For the leakage component different

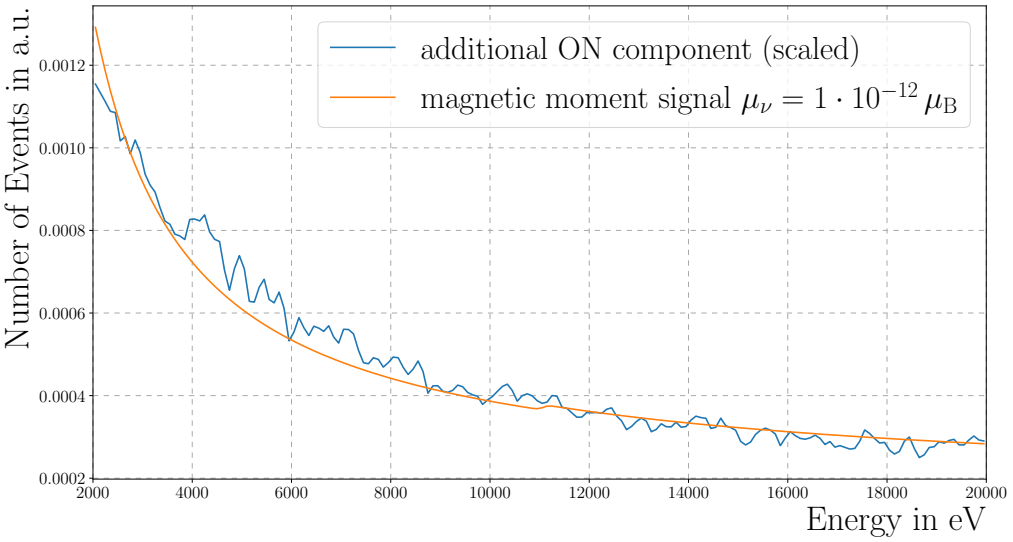

Figure 3.9.: Additional ON component (blue) and signal for an example neutrino magnetic moment of $\mu_\nu = 1 \cdot 10^{-12}\,\mu_B$ (orange). For shape comparability, the additional ON component is scaled to the magnetic moment signal.

functions were tested. The three-parameter-function

$$f_{\text{leakage}}(x) = p_1 \cdot e^{-p_2 \cdot x + p_3} \tag{3.50}$$

fitted the data best for the energy range above 2 keV. In the likelihood function, these three parameters are additionally fitted as nuisance parameters without pull. Moreover, the additional ON component $b_{\text{add.ON}}$ for Run-5 described in Section 3.3.1 has also to be modeled. For this, the simulated muon-induced component of the background model is added with a fitted normalization parameter. A possible difficulty for the likelihood fit is the similarity in shape of the additional ON component and a possible magnetic moment signal in the higher energy range shown in Figure 3.9 for the CONUS-1 detector. Here, the additional ON component in blue is scaled to match the exemplary signal of a magnetic moment of $\mu_\nu = 1 \cdot 10^{-12}\,\mu_B$ in orange. As they both follow almost the same trajectory a likelihood fit can get problems to distinguish between the two components. This is reflected in a correlation of the fit parameters described in Section 3.3.3.
All additional parameters describing the detectors and the reactor are treated as nuisance parameters. During the analysis they are determined, additionally to the NMM and NMC signal parameters, from data. At the same time, the parameter space is constrained by a pull term on the corresponding parameter, which contains the previously externally determined value of the parameter, as well as the corresponding uncertainty. The nuisance parameters include the active mass of the

detectors m_i, the corresponding detection efficiencies c_i^{eff}, the energy scale calibration uncertainty ΔE_i as well as the reduced reactor fluxes $\phi_{\text{reduced,i}}$, which are separated from their spectral shape information. More information on these parameters can be found in [43]. The 41 additional parameters of the reactor antineutrino spectrum dN/dE_ν are fixed to their best-fit values and the spectrum is not fitted. Therefore the corresponding pull term is constant. The uncertainty on the shape of the reactor spectrum is negligible [34]. For the NMM and NMC analysis of this work the reduced reactor fluxes and the reactor antineutrino spectra were kindly provided by T. Rink.

Implementation of Likelihood Function

With the background model and all nuisance parameters, the likelihood function for the analysis is then given by

$$\begin{aligned} -2\log L = &-2\log L_{\text{ON}} - 2\log L_{\text{OFF}} \\ &+ \sum_i (\mu_i - \mu_i^{\text{meas}})^{\mathbf{T}} \text{Cov}_i^{-1} (\mu_i - \mu_i^{\text{meas}}) \\ &+ \sum_i \frac{(\mu_i - \mu_i^{\text{meas}})^2}{\sigma^2_{\mu_i^{\text{meas}}}}, \end{aligned}$$

where $\sum_i (\mu_i - \mu_i^{\text{meas}})^{\mathbf{T}} \text{Cov}_i^{-1} (\mu_i - \mu_i^{\text{meas}})$ accounts for the correlation of the reactor antineutrino spectrum bins. As the spectra are not fitted, this term is irrelevant to the fit. $\sum_i \frac{(\mu_i - \mu_i^{\text{meas}})^2}{\sigma^2_{\mu_i^{\text{meas}}}}$ is the Gaussian pull term for all other nuisance parameters. The likelihood functions for reactor ON and OFF are then functions of all detector-related quantities as the active mass and the efficiencies, the uncertainty on the energy scale, and the reduced reactor flux.
With the above-mentioned parameters the expected number of events in the ON spectrum of detector i in the presence of an NMM is given by

$$\begin{aligned} N_i^{\text{ON}}(E) = &N_{\text{NMM}}(E - \Delta E_i, \mu_\nu, \phi_{\text{reduced,i}}, m_i, c_i^{\text{eff}}, (dN/dE_\nu)_i) \\ &+ N_{\text{E}\nu\text{ES}}(E - \Delta E_i, \phi_{\text{reduced,i}}, m_i, c_i^{\text{eff}}, (dN/dE_\nu)_i) \\ &+ \epsilon_i^{\text{ON}} \cdot (b_{i,\text{ON}} \cdot \frac{t_{i,\text{ON}}}{t_{i,\text{OFF}}} + b_{i,\text{add.ON}}) \end{aligned} \tag{3.51}$$

with N_{NMM} the number of signal counts due to an existing magnetic moment μ_ν and $N_{\text{E}\nu\text{ES}}$ the number of events due to elastic neutrino electron scattering.
Additionally to the events by a non-zero magnetic moment and EνES, the events in the reactor ON spectrum are influenced by the background events b_{ON} in the corresponding runtime t_{ON} of the data collection periods and the efficiency of the muon veto ϵ. For the data analysis of Run-5, the additional ON component has to be added, which is not present for the other runs.
Compared to the previous analysis in [34] the NMC is not only estimated by Equation

3.24, but a full analysis comparable to the NMM is conducted. Therefore, the same likelihood functions as described above are also valid for the NMC with the signal expectation N_{NMC} for a non-zero neutrino millicharge. For the analysis, it is assumed that no NMM is present besides the NMC.
Following the same approach as for reactor ON, the number of events in the OFF spectrum is only determined by the background component and is given by

$$N_i^{\mathrm{OFF}}(E) = \epsilon_i^{\mathrm{OFF}} \cdot b_{i,\mathrm{OFF}}. \tag{3.52}$$

The background for the ON and OFF cases comprises the background nuisance parameter for the normalization, all corresponding efficiencies, and the background model for the respective case. Additionally, the background leakage component is added and the background events are given by

$$b_{i,\mathrm{ON}} = c_i^{\mathrm{eff}} \cdot b_{i,\mathrm{mc}} \cdot f^i_{\mathrm{bkg,ON}}(E - \Delta E) + n_{\mathrm{binning}} \cdot f^i_{\mathrm{leakage}}(E) \tag{3.53}$$

$$b_{i,\mathrm{OFF}} = c_i^{\mathrm{eff}} \cdot b_{i,\mathrm{mc}} \cdot f^i_{\mathrm{bkg,OFF}}(E - \Delta E) + n_{\mathrm{binning}} \cdot f^i_{\mathrm{leakage}}(E) \tag{3.54}$$

with $f_{\mathrm{bkg,ON/OFF}}$ the function describing the background model events for ON and OFF and n_{binning} the chosen binning of the data and background model histograms. To determine signals of NMM and NMC, a binned profile likelihood ratio test, as described in the previous section, is conducted with H_0 the background-only hypothesis and H_1 the signal + background hypothesis. Here, the NMM/NMC signal is fixed to zero for H_0. In the case of zero signal in the best-fit, an upper limit can be calculated. For this purpose, the p-values of several likelihood ratio tests are computed. For each likelihood ratio test the NMM/NMC parameter is fixed to a value in the range of 10^{-12} to 10^{-9}.

3.3.3. Results on Neutrino Magnetic Moment and Millicharge obtained from CONUS Data

With the analysis procedure described above the CONUS Run-4 and Run-5 data is analyzed for a NMM and NMC. For both, a broader energy interval of $2 - 20\,\mathrm{keV}$ is chosen compared to the previous analysis conducted in [43, 34]. This is due to the improved settings after Run-3 where energies up to 30 keV are available. The interval is limited at high energies to 20 keV due to a background line between 23 keV and 25 keV and is limited to low energies at 2 keV to preserve a high exposure with very good measurement stability. The energy range from 8 keV to 12 keV is excluded from the investigation due to the cosmogenic activation lines of germanium. The measured data and the background model data are prepared as histograms with a binning of 100 eV. The data of CONUS-3 in Run-4 are temporarily excluded from the following analysis due to a more sophisticated and time-consuming background model calculation.
Subsequently, also a combined analysis of the new runs 4 and 5 with the already analyzed Run-1 and Run-2 (see Chapters 2.2.3 and 3.1.3) is conducted, hereinafter referred to as combined dataset.
In the following, the expected sensitivities for the given datasets are discussed, as well as the stability of the likelihood fit. Here, only CONUS-1 in Run-5 is shown as an example; the plots for the remaining detectors and runs can be found in Appendix C and D. Finally, the obtained upper limits on NMM and NMC are presented.

Sensitivity Study on Magnetic Moment and Millicharge of the Neutrino

For the available datasets, it is expected to derive only an upper limit on the NMM and NMC. Therefore an expected sensitivity of these datasets can be computed. For the expected sensitivity, the median significance of a hypothesis to be tested is determined. There, the significance is obtained under the assumption of an alternative hypothesis. Here, the ability to reject different values of the parameter of interest is given. For the case of exclusion limits the expected sensitivity is given by the median significance of rejecting a non-zero value of the parameter using data generated under the assumption of the H_0 hypothesis.
To calculate the expected sensitivity on an upper limit of the NMM and NMC, all nuisance parameters are sampled with sufficient amount from a normal distribution with the mean taking the expected or measured values and their corresponding uncertainties. For these parameters, the background spectrum and its Poissonian fluctuation are calculated. A profile likelihood ratio test is performed with the H_0 hypothesis of zero NMM and NMC and the H_1 hypothesis with an NMM or NMC parameter determined during the minimization of the corresponding likelihood. For the sensitivities of Run-4 and Run-5 a sample size of 2000 is used, whereas for the combined sensitivities including Run-1 and Run-2 6000 samples are used.
The median sensitivity on the NMM is given in Table 3.3, as well as on the NMC in Table 3.4. For both cases, the 1σ, 2σ, and 3σ ranges are given additionally. The

Table 3.3.: Median Sensitivity for the upper limit on the neutrino magnetic moment for Run-4 and Run-5, as well as for the combined dataset. For Run-4 and Run-5, a ROI of $2 - 20\,\mathrm{keV}$ is assumed, while for Run-1/2 a ROI of $2 - 8\,\mathrm{keV}$ is used. Additionally to the median sensitivity, the 1σ, 2σ, and 3σ ranges are given.

Combined Runs	Sensitivity NMM	1σ Range	2σ Range	3σ Range
Run-4, Run-5	$5.07 \cdot 10^{-11}$	$[4.80 \cdot 10^{-11}, 5.49 \cdot 10^{-11}]$	$[4.67 \cdot 10^{-11}, 5.69 \cdot 10^{-11}]$	$[4.49 \cdot 10^{-11}, 5.73 \cdot 10^{-11}]$
Run-1/2, Run-4, Run-5	$4.39 \cdot 10^{-11}$	$[4.14 \cdot 10^{-11}, 4.70 \cdot 10^{-11}]$	$[4.02 \cdot 10^{-11}, 4.87 \cdot 10^{-11}]$	$[3.94 \cdot 10^{-11}, 4.94 \cdot 10^{-11}]$

Table 3.4.: Median Sensitivity for the upper limit on the neutrino millicharge for Run-4 and Run-5, as well as for the combined dataset. For Run-4 and Run-5, a ROI of $2 - 20\,\mathrm{keV}$ is assumed, while for Run-1/2 a ROI of $2 - 8\,\mathrm{keV}$ is used. Additionally to the median sensitivity, the 1σ, 2σ, and 3σ ranges are given.

Combined Runs	Sensitivity NMC	1σ Range	2σ Range	3σ Range
Run-4, Run-5	$8.28 \cdot 10^{-13}$	$[7.73 \cdot 10^{-13}, 8.80 \cdot 10^{-13}]$	$[7.43 \cdot 10^{-13}, 9.12 \cdot 10^{-13}]$	$[7.31 \cdot 10^{-13}, 9.34 \cdot 10^{-13}]$
Run-1/2, Run-4, Run-5	$7.32 \cdot 10^{-13}$	$[6.48 \cdot 10^{-13}, 7.86 \cdot 10^{-13}]$	$[6.64 \cdot 10^{-13}, 8.16 \cdot 10^{-13}]$	$[5.74 \cdot 10^{-13}, 8.37 \cdot 10^{-13}]$

expected sensitivity on the NMM of the combined dataset is $4.39 \cdot 10^{-11}\,\mu_\mathrm{B}$, while the sensitivity on the NMC is $7.32 \cdot 10^{-13}\,e_0$. Compared to the previous analyses with values of $\mu_\nu < 7.5 \cdot 10^{-11}\mu_\mathrm{B}$ and $|q_\nu| < 3.3 \cdot 10^{-12}e_0$, a major improvement is expected from the combined dataset regarding NMM and NMC. With this sensitivity, it would be possible to set a new best limit on NMC among the reactor neutrino experiments, while the sensitivities set by dark matter experiments cannot be achieved.

Best Fitting Results for Free and Fixed Neutrino Magnetic Moment

Before determining the upper limits on the NMM a single fit is conducted. Here, two cases are possible: fixing the NMM parameter to zero to check the fit performance of the H_0 hypothesis and allowing the NMM parameter to vary in order to determine the best-fit values of the underlying dataset. The likelihood fit result of CONUS-1 in Run-5 is shown for the H_0 hypothesis in Figure 3.10 for the reactor ON data as well as for the reactor OFF data. Additionally the residuals (data − fit) are shown below. In Figure 3.11 the results for the H_1 hypothesis with no restrictions on the NMM parameter in the fit are illustrated. For both cases, the fit stability is guaranteed, and the fit residuals do not show hints for hidden systematic effects not accounted for in the likelihood. The best-fit value for the NMM parameter in H_1 is zero and no additional events due to a non-zero magnetic moment are included in the fit.
By individually scanning all likelihood parameters over their valid parameter space a sanity check of the fit can be done. For the scan over the likelihood, one parameter is chosen, and all remaining parameters are minimized, resulting in 1D profiles. For the parameters with Gaussian pull term, a parabola shape of the profile indicates a smooth likelihood determination of the parameter. The resulting profiles for all fit

parameters can be found in Figure 3.12. A smooth profile calculation is given for the efficiency parameter c_{eff} in Figure 3.12 (b), the fiducial mass m (d), the reduced flux ϕ_{reduced} (e), the background normalization b_{mc} (f), the additional ON component $b_{\text{add.ON}}$ (g) and one of the leakage test component parameters p_2 (i). As expected for the NMM parameter (a) no minimum is found. For the energy scale uncertainty dE (c) two possible minima are found, which is in general not problematic, but results in a small instability for certain regions of the likelihood function's parameter space. For the first leakage test component parameter p_1 (h) higher values are preferred, while for the third leakage test component parameter p_3 (j) the likelihood profile is flat at almost zero.
Furthermore, the correlation of the likelihood parameters is checked to ensure the stability of the fit. An example matrix for CONUS-1 in Run-5 is shown in Table 3.5. Here, a positive correlation is indicated by shades of red depending on the strength while a negative correlation is indicated in blue. In the correlation matrix, a few features are noteworthy, such as a tiny negative correlation of the magnetic moment with the additional ON component normalization of -0.094. This is due to the fact that the shape of the expected magnetic moment and the additional ON component is very similar as shown in Section 3.3.2. Moreover, the additional ON component normalization is weakly correlated with the normalization of the background model b_{mc} by -0.3. As both parameters are a normalization of the background their correlation is not too problematic. A stronger negative correlation between the parameter for the efficiencies and the normalization of the background model is given with -0.46, whereas a stronger positive correlation of 0.56 is given for b_{mc} with the second leakage test component parameter. All parameters of the leakage test component are correlated with each other where p_1 and p_3 are directly anticorrelated. A solution to this problem can be a different parametrization of the leakage test component. As stated in Section 3.3.2 the chosen parametrization fitted the best and no other description was found.
The overall fit stability is given for all detectors of Run-4 and Run-5, whereby CONUS-2 in both runs and CONUS-4 in Run-4 reveals a small but not significant NMM signal. The respective best-fit values, parameter profiles, and correlation matrices can be found in Appendix C.

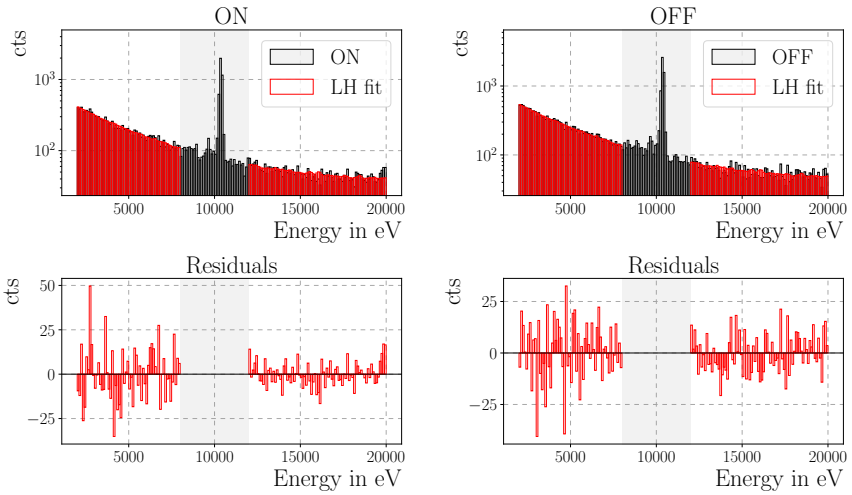

Figure 3.10.: Best-fit result of CONUS-1 in Run-5 for the H_0 hypothesis assuming zero magentic moment. On the left side, the reactor ON spectrum (top) is shown with respective residuals of (data - fit) (bottom), whereas the OFF spectrum is shown on the right side. In both cases, the data (black) is shown with the corresponding likelihood fit (red). The grey shaded area is excluded from the fit due to the activation lines of the germanium.

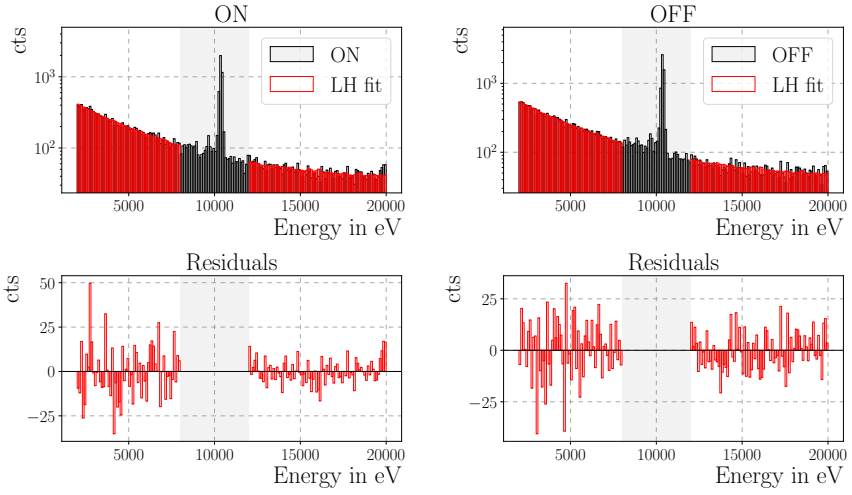

Figure 3.11.: Best-fit result of CONUS-1 in Run-5 for the H_1 hypothesis with free magnetic moment parameter. On the left side, the reactor ON spectrum (top) is shown with respective residuals of (data - fit) (bottom), whereas the OFF spectrum is shown on the right side. In both cases, the data (black) is shown with the corresponding likelihood fit (red). The grey shaded area is excluded from the fit due to the activation lines of the germanium. For the best-fit case, no additional events due to a non-zero magnetic moment are found.

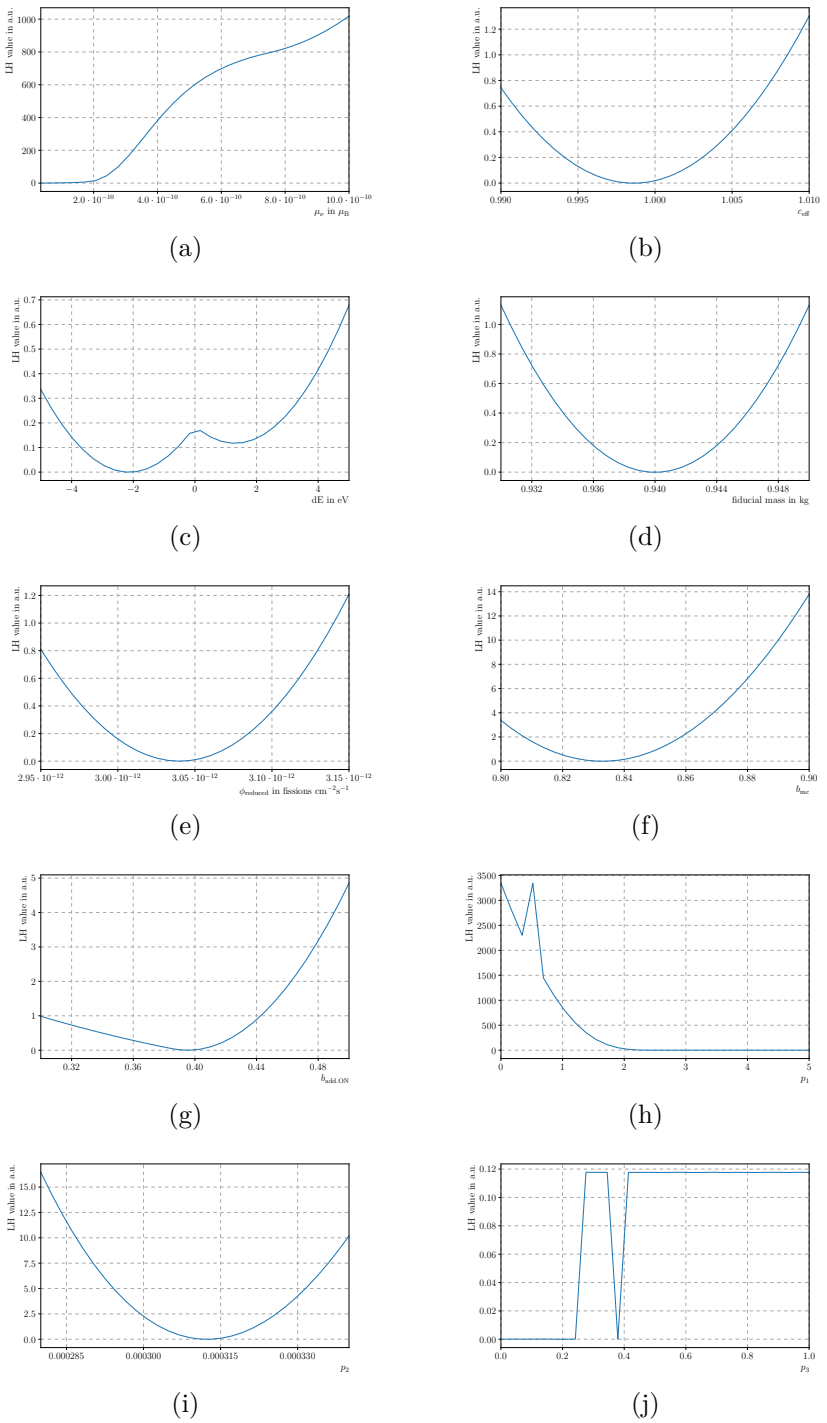

Figure 3.12.: 1D profiles of all likelihood fit parameters for CONUS-1 in Run-5 for the magnetic moment investigation. The respective parameter is scanned over its valid parameter range, while all other parameters are minimized with respect to it. The scanned parameters are the NMM μ_ν (a), the efficiency c_{eff} (b), the energy scale uncertainty dE (c), the fiducial mass m (d), the reduced flux ϕ_{reduced} (e), the background normalization b_{mc} (f), the additional ON component $b_{\text{add.ON}}$ (g) and the three parameters of the leakage test component (h)-(j). On the y-axis, the likelihood value in a.u. is shown.

Table 3.5.: Correlation matrix of the likelihood parameters for CONUS-1 Run-5 for the NMM investigation. The color of the cells indicates the strength of the correlation, where red is positively correlated and blue is negatively correlated.

	μ_ν	ϕ_{reduced}	m	dE	c_{eff}	$b_{\text{add.ON}}$	b_{mc}	p_1	p_2	p_3
μ_ν	1	0	0	0	0	-0.094	0	0	0	0
ϕ_{reduced}	0	1	0	0	0	0	0	0	0	0
m	0	0	1	0	0	0	0	0	0	0
dE	0	0	0	1	0	0	0	0	0	0
c_{eff}	0	0	0	0	1	0	-0.455	0	0	0
$b_{\text{add.ON}}$	-0.094	0	0	0	0	1	-0.322	0	0	0
b_{mc}	0	0	0	0	-0.455	-0.322	1	0	0.561	0
p_1	0	0	0	0	0	0	0	1	0.069	-0.999
p_2	0	0	0	0	0	0	0.561	0.069	1	0
p_3	0	0	0	0	0	0	0	-0.999	0	1

Best Fitting Results for Free and Fixed Neutrino Millicharge

Also for the NMC, the same procedure as for the NMM single fits can be performed. Again the fit performance for the H_0 hypothesis, with the NMC parameter fixed to zero, and the performance of a free NMC fit is checked for all datasets individually. The likelihood fit of CONUS-1 in Run-5 is shown for the H_0 hypothesis in Figure 3.13 for the reactor ON data and the reactor OFF data. Again, the residuals (data − fit) are shown below. In Figure 3.14 the results for the H_1 hypothesis with no restrictions on the NMC parameter in the fit are illustrated. For both cases, the fit stability is guaranteed, and the fit residuals do not show hints of hidden systematic effects not accounted for in the likelihood function. The best-fit value for the NMC parameter of H_1 is zero and no additional events due to a non-zero millicharge are included in the fit.
Also in the case of NMC, the likelihood values for individual parameters are tested over their whole parameter space. The resulting profiles for all likelihood parameters can be found in Figure 3.15. As expected, a smooth profile calculation is given for the efficiency parameter c_{eff} in Figure 3.12 (b), the fiducial mass m (d), the reduced flux ϕ_{reduced} (e), the background normalization b_{mc} (f), the additional ON component $b_{\text{add.ON}}$ (g) and one of the leakage test component parameters p_2 (i). For the NMC parameter (a) no minimum is found reflecting the best-fit value with free NMC parameter as expected. The energy scale uncertainty dE (c), the first leakage test component parameter p_1 (h), and the third leakage test component parameter p_3 (j) show similar behavior as in the case of the NMM.
The correlation matrix of the NMC likelihood fit parameters can be found in Table 3.6 for CONUS-1 in Run-5. Also for the NMC, a positive correlation is indicated by shades of red depending on the strength, while a negative correlation is indicated in blue. In contrast to the magnetic moment, the millicharge parameter is not corre-

Table 3.6.: Correlation matrix of the likelihood parameters for CONUS-1 Run-5 for the NMC investigation. The color of the cells indicates the strength of the correlation, where red is positively correlated and blue is negatively correlated.

	$\lvert q_\nu \rvert$	ϕ_{reduced}	m	dE	c_{eff}	$b_{\text{add.ON}}$	b_{mc}	p_1	p_2	p_3
$\lvert q_\nu \rvert$	1	0	0	0	0	0	0	0	0	0
ϕ_{reduced}	0	1	0	0	0	0	0	0	0	0
m	0	0	1	0	0	0	0	0	0	0
dE	0	0	0	1	0	0	0	0	0	0
c_{eff}	0	0	0	0	1	0	-0.452	0	0	0
$b_{\text{add.ON}}$	0	0	0	0	0	1	-0.321	0	0	0
b_{mc}	0	0	0	0	-0.452	-0.321	1	0	0.548	0
p_1	0	0	0	0	0	0	0	1	0.092	-0.974
p_2	0	0	0	0	0	0	0.548	0.092	1	0.091
p_3	0	0	0	0	0	0	0	-0.974	0.091	1

lated with the additional ON component parameter due to a slightly different shape of the respective spectra. Besides that, the correlations between the fit parameters are comparable to the NMM fit.
The overall fit stability is also given for the NMC likelihood fit for all detectors of Run-4 and Run-5. Only CONUS-2 and CONUS-4 in Run-4 indicate a small but not significant NMC signal. The respective best-fit values, parameter profiles, and correlation matrices can be found in Appendix D.

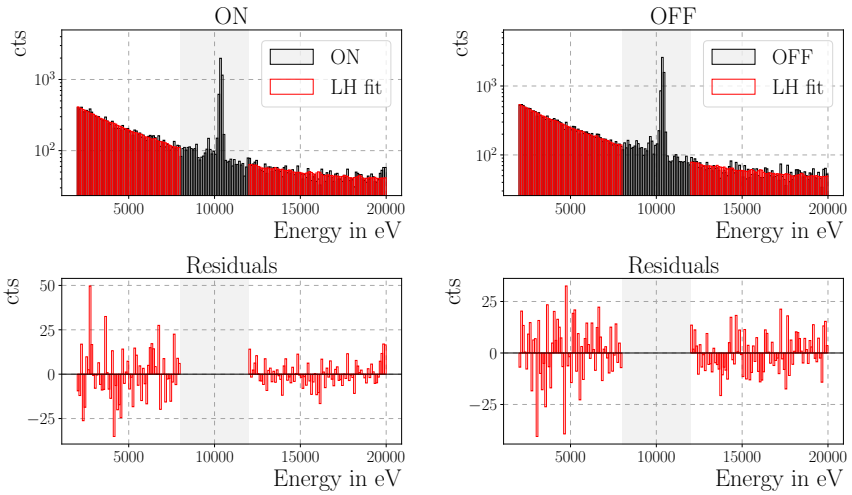

Figure 3.13.: Best-fit value of CONUS-1 in Run-5 for the H_0 hypothesis assuming zero millicharge. On the left side, the reactor ON spectrum (top) is shown with respective residuals of (data - fit) (bottom), whereas the OFF spectrum is shown on the right side. In both cases, the data (black) is shown with the corresponding likelihood fit (red). The grey shaded area is excluded from the fit due to the activation lines of the germanium.

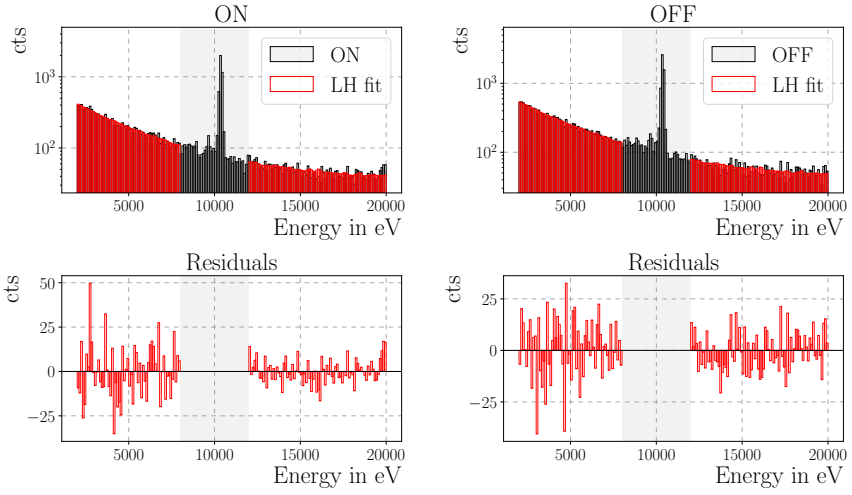

Figure 3.14.: Best-fit value of CONUS-1 in Run-5 for the H_1 hypothesis with free millicharge parameter. On the left side, the reactor ON spectrum (top) is shown with respective residuals of (data - fit) (bottom), whereas the OFF spectrum is shown on the right side. In both cases, the data (black) is shown with the corresponding likelihood fit (red). The grey shaded area is excluded from the fit due to the activation lines of the germanium. For the best-fit case no additional events due to a non-zero millicharge are found.

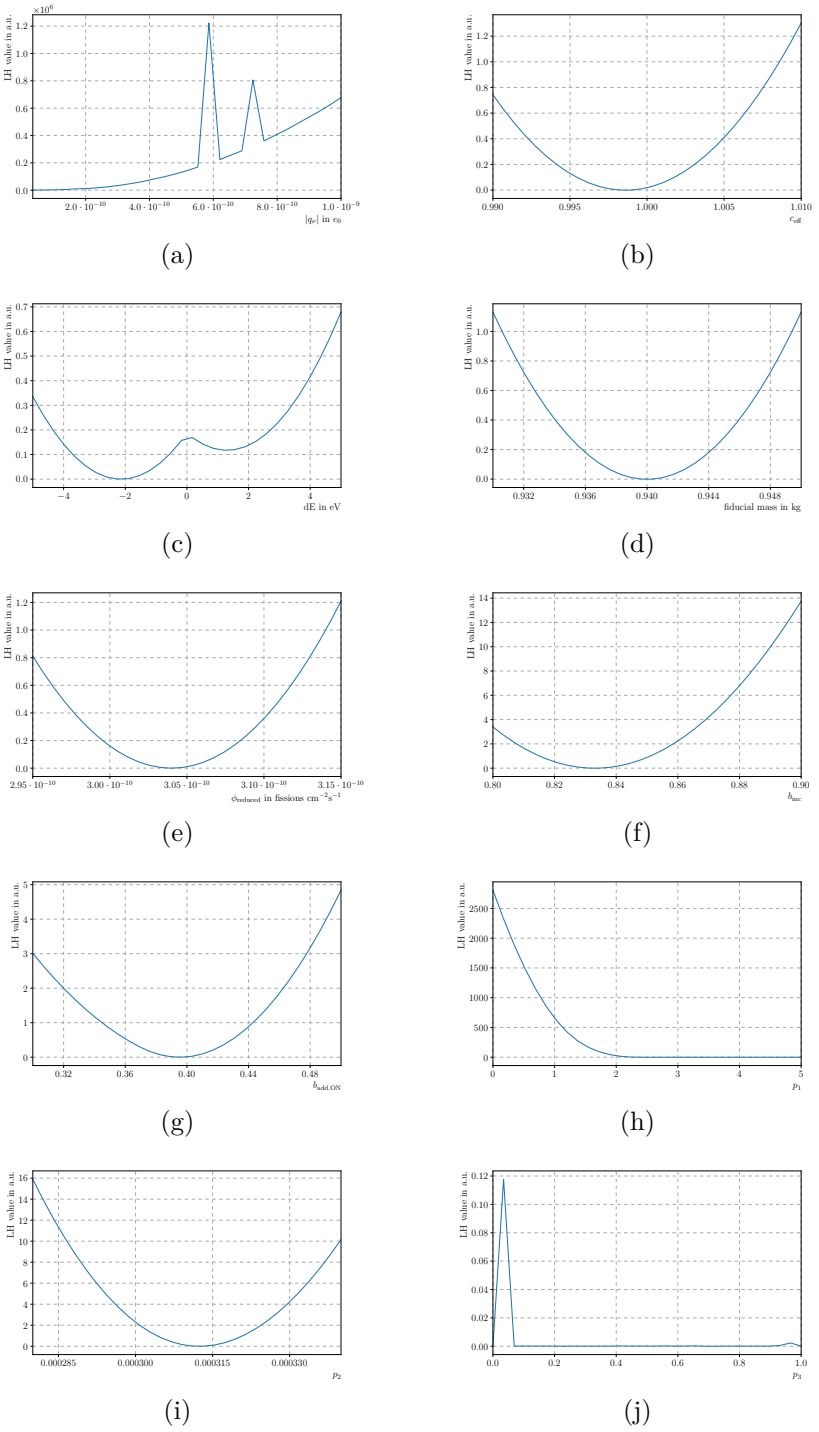

Figure 3.15.: 1D profiles of all likelihood fit parameters for CONUS-1 in Run-5 for the millicharge investigation. The respective parameter is scanned over the whole parameter range, while all other parameters are minimized. The scanned parameters are the NMC $|q_\nu|$ (a), the efficiency c_{eff} (b), the energy scale uncertainty dE (c), the fiducial mass m (d), the reduced flux ϕ_{reduced} (e), the background normalization b_{mc} (f), the additional ON component $b_{\mathrm{add.ON}}$ (g) and the three parameters of the leakage test component (h)-(j). On the y-axis, the likelihood value in a.u. is shown.

Table 3.7.: Exposure of Run-1 and Run-2 as used for the previous analysis conducted in [34].

Run	Detector	Reactor ON in kg d	Reactor OFF in kg d
Run-1	CONUS-1	215.4	29.6
Run-1	CONUS-2	184.6	32.2
Run-1	CONUS-3	248.5	31.7
Run-2	CONUS-1	19.8	18.5
Run-2	CONUS-3	20.8	19.0
combined	-	689.1	131.0

Upper Limit Determination for Neutrino Magnetic Moment and Millicharge

As no significant hints for events due to a non-zero NMM or NMC are found in all datasets of Run-4 and Run-5 an upper limit can be derived. For this purpose, a combined fit for Run-4 and Run-5 is performed, followed by a second step, including also the data of Run-1 and Run-2. In these combined fits an upper limit at 90% C.L. is computed with the profile likelihood ratio test for the one-sided case.
For the upper limit determination of Run-4 and Run-5, data of CONUS-1, CONUS-2 and CONUS-4 is used.
For the analysis of the full CONUS data, the datasets of Run-1 and Run-2 used for the upper limit in [34] are included. The corresponding exposure of Run-1 and Run-2 can be found in Table 3.7. A combined analysis is performed on the datasets of Run-4 and Run-5 and the additional exposure of 689.1 kg d of reactor ON and 131.0 kg d of reactor OFF data of the previous analysis. For these datasets only the energy range up to 8 keV is taken into account, whereas the full energy range up to 20 keV is used for the Run-4 and Run-5 data.
The distribution of the q-values q_{obs} and the respective $1-p$ distribution for the upper limit on the NMM are shown in Figure 3.16 for the Run-4 and Run-5 investigation. The upper limit is derived at the value of the magnetic moment where the $1-p$ distribution is 0.9 and yields

$$\mu_\nu < 5.57 \cdot 10^{-11} \mu_{\text{B}}. \tag{3.55}$$

The unstable behavior of the $1-p$ distribution at small NMM values is a reflection of the two minima of the energy scale uncertainty dE mentioned in Figure 3.12. Depending on which minimum is used the $1-p$ values are different.
For the combined analysis including Run-1 and Run-2 the $1-p$ distribution for the upper limit is shown in Figure 3.17 which yields

$$\mu_\nu < 5.18 \cdot 10^{-11} \mu_{\text{B}}. \tag{3.56}$$

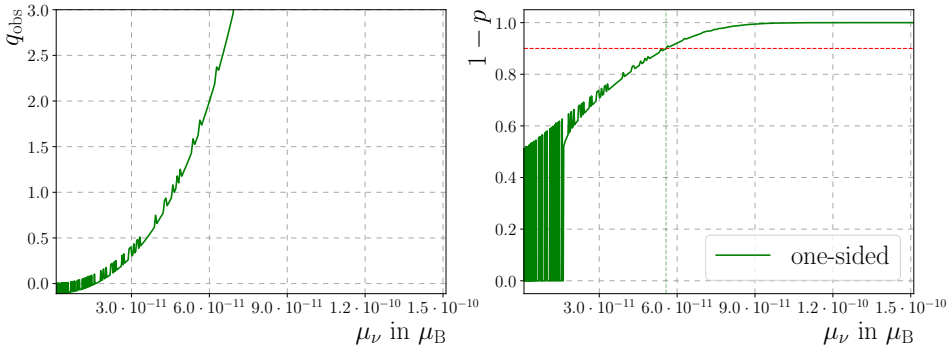

Figure 3.16.: Distribution of q-values q_{obs} (left) and $1-p$ (right) as a function of tested neutrino magnetic moment values for Run-4 and Run-5. The red dotted line indicates the demanded confidence level, i.e. 90%, and the green dotted line shows the corresponding NMM value of $5.57 \cdot 10^{-11}\mu_B$.

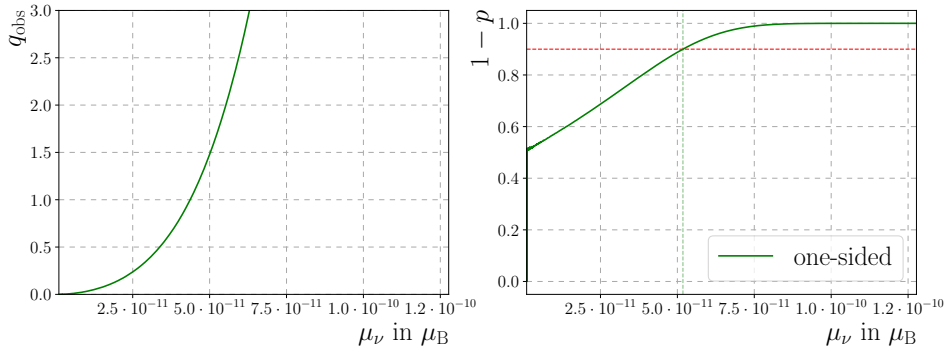

Figure 3.17.: Distribution of q-values q_{obs} (left) and $1-p$ (right) as a function of tested neutrino magnetic moment values for combined datasets. The red dotted line indicates the demanded confidence level, i.e. 90%, and the green dotted line shows the corresponding NMM value of $5.18 \cdot 10^{-11}\mu_B$.

Compared to the past investigation of the CONUS experiment with Run-1 and Run-2 datasets, yielding an upper limit of $\mu_\nu < 7.5 \cdot 10^{-11}\mu_B$, the result of the new datasets obtained in this work improved by $\sim 25\%$ only for Run-4 and Run-5 and improved by $\sim 70\%$ for also including Run-1 and Run-2.
The new CONUS upper limit is only less than a factor 2 above the currently best NMM limit at reactor site, provided by the GEMMA experiment, of $\mu_\nu < 2.9 \cdot 10^{-11}\mu_B$ [48, 49].
The expected sensitivity of $4.39 \cdot 10^{-11}$ is only just missed, the obtained upper limit is slightly worse than the 3σ range. A possible reason for the deviation from the expected value can be the similarity in shapes of the additional ON component and the NMM signal for Run-5 or, more generally, an underestimated systematic uncertainty of the background description. Besides that, a rough sensitivity calculation was done in [34] for the previous upper limit. Here, the future sensitivity expecting

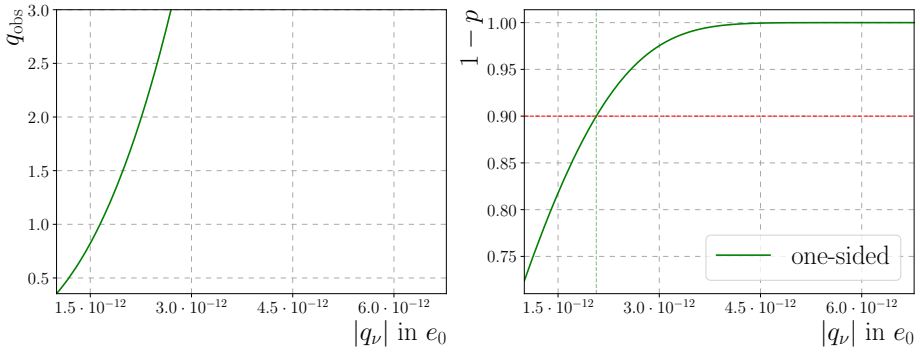

Figure 3.18.: Distribution of q-values q_{obs} (left) and $1 - p$ (right) as a function of tested neutrino millicharge values for Run-4 and Run-5. The red dotted line indicates the demanded confidence level, i.e. 90%, and the green dotted line shows the corresponding NMC value of $2.07 \cdot 10^{-12} e_0$.

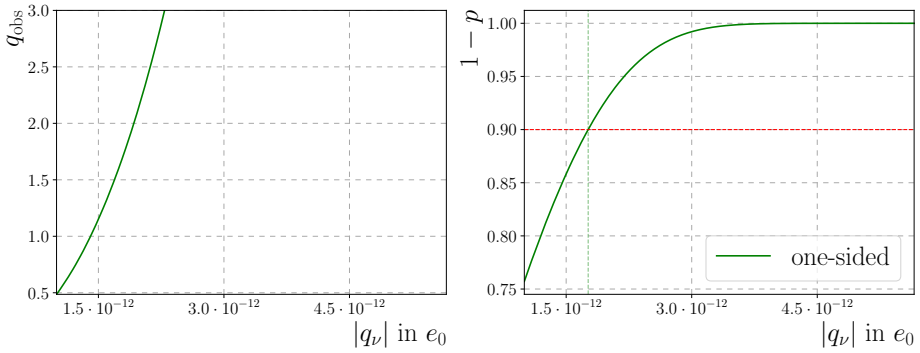

Figure 3.19.: Distribution of q_{obs} (left) and $1 - p$ (right) as a function of tested neutrino millicharge values for combined datasets. The red dotted line indicates the demanded confidence level, i.e. 90%, and the green dotted line shows the corresponding NMC value of $1.76 \cdot 10^{-12} e_0$.

more reactor ON and especially much more reactor OFF exposure was calculated to be $\mu_\nu < 5.2 \cdot 10^{-11} \mu_{\text{B}}$ matching exactly the upper limit obtained in this work.

The distribution of the q-values q_{obs} and the $1 - p$ distribution for the first likelihood fit of the NMC are shown in Figure 3.18. Here, an upper limit at 90% C.L. is found to be

$$|q_\nu| < 2.07 \cdot 10^{-12} e_0 \tag{3.57}$$

for combined Run-4 and Run-5. Including Run-1 and Run-2 the upper limit on the NMC is then given by

$$|q_\nu| < 1.76 \cdot 10^{-12} e_0 \tag{3.58}$$

Table 3.8.: Upper limits on neutrino magnetic moment and millicharge for Run-4 and Run-5 and combined datasets. The upper limits are given at 90% C.L.

Combined Runs	NMM (90% C.L.)	NMC (90% C.L.)
Run-4, Run-5	$5.57 \cdot 10^{-11}\,\mu_B$	$2.07 \cdot 10^{-12}\,e_0$
Run-1, Run-2, Run-4, Run-5	$5.18 \cdot 10^{-11}\,\mu_B$	$1.76 \cdot 10^{-12}\,e_0$

with the $1 - p$ distribution shown in Figure 3.19.
Compared to the previous result on the millicharge obtained by the CONUS experiment using only Run-1 and Run-2 data of $|q_\nu| < 3.3 \cdot 10^{-12} e_0$ [34], the upper limit of the full analysis improved by more than 50%. As the previous limit is only a rough estimation using the upper limit on the magnetic moment and Equation 3.24, the newly derived NMC upper limit yields the improvement of a full likelihood fit analysis including all characteristics of detectors, reactor, and background.
The achieved upper limit is very close to the currently best upper limit on NMC at a reactor of $|q_\nu| < 1.5 \cdot 10^{-12} e_0$, also set by the GEMMA experiment [53], deviating only a factor of below 1.2. It should be noted, that the result of the GEMMA experiment was also obtained using the rough estimation of Equation 3.24 and a full analysis comparable to the analysis used in this work yields an NMC of $|q_\nu| < 2.7 \cdot 10^{-12} e_0$ [53]. Here, the CONUS upper limit is better by a factor of 1.5.
Also in the case of NMC, the expected sensitivity of $7.32 \cdot 10^{-13}\,e_0$ is not reached with the calculated upper limit, hinting for a possible underestimated systematic uncertainty of the background description.
With the analysis of the full combined datasets conducted in this work, improved upper limits on the magnetic moment and the millicharge of the neutrino are set for the CONUS experiment. The results on NMM and NMC are finally summarized in Table 3.8.

4. Pulse-Shape Simulation

With the results on NMM and NMC obtained in Chapter 3, competitive upper limits are set already, and the previous results are improved by increased data stability and exposure. The comparison to the expected sensitivity revealed a hint for still some underestimated systematic effects in the background description. To further improve the results in future measurement campaigns a continuous gain in knowledge on background and detectors is helpful which can be achieved by the intense study of different detector signals. Also, as stated in Chapter 2.1.2, a very low background level has to be achieved for a successful determination of neutrino events at a reactor. Background events that are not suppressed by the CONUS shield can lower the signal-to-background ratio and, therefore, the sensitivity of the experiment. A powerful tool for background suppression is the Pulse-Shape Discrimination (PSD). By analyzing and characterizing the detector pulses, background events can be dismissed while signal events can be kept untouched.
In Section 4.1, the general principle of a semiconductor detector and the particle detection in HPGe detectors will be discussed. In general, events occurring near the surface of the detector, mainly induced by radioactive decays, differ from events in the crystal bulk and can be filtered out. Therefore the production mechanisms and the related shape of these events will be discussed in detail in Section 4.2. Offering a possibility of background suppression for the CONUS experiment, the PSD has to be validated for a reliable data analysis. A great tool for this validation is the simulation of the pulse shapes of events occurring in the detector. With the shape of the pulses also new possible sources of background can be identified. For this reason, a pulse-shape simulation for the CONUS experiment was set up in this thesis, which is explained and carried out in Section 4.3. To validate the simulation itself the simulated pulses are compared to measured ones. Finally, the results and implications are discussed in Section 4.4.

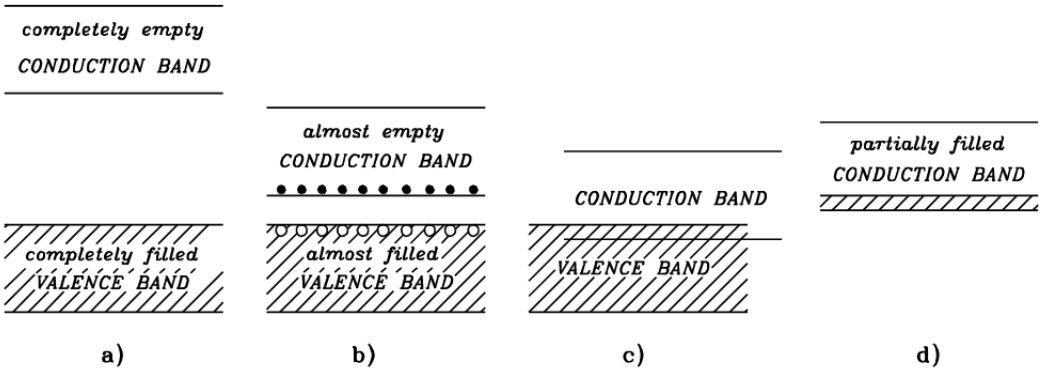

Figure 4.1.: Schematic energy band structure of solids. The valence band of the insulator (a) is filled completely whereas the conduction band is fully empty. Both bands are separated by a large band gap. For the semiconductor (b), the band gap is much smaller, and electrons can be lifted to the conduction band. The valence and conduction band of a conductor (c) are either overlapping or the conduction band is partially filled (d). From [63].

4.1. Particle Detection in Germanium Detectors

The content of this section is based on [25, 62, 63, 61]. HPGe detectors with a sub-keV energy threshold are well suited for low-energy searches as CEνNS. These semiconducting detectors are composed of crystals doped by different materials to increase the number of charge carriers.
When atoms get bound in a solid structure, their atomic energy levels broaden into energy bands with a fixed number of electrons. Between the energy bands, there are energy regions that are forbidden for electrons, called band gaps. The uppermost occupied band is called the valence band followed by a band gap and the conduction band. According to the structure and occupation of their energy bands, solid materials can be categorized into three different classes: insulators, conductors, and semiconductors, which are sketched in Figure 4.1. For an insulator, the valence band is completely occupied, and the conduction band is fully empty. The band gap is of the order of 10 eV. Therefore, the thermal energy is not sufficient to lift electrons to the conduction band, and the electrons are immobile. Consequently, the material can not pass an electrical current. For conductors, either the conduction band is partially filled, or the valence and conduction bands are overlapping. Thermal excitation can lift the electrons continuously to the conduction band and an applied electric field can induce a current. The band structure of a semiconductor is similar to an insulator but the band gap of the order of 1 eV is much smaller than for the insulator. Here, the thermal energy can be high enough to excite the electrons to the conduction band. When electrons are raised to the conduction band a vacancy remains in the valence band. This hole can be treated effectively as a positive charge. Neighbouring electrons can fill the holes resulting in an effective movement

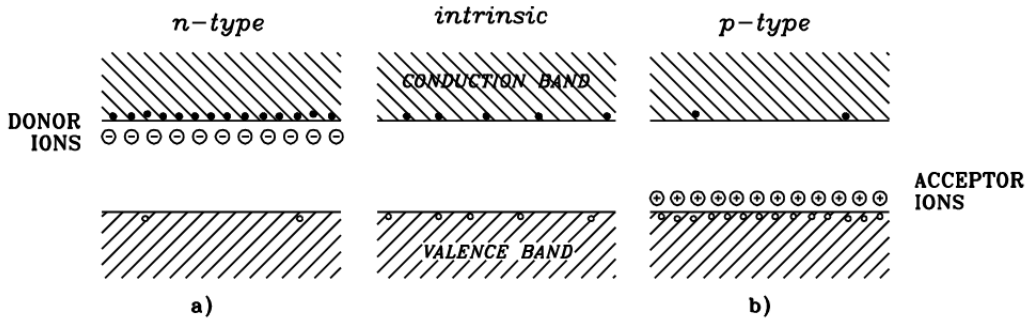

Figure 4.2.: Schematic energy band structure of intrinsic (middle) and extrinsic (left and right) semiconductors. For the n-type semiconductor, an additional donor state below the conduction band forms, whereas for the p-type semiconductor, an additional acceptor state forms above the valence band. From [63].

of the holes. By applying an external electrical field to the material a current is created as the electrons in the conduction band and the holes in the valence band are moving. When a semiconductor holds an equal number of electrons and holes, it is called an intrinsic semiconductor. By adding impurities to the crystal lattice of the semiconducting material, called doping, the number of electrons or holes can be adapted forming an extrinsic semiconductor. For a p-type semiconductor, acceptor impurities with fewer electrons are added. Therefore, an excess of holes is available, and an acceptor state above the valence band is formed. On the contrary, an n-type semiconductor has an excess of electrons by adding donor impurities. Here, a donor state below the conduction band is formed. Both states for n- and p-type will decrease the band gap. A schematic view of the extrinsic semiconductor types and the intrinsic type is shown in Figure 4.2. For very high dopant concentrations, the semiconductor is called p+ or n+, respectively.
To build a semiconductor detector, dissimilar semiconductor types are placed in contact with each other. The contact of these materials will induce a redistribution of the electrons and holes. Holes from the p-type side will diffuse to the n-type side and electrons from the n-side to the p-side. This will lead to a recombining of the free electrons and holes, the free charge carriers are cancelled out and a depletion region forms without free charges. If now a positive voltage is applied to the n-type side, the depletion region will increase as electrons will be withdrawn from this side. Also, the holes will be withdrawn by the negative voltage on the p-type side, forming a reverse-biased junction. The redistribution and depletion region of a semiconductor detector is sketched in Figure 4.3.
For a p-type point contact HPGe detector, a p-type Ge crystal is wrapped lateral and on top with a lithium-diffused n+-layer, typically of the thickness of 1 mm. In terms of charge collection capability this layer is partially dead, the dead layer (DL), and partially semi-active, the transition layer (TL), due to a diffusion of Li-atoms

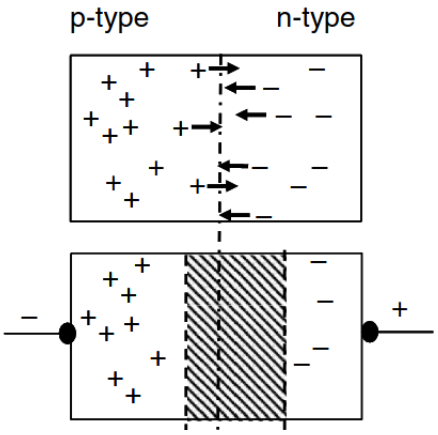

Figure 4.3.: Schematic principle of a p-n junction before charge carrier redistribution (top) and when the depletion region is formed by applying a reverse bias voltage (bottom). From [62].

inwards. In the DL, the efficiency in signal detection ϵ is zero as there is no charge collection, whereas in the TL, the efficiency is $0 < \epsilon < 1$ due to an incomplete charge collection. On the bottom of the crystal, the boron-implanted p+ contact is located with a thickness of $100 - 200\,\text{nm}$ and a diameter of $2.5 - 3\,\text{mm}$. This contact is surrounded by a fully passivated layer, the passivation layer (PL), separating the n+ and p+ contacts. The remaining crystal volume is the active volume (AV) with a full charge collection efficiency $\epsilon = 1$. A schematic view of a p-type point contact HPGe detector crystal is shown in Figure 4.4.
By applying a positive reverse bias voltage of a few kV on the n+ contact, an electric field inside the diode is formed, and the volume of the detectors is electrically depleted. An example field simulated with the simulation framework siggen (see Chapter 4.3) can be found in Figure 4.7. Incoming ionizing particles will create electron-hole pairs proportional to the deposited energy. The produced electrons and holes will drift in opposite directions according to the electric field. This movement of the charge carriers will induce a time-dependent charge $Q(t)$ at the readout electrode. This read-out charge increases over time until all charges inside the diode are collected forming a pulse. The pulses will appear in different shapes depending on the location of the energy deposition inside the crystal and the time between two events. This will be further explained in the next section. Afterwards, the collected charges at the p+ contact will be transformed into a voltage by a charge-sensitive preamplifier, which then can be registered by a DAQ.

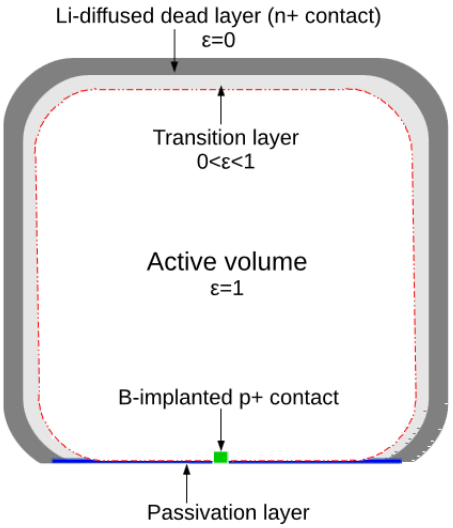

Figure 4.4.: Diode design of p-type point contact HPGe detectors. The different diode regions with specific charge collection efficiencies ϵ are shown. From [25].

4.2. Pulse-Shape Characteristics

A typical pulse of an HPGe detector has some common features. The baseline of the detector is the lowest voltage level without any energy deposition. For an event, an increase of the baseline is observed where the pulse starts with a special rise-time defined as the time for rising from 10% to 90% of the pulse height. After the maximum, the pulse will decay to the baseline with an exponential shape due to the AC coupling of the DAQ [64]. The rise-time is dependent on the location of the energy deposition inside the crystal. Signals originating from the AV of the diode, the fast pulses (FP), have typically a rise-time of about 300 ns [64]. If the event is near the point-contact the FP rise-time is faster due to the acceleration in the weighting potential, which will be introduced in Section 4.3.2. If an interaction occurs in the TL, the produced charge diffuses due to a very weak electric field until it recombines or reaches the depleted volume, leading to partial charge collection and larger collection times [64]. This process will create signals with large rise-times, the slow pulses (SP). Example FP and SP are shown in Figure 4.5.
Depending on the spatial resolution of the detector and the time between two events there is also a difference in the pulse-shapes. The FP and SP shown in Figure 4.5 are single-site events (SSE), pulses of only one energy deposition collected at the p+ contact. SSEs are also classified if two events occurring at the same time are below the spatial resolution of the detector. A multi-site event (MSE) is produced if several energy depositions take place at the same time and with a separation bigger than the spatial resolution of the detector. MSEs are mostly created by high

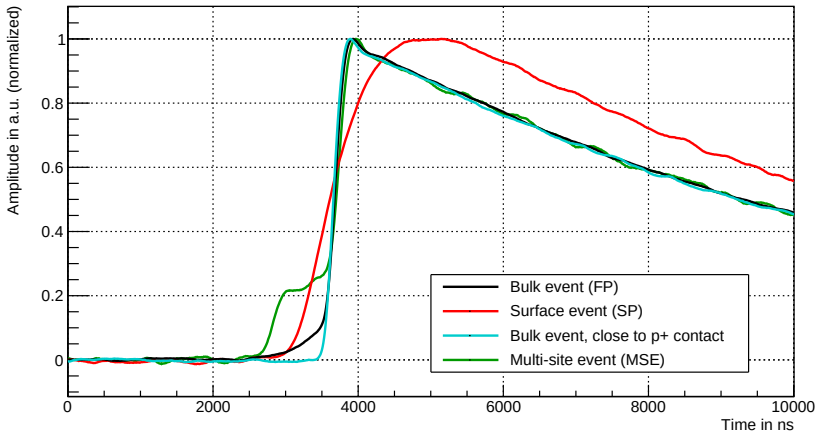

Figure 4.5.: Typical measured example pulses for the CONUS detectors. The rise-time of the fast pulses produced by events in the crystal bulk (black) is very different compared to slow pulses (red) created at the surface of the crystal. If a fast pulse is produced near the point-contact (blue), the rise-time is slightly faster. Several events at the same time will induce a multi-site event (green).

energy[1] particles due to Compton scattering and pair production and can be built up of multiple normal or multiple slow pulses and of the mixture of both. An MSE can be distinguished by its step-like pulse, which is additionally shown in Figure 4.5 in green.

4.3. Pulse-Shape Simulation Framework

For the CONUS experiment a detailed pulse-shape study was carried out [65, 66] and a PSD for background events was developed from this [64]. To validate the experimental PSD method, to gain detailed knowledge and to improve the understanding about the detectors and the background, a pulse-shape simulation framework was set up for the CONUS HPGe detectors in the course of this thesis. This framework consists of two parts. In the first part, the interactions and energy depositions of incoming particles are simulated with a Monte Carlo (MC) simulation [67]; in the second part, the signal formation inside the diode is simulated with an open-source simulation package called siggen [68, 69]. Here, different modifications were made to fulfill the purposes of the CONUS detectors.

[1] In the context of this thesis 'high energy' refers to the energy range definition of the CONUS experiment with 'high' energies above 30 keV.

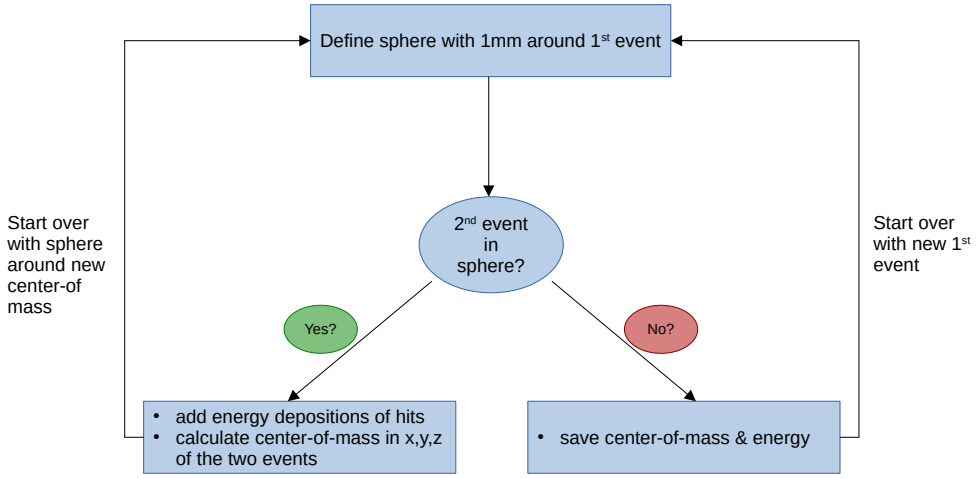

Figure 4.6.: Event clustering algorithm for spatial resolution of the detector and MSEs. A sphere with a diameter matching the spatial resolution is defined around an event. If the position of the second event is inside the sphere, a center-of-mass in all directions is built, all energy depositions are added and a new sphere is built around this new location. If the second event is not inside the sphere, the location and energy are saved, and the calculation is started from the beginning.

4.3.1. Simulation of Interactions and Energy Depositions

As the interaction position inside the detector crystal and also the deposited energy are essential for the shape of the pulse, they have to be determined for a pulse-shape simulation. For this purpose, the Geant4 [70] based framework MaGe [67] is used, which was developed for ultra-low background detectors by the GERDA and MAJORANA Collaborations. In MaGe, the detectors have to be modeled with the actual dimensions and materials, which was done for the CONUS detectors by J. Hakenmüller [61, 28]. A primary particle of specific type, energy, and angular distribution is generated and propagated through the detector. For each energy deposition inside the detector, also of secondary and following particles, the energy, particle type, and location are registered. These properties can then be further processed in a post-processing step.
As for the second part of the pulse-shape simulation the energy and the interaction point of the events are required, an interface between MaGe and siggen has to be developed. This interface is added in the post-processing of the MC simulation. For each simulated event, the x-, y- and z-coordinates inside the diode are read out, as well as the energy and the particle ID. As siggen and MaGe do not have the same origin of coordinates, it is crucial that all interaction points of MaGe have to be

shifted by 3.82 cm in the negative z-direction. In MaGe all energy depositions are registered even if the spatial separation between events is very small. This does not reflect reality as a detector has a finite spatial resolution, and also MSEs are created by scattering of the incoming particle. For this effect, the events in MaGe have to be clustered according to their spatial separation. If the separation between two energy depositions is smaller than the spatial resolution of the detector the events can not be resolved and have to be added. Is the separation bigger than the resolution, two events forming an MSE are registered. For this, a post-processing algorithm was developed based on [71, 72] with a default spatial resolution of 1 mm following [72]. A schematic depiction of the event clustering algorithm is shown in Figure 4.6. If a primary particle of the MC simulation hits the detector for the first time a sphere of the size of the spatial resolution is defined around the location of this event. If the x-, y- and z-coordinates of a second event, induced by the primary particle or a secondary particle, are located inside the sphere, the energy depositions of the two events are added and a center-of-mass in x, y and z is calculated for the location. For the next event, a sphere is defined around this new center-of-mass. If the interaction vertex of the second event is not located inside the sphere, the location and energy of the first event are saved and the sphere is built around the second event. This is done for each energy deposition of one started primary particle. As input for siggen these events are collected and written to a .txt-file:

$$
\begin{aligned}
&x_1\ y_1\ z_1\ E_1\ \mathrm{ID}_1, x_2\ y_2\ z_2\ E_2\ \mathrm{ID}_2, ... && \text{(MSE)}\\
&x\ y\ z\ E\ \mathrm{ID} && \text{(SSE)}\\
&x_1\ y_1\ z_1\ E_1\ \mathrm{ID}_1, x_2\ y_2\ z_2\ E_2\ \mathrm{ID}_2, ... && \text{(MSE)}\\
&... &&
\end{aligned}
$$

Also the particle ID given by MaGe is passed to siggen. With that further studies on pulse-shapes with different particle types are possible.
The algorithm only accounts for MSEs coming from one started primary particle. In reality two incoming particles at the same time can also induce a MSE. This case is not accounted for due to limitations of the MC simulation where particles are started separately after each other.

4.3.2. Simulation of Signal Formation

For the simulation of the electric fields and the actual pulses of the detector the simulation package siggen [68, 69], an open-source pulse-shape simulation code mainly developed by D. Radford, is used. The code was modified to adapt it to the purposes and needs of the CONUS experiment. The siggen software package itself consists of two parts. The first part is called **`mjd_fieldgen`**, a stand-alone code for electric field and potential calculation of point-contact germanium diodes. The calculated electric fields are then used as an input for the second part **`mjd_siggen`**. Here the detector signal is obtained by calculating the drift of charge carriers inside the crystal. To reproduce the actual pulse-shapes measured by the CONUS experiment the option to model MSEs has to be implemented. Furthermore, the simulated pulses have to be convoluted with the electrical response, weighted by the energy and to be calibrated to match exactly the measured pulses with the CONUS DAQ. Finally, the impact of electrical noise is added to the simulated pulses in the post-processing. These steps are described in the following.

Electric Field and Weighting Potential

This section is based on [72, 71, 73]. In **`mjd_fieldgen`**, the electric and weighting potentials inside a point-contact HPGe detector are calculated in two-dimensional cylindrical coordinates. **`mjd_fieldgen`** is also capable of calculating the capacitance and full depletion voltage of the detector as well as the fields of only partially depleted detector crystals. In a p-type detector free-moving holes, charge carriers which are not used in forming covalent bonds between atoms, are pushed out of the crystal bulk by applying a high bias voltage. At the so-called depletion, the ions are left behind as they are fixed in their locations, forming space-charges and, therefore, an electric field. The total electric field of the crystal is then a combination of this field and the external electric field induced by the bias voltage. The electric field has to be simulated for the signal generation part as the field determines the drift of the electrons and holes created by any particle interaction inside the detector. To obtain the electric potential Φ at position $\mathbf{r} = (r, \phi, z)$ the Poisson equation

$$\nabla^2 \Phi(\mathbf{r}) = -\frac{\rho(\mathbf{r})}{\epsilon_0 \epsilon_\mathrm{R}} \tag{4.1}$$

has to be solved. Here $\epsilon_0 \approx 8.854 \cdot 10^{-12}\,\mathrm{F/m}$ is the vacuum permittivity, $\epsilon_\mathrm{R} \approx 16.0$ is the relative permittivity or dielectric constant of germanium and $\rho(\mathbf{r})$ is the space charge density distribution. The space charge density distribution $\rho = -(N_\mathrm{A} - N_\mathrm{D})e$, with N_A the acceptor concentration, N_D the donor concentration and e the elementary charge, is dependent on the position in the crystal. As the electric field inside the diode is also of interest the electric field vector $\mathbf{E}$ is obtained from the potential by

$$\mathbf{E} = -\nabla \Phi. \tag{4.2}$$

Table 4.1.: Basic properties of the CONUS detectors. Here, the working bias voltages U_{working}, the depletion voltages $U_{\text{depletion}}$ (taken from [25] for C1-C4) and the crystal temperatures T_{crystal} are shown.

Detector	U_{working} in V	$U_{\text{depletion}}$ in V	T_{crystal} in K
CONUS-1	3000	2710 ± 25	85
CONUS-2	2700	2560 ± 25	78
CONUS-3	3000	2810 ± 25	81
CONUS-4	3400	3200 ± 25	76
CONUS-5	2800	~ 2380	76

Furthermore, for the simulation of the detector signals the weighting potential is necessary. It is used to calculate the electric charges on an electrode which are induced by the drifting charge carriers inside the diode. The weighting potential is purely determined by the boundary conditions where the impurity concentration is set to zero and the potential on the point contact, the electrode of interest, is 1, whereas on the n^+ surface the potential is zero. The weighting potential Φ_0 can be calculated by solving the Laplace equation

$$\nabla^2 \Phi_0(\mathbf{r}) = 0. \tag{4.3}$$

In the simulation code, both equations for the two potentials are solved in discrete space. Here the Successive Over-Relaxation (SOR) method is used to calculate the potential first on a coarse grid. The result is then used for a more precise calculation on a finer grid making **`mjd_fieldgen`** fast and accurate.
As an input for **`mjd_fieldgen`**, a configuration file with various detector parameters, such as geometry and impurity concentrations, as well as simulation parameters, as the grid size, is passed. This file was adapted for the CONUS detectors with their respective geometry and impurity concentrations. All five detectors have the same spatial dimensions but different impurity concentrations, working voltages, and temperatures, which can be found in Table 4.1 and 4.2. The simulated electric and weighting potentials of the CONUS-1 detector are shown in Figure 4.7. The electric potential is high on the surface of the diode and decreases towards the point-contact region. This is different for the weighting potential where the potential is highest only at the point-contact. It decreases very fast with only a few mm distance to the point-contact until it is almost zero in the bulk volume. The potentials for CONUS-2 to CONUS-5 can be found in Appendix E.

Table 4.2.: Input detector properties for **`mjd_fieldgen`**. The crystal dimensions, given by crystal height h_d and crystal radius r_d, as well as the point-contact radius r_pc are the same for all detectors. Each detector has an individual dead-layer thickness d_DL, a net impurity concentration n_i and an impurity gradient.

Detector	h_d, r_d in mm	r_pc in mm	d_DL in mm	n_i in $10^{10}\,\mathrm{e/cm^3}$	impurity gradient in $10^{10}\,\mathrm{e/cm^4}$
CONUS-1	62, 31	1.25	0.57	-1.16	0.062
CONUS-2	62, 31	1.25	0.52	-0.76	0.026
CONUS-3	62, 31	1.25	0.48	-1.2	0.053
CONUS-4	62, 31	1.25	1.08	-1.16	0.0032
CONUS-5	62, 31	1.25	0.57	-1.02	0.0032

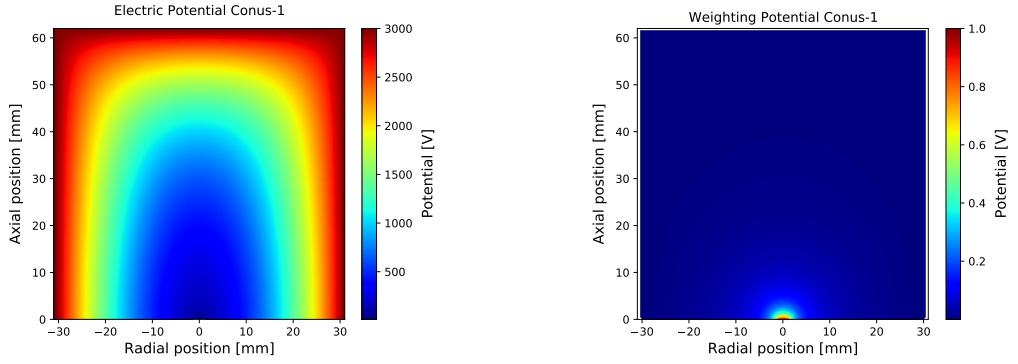

(a) (b)

Figure 4.7.: Simulated electric (a) and weighting (b) potentials for the C1 detector. The electric potential is decreasing towards the point-contact whereas the weighting potential has reached its maximum value in the region of the contact and is small in all other areas.

Signal Generation

To generate the actual detector pulses **mjd_siggen** is used. It calculates the charges as a function of time depending on the position of the interaction. Therefore, the fields and potentials obtained by **mjd_fieldgen** are used as input. As stated in Chapter 4.1 incoming particles create electron- and hole-clouds inside the detector, which are drifting to the respective electrode. **mjd_siggen** computes within the charge-drift model the charge trajectories $\mathbf{r}$ at each time-step. Afterwards, the induced charge Q at the electrode is calculated using the Shockley-Ramo theorem [74]

$$Q = -q\Phi_0(\mathbf{r}), \tag{4.4}$$

with q the total charge carried by the electrons and holes and Φ_0 the weighting potential. This is done until all charges are collected at the electrodes, whereat Q is increasing over time. It can be seen from Equation 4.4 that the induced charge is linearly dependent on the weighting potential, and therefore, the pulse is mainly driven by the drift of the charges in the high Φ_0 regions at the point-contact. For this reason the position dependency of the pulse is weak for interactions inside the bulk volume and the shapes differ only for interactions close to the point-contact.
As **mjd_siggen** is only capable of simulating pure SSEs different adaptions have to be made to simulate the pulse-shapes of the CONUS detectors. Furthermore, the impact of noise and the electronic response of the preamplifier electronics and the readout chain have to be included to reproduce the measured pulses in detail with the simulation. This is done partly in **mjd_siggen** and partly in the post-processing of the simulation and discussed in the following section.
In the standard version of siggen, the input for one SSE pulse, regarding the x-, y- and z-coordinates and the energy of the interaction, is passed to the program, resulting in the direct simulation output of the pulse parameters, the time and the amplitude of the pulse. The code was adapted to pass an input file to the program with the interaction positions, energies, and particle IDs of all energy depositions, including MSEs, as discussed in Section 4.3.1. Furthermore, the C++-based framework ROOT [75] was included in the code to gain benefit from the output storage possibilities of ROOT. The simulation output is stored in a ROOT tree similar to the data structure of the CONUS data. With these adaptions it is possible to simulate a large number of pulses and to run dedicated CONUS analyses with the simulation data. A simulated pulse of the CONUS-1 detector is shown in Figure 4.8. An energy of $E = 5\,\mathrm{keV}$ and an interaction position in the middle of the crystal at $x = 0\,\mathrm{mm},\ y = 0\,\mathrm{mm},\ z = 30\,\mathrm{mm}$ is assumed. The amplitude of the simulated pulse is normalized to 1 by construction from siggen, neglecting the pulse height induced by the respective energy deposition. Furthermore, the pulse remains constant after increasing to 1, neglecting the exponential decay at the end, induced by the AC coupling of the DAQ and the preamplifier.
As siggen simulates the pulse-shapes only for a bare point-contact HPGe crystal

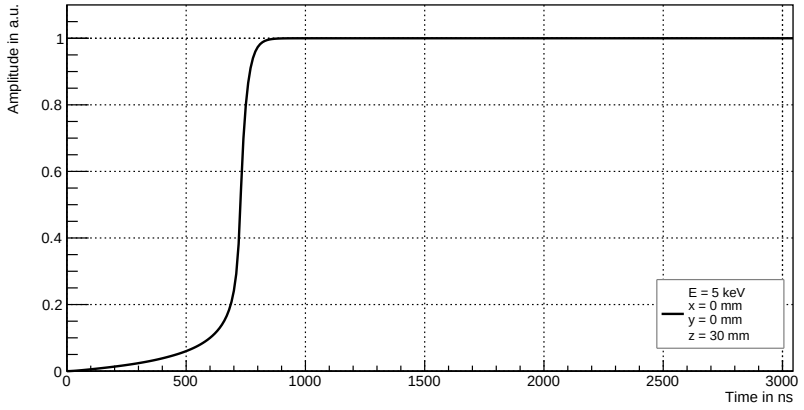

Figure 4.8.: Simulated raw pulse of the CONUS-1 detector with unmodified siggen version. Here, an energy of 5 keV and an interaction position in the middle of the crystal was chosen. Preamplifier effects and noise are not included.

with applied voltage the effects related to the preamplifier and the readout chain in a real detector are not included. For a direct comparison between simulated and experimental pulse-shapes, this electronic response has to be added to the pulses generated by siggen. The input signal $I(t)$, given by the raw detector, is altered by the response function of the electronics $H(t)$. The measured time-dependent output signal $S(t)$ is then obtained by the convolution of the input signal with the response [76]

$$S(t) = (H * I)(t) = \int_{-\infty}^{\infty} H(t') \cdot I(t - t')dt'. \tag{4.5}$$

To experimentally determine the response function of a system a step function signal $\Theta(t)$ with a fast rise-time [77] can be injected with a pulser in the test input of the preamplifier. Using the step function as input function, the derivation of Equation 4.5 yields [76]

$$\frac{\partial}{\partial t}S(t) = \frac{\partial}{\partial t}(H(t) * \Theta(t)) = \left(H(t) * \frac{\partial \Theta(t)}{\partial t}\right) = (H(t) * \delta(t)) = H(t). \tag{4.6}$$

with $\delta(t)$ the Dirac delta function. Therefore the response function can be obtained by differentiation of the output signal

$$H(t) = \frac{\partial}{\partial t}S(t). \tag{4.7}$$

To get rid of noise effects the response function is averaged over a certain amount of output pulses. For the CONUS detectors the electronic response was measured by J. Stauber [66] and is depicted in Figure 4.9. It is different for each of the five

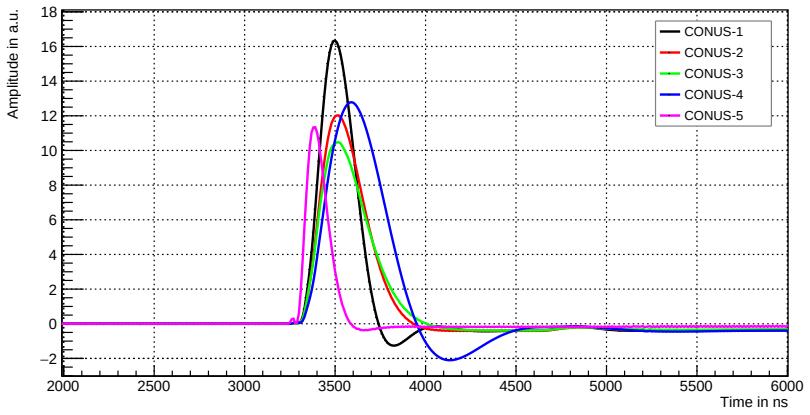

Figure 4.9.: Measured electronic response of the five CONUS detectors. The response function is different for each detector due to small differences in preamplifier and DAQ channel settings. Data kindly provided by J. Stauber.

detectors due to the differences in DAQ channel and preamplifier settings. After convoluting the raw output pulses of siggen with the electronic response, the characteristic exponential decay of the pulse is reproduced, as can be seen in Figure 4.10 for the CONUS-1 detector.
Since the electronic response functions were measured with a pulser-amplitude of 200 mV, corresponding to $\sim$ 25 keV, the electronic response has to be normalized to each simulated energy otherwise the amplitude of the simulated pulse will not match the exact measured amplitude. For this, the electronic response functions are normalized by a factor F for each simulated pulse. The factor is composed of the maximum amplitude of the respective measured electronic response function $A_{\text{max,response}}$, the energy corresponding to the measured pulser-amplitude in channels E_{pulser}, and the energy of the simulated pulse in channels E_{pulse} and can be derived by

$$F = \frac{A_{\text{max,response}}}{E_{\text{pulser}}} \cdot E_{\text{pulse}}. \tag{4.8}$$

The energy of the simulated pulse in channels has to be calculated by the energy calibration coefficients of the background spectrum.
Moreover, a calibration from arbitrary units to ADC channels is needed. For this purpose, the convoluted pulse has to be multiplied by a scaling factor. The calibration coefficients are obtained by analyzing the pulse height of only fast pulses of a background spectrum measurement. Including SP will distort the calibration. Here the maximum of each measured pulse in ADC channels is plotted against the energy of the pulse in ACD channels, shown in Figure 4.11 for the CONUS-1 detector. This is done for all CONUS detectors shown in Appendix F. With the slope b_{ADC} of this

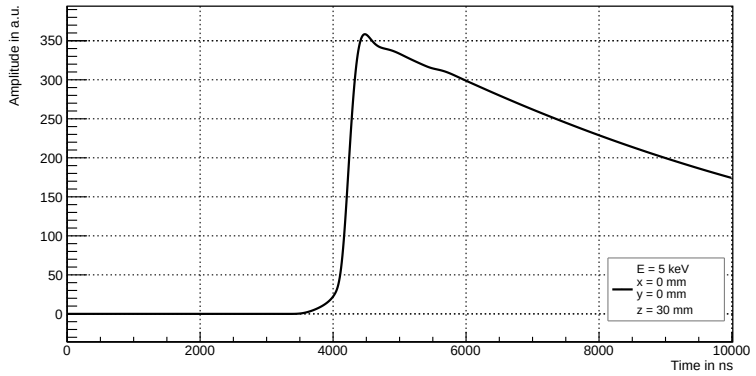

Figure 4.10.: Simulated pulse of the CONUS-1 detector with electronic response. Here an energy of 5 keV and an interaction position in the middle of the crystal was chosen. The characteristic exponential decay after the maximum of the pulse is obtained by the convolution of the raw simulation pulse with the electronic response function.

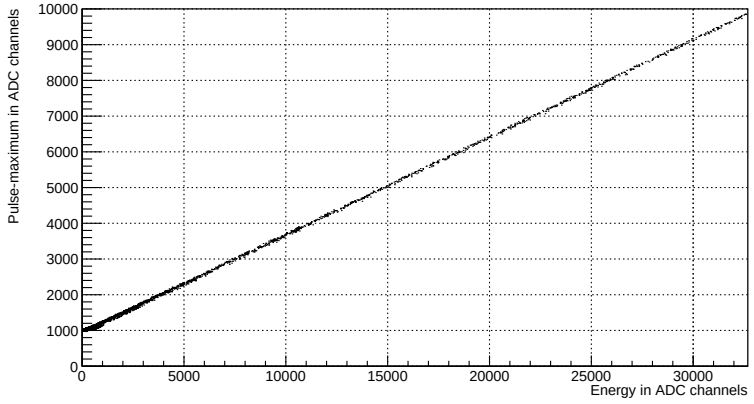

Figure 4.11.: Simulation calibration line for the CONUS-1 detector. The maximum pulse height is linear dependent on the energy of the event. For the calibration from arbitrary units to channels, a background measurement was used, and all pulses deviating from fast pulses were cut.

Table 4.3.: Calibration coefficients for simulation and spectrum for the CONUS detectors. The energy corresponding to the measured pulser-amplitude was measured at 200 mV.

Detector	E_{pulser} in channels	a_{ADC} in channels	b_{ADC}	a_{spectrum} in keV	b_{spectrum} in keV/channel
CONUS-1	26090.1	944 ± 1	272.6 ± 0.1	-0.0103 ± 0.0058	0.000975 ± 0.000000568
CONUS-2	26489.1	958 ± 2	262.4 ± 0.2	-0.0039 ± 0.0059	0.000993 ± 0.000000588
CONUS-3	24987.0	810 ± 2	262.5 ± 0.2	-0.0104 ± 0.0044	0.001040 ± 0.000000460
CONUS-4	31150.7	908 ± 3	284.8 ± 0.2	-0.0022 ± 0.0067	0.000979 ± 0.000000651

calibration line and the maximum amplitude of the simulated uncalibrated pulse $A_{\mathrm{max,pulse}}$ the multiplier m can be calculated

$$m = \frac{b_{\mathrm{ADC}}}{A_{\mathrm{max,pulse}}} \cdot E. \tag{4.9}$$

Here, E is the energy of the simulated pulse in keV. A simulated pulse of e.g. 1 keV yields a maximum amplitude of $\mathrm{max}_{\mathrm{pulse}} = 552$ channels. With a calibration coefficient of $b_{\mathrm{ADC}} = 272$ a multiplier of 0.49 keV/channel is obtained. This factor is then multiplied to the convoluted simulation pulse. The step of electronic response normalization and calibration was not possible for CONUS-5 as it was no longer available for the measurements due to the detector upgrade described in Chapter 5.2. A summary of all calibration coefficients and input parameters of the other four detectors is given in Table 4.3.
As only normalized pulses are generated by `mjd_siggen` the amplitude of the simulated pulses has to be weighted with the respective deposited energy. This is done on the raw pulses before the convolution with the electronic response. The effects of the energy weighting on the amplitudes of the raw pulses as well as on convoluted pulses are shown in Figure 4.12. The weighted amplitude of the raw pulse corresponds to the energy of the event whereas the amplitude of the convoluted pulse is stretched according to the electronic response.
For an MSE, the energy is deposited in multiple locations (see Chapter 4.2), and multiple electron-hole clouds are created simultaneously. The total pulse-shape of such an event is then a linear superposition of the SSEs of each cloud weighted by the respective deposited energy [78, 79]. The individual SSEs forming the total MSE have a time offset in accordance with the drift-time to the contact. A simulated MSE for the CONUS-1 detector is shown in Figure 4.13. The two individual events forming this pulse have both the same energy of 5 keV but different locations inside the crystal. Therefore, the time difference according to the different drift-times of the events forms the characteristic step shape for an MSE pulse in an HPGe detector.
Siggen does not account for an important feature of an actual HPGe detector: the slow pulses originating in the transition layer of the diode. Here, the produced charges are diffusing in regions with higher electric field. The time for this process is enhanced compared to the drift time of the charges alone and the pulse is stretched in time. This is not implemented in the charge-drift model of siggen and is not part of this thesis.

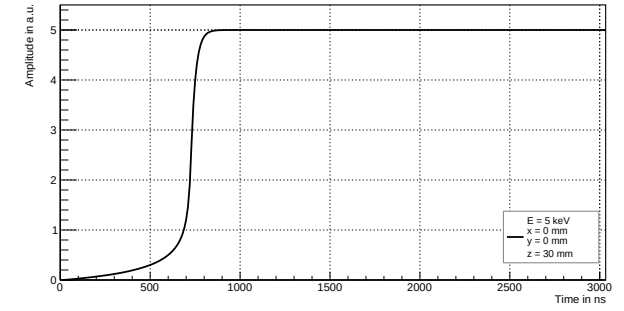

(a)

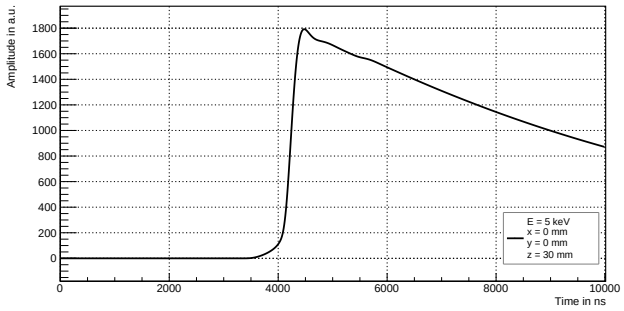

(b)

Figure 4.12.: Simulated pulses weighted by energy for the CONUS-1 detector. The maximum amplitude of the raw pulse (a) corresponds to the energy of the simulated event. This amplitude is modified due to the convolution with the electronic response (b).

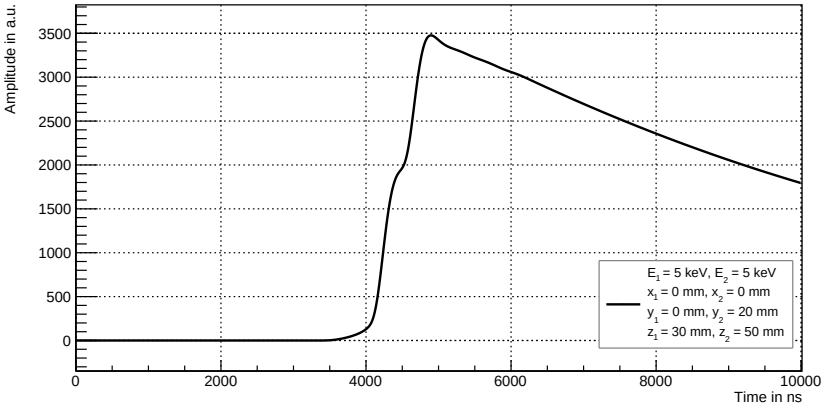

Figure 4.13.: Simulated MSE pulse for the CONUS-1 detector. Two events at the same time with $E_1 = 5\,\mathrm{keV}$, located at $x_1 = 0\,\mathrm{mm}$, $y_1 = 0\,\mathrm{mm}$ and $z_1 = 30\,\mathrm{mm}$, and $E_2 = 5\,\mathrm{keV}$, located at $x_2 = 0\,\mathrm{mm}$, $y_2 = 20\,\mathrm{mm}$ and $z_2 = 50\,\mathrm{mm}$, forming this pulse with the characteristic step shape.

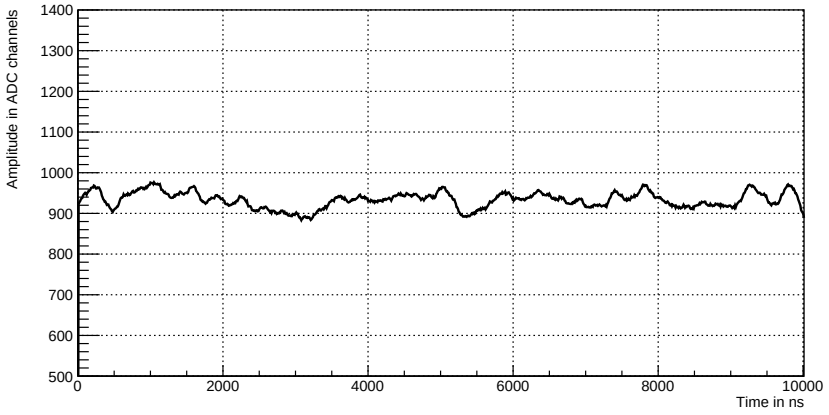

Figure 4.14.: Generated noise template for the CONUS-1 detector.

Simulation Post-Processing

With all the modifications done in siggen, the simulated pulses still do not reproduce measured pulses from the detector as the effects of the electronics noise are not included. This is then done in the post-processing of the simulation data. For this purpose, measured noise samples of each detector are processed by the 'Noise Generator' developed by J. Stauber [66]. Here, the mean frequencies and the standard deviation of one noise sample are calculated by a Fourier transform. To obtain for each simulated pulse a slightly different noise template, the frequencies are varied around the standard deviation, and the inverse Fourier transform is calculated. The noise template for the CONUS-1 detector is shown in Figure 4.14, while the noise templates for the other detectors can be found in Appendix G. The noise shape and amplitude are different for the CONUS-5 detector compared to the other detectors, which are installed in the experiment. The reason for this are the different preamplifier and DAQ settings. Finally, the noise template is added to the convoluted and calibrated pulse generated by siggen. This will shift the baseline of the pulse from zero to the detector-dependent value, as the baseline amplitude of the detector pulse is visible in the noise templates. The final simulated detector pulses for 500 eV and 5 keV events of the CONUS-1 detector are shown in Figure 4.15. The impact of the noise on the pulse is clearly visible as the signal-to-noise ratio of the low energy pulse is much smaller than for the 5 keV pulse.

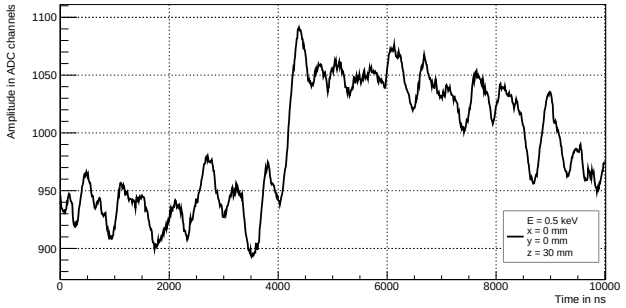

(a)

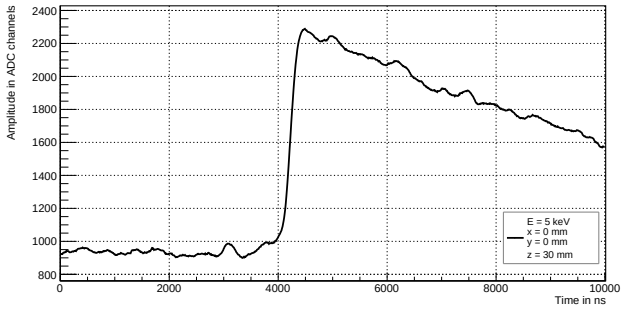

(b)

Figure 4.15.: Final simulated pulses of the CONUS-1 detector. The impact of the noise on the simulated pulses is clearly visible. The signal-to-noise ratio of a pulse produced by a 500 eV event (a) is much smaller than that of a pulse produced by a 5 keV event (b).

4.4. Validation and Results of the Pulse-Shape Simulation

To verify the simulated pulse-shapes a detailed comparison to measured pulses from the detectors is done. For this purpose measured example pulses are selected from the CONUS Run-5 data. Here, a few criteria for the pulse selection have to be considered. First of all, the measured pulses need to be SSEs, as the single energy depositions are not known for MSEs. The selection criteria for SSEs is a straight rise of the pulse without any visible step. Second, the selected pulses should be fast pulses, as siggen is not capable of simulating slow pulses. Furthermore, four different energies between 500 eV and 25 keV are selected for the comparison. At these energies also a simulation was performed, where all pulses are simulated at the same interaction position inside the active volume at $x = 0\,\text{mm}$, $y = 0\,\text{mm}$ and $z = 30\,\text{mm}$. For the comparison, the simulated pulses are shifted in time to match the rise of the measured pulses, which is dependent on the pre-trigger value of the DAQ settings.
The simulated and measured pulses of the CONUS-1 detector are shown in Figure

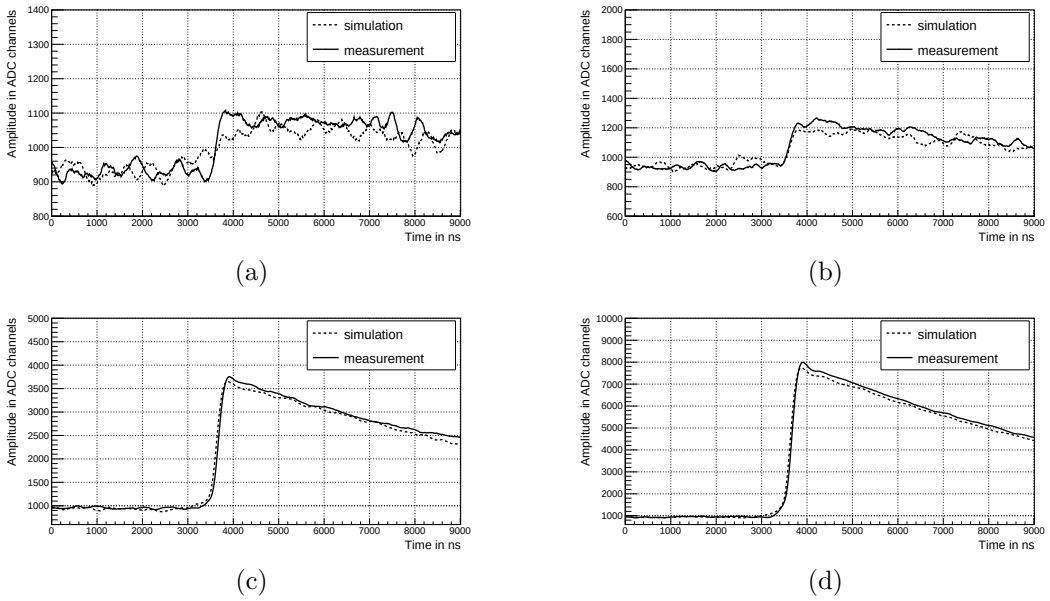

Figure 4.16.: Comparison between simulated and measured pulses for the CONUS-1 detector at 500 eV (a), 1 keV (b), 10 keV (c) and 25 keV (d). The simulated pulse (dashed) is shifted in time to match the rise of the measured pulse (solid).

4.16 for all four energies. The pulses for detectors C2 to C4 are shown in Appendix H. To compare the different pulses of measurement and simulation a waveform fit is performed [64]. The pulses can be described by

$$f(t) = A_0 \left[\tanh\left(\frac{t - t_0}{\tau} \right) + 1 \right] \exp(-\tau_c (t - t_0)) + P_0, \tag{4.10}$$

with A_0 the amplitude of the pulse, t_0 the timing offset until the rise of the pulse starts, τ the parameter related to the rise-time of the pulse, τ_c the parameter related to the exponential decay due to the AC coupling of the DAQ and P_0 the baseline level of the detector. For the fit the decay parameter τ_c is fixed to a certain value, same for simulation and measurement. Due to the impact of noise the parameters can differ a lot in the low energy range. For this reason, the comparison of the fit parameters is mainly done at higher energies above 1 keV. The fit parameters of the measured and simulated pulses at the four energies for the CONUS-1 detector are shown in Table 4.4. The parameters for the other detectors can be found in Appendix H. It becomes visible, that the baseline of the simulated pulses matches the measured baseline very well. This is also true for the rise-time parameter τ. The maximum amplitude of the simulated pulses is slightly deviating from the measured amplitude. This deviation is energy dependent, the higher the energy, and therefore, the amplitude, the higher the deviation. For C1 and C4, the amplitude is slightly underestimated, whereas for C3, it is overestimated. For C2, the amplitude of the simulated pulse matches the amplitude of the measured pulse. The reason for this

Table 4.4.: Fit parameters of measured and simulated pulses for the CONUS-1 detector. The constant of the exponential decay τ_c is fixed in the fit to 0.000131 ns for measurement and simulation as well.

Energy in keV		A_0 in ADC channels	t_0 in ns	τ in ns	τ_c in ns	P_0 in ADC channels
0.5	measurement	92.54 ± 0.90	3647.80 ± 5.56	85.15 ± 8.75	0.000131	933.01 ± 1.01
	simulation	77.90 ± 0.10	3519.35 ± 9.06	142.04 ± 12.35	0.000131	925.89 ± 1.11
1	measurement	161.94 ± 0.89	3621.38 ± 3.72	140.58 ± 7.79	0.000131	932.92 ± 0.98
	simulation	127.47 ± 1.15	3624.81 ± 5.60	109.75 ± 9.88	0.000131	947.26 ± 1.28
10	measurement	1444.53 ± 1.17	3672.99 ± 0.53	124.24 ± 0.95	0.000131	961.25 ± 1.30
	simulation	1416.44 ± 1.64	3629.56 ± 0.77	132.86 ± 1.43	0.000131	942.67 ± 1.81
25	measurement	3634.95 ± 2.33	3662.67 ± 0.43	129.20 ± 0.77	0.000131	958.81 ± 2.59
	simulation	3538.49 ± 2.68	3630.69 ± 0.50	130.72 ± 0.93	0.000131	961.08 ± 2.97

is most likely the determination of the calibration coefficients for the ADC channel calibration of the simulation. For this calibration, only a small dataset was used. By using a larger dataset it is assumed that this difference in amplitude can be reduced. By comparing the plots, it becomes visible that the simulated noise matches the measured noise in amplitude and frequency. The exponential decay induced by the AC coupling of the DAQ is also reproduced exactly by the simulation.
For the 25 keV measurements and simulations a difference in the starting rise of the pulse can be observed, especially for Figure H.1 (d) and H.3 (d). This observable feature is produced by the distance of the event location to the point-contact as discussed in Section 4.2. The dependence of the rise of the simulated pulse on the interaction position is shown in Figure 4.17. Here, different interaction positions inside the active volume of the CONUS-1 detector with an energy of 25 keV are simulated and compared to a measured example pulse. The pulses are plotted on top of each other defining the position in time of the maximum amplitude as t_0. Depending on the distance to the point-contact the rise of the pulse starts earlier or later. If the interaction position is very close to the point-contact the rise is delayed and rather steep. If the interaction position is distant from the contact, the rise starts earlier, forming the characteristic pre-increase of the pulse [64, 65]. For the example pulse of C1, a medium distance in z-direction and a small distance to the point-contact in x-direction is fitting the best.
As the pre-increase will slightly modify the rise-time of the pulses, a detailed study on the rise-time in dependence of the interaction position can be done. For this purpose 25 keV pulses with different distances in z-direction to the point-contact were simulated. Here, the rise-time of the pulses is not determined via a fit of Equation 4.10 but by calculating the time difference between 10% and 90% of the pulse maximum. This is done as the fit is not able to reproduce the pre-increase and the bump precisely enough. The rise-times of this $10-90\%$ method and the rise-time fit can be compared by dividing the rise-times of the $10-90\%$ method by $2\,\mathrm{arctanh}(0.8)$ [65]. The rise-time in dependence of the distance to the point-contact for CONUS-1 to CONUS-4 is shown in Figure 4.18. It can be seen, that the rise-time behavior is different in the regions near and far from the point-contact. Above a distance of

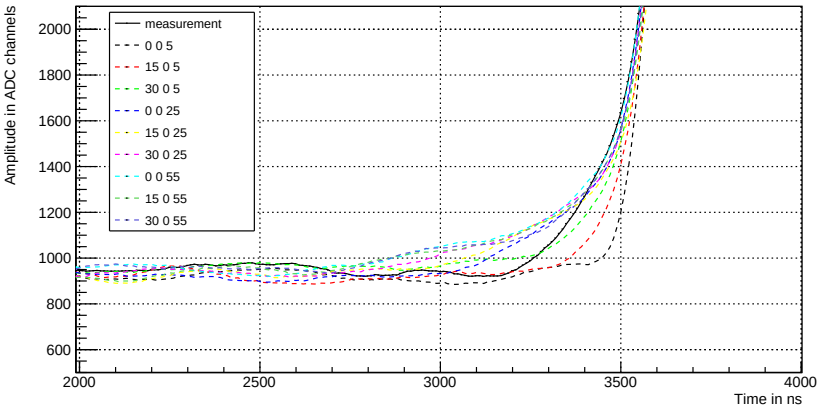

Figure 4.17.: Dependence of the interaction position on the pulse rise for the CONUS-1 detector. Events with 25 keV and different interaction positions were simulated (dashed) and compared to a measured example pulse (solid black). The interaction positions are given as x, y, and z positions starting from the point-contact. The observed pre-increase of the pulses can be explained by the interaction position far from the point-contact.

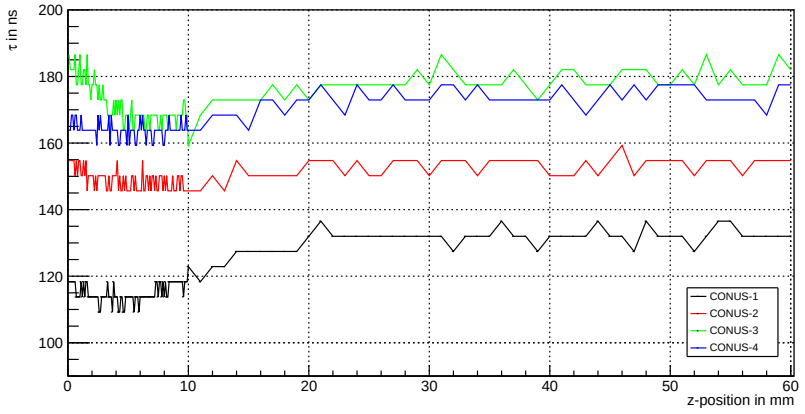

Figure 4.18.: Dependence of the pulse rise-time on distance to point-contact for CONUS-1 (black), CONUS-2 (red), CONUS-3 (green) and CONUS-4 (blue). The pulses were simulated for varying z-positions with $x = 0\,\text{mm}$ and $y = 0\,\text{mm}$ at 25 keV.

Table 4.5.: Typical measured and simulated rise-times for the CONUS detectors. The measured rise-times, taken from [65], are obtained from 15 keV pulses in the whole active volume while the simulated pulses are only at $x = 0$ mm and $y = 0$ mm with varying z-position at 25 keV.

Detector	τ_{measured} in ns	$\tau_{\text{simulated}}$ in ns
CONUS-1	100 - 150	105 - 140
CONUS-2	140 - 195	145 - 160
CONUS-3	145 - 215	155 - 190
CONUS-4	125 - 190	155 - 180

~ 20 mm, the rise-time is stable, while the rise-time evolves differently below this distance. In the closest distance of < 10 mm to the contact the rise-time is decreasing until it reaches its lowest value. Above this, it increases until the stable region is reached. The range of rise-times for the different detectors matches the measured rise-times depicted in Table 4.5.
For the measured pulses of the CONUS detectors, a characteristic 'bump' at maximum amplitude was observed. With the help of a pulser measurement, it was figured out that this bump is induced by the preamplifier and DAQ electronics [65]. This origin can also be validated with the pulse-shape simulations. The bump in the pulses occurs only after applying the electronic response to the simulated pulses; therefore, it is induced by the electronics, and it is not a characteristic of the crystal. The bump is already visible in Figure 4.9 as a bump in negative amplitude. Here, also the explanation for the different bump strengths and forms of the five detectors is visible.
To validate the pulse-shape simulation not only for single pulses but also for a whole spectrum a complete spectrum simulation of a ^{228}Th-source up to 1000 keV was performed. First, the energy depositions were simulated using the MaGe-interface followed by the signal simulation done with siggen. Due to limitations in computing, only about 6000 events were simulated, resulting in relatively weak statistics. To compare the simulation with real data a ^{228}Th-calibration measurement of the CONUS-1 detector in the commissioning phase of Run-5 is used. Here, the final Run-5 settings were not yet fixed, and therefore, slightly different DAQ settings and channels were used. This will induce some small differences in the comparison to the simulated data, as the simulation was calibrated with the final Run-5 settings. Unfortunately, it was not possible to use a measurement with the final settings due to the lack of high energy ^{228}Th-measurements during Run-5 and the following dismantling of the experiment in KBR. For the comparison, the rise-time fit according to Equation 4.10 was applied following the procedure discussed in [64]. This was done for the measured and the simulated data and the fitted rise-time is then plotted against energy. The rise-time plots for measurement and simulation are shown in Figure 4.19. For the simulation, two rise-time populations are visible.

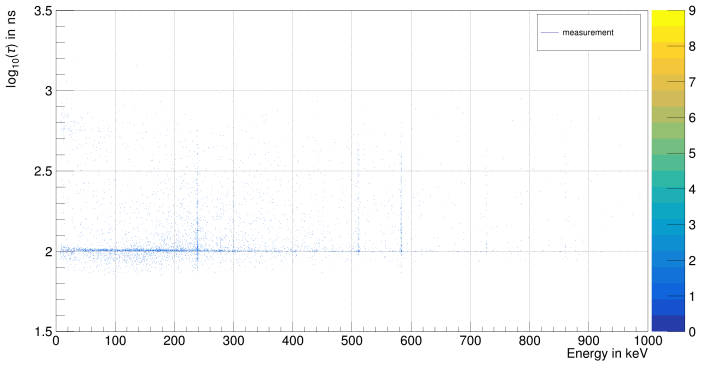

(a)

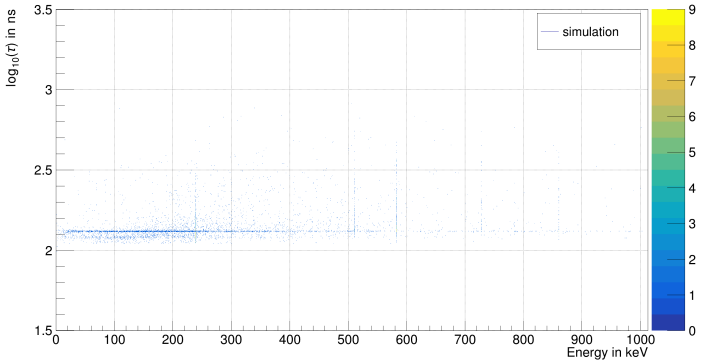

(b)

Figure 4.19.: Rise-time against energy for measurement (a) and simulation (b) of ^{228}Th-spectrum for the CONUS-1 detector. Here, the logarithm of the rise-time parameter τ is plotted and the color bar indicates the number of events per bin.

They correspond to the interaction position inside the crystal near and far from the point-contact. This feature is not clearly visible in the measured dataset due to the lack of statistics but is present in overall measured data as stated in [65]. The FP $\log_{10}(\tau)$ population mean value of the simulated data is 0.15 ns higher than the one of the measured data. This is related to the different settings mentioned above. As the simulation is not able to reproduce slow pulses, the rise-times around $\log_{10}(\tau) = 3$ ns are not represented in Figure 4.19 (b), while they are visible in the measurement in Figure 4.19 (a). At the peaks of the ^{228}Th-source the rise-times are spread over a large range from ~ 0.1 ns below the FP band to ~ 0.7 ns above this band. This feature is well reproduced in the simulation. If the projection of these spectra is done on the y-axis, the number of events at each $\log_{10}(\tau)$ is given. These projections for measurement and simulation are depicted in Figure 4.20. Again here, the impact of the slow pulses in the measurement is visible as there are more events

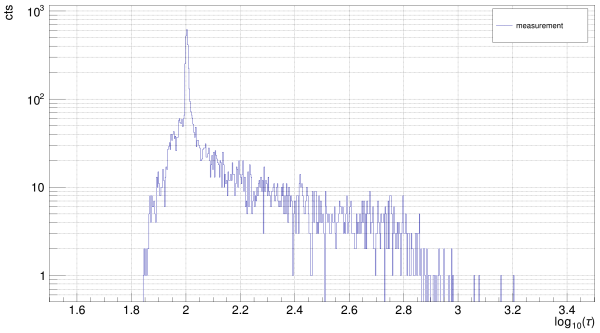

(a)

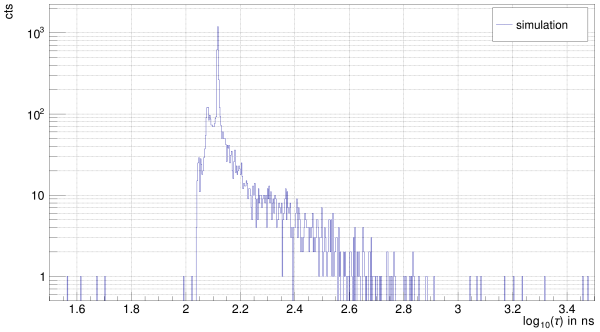

(b)

Figure 4.20.: Rise-time projection for measurement (a) and simulation (b) of ^{228}Th-spectrum for the CONUS-1 detector. Here, a projection of Figure 4.19 on the y-axis is done, and the number of events is plotted against the logarithm of the rise-time parameter τ.

at $\log_{10}(\tau) > 2.5\,\text{ns}$ than in the simulation. The distribution for the measurement is broader than for the simulation. Also, the impact of the settings on the value of the mean FP band is visible as the maximum value of the peaks is slightly different for measurement and simulation with $\log_{10}(\tau) = 2\,\text{ns}$ for the measurement and $\log_{10}(\tau) = 2.15\,\text{ns}$ for the simulation. A major difference between the two spectra is the small peak in the simulation data at $\log_{10}(\tau) = 2.1\,\text{ns}$. This peak is induced by the second band of the FP distribution as mentioned above, which is strongly visible in the simulation data but only weak in the measured data.
All in all the simulation is reproducing the measured spectrum very well in all features. For future work, a comparison with higher statistics and the same settings input has to be done, which is not part of this thesis due to the lack of experimental data.

5. Conus+ and the Germanium Detector Upgrade

Besides a precise knowledge of all background components, an improvement in hardware can increase the sensitivity of the experiment. With the relocation of the CONUS setup from KBR to the nuclear reactor in Leibstadt a full detector optimization is feasible. For the upgrade a focus on the improvement in noise, energy resolution and detection efficiency is set as these components are responsible for an improvement of the energy threshold and therefore an improvement in the expected sensitivity.
In the following the modified experimental setup of CONUS+ and the new nuclear reactor are explained. After that, the detector upgrade is summarized in Section 5.2. Finally, the process of detector characterization at MPIK and during commissioning at reactor site is described with results regarding the resolution and the threshold of the refurbished detectors in Section 5.3.

5.1. The Conus+ Experiment

As the KBR reactor stopped operation at the end of 2021 and thus the CONUS experiment finished data collection after a long reactor OFF period of almost one year in 2022, a follow-up experiment for the CEνNS search at nuclear reactors was planned. CONUS+, the successor of the CONUS experiment, is located at the Leibstadt nuclear power plant (KKL) in Switzerland. The new experimental site inside KKL is located at a distance of 20.7 m from the 3.6 GW_{th} reactor core. Therefore a slightly lower antineutrino flux of $1.45 \cdot 10^{13}\,cm^{-2}s^{-1}$ compared to KBR is achieved. Also the overburden with a shallow-depth of $7 - 8$ m w.e. is reduced compared to the old CONUS location.
For CONUS+, the existing CONUS shield was moved from Brokdorf to the new power plant, and several upgrades are realized to meet the changed demands of the new experimental site. The setup of the CONUS+ experiment is shown in Figure 5.1. Among other things, a second active muon-veto was installed. For this, a lead layer inside the shield was replaced by a plastic scintillator, increasing the efficiency

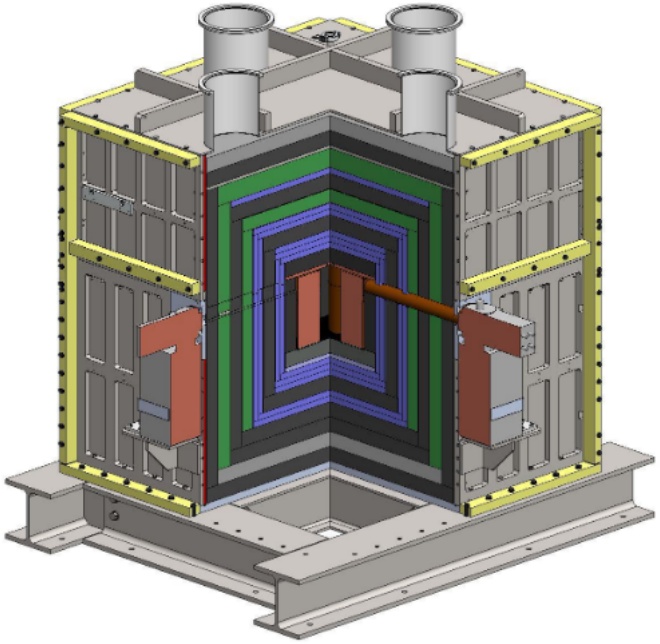

Figure 5.1.: Layout of the CONUS+ setup. The four refurbished and upgraded HPGe detectors (brown) are placed inside the detector chamber. The shield is composed of layers of lead (dark grey), (borated) polyethylene (blue), and the two muon-veto layers (green). From [37].

of rejecting background events. In the following, the new muon-veto is referred to as inner veto. The main improvement in CONUS+ is the optimized HPGe detectors. For this, the old CONUS detectors are completely refurbished by Mirion Lingolsheim to optimize the detectors in terms of energy threshold, trigger efficiency, vibrations, and stability. The energy threshold of a detector is a major influence on the CeνNS sensitivity as the number of expected events strongly increases with lower energies. Therefore, with this optimization, the sensitivity of CONUS+ is expected to increase strongly, although the lead shielding is slightly reduced, and the neutrino flux and overburden are less than at KBR.
In the following the implemented upgrades of the detectors are discussed in detail.

5.2. Detector Upgrade

For a successful and precise measurement of the CEνNS process, it is crucial to have the best available detector performance. The five CONUS runs in the past revealed a few points for optimization of the detectors. It turned out that the energy threshold of 210 eV in Run-5 is still too high to have a satisfying amount of expected CEνNS-events in the ROI as well as the trigger-efficiency at the threshold is rather low with $20-30\%$. Another problem is the strong (vibration-induced) noise

component, which is linked to the ambient temperature requiring the TDD and the NTC data cuts (see Chapter 3.3.1).
For these reasons a R&D campaign was started in 2022 with the detector manufacturer Mirion Canberra in Lingolsheim to get significant improvements in detector performance. For this purpose, CONUS-5 was optimized first to achieve an overall better detector behavior, followed by the four KBR detectors. The characterization and resulting measurements regarding the improvements mentioned hereinafter are discussed in Section 5.3.
As the energy threshold of a detector is one of the most important parameters for the signal search, it is required to have the lowest possible threshold for the new experiment. The threshold is highly dependent on the noise edge [25] of the detector. It is defined for CONUS Run-5 as the energy until which the trigger-efficiency is $> 20\%$ and the contribution of the noise peak to the spectrum is below $1\,\mathrm{cts\ d^{-1}\ keV^{-1}}$ [31]. The noise edge is made up of electronic noise at the low energy part of the measured spectrum. To directly characterize the noise level of a detector the energy resolution is a good tool as the noise edge is roughly two to three times the energy resolution [80] of an injected test pulse. In theory, a monoenergetic particle produces a sharp line in the energy spectrum of a detector, but noise induced by electronic components and statistical fluctuations in the ionization process lead to a broadening of the peak [81]. This peak can be described by a Gaussian

$$g(x) = \frac{S_\mathrm{g}}{\sqrt{2\pi}\sigma} e^{-\frac{(x-x_0)^2}{2\sigma^2}} \tag{5.1}$$

with variance σ, events in the peak S_g and peak position x_0. As the energy resolution ΔE is defined as the full width at half maximum (FWHM) of the peak it is given by

$$\Delta E = \sigma \cdot \sqrt{8\ln(2)} = 2.35 \cdot \sigma. \tag{5.2}$$

The total energy resolution is made up of several components [62] and can be written as

$$\Delta E^2 = \Delta E_\mathrm{I}^2 + \Delta E_\mathrm{P}^2 + \Delta E_\mathrm{C}^2 + \Delta E_\mathrm{E}^2. \tag{5.3}$$

First of all, the total resolution contains the intrinsic line width of the nuclear levels ΔE_I. It is inversely related to the mean lifetime of the energy levels $t_{1/2}$

$$\Delta E_\mathrm{I} = \frac{10^{-15}}{t_{1/2}} \tag{5.4}$$

and therefore, it is negligible. Furthermore, the uncertainty on the number of created electron-hole pairs in the detector ΔE_P contributes. In germanium, it takes on average $\epsilon = 2.96\,\mathrm{eV}$ to create a single electron-hole pair, and with that the number

n of created pairs at an energy deposition E in the detector can be estimated by

$$n = \frac{E}{\epsilon}. \tag{5.5}$$

Therefore the inherent statistical fluctuation of n limits the resolution and the uncertainty is given by [82]

$$\Delta E_{\mathrm{P}} = 2.35 \cdot \sqrt{F\epsilon E} \tag{5.6}$$

with F the Fano-factor, which is defined as the ratio between the observed variance in the created number of electron-hole pairs and the variance predicted by Poisson statistics. ΔE_{C} is the variability on the proportion of the collected charge inside the detector and the preamplifier due to incomplete charge collection. Lost or delayed charges do not contribute to the output pulse and can therefore worsen the resolution. The last contribution to the resolution is the impact of electronic noise ΔE_{E}. The event energy in the DAQ is calculated by extracting the pulse height from a constant baseline. Noise on the baseline will introduce a variability of this value and the pulse height measurement is affected by that. As for each pulse the baseline is disturbed in the same way, the effect of the noise is bigger for smaller pulses. As electric noise is a major component of the resolution, noise optimization also offers the possibility of optimizing the detector's energy resolution. Lowering the noise and, therefore, the resolution and the energy threshold, is the main approach for the CONUS+ detector optimization. To improve the noise level of an HPGe detector, the total detector capacitance has to be lowered [81]. The capacitance of a point-contact HPGe detector is given by [83]

$$C = 2\pi K \epsilon_0 r \tag{5.7}$$

with K the dielectric constant of germanium, $\epsilon_0 = 8.85 \cdot 10^{-12}\,\mathrm{Fm}^{-1}$ the free space permittivity and r the radius of the point-contact electrode. Here, it becomes visible that by reducing the point-contact size of the detector, the capacitance is also reduced and, thus, the noise. Reducing the point-contact size also has another advantage, as the rise-time of the detector output pulses is getting faster, confirmed by J. Hakenmüller with the siggen pulse-shape simulation. From observations with a different germanium detector optimized for quenching factor measurements in germanium [32] a faster rise-time cause a better detection efficiency. The five CONUS detectors CONUS-1 to CONUS-5 were all equipped with a point-contact radius of 1.25 mm. After the reworking of the crystals, the point-contact radius for all five detectors is $r \leq 0.5\,\mathrm{mm}$ resulting in a very low theoretical capacitance of 0.45 pF.
The last optimization step is located in the cold front-end electronics of the detectors. Here, the old custom-built junction-gate field-effect transistor (JFET) [25] is replaced by an application-specific integrated circuit (ASIC) which is able to achieve ultra-low noise levels. As they also have a faster response, the rise-time of the pulses

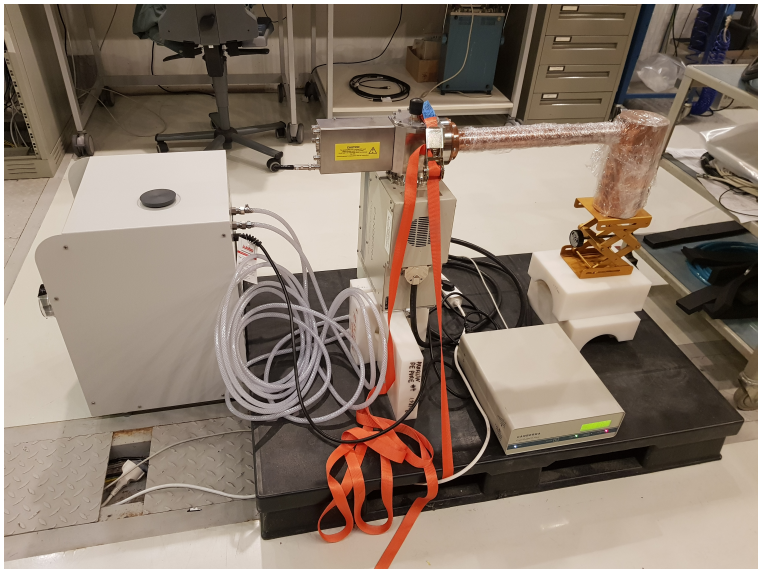

Figure 5.2.: Water cooling of the CONUS-5 detector. The chiller for cooling and pumping the water is placed on the left side. An inlet and outlet water tube is connecting the chiller with the detector. The coolant is inserted by valves on the side of the cryocooler housing. On the cryocooler housing, the old air inlet window for the fan is visible, whereat the fan is not used anymore.

will be again faster, leading to better trigger-efficiency.
As mentioned in Chapter 3.3.1 the noise rate of the detector is correlated to the cryocooler power consumption. Also, there is a noise component made up of microphonic events. These vibrations are induced by the electrical cryocooler. The pulse-tube of the cryocooler is driven by a compressor which is in turn cooled by an air flow produced by a fan. If the power consumption of the cryocooler is higher, the compressor is more active and the fan needs to cool stronger. By the fan and the compressor, mechanical vibrations are introduced to the detector, whereat microphonic noise is induced. It was found, that the frequency of the compressor is $44 - 47\,\mathrm{Hz}$ [61]. The fan induces various frequencies but the frequency peak around $55\,\mathrm{Hz}$ is the most prominent. For both devices, several higher resonance frequencies exist.
To get rid of a part of the vibrations, the fan was replaced by a water cooling system in the course of the modification measures. For the water cooling, the compressor is wrapped by a water tube coil, where cooled water is pumped by a Julabo F500 chiller. The new setup of CONUS-5 is shown in Figure 5.2. The chiller and the detector are connected by inlet and outlet water tubes made from halogen-free material due to KKL restrictions. The inner compressor tube coil is connected to the outer water tubes with valves on the side of the cryocooler housing. For CONUS-5 the valves were first mounted on the bottom of the housing but in the development process they were moved to the side due to feasibility reasons for the CONUS+

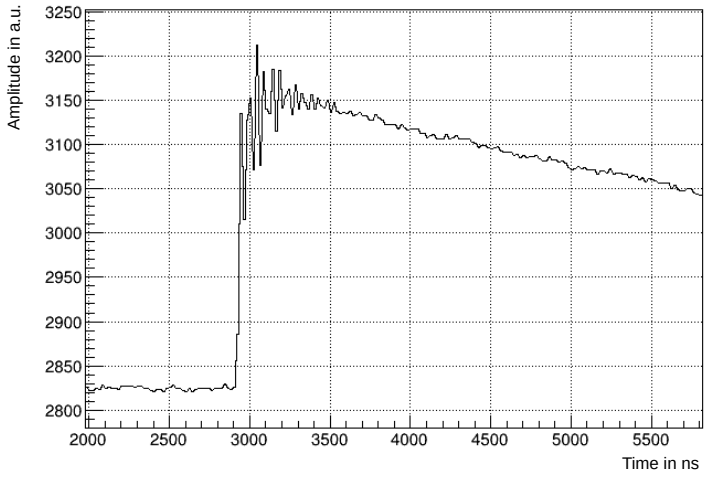

Figure 5.3.: Oscillating behavior of detector pulses during the R&D phase. The feature showed up for injected test pulses to the preamplifier and is produced by reflections.

setup. With the upgrade to water cooling instead of air cooling of the compressor the vibrations induced by the fan should be removed and therefore also a part of the microphonics noise and the temperature dependence of the noise should be reduced. During the R&D phase at Mirion a few problems with the detectors showed up. CONUS-2 and CONUS-3 showed a problem with infrared radiation from warmer components inside the endcap. Therefore, Mirion added a mylar foil around the detector crystal, shielding the crystal from the infrared. For all detectors, the pulses induced by a pulser showed an unexpected oscillation at the maximum. An example pulse for CONUS-5 is shown in Figure 5.3. By injecting a test pulse into the preamplifier, some reflections arise at the measured pulse, and the maximum of the pulse is distorted. The problem emerged from a resonance of the high voltage cable inside the preamplifier and was solved by Mirion by an improved cabling, which will be called high voltage filter hereinafter. Additionally, CONUS-5 differs from the other detectors by a Nickel plating at the cryocooler contact. These additional detector properties after the optimization are summarized in Table 5.1.

Table 5.1.: Additional detector properties after optimization. For some detectors a mylar foil is added around the crystal to avoid infrared radiation of warmer components. Also an electrical filter is applied to some of the high voltage cables in the preamplifier. Additional the cryocooler contact of CONUS-5 is plated with Nickel.

Detector	Mylar Foil	Ni plated CP5	HV Filter
CONUS-1	✗	✗	✓
CONUS-2	✓	✗	✓
CONUS-3	✓	✗	✓
CONUS-4	✗	✗	✓
CONUS-5	✗	✓	✓

5.3. Detector Characterization and Commissioning

After the refurbishment at Mirion Lingolsheim, the detectors were tested and characterized in the Lowlevel Laboratory (LLL) at MPIK with an overburden of 15 m w.e. [26]. Before shipping to MPIK, each detector was tested in the Factory Acceptance Test (FAT) by the manufacturer. Here, the nominal values of energy resolution and trigger-efficiency, and the overall performance of the detectors after the optimization were specified by Mirion. The Site Acceptance Test (SAT) was then carried out at MPIK with the CONUS equipment. For this purpose, the same DAQ was used as in CONUS Run-5 at KBR. For the Ge-data the CAEN board V1782 with the CoMPASS software was used. To obtain the best results in detector performance the board settings play a major role and have to be tuned in an iterative process. A noticeable difference in the CoMPASS settings before and after the optimization, especially in the input rise-time and the trapezoidal settings, was required to have the optimum configuration for the detector characterization. A comparison of selected settings between Run-5 and after refurbishment for CONUS-2 is shown in Table 5.2. The settings for the other detectors are similar. It becomes visible that the optimization affects the rise-time of the pulses as the input rise-time is now much shorter than before. For the trigger and energy determination of the pulses the standard $\mathrm{RC}-\mathrm{CR}^2$ algorithm of the CAEN board was replaced by a combination of a slow and a fast triangular discriminator similar to Run-5 [64, 31].
For the detector characterization, the energy resolution and the trigger-efficiency were measured. Here, the stability of the calibration peak position was also determined. Furthermore, the depletion voltage and the vibrations were measured. The results are shown in the following.
Upon delivery of the CONUS-2 and CONUS-3 detectors, Mirion stated the mixing up of the germanium crystals of these two detectors. For comparison of the new detector results to before the optimization, it is important to know which crystal is

Table 5.2.: Comparison of CoMPASS settings before and after the detector optimization for the CONUS-2 detector. Here, only a selection of settings with the largest deviation is shown.

Settings	Before	After
Fast discriminator smoothing	32	16
Input rise time	800 ns	600 ns
Trap. rise-time	12 μs	3 μs
Trap. flat top	5 μs	0.3 μs
Trap. pole zero	6.9 μs	6.8 μs
N samples peak	16	1

in which cryostat and how the detector is called. During the characterization phase, it was found at depletion voltage measurements that the crystal of CONUS-3 was placed inside the CONUS-2 cryostat, which was delivered as CONUS-2. Due to this incident the detectors are named after the crystal inside the cryostat.
Before installing at KKL, the four CONUS+ detectors were tested in a semi-complete setup together with the new inner muon-veto in LLL. The test setup is shown in Figure 5.4. As in the setup no grounding was applied, the measurements that were performed were slightly worse than with the single detectors. Due to a delivery delay of the CONUS-1 detector, it was replaced in this test by CONUS-5. The choice of using CONUS-5 instead of CONUS-1 was also made for the installation at KKL. CONUS-5 was produced at the same time than the other four detectors and does not differ significantly in design and performance but due to a longer storage above ground it was exposed longer to cosmic radiation and hence the activation is slightly higher [25].
After the successful characterization at LLL, the detectors were installed inside the CONUS+ shielding in KKL in August 2023. In the following, the results of the four detectors inside the CONUS+ setup during the commissioning phase are shown, as well as the results in the LLL.

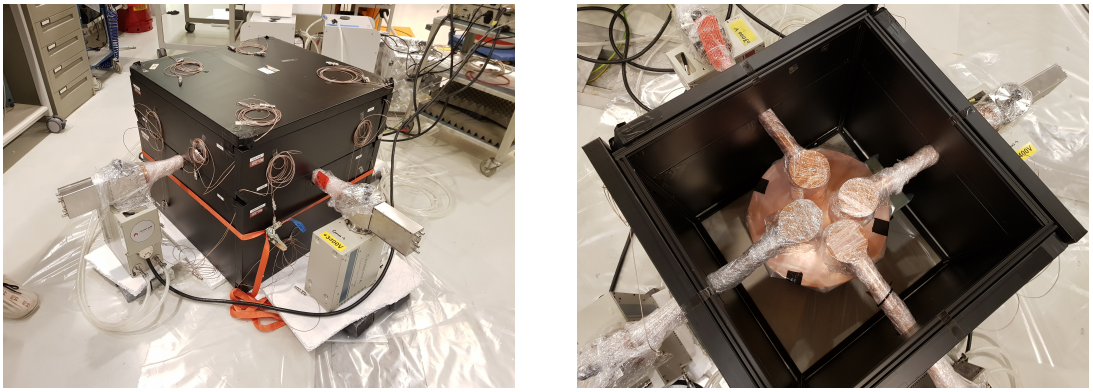

(a) (b)

Figure 5.4.: Semi-complete test setup with all four CONUS+ detectors and new inner muon-veto (black) in LLL. The detectors are fully enclosed by the plastic scintillator (a). In the inner chamber (b) the detectors face each other as in the CONUS setup.

5.3.1. Energy Resolution

To determine the total energy resolution of the detectors measurements with an ^{241}Am-source were conducted and the FWHM of the 59.5 keV peak was determined. To quantify the influence of the electronics noise ΔE_{E}, additionally a pulser signal can be injected as described in Chapter 2.2. The optimization of this pulser resolution was the focus of the characterization. To achieve the best possible pulser resolution, the settings were tuned as mentioned above. With the optimum settings a pulser resolution of around 50 eV was achieved for all detectors which are even slightly lower in the complete CONUS+ setup at KKL. The measured pulser resolutions match perfectly the nominal values $\Delta E_{\mathrm{Mirion,KKL}}$ given by Mirion. The pulser resolution values before the refurbishment ΔE_{KBR}, the nominal values, and the measured resolutions for the optimized detectors are given in Table 5.3. Here, the given pulser resolution ΔE_{KBR} was measured by the LYNX DAQ system. The resolution of the CAEN DAQ achieved at KBR is slightly worse. Compared to the pulser resolutions before the optimization the resolution improved by $23-36\%$ for CONUS-2 to CONUS-4. CONUS-5 even improved by 84%. This is due to the rather poor performance before the upgrade.
Regarding the total resolution obtained by the 59.5 keV peak of ^{241}Am the measured values are in the range between $280-350$ keV during the characterization phase depending on the CAEN settings. In the final measurement with the test setup before shipping to KKL, the pulser resolution was not optimal due to noise in the setup, and therefore, it can be assumed that the total resolution shown in Table 5.4 is also not ideal. Also, the measurement time was short, and hence, the statistics were low, resulting in high errors. The measured resolution is close to or slightly better than the nominal values given by Mirion.

Table 5.3.: Pulser resolution ΔE_{KKL} for the CONUS+ detectors compared to values measured at KBR before the optimization and nominal values $\Delta E_{\mathrm{Mirion,KKL}}$ specified by Mirion for the optimized detectors. It should be taken into account that ΔE_{KBR} was obtained with the LYNX DAQ and resolutions with the CAEN DAQ at KBR are slightly worse.

Detector	ΔE_{KBR} in eV	$\Delta E_{\mathrm{Mirion,KKL}}$ in eV	ΔE_{KKL} in eV
CONUS-2	77 ± 1	51	49 ± 1
CONUS-3	64 ± 1	51	49 ± 1
CONUS-4	68 ± 1	48	50 ± 1
CONUS-5	$300 - 500$	49	48 ± 1

Table 5.4.: Total resolution measured for the 59.5 keV peak of ^{241}Am for the CONUS+ detectors compared to nominal values $\Delta E_{\mathrm{Mirion}}$ specified by Mirion for the optimized detectors. The values were measured in a not-optimized setup with very low statistics.

Detector	$\Delta E_{\mathrm{Mirion}}$ in eV	$\Delta E_{59.5\,\mathrm{keV}}$ in eV
CONUS-2	326	317.5 ± 10.32
CONUS-3	318	323.5 ± 9.28
CONUS-4	308	308.9 ± 10.11
CONUS-5	314	339.7 ± 5.26

Regarding the main characterization focus a huge improvement in pulser resolution compared to the KBR values is achieved by the optimization which is visualized in Figure 5.5. Here, exemplary the injected pulser signal peaks are shown for the CONUS-2 detector before the optimization at KBR in blue and after the optimization at KKL in red. The peaks are normalized to 1, and the position on the x-axis is also normalized to 1 for better comparison. It becomes clearly visible that the width of the red peak is much smaller than the width of the blue peak. As the pulser resolution reflects the amount of noise in the system, the noise edge and the estimated energy threshold of the experiment are expected to be lowered.

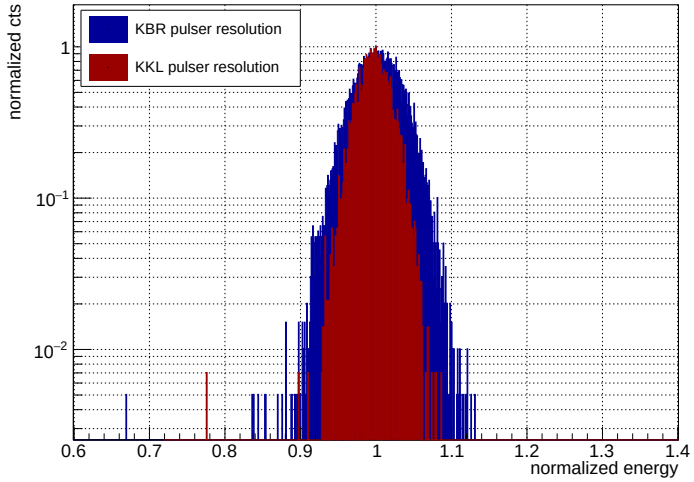

Figure 5.5.: Pulser resolution before (blue) and after (red) the optimization phase for the CONUS-2 detector. For better comparison the position of the peak on the x-axis corresponding to energy is normalized to 1 as well as the peak height in counts.

5.3.2. Noise Edge and Energy Threshold

As stated above the noise edge is expected to improve according to the improved pulser resolution. During the characterization, it became evident that there is a second low-energy component in addition to the electronic noise in the raw data at the noise edge. While the electronic noise component of the noise edge is limited to energies below 200 eV the second component extends up to above 1 keV. When looking at the corresponding pulses obviously the pulse-shape differ from the expected shape. The recorded events responsible for the increase of the noise edge are flat without visible pulse, only the baseline is shifted to higher values. The reason for that behavior is unknown, but it is likely that it is correlated with the choice of CAEN settings. To get rid of these additional events two different cuts can be applied. The first cut is based on the pulse-shape of the events and can be applied as described in [64]. The pulses can be fitted with the pulse-shape fit function of Equation 4.10 in Chapter 4.4. Also here the decay parameter τ_c is fixed. It turned out that the value for the optimized CONUS-2 is the same as for CONUS-2 before the upgrade. For the elimination of the additional noise, the cut is based on P_0 and t_0. If the baseline is shifted to above 1200 ADC the pulses are removed and also if the pulse starts earlier than 200 ns. These values are only for the CONUS-2 detector and can also be considered more conservative or aggressive. In Figure 5.6 (a) the pulses before and in (b) the pulses after the cut are displayed for the CONUS-2 detector. The shifted baseline pulses can be easily identified. Depending on the intensity of the cut criteria the additional pulses can be removed more or

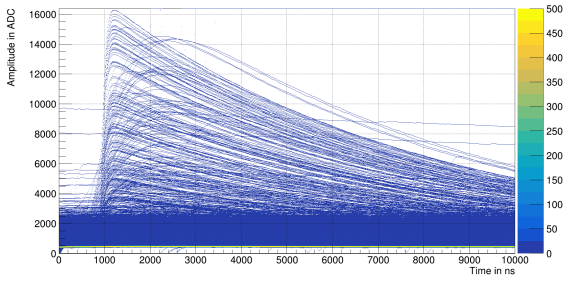

(a)

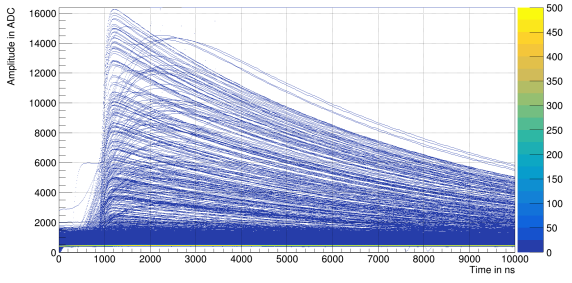

(b)

Figure 5.6.: Raw detector Pulses before (a) and after (b) the additional noise cut for the CONUS-2 detector. The measured signal amplitude is plotted over the duration time of the event. For the noise cut an upper limit of $P_0 = 1200\,\mathrm{ADC}$ and $t_0 = 200\,\mathrm{ns}$ is used.

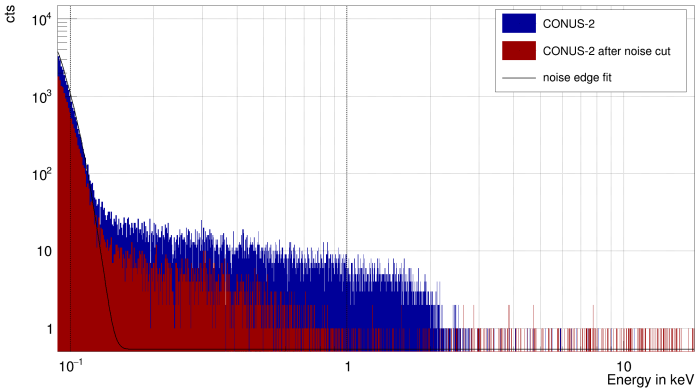

Figure 5.7.: Raw energy spectrum before (blue) and after (red) additional noise cut for CONUS-2. The number of events is plotted over the energy in keV. Additionally, the electronic noise part of the noise edge is fitted with a Gaussian (black). For the noise cut an upper limit of $P_0 = 1200\,\mathrm{ADC}$ and $t_0 = 200\,\mathrm{ns}$ is used.

less completely whereas also low energy pulses can be removed accidentally due to the small amplitude to noise ratio. Here, the best cut value has to be found for the future analysis of the CONUS+ data to obtain the best cut efficiency. The energy spectra before in blue and after the cut in red are shown in Figure 5.7. Additionally, the noise edge is fitted with a Gaussian. Here, the reduction of the additional noise events is strongly visible and also the impact of the additional noise to the threshold can be estimated.
The second, more reliable cut is in connection with the TRP and muon-veto. As the spectra above are based on raw data also spectra with applied muon-veto and TRP cut are considered. In the muon-veto cut all events in a coincidence window of 650 μs with the muon-veto are cut to reject muon induced events. For the TRP cut all events in a coincidence window of 1 ms with the baseline reset of the preamplifier are cut to account for additional events induced by the reset. The corrected spectra shown in blue in Figure 5.9 are not showing the additional noise bump. Thus, it is likely that the additional noise contribution is induced by TRP events. Most of the flat pulses, now assuming to be TRP related events, are reduced as shown in Figure 5.8 (a) but there are pulses with a slight slope still left. These pulses are probably produced by the DAQ triggering on the falling tail of a previous pulse. To get rid of these pulses a higher trigger holdoff window in the DAQ settings can be chosen, resulting in a higher dead-time, or the cut based on the pulse shape can be applied again. When applying the same pulse shape cut as for the raw data the remaining unusual pulses are removed as can be seen in Figure 5.8 (b). For the energy spectrum in red in Figure 5.9 some events are rejected but it has almost no impact on the threshold. From the processed spectra an unprecedented low energy threshold around 150 eV can be expected. From the threshold in Run-5 of 210 eV this is an major improvement of $\sim 30\%$.

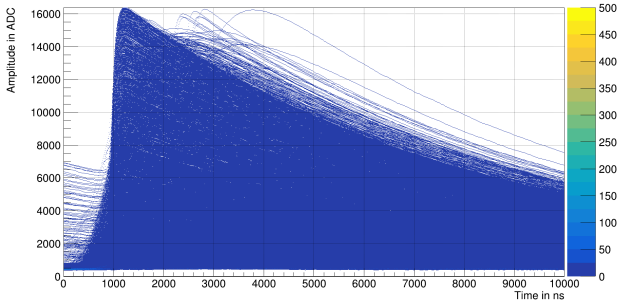

(a)

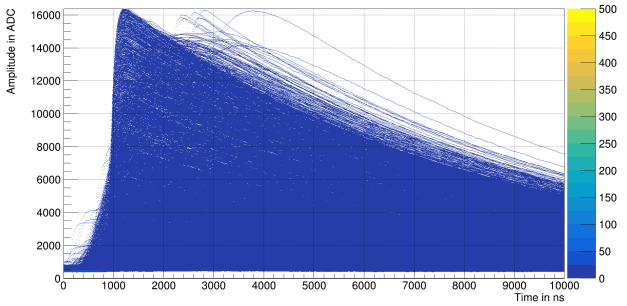

(b)

Figure 5.8.: Detector Pulses before (a) and after (b) the additional noise cut for the CONUS-2 detector after TRP and muon-veto cut. The measured signal amplitude is plotted over the duration time of the event. For the noise cut an upper limit of $P_0 = 1200\,\mathrm{ADC}$ and $t_0 = 200\,\mathrm{ns}$ is used.

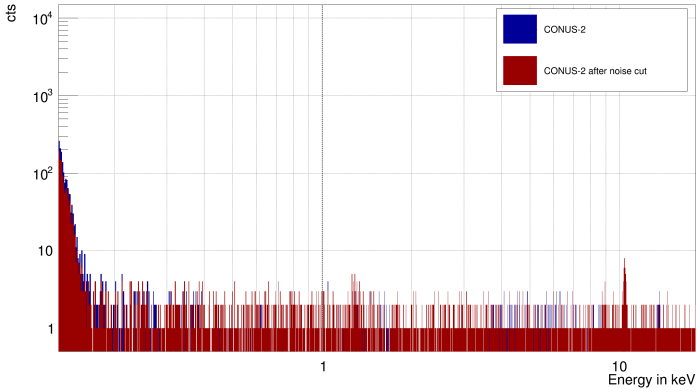

Figure 5.9.: Energy spectrum before (blue) and after (red) additional noise cut for CONUS-2 after TRP and muon-veto cut. The number of events is plotted over the energy in keV. For the noise cut an upper limit of $P_0 = 1200\,\mathrm{ADC}$ and $t_0 = 200\,\mathrm{ns}$ is used.

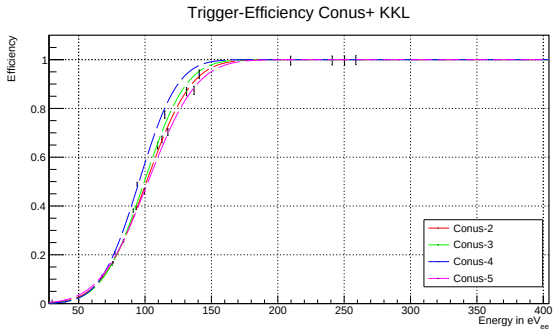

(a)

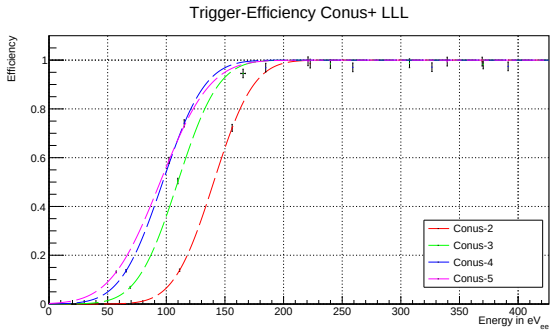

(b)

Figure 5.10.: Trigger-efficiency for the CONUS+ detectors at (a) KKL and (b) LLL. The energy-dependent trigger-efficiencies for CONUS-5 (magenta), CONUS-2 (red), CONUS-3 (green), and CONUS-4 (blue) are fitted with an error function (dashed).

5.3.3. Trigger-Efficiency

The detection efficiency, hereinafter referred to as the trigger-efficiency, plays an important role for the signal search near the detector threshold. When the energy of the signals gets smaller, also the amplitude of the detector pulse decreases. If the pulse amplitude is near or at the same level than the amplitude of the noise on the baseline the DAQ algorithm can not distinguish anymore. Therefore noise can be triggered randomly or real pulses can be lost as the signal is not triggered. For a rare event search as CEνNS a high trigger-efficiency even at low energies is essential. To improve the trigger-efficiency lowering the noise is of benefit as low energy pulses can be distinguished better from noise on the baseline. Furthermore a steeper rise-time will also lead to a better trigger-efficiency. As discussed in Section 5.2, improvements on the detector were conducted to address these points.
The trigger-efficiency can be determined by injecting a pulser signal of different energies. The efficiency can be estimated by coincidence between the time of the injected pulser event and the triggered event in the germanium. The trigger-efficiency as a function of the energy measured at MPIK during the characterization and measured at KKL during commissioning is shown in Figure 5.10. The efficiency curves are

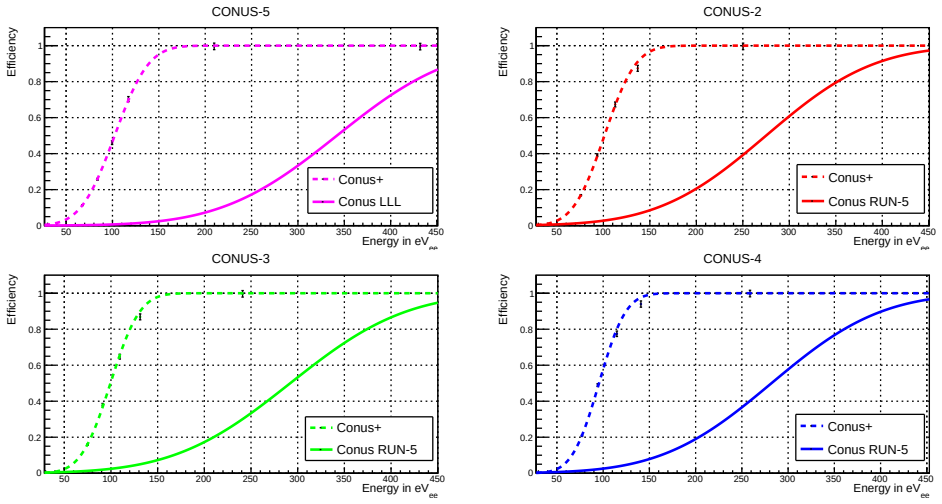

Figure 5.11.: Trigger-efficiency comparison between KKL commissioning (dashed) and KBR Run-5 (solid) for the CONUS+ detectors. As CONUS-5 was not part of the KBR detectors the values were obtained in LLL.

fitted by the function [64]

$$\epsilon_{\text{trig}} = 0.5 \left(1 + \text{erf}\left(\frac{E_{\text{ee}} - t_1}{t_2}\right)\right) \tag{5.8}$$

with erf the error function, t_1 in $(96 - 102)$ eV and t_2 in $(35 - 40)$ eV depending on the detector for the KKL measurement. Comparing the measurement at KKL and in LLL it becomes obvious that the efficiencies for all detectors in the KKL setup are closer together than in LLL. A reason for the change is the slightly adapted settings and also the reduced noise in the overall setup at KKL. Figure 5.11 shows the trigger-efficiency of the four CONUS+ detectors in comparison to the trigger-efficiencies obtained in Run-5 at KBR before the optimization. As CONUS-5 was not part of the detectors in the CONUS setup at the reactor, the trigger-efficiency was measured in LLL, but the CAEN settings were not optimum. Compared to Run-5, the efficiencies after the upgrade of the detectors extremely improved. The decrease starts at much lower energies and also the slope of the efficiency curve is much steeper. That means that pulses with lower amplitude are triggered with a higher probability than before. The efficiency is still 100% for the upgraded detectors whereas the efficiency was below 20% in Run-5 for energies below 200 keV. For the CONUS+ detectors and DAQ the efficiency starts to degrade only below 180 eV. In contrast to that, the degradation started already at around 500 eV for Run-5. In Table 5.5 the corresponding energy values E_{trig} are given for the characteristic trigger-efficiencies $\epsilon = 50\%$, 90% and 99%. Furthermore, the energy values for Run-5 are given in brackets for comparison. With these results a high trigger-efficiency in the ROI is guaranteed and also, only taking into account the efficiency, the threshold

Table 5.5.: Characteristic trigger-efficiency values ϵ and corresponding energies E_{trig} for the CONUS+ detectors after the upgrade. For comparison, the corresponding values of Run-5 before the upgrade are given in brackets.

Detector	E_{trig} in eV_{ee} for:		
	$\epsilon = 50\%$	$\epsilon = 90\%$	$\epsilon = 99\%$
CONUS-2	101 *(275)*	135 *(391)*	163 *(487)*
CONUS-3	99 *(292)*	131 *(417)*	157 *(519)*
CONUS-4	95 *(282)*	124 *(401)*	148 *(499)*
CONUS-5	102 *(342)*	139 *(467)*	169 *(569)*

could be lowered from 210 eV in Run-5 to at least below 180 eV without any efficiency losses.

5.3.4. Depletion Voltage

During the characterization phase at MPIK, the depletion voltage of the individual crystals was measured. The depletion voltage is the voltage applied to the detector crystal where all free charges inside the diode are collected and the detector is fully operational. To measure the depletion voltage, scans with an ^{241}Am-source were conducted, and the peak rate, resolution, and position were measured for increasing high-voltage following the procedure in [61]. The choice for ^{241}Am instead of ^{57}Co was only due to the tuned energy range up to $\sim$ 60 keV. The depletion voltage measurement was only conducted for CONUS-5 and CONUS-3. Due to the measurement behavior of the CAEN DAQ spectra were only measurable if the bias voltage is equal or higher than the depletion voltage. Below the depletion voltage, no spectra could be obtained, and therefore, the respective values are zero. As it is not expected that the depletion voltage changed during the upgrade of the detectors as the crystals are still the same only a rough scan was conducted. By increasing the bias voltage the peak count rate, resolution and position will change slightly until the depletion voltage is reached. There a steep drop or increase followed by a stable region indicates the depletion of the crystal. In Figure 5.12 the obtained values in peak count rate, peak resolution and peak position for CONUS-5 and CONUS-3 are shown. For comparison, the more detailed depletion voltage scans before the upgrade performed by J. Hakenmüller for all CONUS detectors [61] and by E. van der Meeren for CONUS-5 [84] are shown in Figure 5.13. Here, a ^{133}Ba- and a ^{57}Co-source was used for the scan of CONUS-5 and a ^{57}Co-source for the other detectors. Concluding from Figure 5.12 the depletion voltage of CONUS-5 is $\sim$ 2400 V and of CONUS-3 $\sim$ 2800 V. This is consistent with the measurements conducted before the upgrade where a depletion voltage of $\sim$ 2380 V was measured for CONUS-5 [84] and 2810 ± 25 for CONUS-3 [61]. As mentioned in Section 5.2 the cryostats and crystals of CONUS-2 and CONUS-3 were swapped during the reprocessing. With

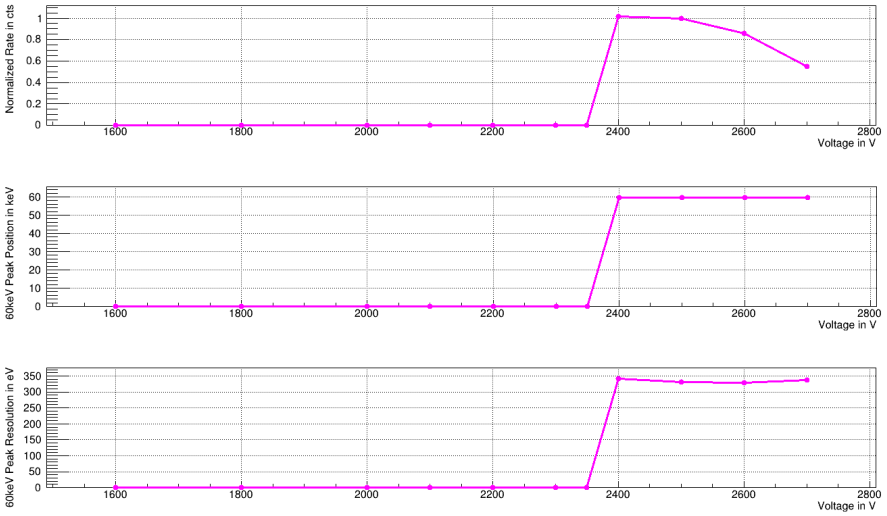

(a)

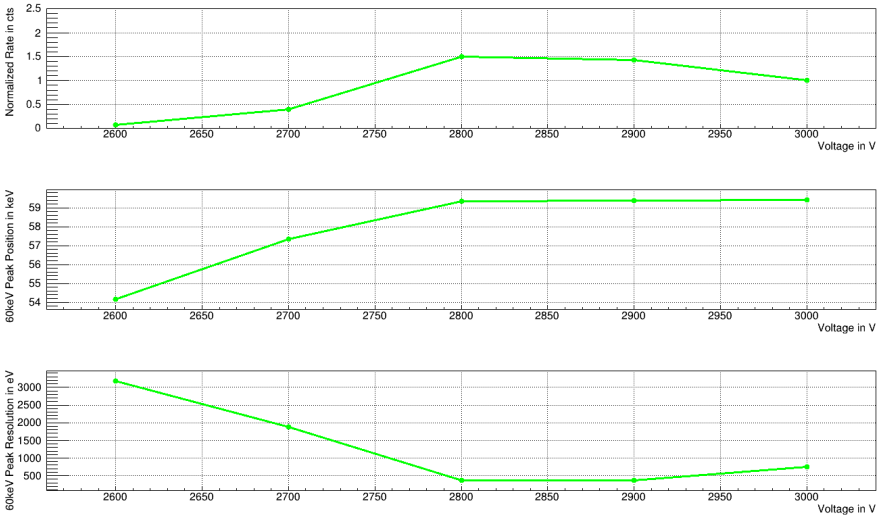

(b)

Figure 5.12.: Depletion voltage scan of CONUS-5 (a) and CONUS-3 (b). In both, the measured 60 keV line resolution, position, and count rate of the detectors after optimization are plotted over the applied bias voltage.

the depletion voltage measurement it was identified that the crystal of the former CONUS-3 was placed inside the cryostat of the former CONUS-2 leading to a mix-up in naming convention. Hence, all CONUS+ detectors are named after the crystal of the former CONUS detectors.

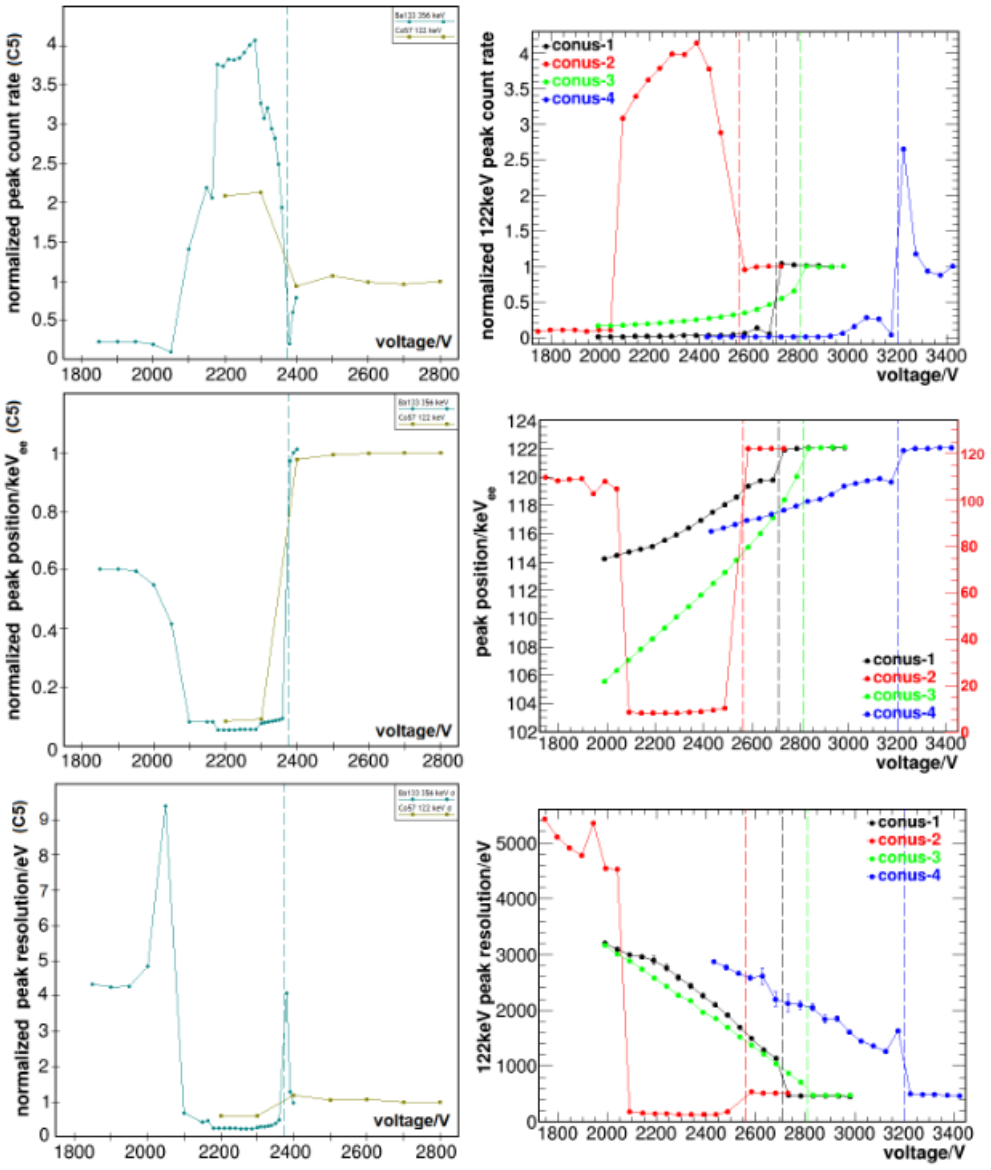

Figure 5.13.: Depletion voltage scan of CONUS-5 (left) and the KBR detectors (right). In both, the measured line resolution, position, and count rate of the detectors before upgrading are plotted over the applied bias voltage. For CONUS-5 a ^{133}Ba- and a ^{57}Co-source was used whereas for the other detectors only a ^{57}Co-source was used. The dashed lines indicate the depletion voltage which is $\sim$ 2380 V for CONUS-5 and 2810 V for CONUS-3. Left figure is taken from [84] and right figure from [61].

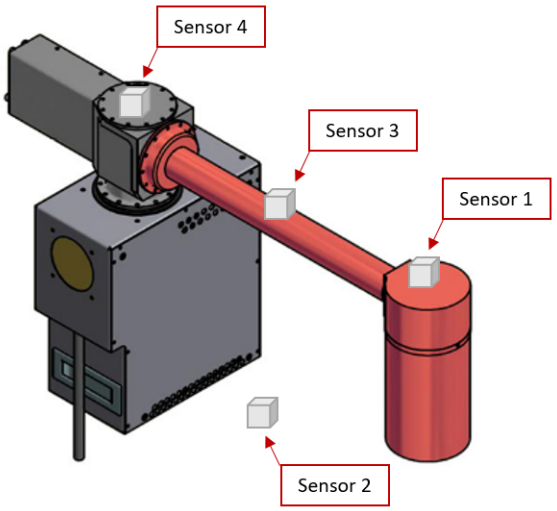

Figure 5.14.: Measurement position of the vibration sensors on CONUS-5. Sensor 1 is placed on the endcap of the detector, whereas sensor 4 sits on the cryocooler. Sensor 3 on the coldfinger and sensor 2 on the floor supplement the measurement. Modified adopted from [25].

5.3.5. Vibrations

With the choice of water cooling instead of air cooling, the vibrations induced by the cryocooler should decrease strongly. For the vibration measurement, four piezoelectric acceleration sensors produced by Kistler were used. The miniature PiezoBeam accelerometer of type 8640A5 [85] was used in combination with the Kistler LabAmp type 5165A amplifier [86]. With a measuring range of $\pm 5\,\mathrm{g}$ and a sensitivity of $\sim 1000\,\mathrm{mV/g}$ the sensors are well suited to measure the small vibrations of the cryocoolers.
The vibration measurements were only performed for CONUS-5. For this detector, initial vibration measurements and studies were performed by J. Hakenmüller and H. Bonet right before it was optimized. For comparison, the vibration measurements after the upgrade were performed similarly, especially with the sensors placed in the same spots on the detector. The measurement positions of the sensors on the detector are shown in Figure 5.14. Sensor 1 was placed on the endcap of the detector, whereas sensor 4 was located on top of the cryocooler. Both sensors provide the best data for the vibration comparison as the position was stable, and moreover, the vibrations on the endcap and cryocooler are the most interesting. For completeness, also sensor 2 was placed on the floor and sensor 3 was placed on the coldfinger. The sensors measure the acceleration of the surface they are placed on, and the frequency range can be obtained by a fast Fourier transform of this data. The comparison of the vibrations before and after the optimization of CONUS-5 are shown in Figure 5.15 for the frequencies and in Figure 5.16 for the acceleration. For the frequency

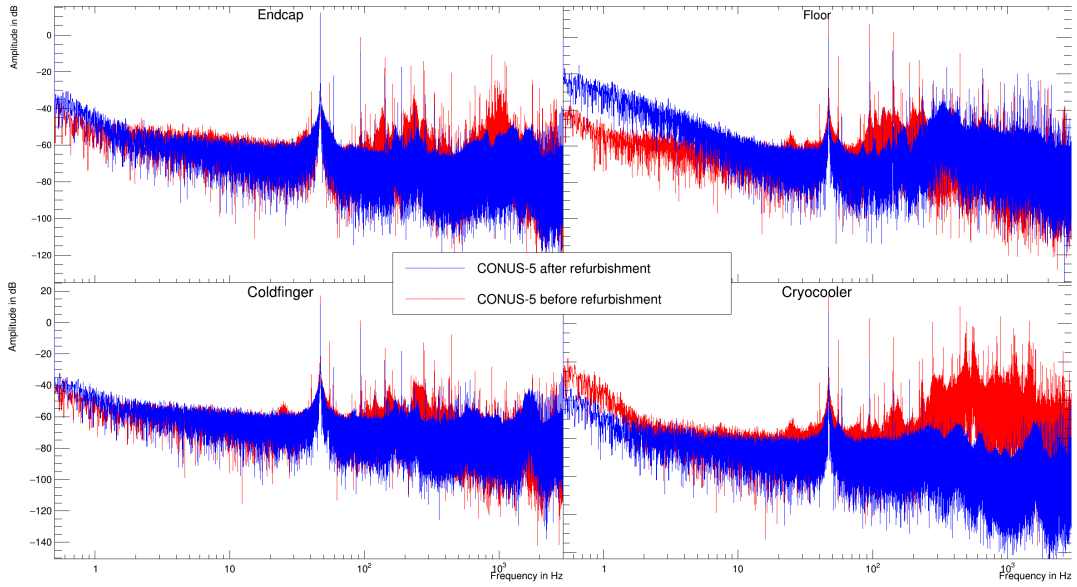

Figure 5.15.: Vibration frequencies before (red) and after (blue) the optimization for CONUS-5. The amplitude is plotted over the respective frequency of the measured vibrations. The difference in low frequencies for the measurement on the floor originates from different vibration levels in the room.

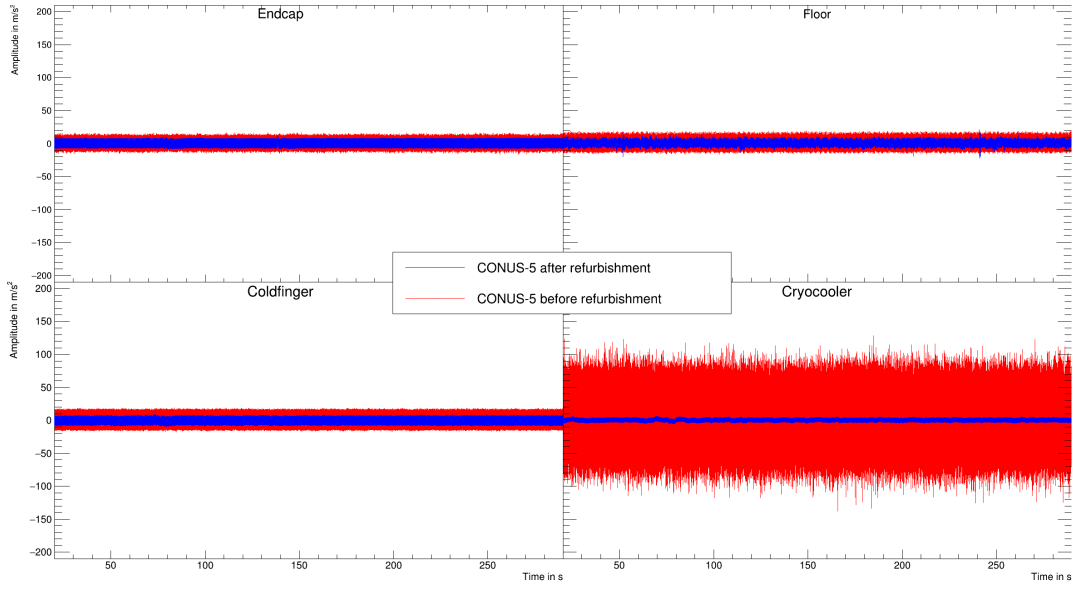

Figure 5.16.: Vibration acceleration before (red) and after (blue) the optimization for CONUS-5. The acceleration amplitude of the vibration is plotted over the measurement time.

range, it is clearly visible for the endcap and the cryocooler that above the 47 Hz peak, the higher frequencies are strongly reduced for the water cooling. The 55 Hz line of the fan obviously vanished as well as all respective resonance frequencies. Also, the width of the compressor line is slightly reduced, but this is mainly related to the ambient temperature and the power consumption of the cryocooler. Besides, a new frequency line at ~ 200 Hz shows up, which is probably related to the water cooling and the chiller. Regarding the measured acceleration, the improvement on the endcap position is about 50%. The impact of the water cooling on the cryocooler is strongest. Here, the acceleration amplitude improved from $\sim 100\,\mathrm{m/s^2}$ to about $5\,\mathrm{m/s^2}$ by 95%. Consequently the switch from air cooling to water cooling of the compressor lead to a substantial improvement regarding the vibrations of the cryocooler.

5.3.6. Ambient Temperature Dependence

During Run-1 and Run-2, a strong positive correlation of the cryocooler power with the room temperature at KBR was observed. As the cryocooler power is correlated with the vibrations induced by the fan and therefore with the noise rate of the detector a strong temperature dependence of the cryocooler power is disadvantageous for a stable measurement. With the modifications of the water-cooling the correlation is expected to decrease strongly. For the temperature correlation of the cryocooler power and, therefore, the noise-temperature correlation, tests were performed with CONUS-5. For this purpose a tent made from plastic foil was built around CONUS-5 and the air volume was heated with a heat-gun or cooled with an AC. The tent setup is shown in Figure 5.17. All parts of the detector as well as the cryocooler controller were placed inside the tent except the chiller. Also, two different temperature settings of the chiller, 18 °C and 10 °C, were tested to get the optimum temperature for the water cooling. During the increase or decrease of the temperature, the cryocooler power, temperature in the tent, and the measured rate in the detectors were monitored. Four sensors were available for the temperature. Hence, the sensors were distributed over the volume of the tent and also outside. The two sensors outside monitored the ambient room temperature and the temperature of the DAQ crate while the two sensors inside the tent monitored the temperature at the endcap of the detector and the cryocooler controller.
At the beginning, three tests with the heated tent were conducted. In test 1, the chiller temperature was set to 18 °C, and the tent air was heated up to 40 °C. The test was running for ~ 2.5 h to see the increase in rate and the decrease later. The event rate in the detectors, the temperature in the tent, and the cryocooler power over time are shown in Figure 5.18 (a) as well as the status of the single cryocooler parts namely the coldtip temperature, the coldhead temperature, the compressor temperature, and the controller temperature in Figure 5.18 (b). In both, the time of closing the tent (pink), start heating (green), stop heating (red), and reopening the tent (blue) is indicated. In (a), the direct correlation of the rate with the cryocooler

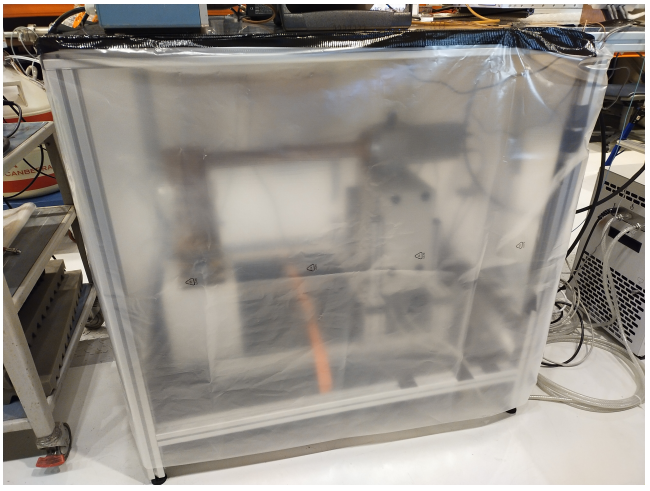

Figure 5.17.: Tent around CONUS-5 detector for ambient temperature dependence tests. The tent is made from plastic foil, and the air volume inside can be heated up with a heat gun or can be cooled with an AC. All parts of the detector, including the cryocooler controller, are enclosed by the tent except the chiller. Photo kindly provided by E. Sanchez.

power and, therefore, the temperature is strongly visible. If the air volume in the tent is heated, the temperature increases, and the cryocooler power also increases with a slight delay. The rate in the detectors directly increases with the cryocooler power. By stopping heating the cryocooler power and rate increase is still ongoing until the decrease also sets in here with a slight delay. It becomes visible that the cryocooler power and, thus, the rate takes more time to stabilize even if the room temperature is already back at its starting point. In Figure 5.18 (b), it becomes obvious that not only the power consumption is increasing at heating but also the working temperatures of the single cryocooler parts. They are all directly correlated to each other and to the room temperature, except the coldtip temperature, as it is the temperature the crystal is kept on and has to be stable at the respective set value. In Figure 5.19, the normalized rate is plotted with the cryocooler power to emphasize the direct correlation again. The rate is normalized to the highest value and the cryocooler power is scaled respectively. Here, the rate follows the cryocooler increase and decrease immediately. The correlation coefficients are calculated to quantify the relation between the individual parameters. The correlation between parameters X and Y is given by the Pearson correlation coefficient [87]

$$\mathrm{cor}(X,Y) = \frac{\mathrm{cov}(X,Y)}{\sigma_X \sigma_Y} \tag{5.9}$$

with $\mathrm{cov}(X,Y)$ the covariance of X and Y and σ_i the standard deviation of the respective parameter. The coefficient is defined from -1 to 1, indicating a strong negative correlation for -1, no correlation for 0, and a strong positive correlation for 1. For

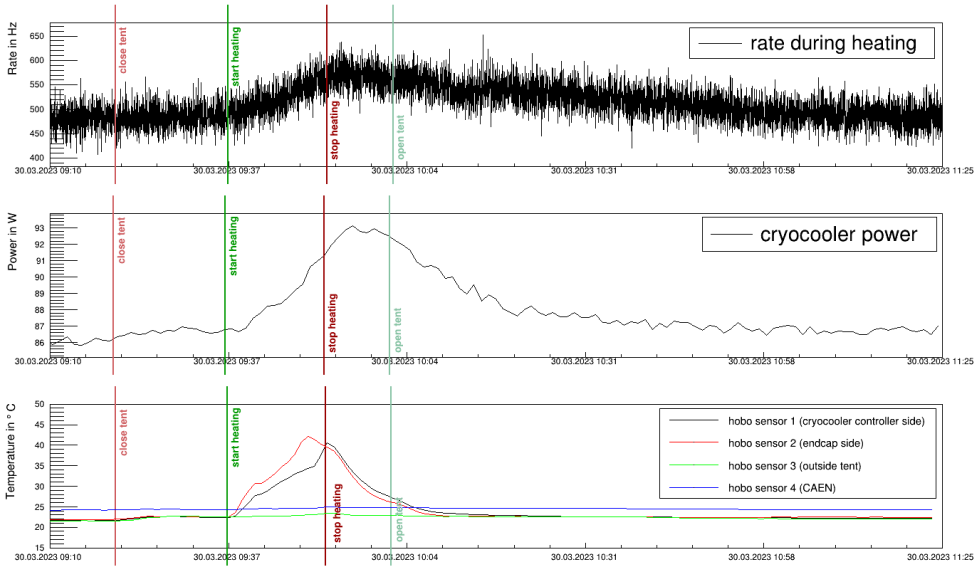

(a)

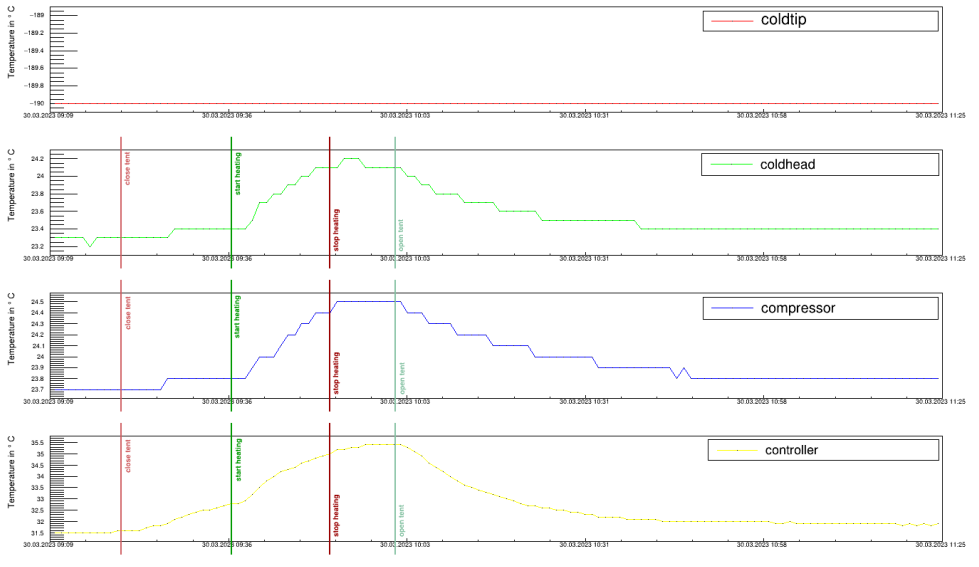

(b)

Figure 5.18.: Rate, cryocooler properties and room temperature for the first test with a chiller temperature of 18 °C. The temperature in the tent was heated up to 40 °C, and the detector rate (top), cryocooler power (middle), and temperature (bottom) were recorded over time (a). Additionally, the cryocooler properties, as the coldtip temperature (red), the coldhead temperature (green), the compressor temperature (blue) and the controller temperature (yellow), are recorded over time (b). The times of closing the tent, starting and stopping heating, and reopening the tent are also marked.

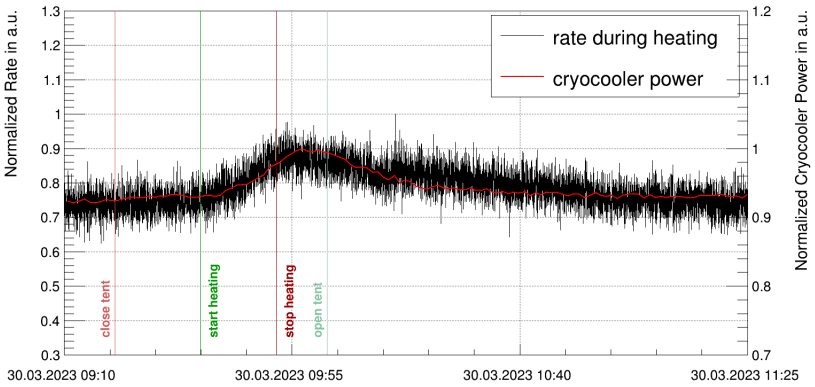

Figure 5.19.: Normalized detector rate (black) and normalized cryocooler power (red) plotted over time for the first test with a chiller temperature of 18 °C. The time of closing the tent, start and stop heating and reopen the tent are marked additionally.

Table 5.6.: Correlation coefficients of rate and cryocooler power or temperature and of cryocooler power and temperature for the first test. The parameters of a linear fit for the correlation of rate, cryocooler power, and temperature are given additionally. The values were fitted by the function $f(x) = m \cdot x + c$.

Parameters	$\mathrm{cor}(X, Y)$	m	c
Rate - Cryocooler power	0.66	$12.30 \pm 1.35\ \frac{\mathrm{Hz}}{\mathrm{W}}$	$-567.96 \pm 118.55\,\mathrm{Hz}$
Rate - Temperature	0.53	$5.03 \pm 0.76\ \frac{\mathrm{Hz}}{^\circ\mathrm{C}}$	$389.68 \pm 18.69\,\mathrm{Hz}$
Cryocooler power - Temperature	0.75	$0.36 \pm 0.04\ \frac{\mathrm{W}}{^\circ\mathrm{C}}$	$79.11 \pm 0.95\,\mathrm{W}$

test 1, the correlation coefficient for rate and cryocooler power is $\mathrm{cor}(R, P) = 0.66$, for rate and temperature $\mathrm{cor}(R, T) = 0.53$ and for cryocooler power and temperature the coefficient is $\mathrm{cor}(P, T) = 0.75$. All three correlation coefficients are close to 1 indicating a positive correlation. The correlation for all three parameters is also shown in Figure 5.20. Here the rate is plotted against the cryocooler power in (a) and the temperature in (b) and additional the cryocooler power is plotted against the temperature in (c). Also, a linear fit is performed for all three correlations. The fit parameters are summarized in Table 5.6. In Figure (b) and (c) the delay of cryocooler power/rate to the temperature is visible by the curved shape. This delay is also the reason for the correlation coefficients not being closer to 1 as expected from Figure 5.18.
After test 1, the chiller temperature was set to 10 °C, and the test was repeated. For the third test, test 1 was repeated with a significantly longer measurement time of $\sim 10\,\mathrm{h}$ to observe the rate decay back to the initial level. The rate, power, and temperature over time, the cryocooler part temperatures, and the rate superimposed with the cryocooler power for both tests are shown in Appendix I as well as the

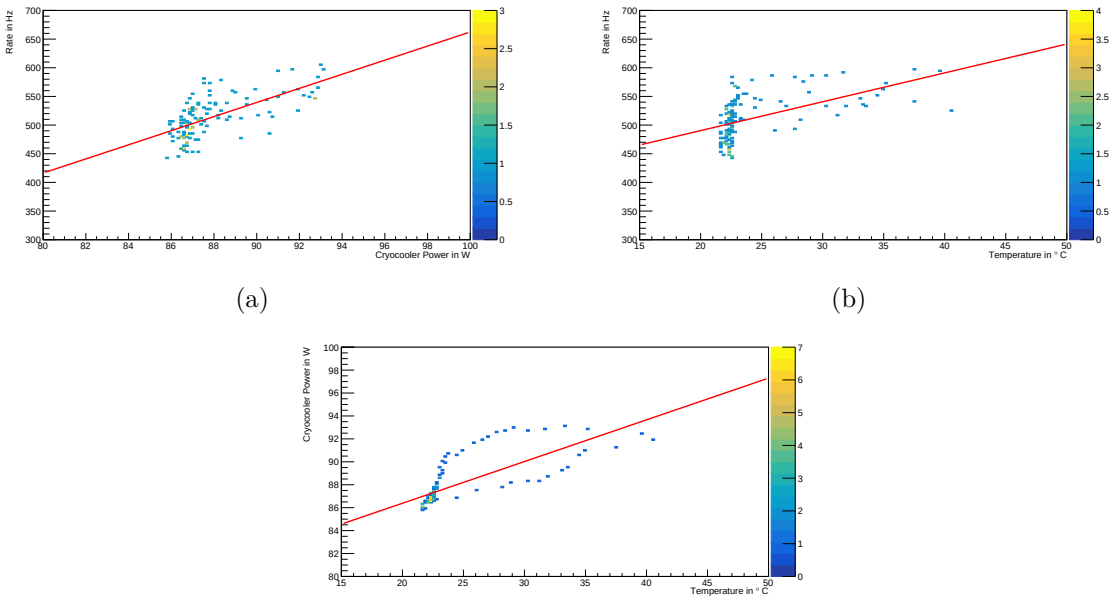

(a) (b)

(c)

Figure 5.20.: Correlation between detector rate and cryocooler power (a), detector rate and temperature (b), and cryocooler power and temperature (c) for the first test. Here, the chiller temperature was set to 18 °C, and the room temperature was heated to 40 °C. The correlation coefficients are $\mathrm{cor}(R, P) = 0.66$, $\mathrm{cor}(R, T) = 0.53$ and $\mathrm{cor}(P, T) = 0.75$. A linear fit is indicated by the red lines.

correlation coefficients. With a lower chiller temperature, the cryocooler power and the rate are still correlated to the room temperature. The initial cryocooler power is lower by about 6 W in the test with the lower chiller temperature and increased by ~ 10 W during the test. Here, the rate increased also by about 200 Hz. By comparing to the tests with higher chiller temperature, where the increase in power and rate is also around 10 W and 200 Hz, it becomes apparent that the increase in rate is only dependent on the relative increase in cryocooler power and is not dependent on the initial value of the power. Therefore the increase in rate with cryocooler power is linear. For the temperatures of the cryocooler parts, the initial values are also at a lower level than in the test with a higher chiller temperature. The temperatures of the coldhead and the compressor are about 6 °C lower in the beginning, and also, when the room temperature reaches the highest value, the temperatures are still lower than in test 1. From test 3, it is clear that the rate and the cryocooler power take about two to three hours after the normalized room temperature to normalize to the initial value.
For all three tests, the increase in temperature ΔT and cryocooler power consumption ΔP for 10% and 5% increase in rate is estimated. The results are shown in Table 5.7. For this purpose, the increase in rate is fitted by an exponential. Com-

Table 5.7.: Temperature and cryocooler power changes for 5% and 10% rate increase for the three tests performed with increasing temperature. Test 1 and test 3 were conducted with a chiller temperature of 18 °C, and test 2 was performed with 10 °C. For all tests, the air temperature in the tent was heated up to 40 °C. The temperature increase ΔT and the cryocooler power increase ΔP are obtained for an increase in detector rate of 5% and 10%.

Rate increase	Test 1		Test 2		Test 3	
	ΔT_1	ΔP_1	ΔT_2	ΔP_2	ΔT_3	ΔP_3
10%	10.83 °C	2.64 W	12.93 °C	2.86 W	14.80 °C	3.68 W
5%	6.31 °C	1.70 W	10.35 °C	0.78 W	12.33 °C	1.66 W

paring the values of the different tests, no conclusive statement can be drawn as the values are diverging, also for tests 1 and 3, which were carried out in the same way. The explanation for this could be the delay between temperature and power/rate and the fact that the rate was not stabilized at one temperature. Despite that, an overall trend can be extracted from the data. For an increase of 10% in rate, the power needs to increase several W as well as the temperature. Small temperature and power changes will not strongly affect the rate.
To confirm this trend, another measurement was performed. Instead of heating the air in the tent, the volume was cooled with an AC. With the AC, the temperature in the tent is much more stable for a long time than with the heat gun. For the cooling test, the chiller temperature was set even lower to 8 °C. In the beginning, the AC was set to the lowest possible temperature (18 °C AC setting), resulting in ~ 8 °C in the tent. When the cryocooler power stabilized over time, the temperature of the AC was increased gradually, each time waiting for stable power consumption. Again, the detector rate, the cryocooler power, and the room temperature were recorded during the time, which is shown in Figure 5.21. Here, each temperature step is indicated by a green line. When the rate was stabilized, a pulser measurement was conducted, indicated by a blue line, to obtain the energy resolution at different room temperatures, which will be discussed later. For each step, it took about three hours to stabilize, and the rate, cryocooler power, and temperature were fitted by a constant in the stable period. The obtained values are summarized in Table 5.8 for the temperature, the rate, and the power increase at each step. In Table 5.9, the total increase in rate, cryocooler power, and temperature compared to the starting values with an AC setting of 18 °C is given. Here, the linear connection between temperature and power gets obvious. Also at higher temperature increases, the rate is positively correlated, but at lower temperature gradients, the rate does not change much and is within the errors comparable to the starting value. This is likely due to the oscillating feature of the AC at low temperatures. For this test, the correlation coefficients can be obtained also and the correlation is shown in Figure 5.22. The coefficient for rate and cryocooler power is $\mathrm{cor}(R, P) = 0.86$, for

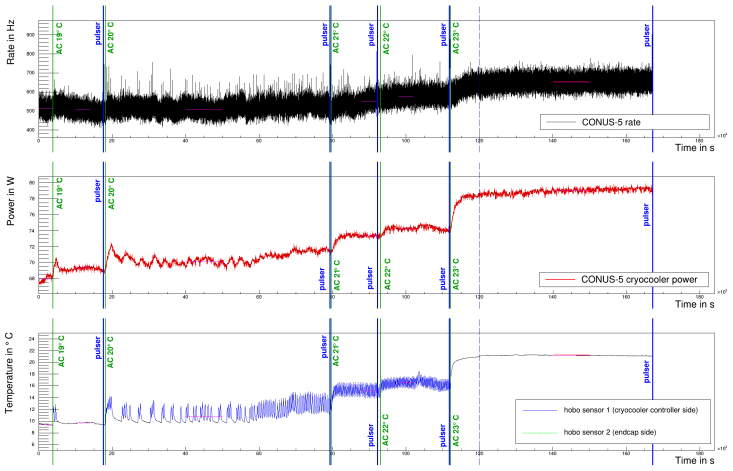

Figure 5.21.: Detector rate (black), cryocooler power (red) and air temperature (blue) during the cooling test with chiller temperature 8 °C. The steps of increasing the AC temperature are marked in green. Pulser measurements conducted at the single temperature stages are marked in blue.

Table 5.8.: Temperature, rate, and cryocooler power during the cooling test. In the beginning, the AC was set to the lowest possible temperature of 18 °C, resulting in an air temperature in the tent of $\sim 9\,^{\circ}$C. Step by step, the temperature of the AC was increased, and at each step, the air temperature T_{step}, the detector rate R_{step} and the cryocooler power P_{step} was obtained by a linear fit in a stable region.

T_{AC} in °C	T_{step} in °C	R_{step} in Hz	P_{step} in W
18	9.41 ± 0.2	512.41 ± 25.30	67.98 ± 0.05
19	9.71 ± 0.2	506.90 ± 24.76	69.35 ± 0.02
20	10.81 ± 0.2	507.27 ± 26.21	70.18 ± 0.03
21	15.18 ± 0.2	552.77 ± 26.54	73.38 ± 0.02
22	16.58 ± 0.2	577.74 ± 26.07	74.23 ± 0.02
23	21.19 ± 0.2	651.74 ± 26.58	79.04 ± 0.01

Table 5.9.: Total temperature ΔT_{total}, rate ΔR_{total} and cryocooler power ΔP_{total} changes during the cooling test for an AC temperature increase T_{AC} from the initial 18 °C. The rate increase in % is given additionally.

T_{AC} in °C	ΔT_{total} in °C	ΔR_{total} in Hz	ΔR_{total} in %	ΔP_{total} in W
$18 \rightarrow 19$	0.30 ± 0.42	-5.52 ± 35.40	-1.1	1.37 ± 0.05
$18 \rightarrow 20$	1.40 ± 0.42	-5.14 ± 36.43	-1.0	2.20 ± 0.04
$18 \rightarrow 21$	5.77 ± 0.42	40.36 ± 36.67	7.88	5.40 ± 0.04
$18 \rightarrow 22$	7.16 ± 0.42	65.33 ± 36.33	12.75	6.25 ± 0.03
$18 \rightarrow 23$	11.77 ± 0.42	139.33 ± 36.70	27.19	11.06 ± 0.02

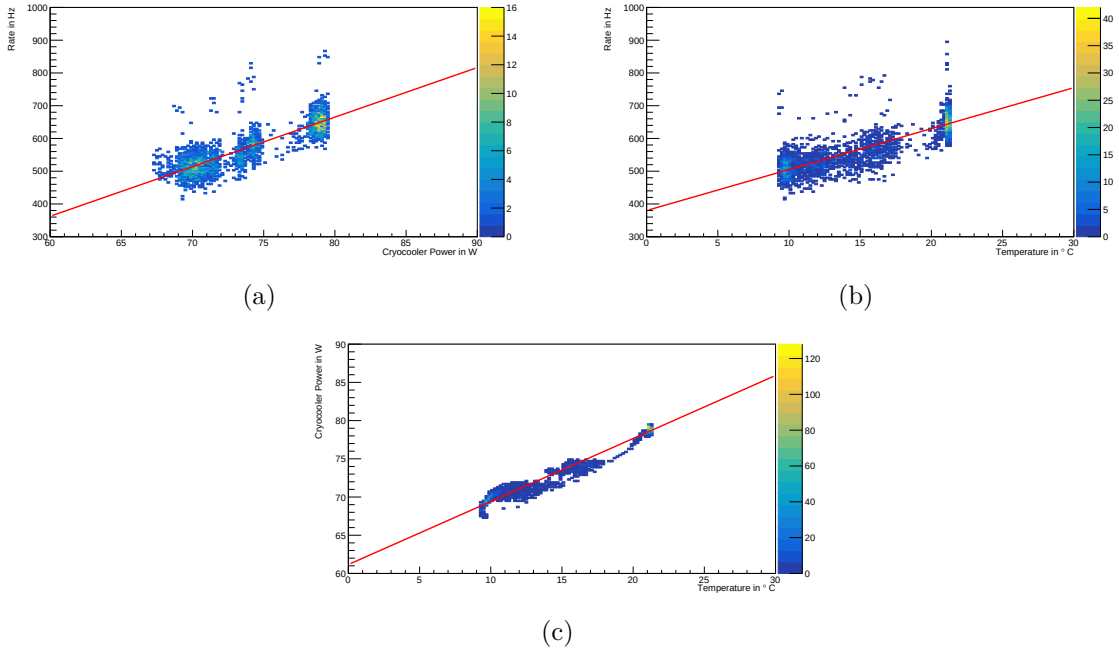

Figure 5.22.: Correlation between detector rate and cryocooler power (a), detector rate and temperature (b) and cryocooler power and temperature (c) for the cooling test. Here, the chiller temperature was set to 18 °C, and the room temperature was cooled with an AC. The temperature was increased only if the cryocooler power stabilized. The correlation coefficients are $\mathrm{cor}(R, P) = 0.86$, $\mathrm{cor}(R, T) = 0.85$ and $\mathrm{cor}(P, T) = 0.98$. A linear fit is indicated by the red lines.

rate and temperature $\mathrm{cor}(R, T) = 0.85$ and for cryocooler power and temperature the coefficient is $\mathrm{cor}(P, T) = 0.98$. Additionally, they are summarized in Table 5.10 with the linear fit parameters. Without the impact of the delayed power/rate, the strong linear correlation is also visible in the coefficients, which are almost 1.
The cooling test was also performed with a higher chiller temperature of 18 °C. It must be taken into account that for the second test with higher chiller temperature only two AC temperature steps were performed, from 18 °C to 20 °C and from 20 °C to AC OFF. The corresponding rate evolution can be found in Appendix I in Figure I.7. In Figure 5.23, the total rate increase in both tests is compared to the total cryocooler power increase and the total temperature increase. Moreover, the total cryocooler power increase is plotted over the total temperature increase. The slope and offset of a linear fit of both measurements are summarized in Table 5.11. The values for the test with higher chiller temperature are given in brackets. For all three comparisons, the linear correlation is visible, whereas the correlation between rate increase and cryocooler power increase/temperature increase is stronger for a higher temperature of the water cooling as the slope of the line is steeper. Here, the increase in room temperature is probably slightly damped by the lower coolant

Table 5.10.: Correlation coefficients of rate and cryocooler power or temperature and of cryocooler power and temperature for the cooling test with a chiller temperature of 18 °C. The linear fit parameters for the correlation of rate, cryocooler power, and temperature are given. The values were fitted by the function $f(x) = m \cdot x + c$.

Parameters	$\mathrm{cor}(X, Y)$	m	c
Rate - Cryocooler power	0.86	$15.13 \pm 0.31 \frac{\mathrm{Hz}}{\mathrm{W}}$	$-545.45 \pm 22.65\,\mathrm{Hz}$
Rate - Temperature	0.85	$12.50 \pm 0.25 \frac{\mathrm{Hz}}{°\mathrm{C}}$	$380.02 \pm 4.01\,\mathrm{Hz}$
Cryocooler power - Temperature	0.98	$0.82 \pm 0.01 \frac{\mathrm{W}}{°\mathrm{C}}$	$61.16 \pm 0.12\,\mathrm{W}$

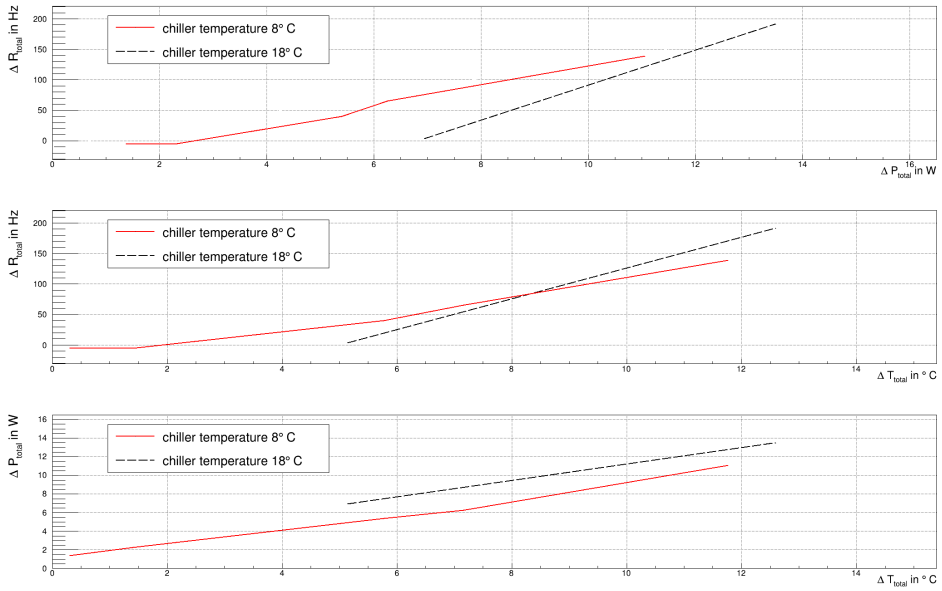

Figure 5.23.: Comparison of total rate, cryocooler power, and temperature during the cooling test for chiller temperatures of 8 °C (solid red) and 18 °C (dashed black). Above the total rate increase $\Delta R_{\mathrm{total}}$ is compared to the total cryocooler power increase $\Delta P_{\mathrm{total}}$, whereas, in the middle, the total rate increase is compared to the total temperature increase $\Delta T_{\mathrm{total}}$. In the bottom figure, the total cryocooler power increase is plotted over the total temperature increase.

Table 5.11.: Parameters of a linear fit for total increase in rate, cryocooler power and temperature for the cooling tests with chiller temperatures of 8 °C (18 °C). The increase in rate, cryocooler power, and temperature was fitted by the function $f(x) = m \cdot x + c$.

Parameters	m	c
Rate - Cryocooler power	$15.50 \pm 0.99\,\frac{\mathrm{Hz}}{\mathrm{W}}$ ($28.75 \pm 0.22\,\frac{\mathrm{Hz}}{\mathrm{W}}$)	$-34.57 \pm 6.24\,\mathrm{Hz}$ ($-195.99 \pm 2.31\,\mathrm{Hz}$)
Rate - Temperature	$12.75 \pm 1.27\,\frac{\mathrm{Hz}}{^\circ\mathrm{C}}$ ($25.28 \pm 0.19\,\frac{\mathrm{Hz}}{^\circ\mathrm{C}}$)	$-20.46 \pm 8.54\,\mathrm{Hz}$ ($-126.41 \pm 1.82\,\mathrm{Hz}$)
Cryocooler power - Temperature	$0.83 \pm 0.05\,\frac{\mathrm{W}}{^\circ\mathrm{C}}$ ($0.89 \pm 0.19\,\frac{\mathrm{W}}{^\circ\mathrm{C}}$)	$0.90 \pm 0.34\,\mathrm{W}$ ($2.42 \pm 1.82\,\mathrm{W}$)

temperature. For both chiller temperatures the increase in power is the same with increasing room temperature. For the test with a higher coolant temperature, the increase in room temperature causes a higher increase in cryocooler power. This is also maybe due to the effect of absorbing the temperature increase for the lower temperature coolant.
As stated above, the pulser resolution was measured during the tests with different room temperatures. The results are summarized in Figure 5.24. Here, the pulser resolution, as well as the pulser peak position, are plotted over the temperature. The red points correspond to tests performed on 17.04.2023 with increasing temperature and a chiller temperature of 18 °C whereas the pink point at 8 °C corresponds to a pulser reference measurement performed after cool down with the AC on the same day. The blue point corresponds to the measurement performed at 18.04.2023 with the AC. Here, the chiller temperature was set to 8 °C, and the pulser reference was done in the same way as the day before. The green points correspond to the cooling test with increasing AC temperature explained above. A clear correlation between the room temperature and the pulser resolution of the detector is visible. The higher the temperature, the larger the value for the resolution, and vice versa. Therefore, a low room temperature should be preferred for the best detector resolution. With the two measurements at 8 °C room temperature also an impact of the chiller temperature is visible. The resolution is lower for lower chiller temperatures. For the peak position, the room temperature has no impact except for the very high temperatures. Here, a shift in peak position is visible.
Concluding six points regarding the correlation between room temperature and detector rate can be gathered from the conducted temperature tests:

1. The detector rate is still heavily correlated to the cryocooler power, which is in turn also still strongly correlated to the ambient temperature
2. The rate increase is linearly dependent on the cryocooler power increase
3. The cryocooler power changes, and therefore the rate changes, are slightly delayed to the temperature change
4. The cryocooler power/rate takes several hours to normalize after the temperature has normalized

5. The chiller temperature affects the strength of the correlation between cryocooler power/rate and temperature. The coupling between temperature and power for lower chiller temperatures is also lower.

6. The pulser resolution is dependent on the room temperature. Better resolution for lower temperatures. This effect is again stronger for lower chiller temperatures.

Thus, the observed noise-temperature correlation for the KBR CONUS detectors is not gone after the upgrade to water-cooling but it is likely that the correlation is damped. Compared to the rate-temperature correlation of almost 1 in Run-1 and Run-2, the correlation of the water-cooled detectors, with around 0.5 for the heating tests and around 0.8 for the cooling test, has halved or at least decreased depending on the test. Also during commissioning and Run-1 at KKL, less impact of temperature fluctuations on the rate evolution of the detectors is observed compared to KBR. Here, a comparable correlation of rate and temperature between 0.3 and 0.8 was observed during a period with a strong temperature increase inside the room and a chiller temperature of 12 °C.

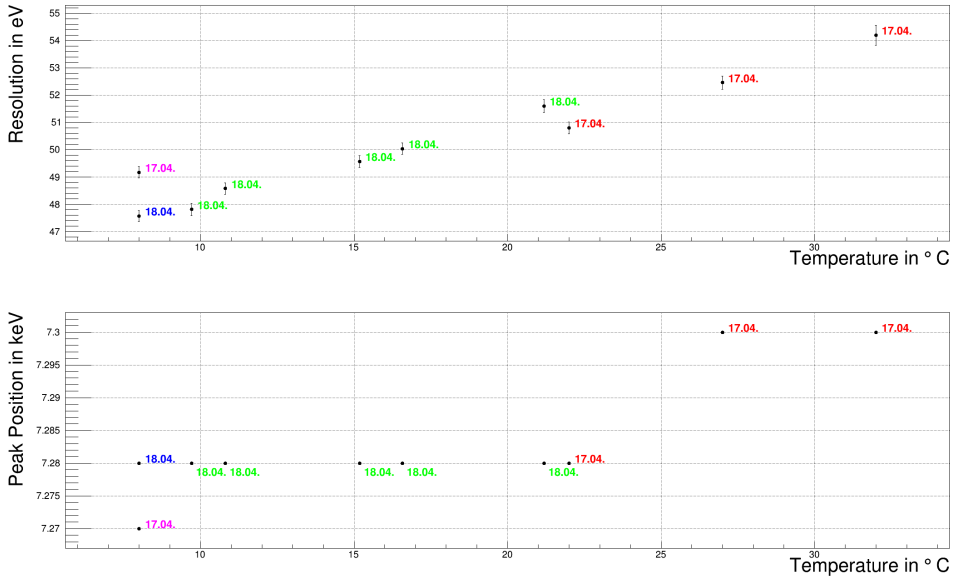

Figure 5.24.: Pulser resolution and pulser peak position for different room temperatures. The red points correspond to tests performed on 17.04.2023 with increasing temperature and a chiller temperature of 18 °C whereas the pink point at 8 °C corresponds to a pulser reference measurement performed after cool down with the AC on the same day. The blue point corresponds to the measurement performed at 18.04.2023 with the AC. Here, the chiller temperature was set to 8 °C, and the pulser reference was done in the same way as the day before. The green points correspond to the cooling test with increasing AC temperature.

6. Conclusion

This work was carried out in the context of the CONUS/CONUS+ experiment, which aim to measure coherent elastic neutrino nucleus scattering at a nuclear reactor. Between Mai 2018 and December 2022, the four high-purity germanium detectors of CONUS collected data in five measurement runs at a distance of 17 m from the Brokdorf nuclear reactor (KBR). Leading results regarding SM and BSM physics were obtained from these measurement campaigns. With the stopped operation of the KBR reactor, the experiment was relocated to the nuclear power plant of Leibstadt in Switzerland (KKL). This thesis deals with the first data analysis of the last two runs at KBR in terms of neutrino electromagnetic properties, as well as with the improvements in detector technology and understanding for CONUS+ at KKL.

In a comprehensive maximum likelihood analysis, the CONUS data of Run-4 and Run-5, measured with the LYNX DAQ system, are analyzed for a possible neutrino magnetic moment and neutrino millicharge. For this purpose, data with a total exposure of 828 kg d of reactor ON and 672 kg d of reactor OFF are selected according to quality and stability in the region of interest of $[2, 20]$ keV. Subsequent to the dataset preparation, an extended binned likelihood fit is performed and a profile likelihood ratio test is conducted to determine upper limits on the magnetic moment and millicharge. Furthermore, a combined analysis with Run-1 and Run-2 is performed. The upper limit at 90% C.L. on the neutrino magnetic moment using the full combined dataset yields $\mu_\nu < 5.18 \cdot 10^{-11} \mu_\mathrm{B}$, while the neutrino millicharge accounts to $|q_\nu| < 1.76 \cdot 10^{-12} e_0$. The results obtained in this work improve the past results on neutrino electromagnetic properties of CONUS ($\mu_\nu < 7.5 \cdot 10^{-11} \mu_\mathrm{B}$ and $|q_\nu| < 3.3 \cdot 10^{-12} e_0$) by a factor of 1.5 for the NMM and by almost a factor of 2 for the NMC. Compared to the currently best upper limits obtained from reactor neutrinos set by the GEMMA experiment ($\mu_\nu < 2.9 \cdot 10^{-11} \mu_\mathrm{B}$ and $|q_\nu| < 1.5 \cdot 10^{-12} e_0$) the limits obtained in this work are less than a factor of 2 for the NMM and only a factor of 1.2 for the NMC away.

To further improve these limits and also to achieve a CEνNS measurement, the knowledge of the different types of detector signals and the background understanding should be improved. For this reason, a pulse-shape simulation is set up to study the detector pulses originating from neutrino signals and background events. With

the study of pulse-shapes, surface events can be distinguished from bulk events. For this reason, the signal-to-background ratio can be increased by rejecting background events by means of the shape. The open-source pulse-shape simulation framework siggen is modified to fit the CONUS detectors and a comparison to actual measured detector pulses is done. A good agreement between simulation and measurement is found, reproducing all important features of the signal pulses. With the validated pulse-shape simulation a powerful tool for signal-like and background event studies is now available for the CONUS experiment.
With the move of the CONUS experiment to the new reactor, a unique possibility of increasing the experimental sensitivity is given. In the course of the experiment transfer from KBR to KKL, the detectors were refurbished and optimized by the manufacturer to improve the detector performance in terms of detection efficiency and energy threshold. Among other things, the internal air cooling of the electrical cryocooling system of the detectors is replaced by a water cooling system, decreasing the noise of the detector. In this thesis, the optimized detectors for CONUS+ are tested and characterized. The new detectors provide excellent performance in trigger-efficiency and energy resolution with a new possible energy threshold of around 150 eV. Compared to the energy threshold before the refurbishment of 300 eV to 210 eV, this yields a major improvement and a huge increase in sensitivity for the experiment. Furthermore, a major reduction in terms of vibrations and therefore in microphonic noise is achieved, as well as the impact of the ambient temperature on the noise rate is decreased with the optimization.
The results obtained in this work have shown that the improvements in data collection stability and all optimization procedures in the CONUS setup contributed intensely to better results. With this refinement, a big step towards the measurement goals of the CONUS experiment was made. With the CONUS+ experiment and the optimized detectors, the sensitivity is increased, and with the first measurement run at KKL, a promising future has started. With these measurement conditions, the first CEνNS signal at a reactor and further best limits regarding BSM physics are within reach in the near future. The results of the CONUS experiment, past and also upcoming, help to nail down the elusive character of the neutrino and offer additionally the possibility to catch a glimpse of what lies beyond the SM.

List of Figures

List of Tables

Appendix

A. Impact of the TDD Cut

In the following the impact of the TDD cut on ON and OFF spectra in the energy range of $2 - 20\,\mathrm{keV}$ for Run-4 and Run-5 is shown.

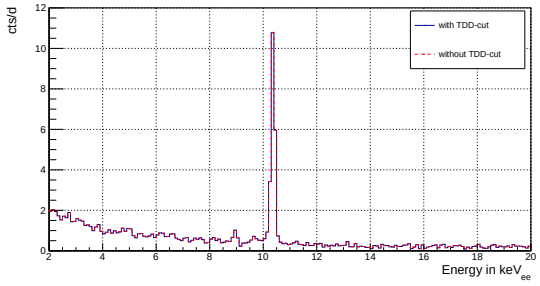

(a)

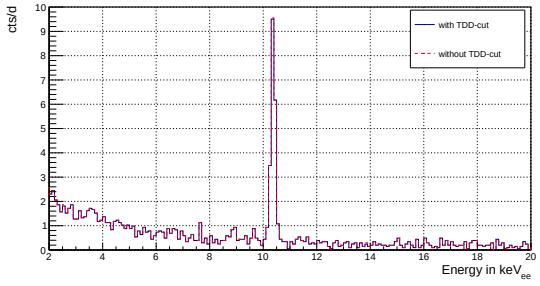

(b)

Figure A.1.: TDD cut impact on ON (a) and OFF (b) spectra for Run-4 for the CONUS-1 detector in the region $[2, 20]\mathrm{keV}_{ee}$.

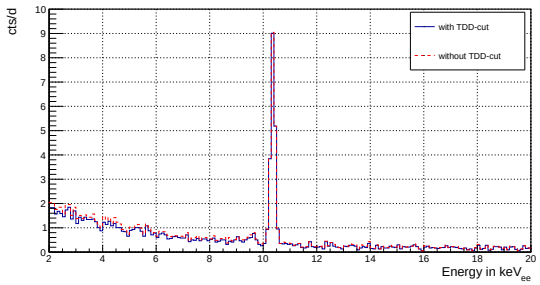

(a)

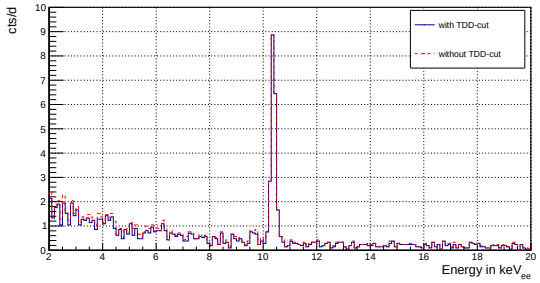

(b)

Figure A.2.: TDD cut impact on ON (a) and OFF (b) spectra for Run-4 for the CONUS-2 detector in the region $[2, 20]\text{keV}_{\text{ee}}$.

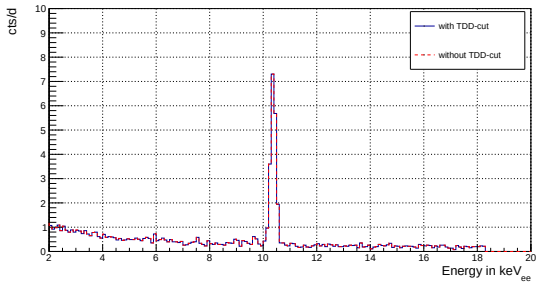

(a)

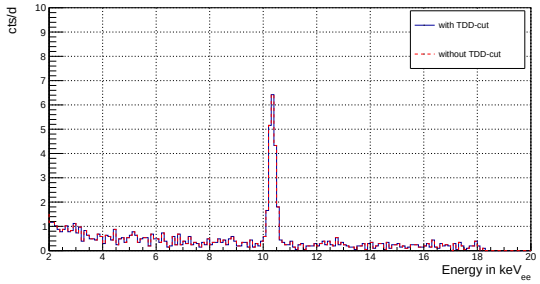

(b)

Figure A.3.: TDD cut impact on ON (a) and OFF (b) spectra for Run-4 for the CONUS-3 detector in the region $[2, 20]\text{keV}_{\text{ee}}$.

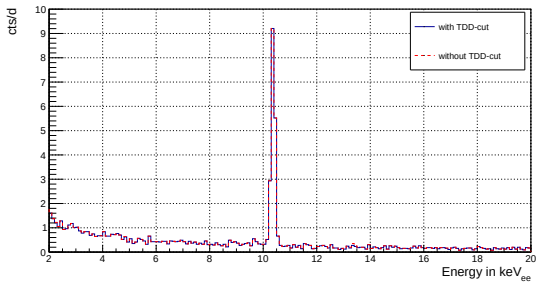

(a)

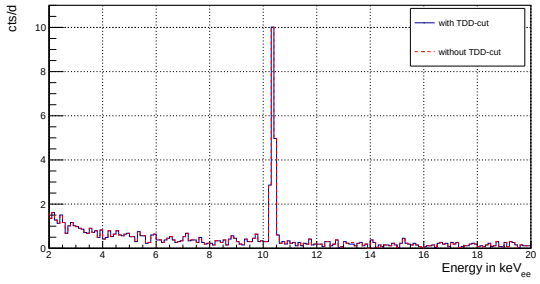

(b)

Figure A.4.: TDD cut impact on ON (a) and OFF (b) spectra for Run-4 for the CONUS-4 detector in the region $[2, 20]\text{keV}_{\text{ee}}$.

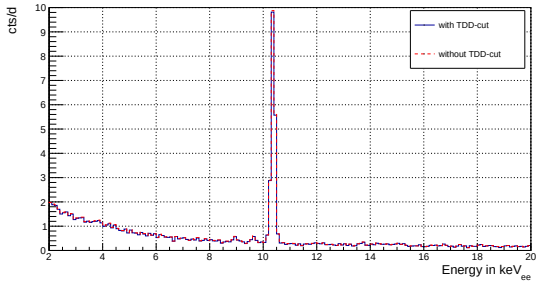

(a)

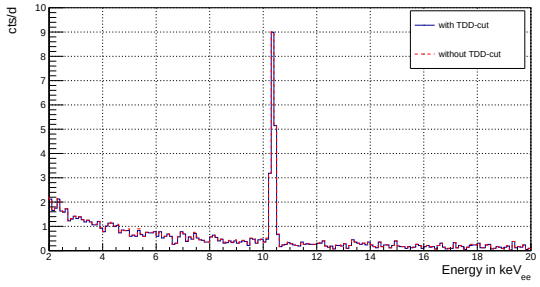

(b)

Figure A.5.: TDD cut impact on ON (a) and OFF (b) spectra for Run-5 for the CONUS-2 detector in the region $[2, 20]\text{keV}_{\text{ee}}$.

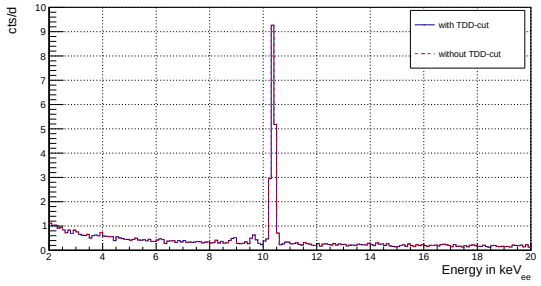

(a)

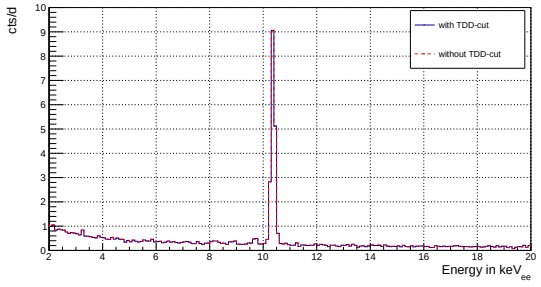

(b)

Figure A.6.: TDD cut impact on ON (a) and OFF (b) spectra for Run-5 for the CONUS-4 detector in the region $[2, 20]\text{keV}_{\text{ee}}$.

B. Stability Plots for Dataset Preparation

Hereinafter, the data stability regarding the detector rate and the stability of the ^{228}Th-calibrations over Run-4 and Run-5 is plotted. For the stability plots, all available data is used, and data cuts are still not applied.

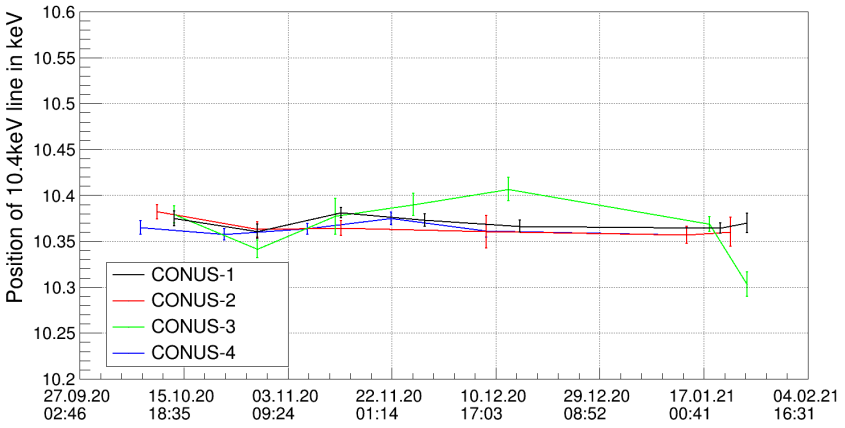

(a)

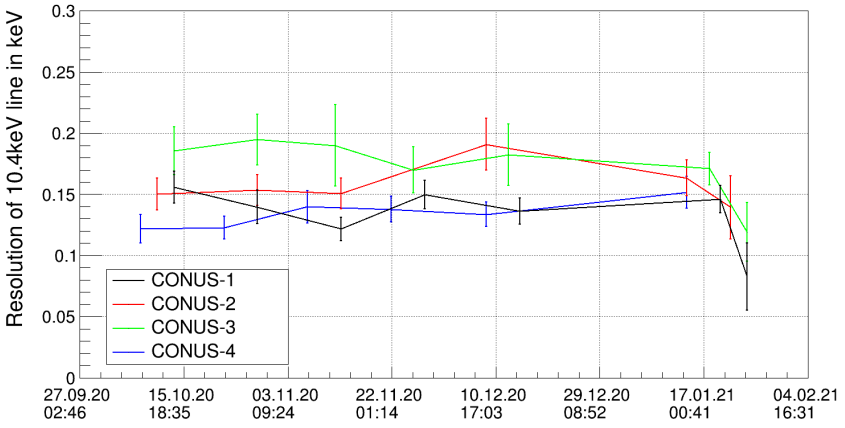

(b)

Figure B.1.: Evolution of the 10.4 keV line during Run-4 for CONUS-1 (black), CONUS-2 (red), CONUS-3 (green), and CONUS-4 (blue). The position (a) and the resolution (b) of the cosmogenic activation line are constant over the whole Run-4.

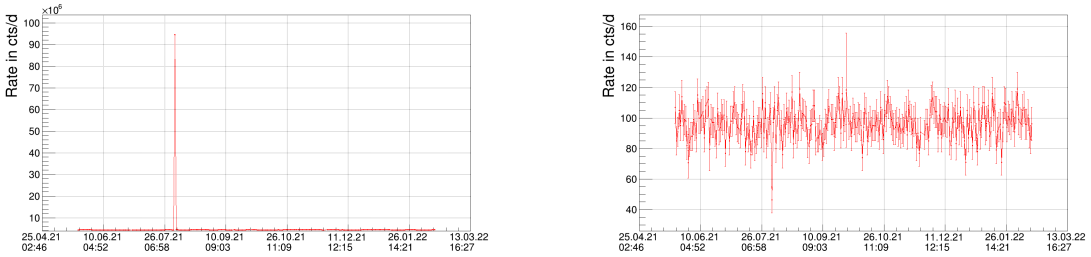

(a) (b)

Figure B.2.: Count rate evolution of CONUS-2 during Run-5. The full low energy range from $[0, 30]$ keV (a) is subject to strong fluctuations due to noise variations, while the region of interest for the electromagnetic properties analysis of $[2, 20]$ keV is much more stable. The rate evolution is plotted before the stability cuts.

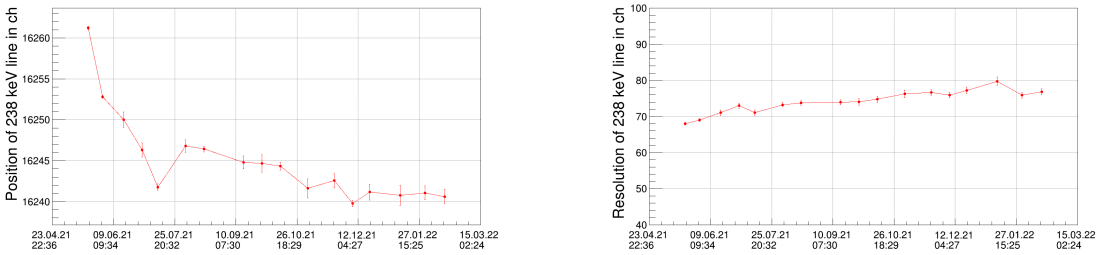

(a) (b)

Figure B.3.: Evolution of the 238 keV line by ^{228}Th-calibrations for CONUS-2 during Run-5. The evolution of the peak position is depicted in (a), while the resolution is shown in (b).

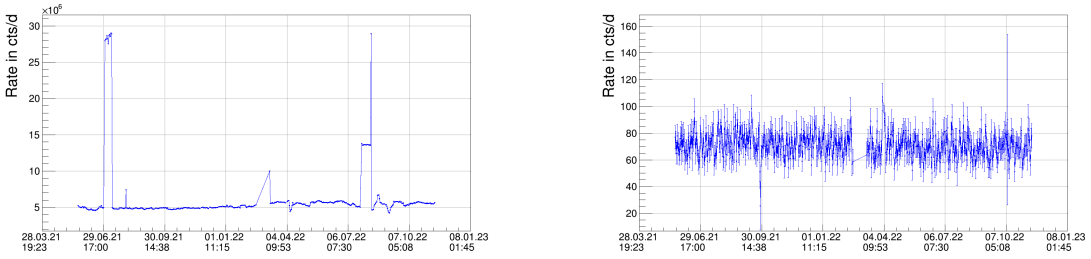

(a) (b)

Figure B.4.: Count rate evolution of CONUS-4 during Run-5. The full low energy range from $[0, 30]$ keV (a) is subject to strong fluctuations due to noise variations, while the region of interest for the electromagnetic properties analysis of $[2, 20]$ keV is much more stable. The rate evolution is plotted before the stability cuts.

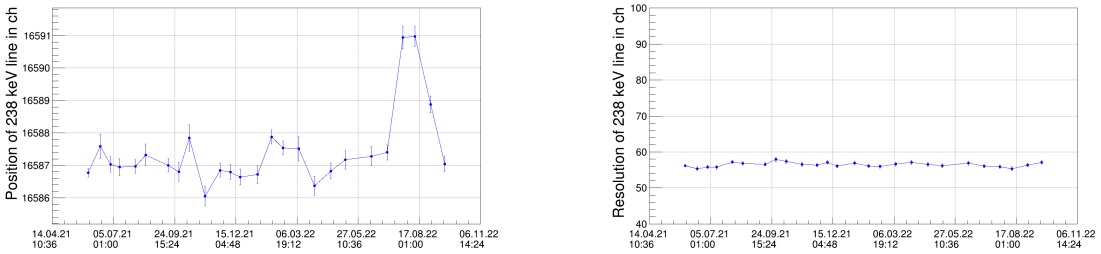

(a) (b)

Figure B.5.: Evolution of the 238 keV line by ^{228}Th-calibrations for CONUS-4 during Run-5. The evolution of the peak position is depicted in (a), while the resolution is shown in (b).

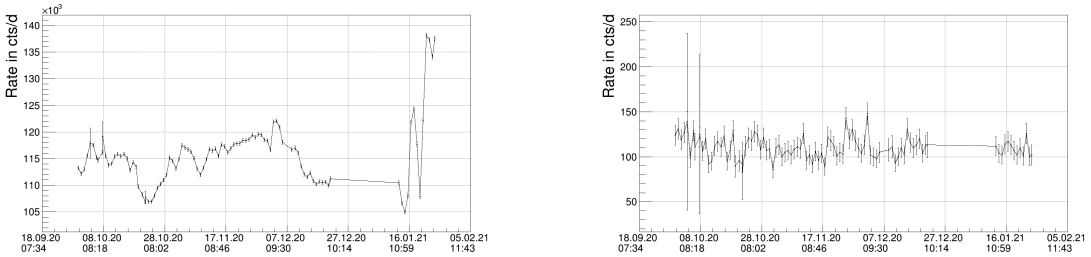

(a) (b)

Figure B.6.: Count rate evolution of CONUS-1 during Run-4. The full low energy range from $[0, 30]$ keV (a) is subject to strong fluctuations due to noise variations, while the region of interest for the electromagnetic properties analysis of $[2, 20]$ keV is much more stable. The rate evolution is plotted before the stability cuts.

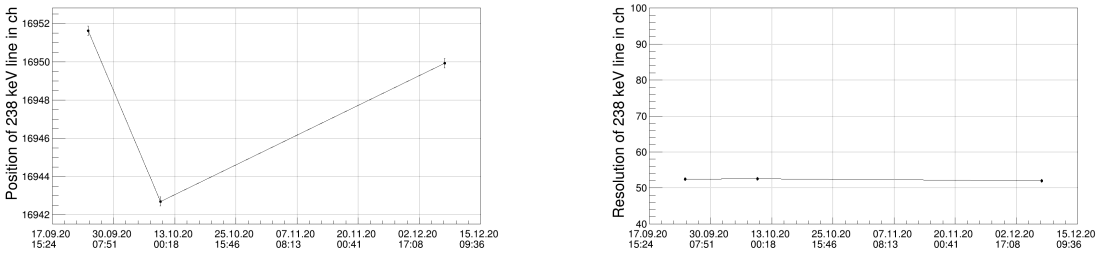

(a) (b)

Figure B.7.: Evolution of the 238 keV line by ^{228}Th-calibrations for CONUS-1 during Run-4. The evolution of the peak position is depicted in (a), while the resolution is shown in (b). For the ^{228}Th-calibrations only a small amount of measurements are given.

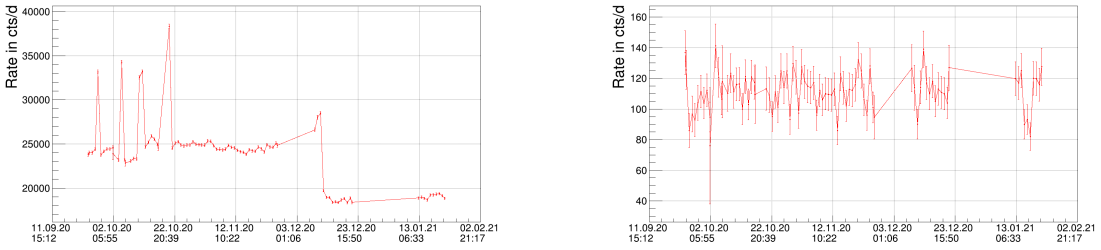

(a) (b)

Figure B.8.: Count rate evolution of CONUS-2 during Run-4. The full low energy range from $[0, 30]$ keV (a) is subject to strong fluctuations due to noise variations, while the region of interest for the electromagnetic properties analysis of $[2, 20]$ keV is much more stable. The rate evolution is plotted before the stability cuts.

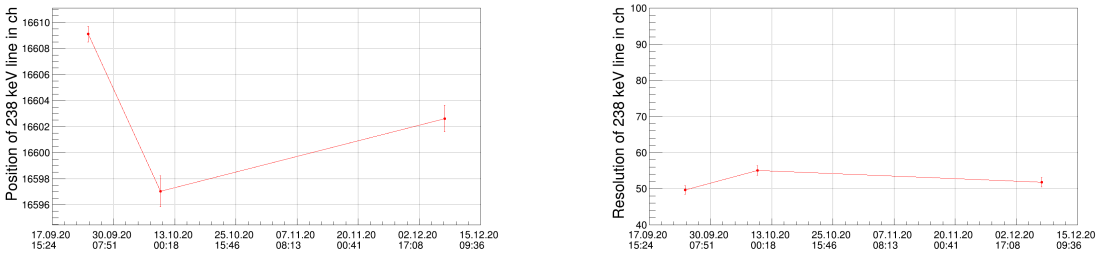

(a) (b)

Figure B.9.: Evolution of the 238 keV line by ^{228}Th-calibrations for CONUS-2 during Run-4. The evolution of the peak position is depicted in (a), while the resolution is shown in (b). For the ^{228}Th-calibrations only a small amount of measurements are given.

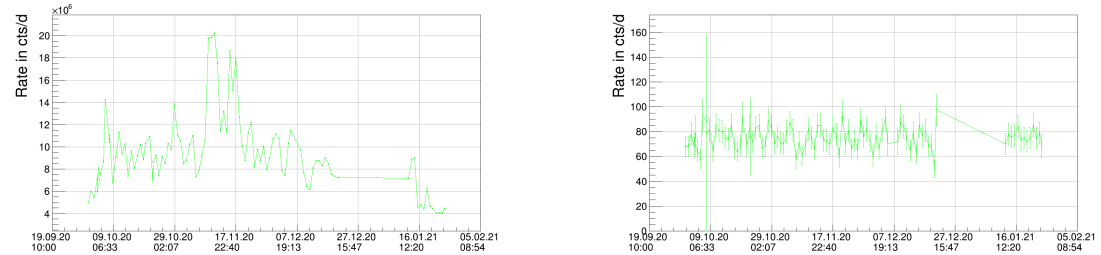

(a) (b)

Figure B.10.: Count rate evolution of CONUS-3 during Run-4. The full low energy range from $[0, 30]$ keV (a) is subject to strong fluctuations due to noise variations, while the region of interest for the electromagnetic properties analysis of $[2, 20]$ keV is much more stable. The rate evolution is plotted before the stability cuts.

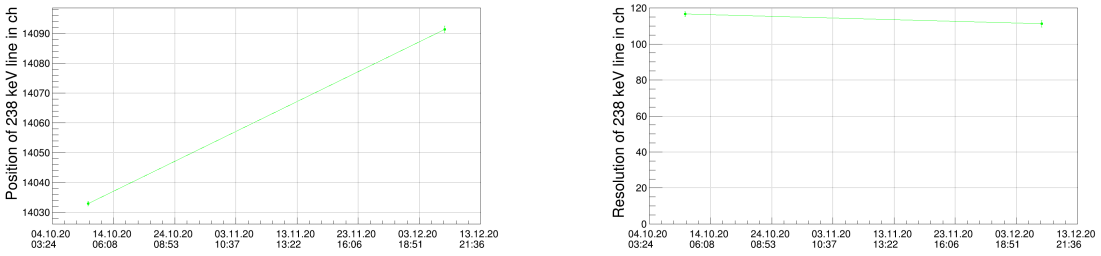

(a) (b)

Figure B.11.: Evolution of the 238 keV line by ^{228}Th-calibrations for CONUS-3 during Run-4. The evolution of the peak position is depicted in (a), while the resolution is shown in (b). For the ^{228}Th-calibrations only a small amount of measurements are given.

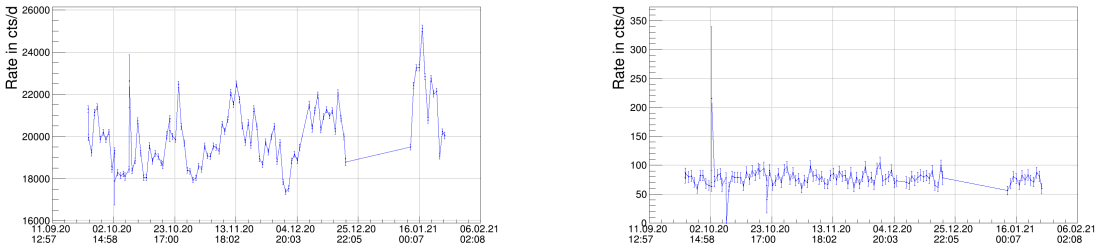

(a) (b)

Figure B.12.: Count rate evolution of CONUS-4 during Run-4. The full low energy range from $[0, 30]$ keV (a) is subject to strong fluctuations due to noise variations, while the region of interest for the electromagnetic properties analysis of $[2, 20]$ keV is much more stable. The rate evolution is plotted before the stability cuts.

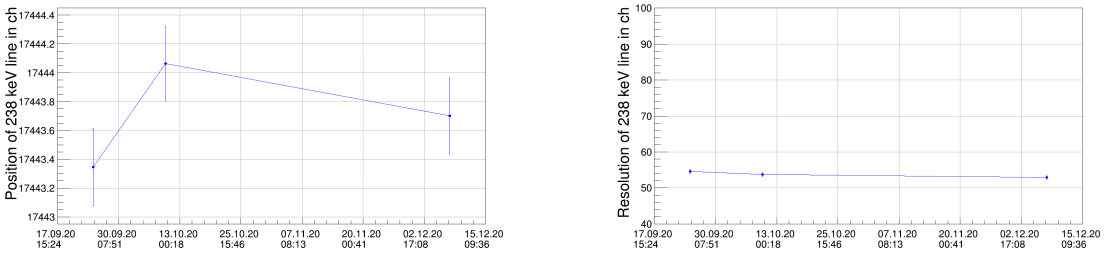

(a) (b)

Figure B.13.: Evolution of the 238 keV line by ^{228}Th-calibrations for CONUS-4 during Run-4. The evolution of the peak position is depicted in (a), while the resolution is shown in (b). For the ^{228}Th-calibrations only a small amount of measurements are given.

C. Best Fitting Results and Correlation Matrices for the Magnetic Moment

In the following, the best-fit values for the likelihood fit assuming the H_0 hypothesis of zero magnetic moment and for the H_1 hypothesis with free magnetic moment parameter are shown for all detectors in Run-4 and Run-5. Furthermore, the correlation matrices and 1D profiles of all parameters are plotted for the case of neutrino magnetic moment.

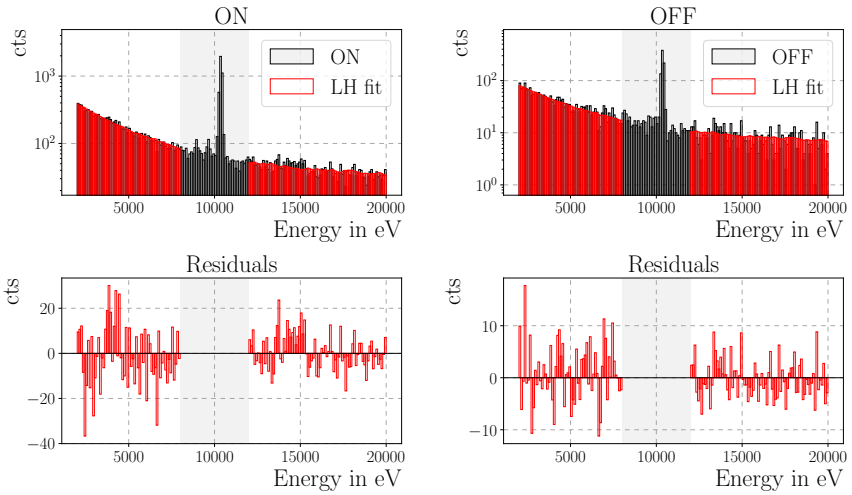

Figure C.1.: Best-fit result of CONUS-2 in Run-5 for the H_0 hypothesis assuming zero magentic moment. On the left side, the reactor ON spectrum (top) is shown with respective residuals of (data - fit) (bottom), whereas the OFF spectrum is shown on the right side. In both cases, the data (black) is shown with the corresponding likelihood fit (red). The grey shaded area is excluded from the fit due to the activation lines of the germanium.

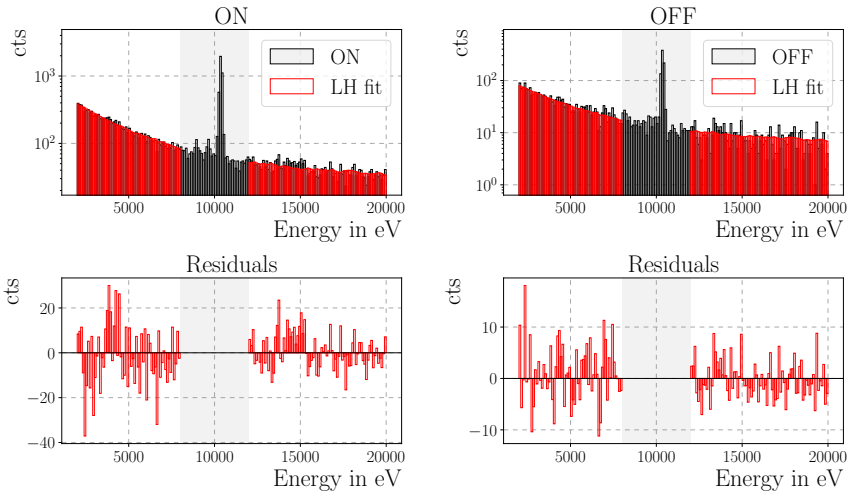

Figure C.2.: Best-fit result of CONUS-2 in Run-5 for the H_1 hypothesis with free magnetic moment parameter. On the left side, the reactor ON spectrum (top) is shown with respective residuals of (data - fit) (bottom), whereas the OFF spectrum is shown on the right side. In both cases, the data (black) is shown with the corresponding likelihood fit (red). The grey shaded area is excluded from the fit due to the activation lines of the germanium. For the best-fit case a small but not significant magnetic moment is found.

Table C.1.: Correlation matrix of the likelihood parameters for CONUS-2 Run-5 for the magnetic moment investigation. The color of the cells indicates the strength of the correlation, where red is positively correlated and blue is negatively correlated.

	μ_ν	ϕ_{reduced}	m	dE	c_{eff}	$b_{\text{add.ON}}$	b_{mc}	p_1	p_2	p_3
μ_ν	1	0	0	0	0	-0.954	0.386	-0.109	0	-0.117
ϕ_{reduced}	0	1	0	0	0	0	0	0	0	0
m	0	0	1	0	0	0	0	0	0	0
dE	0	0	0	1	0	0	0	0	0	0
c_{eff}	0	0	0	0	1	0	-0.244	0	0	0
$b_{\text{add.ON}}$	-0.954	0	0	0	0	1	-0.573	0.104	0	0.112
b_{mc}	0.386	0	0	0	-0.244	-0.573	1	0	0.292	0
p_1	-0.109	0	0	0	0	0.104	0	1	0.124	-0.934
p_2	0	0	0	0	0	0	0.292	0.124	1	0.133
p_3	-0.117	0	0	0	0	0.112	0	-0.934	0.133	1

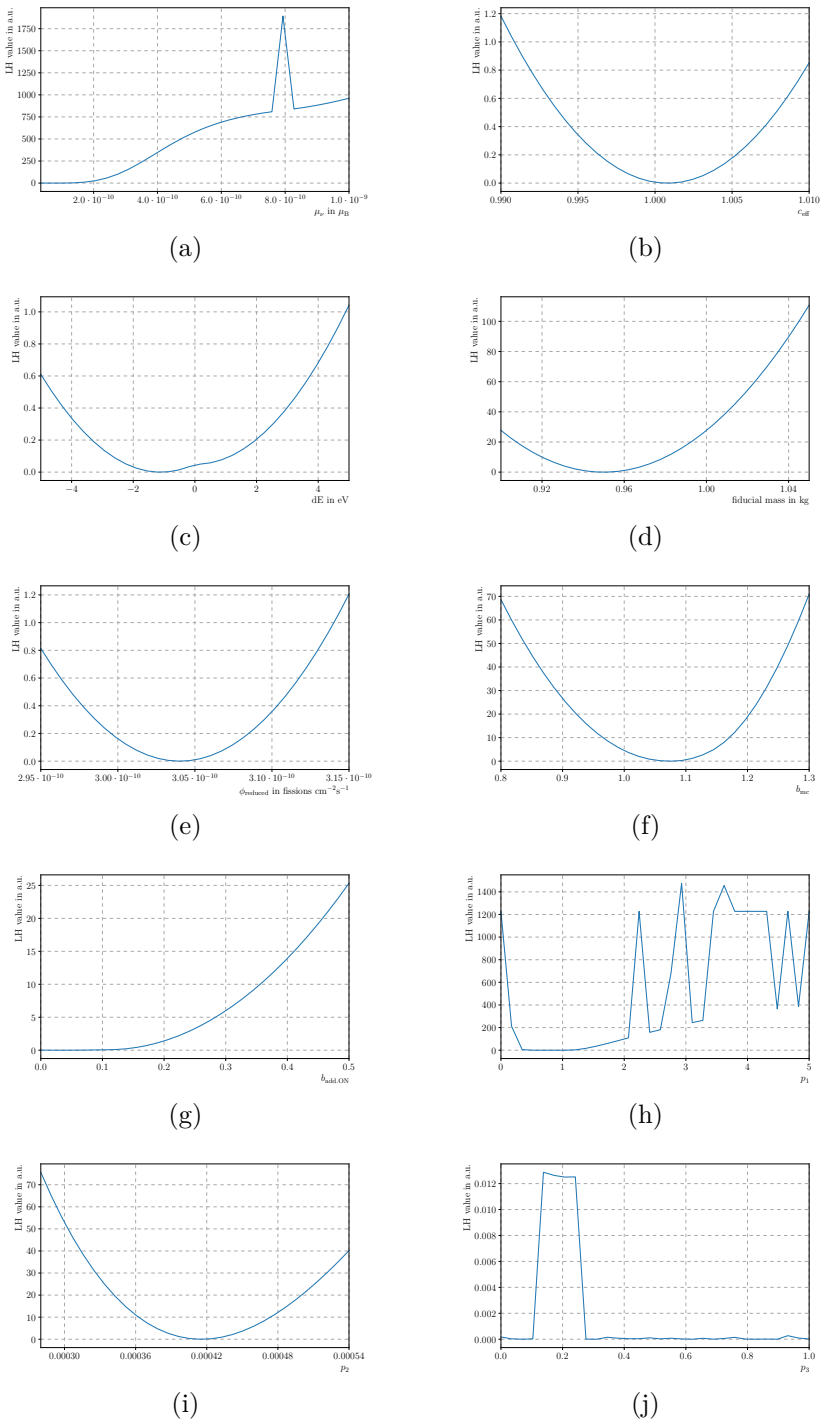

Figure C.3.: 1D profiles of all likelihood fit parameters for CONUS-2 in Run-5 for the magnetic moment investigation. The respective parameter is scanned over its valid parameter range, while all other parameters are minimized. The scanned parameters are the NMM μ_ν (a), the efficiency c_{eff} (b), the energy scale uncertainty dE (c), the fiducial mass m (d), the reduced flux ϕ_{reduced} (e), the background normalization b_{mc} (f), the additional ON component $b_{\text{add.ON}}$ (g) and the three parameters of the leakage test component (h)-(j). On the y-axis, the likelihood value in a.u. is shown.

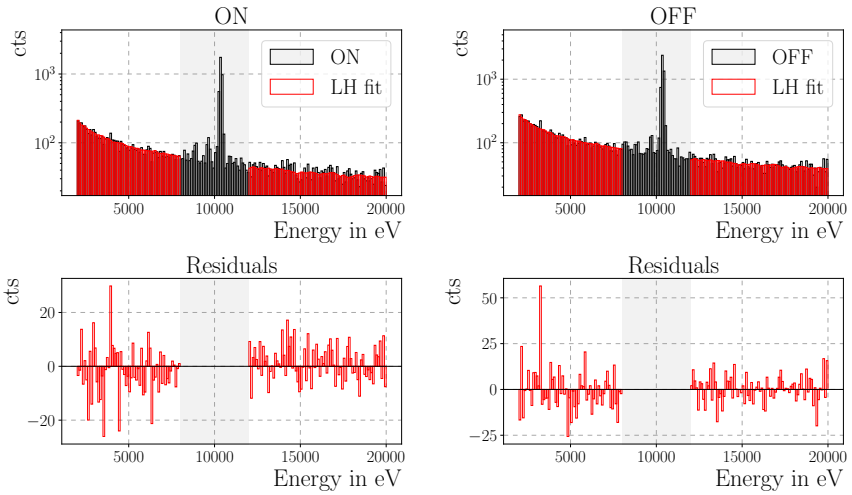

Figure C.4.: Best-fit result of CONUS-4 in Run-5 for the H_0 hypothesis assuming zero magentic moment. On the left side, the reactor ON spectrum (top) is shown with respective residuals of (data - fit) (bottom), whereas the OFF spectrum is shown on the right side. In both cases, the data (black) is shown with the corresponding likelihood fit (red). The grey shaded area is excluded from the fit due to the activation lines of the germanium.

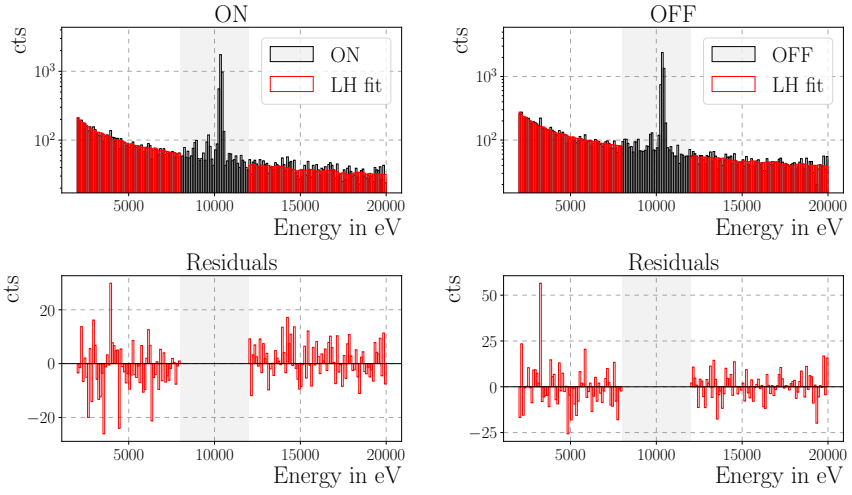

Figure C.5.: Best-fit result of CONUS-4 in Run-5 for the H_1 hypothesis with free magnetic moment parameter. On the left side, the reactor ON spectrum (top) is shown with respective residuals of (data - fit) (bottom), whereas the OFF spectrum is shown on the right side. In both cases, the data (black) is shown with the corresponding likelihood fit (red). The grey shaded area is excluded from the fit due to the activation lines of the germanium. For the best-fit case, no additional events due to a non-zero magnetic moment are found.

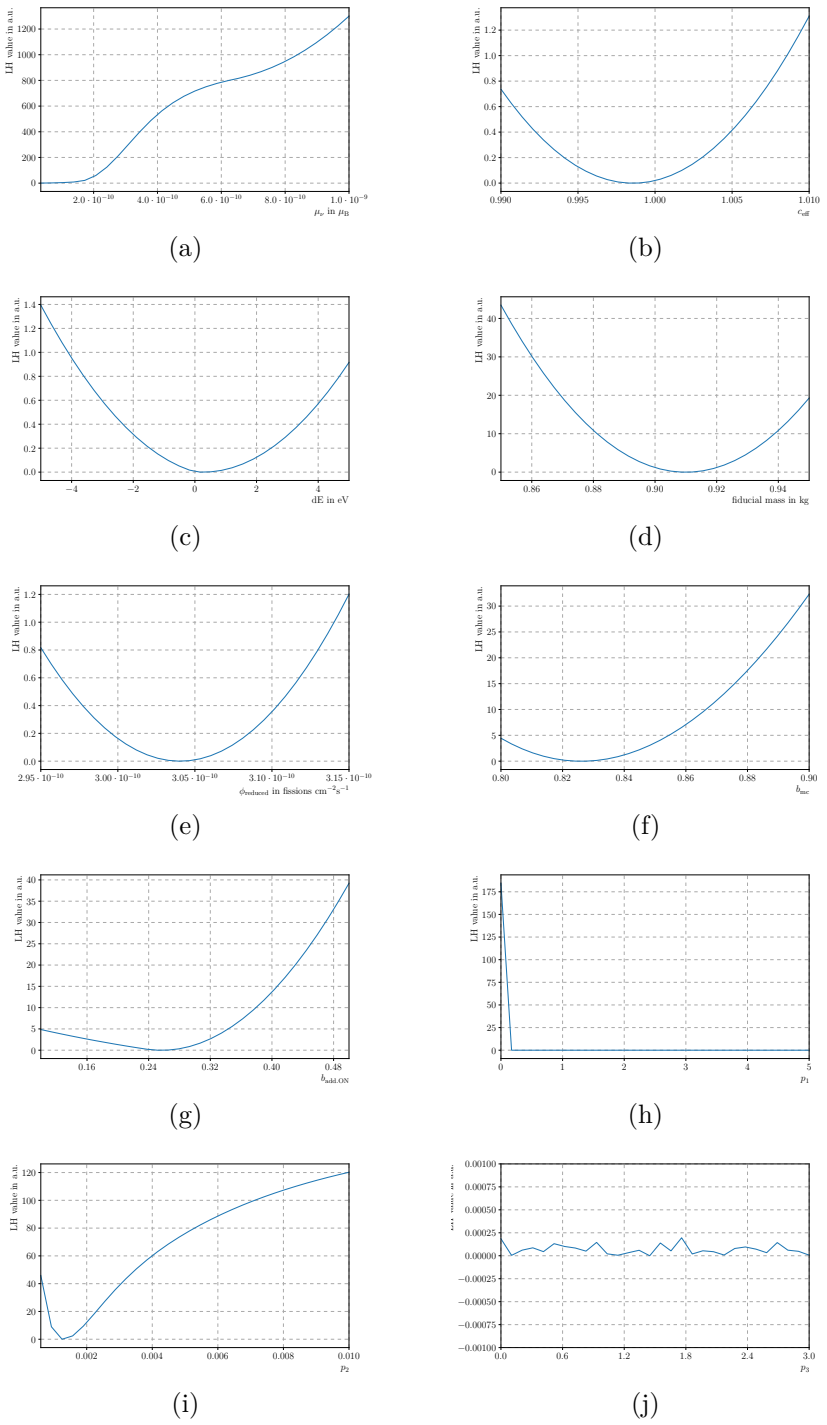

Figure C.6.: 1D profiles of all likelihood fit parameters for CONUS-4 in Run-5 for the magnetic moment investigation. The respective parameter is scanned over the whole parameter range, while all other parameters are minimized. The scanned parameters are the NMM μ_ν (a), the efficiency c_{eff} (b), the energy scale uncertainty dE (c), the fiducial mass m (d), the reduced flux ϕ_{reduced} (e), the background normalization b_{mc} (f), the additional ON component $b_{\text{add.ON}}$ (g) and the three parameters of the leakage test component (h)-(j). On the y-axis, the likelihood value in a.u. is shown.

Table C.2.: Correlation matrix of the likelihood parameters for CONUS-4 Run-5 for the magnetic moment investigation. The color of the cells indicates the strength of the correlation, where red is positively correlated and blue is negatively correlated.

	μ_ν	ϕ_{reduced}	m	dE	c_{eff}	$b_{\text{add.ON}}$	b_{mc}	p_1	p_2	p_3
μ_ν	1	0	0	0	0	-0.237	0	-0.059	-0.067	-0.066
ϕ_{reduced}	0	1	0	0	0	0	0	0	0	0
m	0	0	1	0	0	0	0	0	0	0
dE	0	0	0	1	0	0	0	0	0	0
c_{eff}	0	0	0	0	1	0	-0.661	0	0	0
$b_{\text{add.ON}}$	-0.237	0	0	0	0	1	-0.400	0	0	0
b_{mc}	0	0	0	0	-0.661	-0.400	1	0.185	0.258	0.195
p_1	-0.059	0	0	0	0	0	0.185	1	0.945	0.878
p_2	-0.067	0	0	0	0	0	0.258	0.945	1	0.952
p_3	-0.066	0	0	0	0	0	0.195	0.878	0.952	1

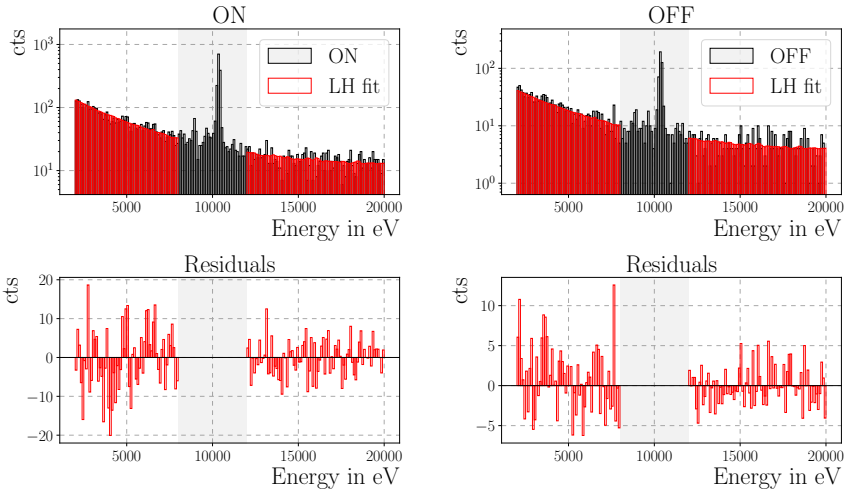

Figure C.7.: Best-fit result of CONUS-1 in Run-4 for the H_0 hypothesis assuming zero magentic moment. On the left side, the reactor ON spectrum (top) is shown with respective residuals of (data - fit) (bottom), whereas the OFF spectrum is shown on the right side. In both cases, the data (black) is shown with the corresponding likelihood fit (red). The grey shaded area is excluded from the fit due to the activation lines of the germanium.

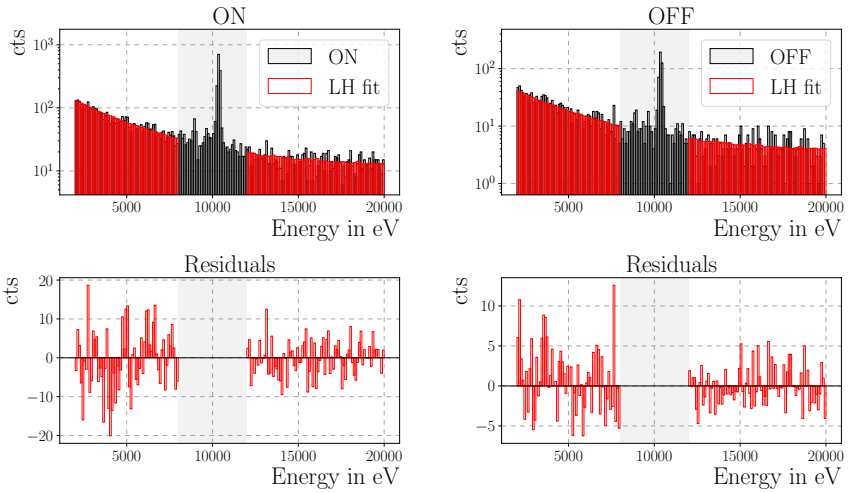

Figure C.8.: Best-fit result of CONUS-1 in Run-4 for the H_1 hypothesis with free magnetic moment parameter. On the left side, the reactor ON spectrum (top) is shown with respective residuals of (data - fit) (bottom), whereas the OFF spectrum is shown on the right side. In both cases, the data (black) is shown with the corresponding likelihood fit (red). The grey shaded area is excluded from the fit due to the activation lines of the germanium. For the best-fit case, no additional events due to a non-zero magnetic moment are found.

Table C.3.: Correlation matrix of the likelihood parameters for CONUS-1 Run-4 for the magnetic moment investigation. The color of the cells indicates the strength of the correlation, where red is positively correlated and blue is negatively correlated.

	μ_ν	ϕ_{reduced}	m	dE	c_{eff}	b_{mc}	p_1	p_2	p_3
μ_ν	1	0	0	0	0	0	0	0	0
ϕ_{reduced}	0	1	0	0	0	0	0	0	0
m	0	0	1	0	0	0	0	0	0
dE	0	0	0	1	0	0	0	0	0
c_{eff}	0	0	0	0	1	-0.274	0	0	0
b_{mc}	0	0	0	0	-0.274	1	0	0.564	0
p_1	0	0	0	0	0	0	1	0.068	-0.975
p_2	0	0	0	0	0	0	0.068	1	0.117
p_3	0	0	0	0	0	0	-0.975	0.117	1

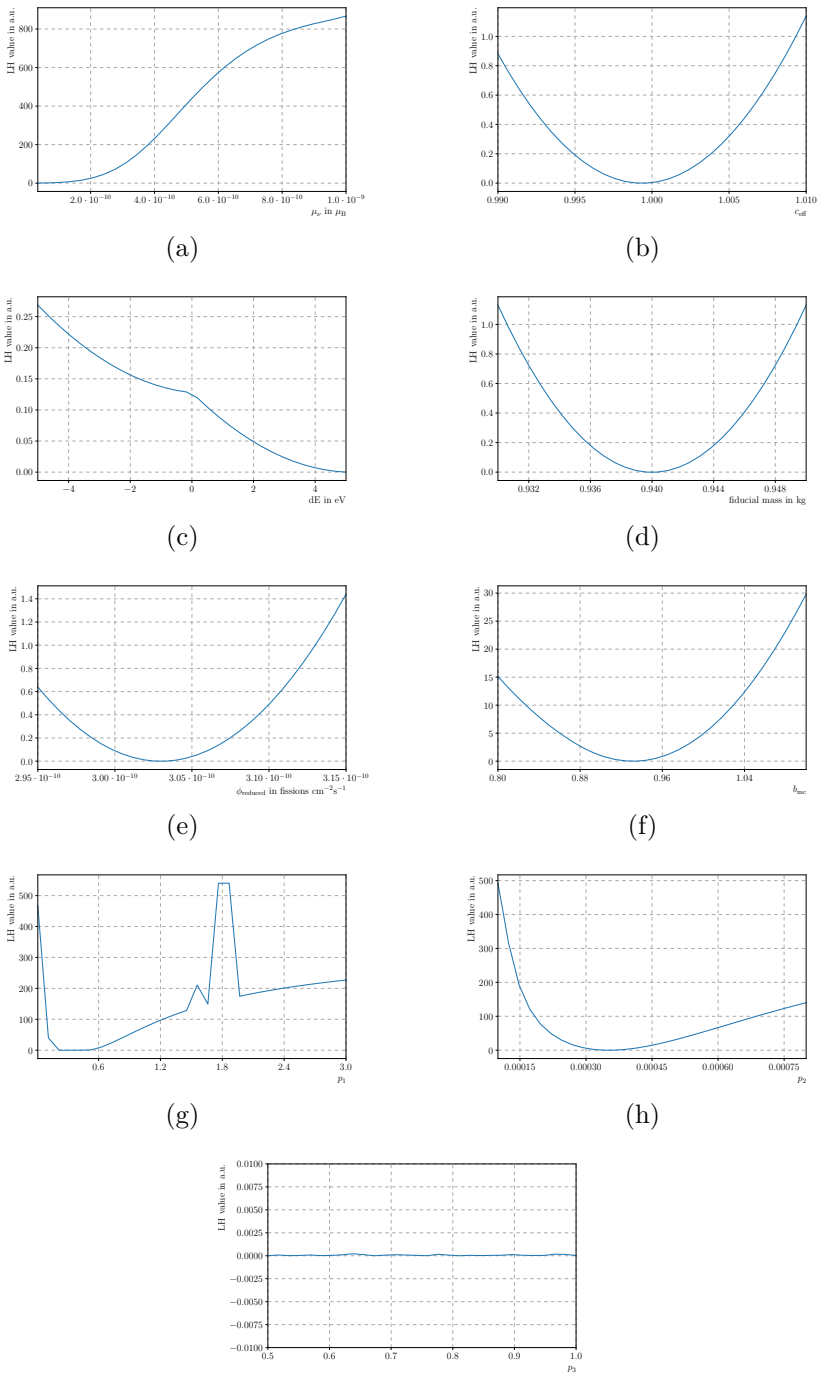

Figure C.9.: 1D profiles of all likelihood fit parameters for CONUS-1 in Run-4 for the magnetic moment investigation. The respective parameter is scanned over the whole parameter range, while all other parameters are minimized. The scanned parameters are the NMM μ_ν (a), the efficiency c_{eff} (b), the energy scale uncertainty dE (c), the fiducial mass m (d), the reduced flux ϕ_{reduced} (e), the background normalization b_{mc} (f) and the three parameters of the leakage test component (g)-(i). On the y-axis, the likelihood value in a.u. is shown.

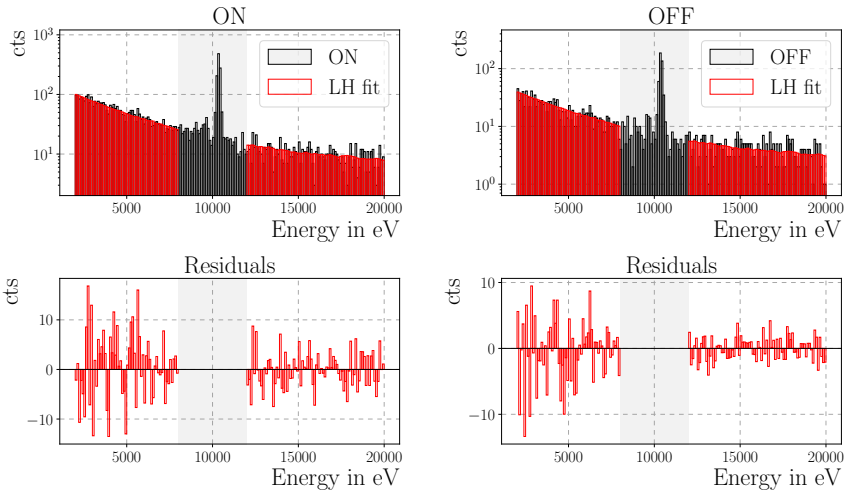

Figure C.10.: Best-fit result of CONUS-2 in Run-4 for the H_0 hypothesis assuming zero magentic moment. On the left side, the reactor ON spectrum (top) is shown with respective residuals of (data - fit) (bottom), whereas the OFF spectrum is shown on the right side. In both cases, the data (black) is shown with the corresponding likelihood fit (red). The grey shaded area is excluded from the fit due to the activation lines of the germanium.

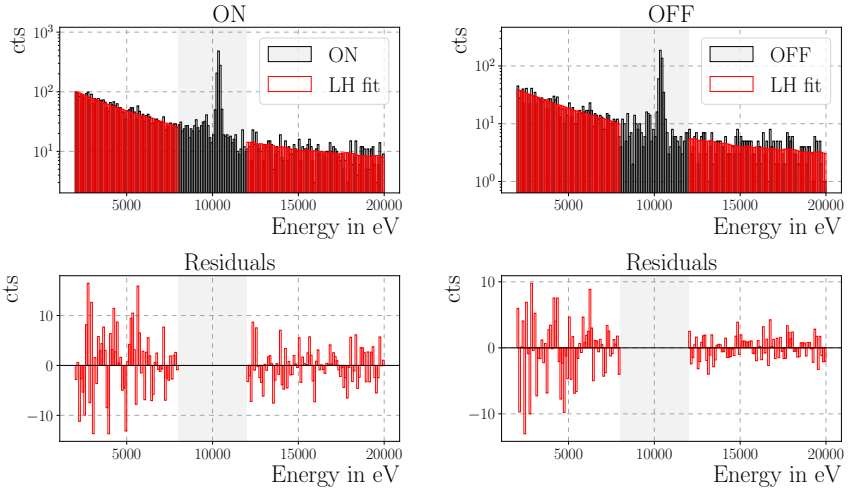

Figure C.11.: Best-fit result of CONUS-2 in Run-4 for the H_1 hypothesis with free magnetic moment parameter. On the left side, the reactor ON spectrum (top) is shown with respective residuals of (data - fit) (bottom), whereas the OFF spectrum is shown on the right side. In both cases, the data (black) is shown with the corresponding likelihood fit (red). The grey shaded area is excluded from the fit due to the activation lines of the germanium. For the best-fit case a small but not significant magnetic moment is found.

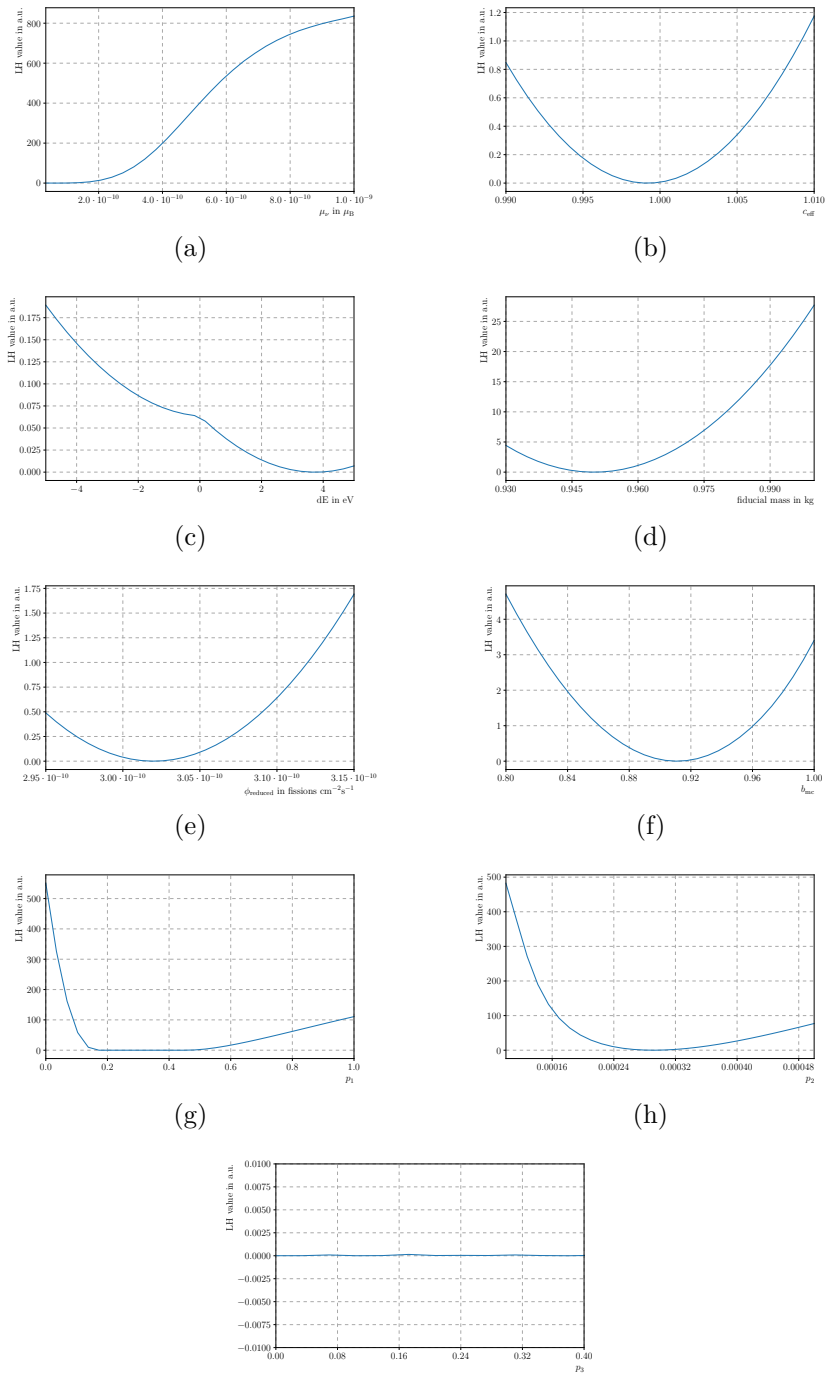

Figure C.12.: 1D profiles of all likelihood fit parameters for CONUS-2 in Run-4 for the magnetic moment investigation. The respective parameter is scanned over the whole parameter range, while all other parameters are minimized. The scanned parameters are the NMM μ_ν (a), the efficiency c_{eff} (b), the energy scale uncertainty dE (c), the fiducial mass m (d), the reduced flux ϕ_{reduced} (e), the background normalization b_{mc} (f) and the three parameters of the leakage test component (g)-(i). On the y-axis, the likelihood value in a.u. is shown.

Table C.4.: Correlation matrix of the likelihood parameters for CONUS-2 Run-4 for the magnetic moment investigation. The color of the cells indicates the strength of the correlation, where red is positively correlated and blue is negatively correlated.

	μ_ν	ϕ_{reduced}	m	dE	c_{eff}	b_{mc}	p_1	p_2	p_3
μ_ν	1	0	0	0	0	-0.454	0	0	0
ϕ_{reduced}	0	1	0	0	0	0	0	0	0
m	0	0	1	0	0	0	0	0	0
dE	0	0	0	1	0	0	0	0	0
c_{eff}	0	0	0	0	1	-0.141	0	0	0
b_{mc}	-0.454	0	0	0	-0.141	1	0	0.569	0
p_1	0	0	0	0	0	0	1	0	-0.976
p_2	0	0	0	0	0	0.569	0	1	0.145
p_3	0	0	0	0	0	0	-0.976	0.145	1

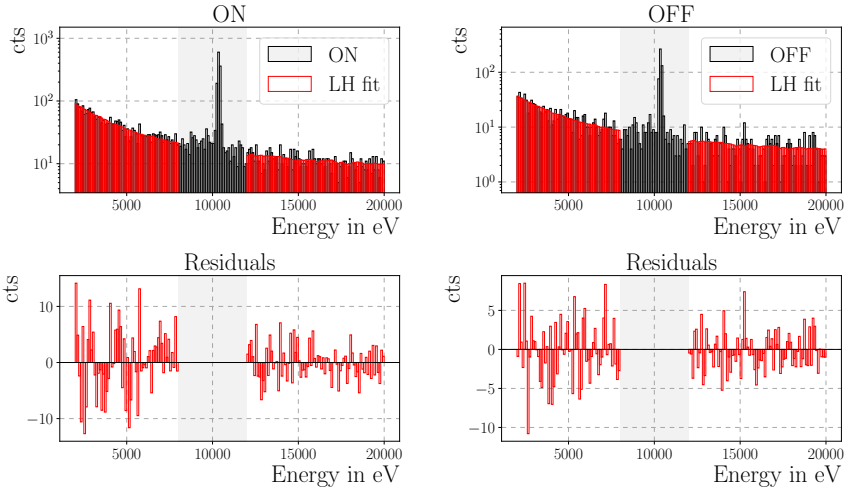

Figure C.13.: Best-fit result of CONUS-4 in Run-4 for the H_0 hypothesis assuming zero magentic moment. On the left side, the reactor ON spectrum (top) is shown with respective residuals of (data - fit) (bottom), whereas the OFF spectrum is shown on the right side. In both cases, the data (black) is shown with the corresponding likelihood fit (red). The grey shaded area is excluded from the fit due to the activation lines of the germanium.

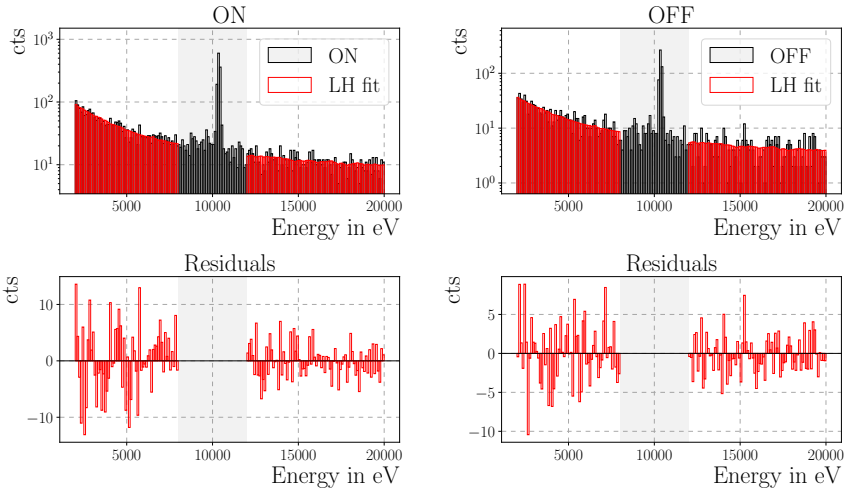

Figure C.14.: Best-fit result of CONUS-4 in Run-4 for the H_1 hypothesis with free magnetic moment parameter. On the left side, the reactor ON spectrum (top) is shown with respective residuals of (data - fit) (bottom), whereas the OFF spectrum is shown on the right side. In both cases, the data (black) is shown with the corresponding likelihood fit (red). The grey shaded area is excluded from the fit due to the activation lines of the germanium. For the best-fit case a small but not significant magnetic moment is found.

Table C.5.: Correlation matrix of the likelihood parameters for CONUS-4 Run-4 for the magnetic moment investigation. The color of the cells indicates the strength of the correlation, where red is positively correlated and blue is negatively correlated.

	μ_ν	ϕ_{reduced}	m	dE	c_{eff}	b_{mc}	p_1	p_2	p_3
μ_ν	1	0	0	0	0.110	-0.673	-0.072	0	0
ϕ_{reduced}	0	1	0	0	0	0	0	0	0
m	0	0	1	0	0	0	0	0	0
dE	0	0	0	1	0	0	0	0	0
c_{eff}	0.110	0	0	0	1	-0.254	0	0	0
b_{mc}	-0.673	0	0	0	-0.254	1	0.334	0.439	0.293
p_1	-0.072	0	0	0	0	0.334	1	0.866	0.720
p_2	0	0	0	0	0	0.439	0.866	1	0.868
p_3	0	0	0	0	0	0.293	0.720	0.868	1

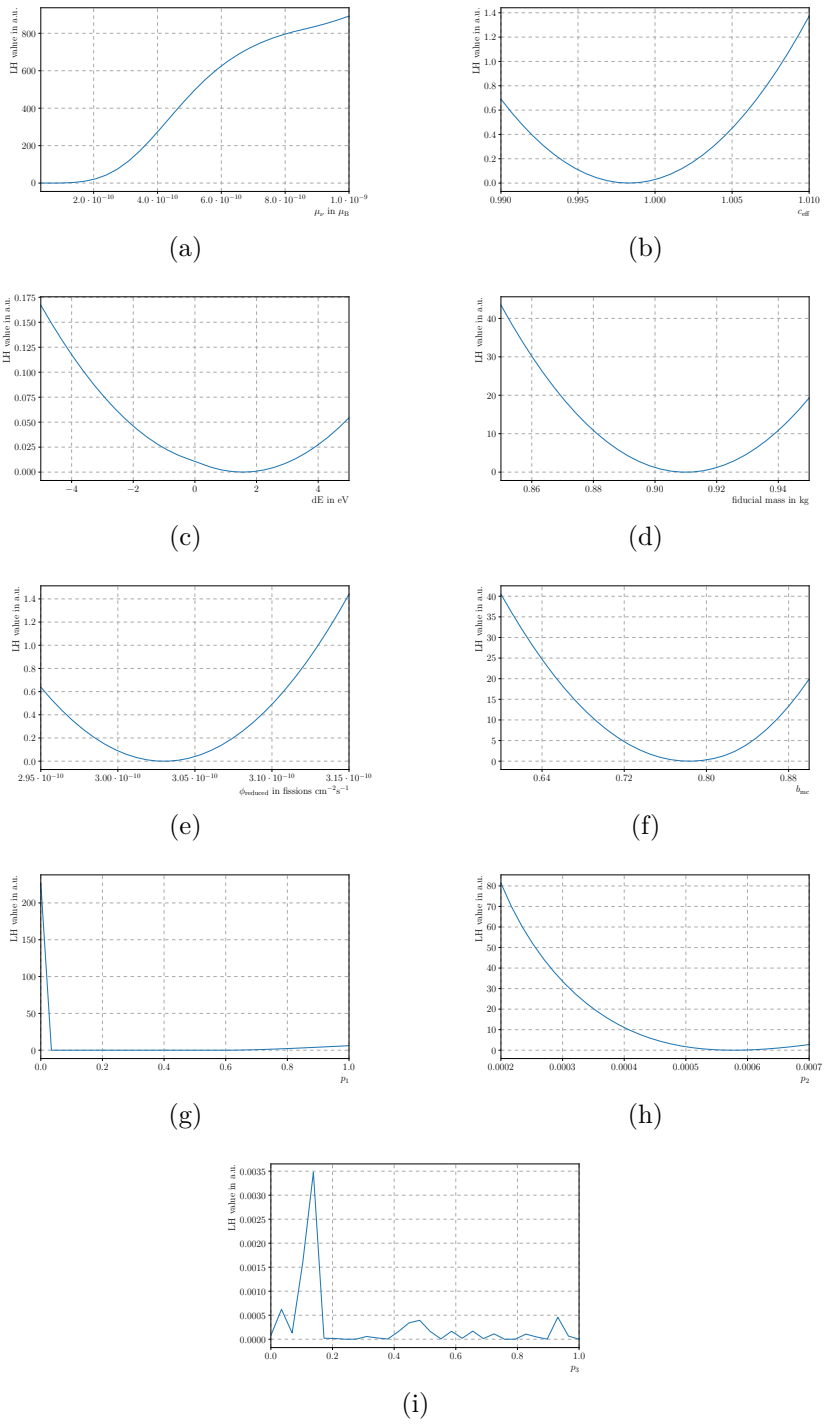

Figure C.15.: 1D profiles of all likelihood fit parameters for CONUS-4 in Run-4 for the magnetic moment investigation. The respective parameter is scanned over the whole parameter range, while all other parameters are minimized. The scanned parameters are the NMM μ_ν (a), the efficiency c_{eff} (b), the energy scale uncertainty dE (c), the fiducial mass m (d), the reduced flux ϕ_{reduced} (e), the background normalization b_{mc} (f) and the three parameters of the leakage test component (g)-(i). On the y-axis, the likelihood value in a.u. is shown.

D. Best Fitting results and Correlation Matrices for the Millicharge

Here, the best-fit values for the likelihood fit assuming the H_0 hypothesis of zero millicharge and for the H_1 hypothesis with free millicharge parameter are shown for all detectors in Run-4 and Run-5. Furthermore, the correlation matrices and 1D profiles of all parameters are plotted for the case of neutrino millicharge.

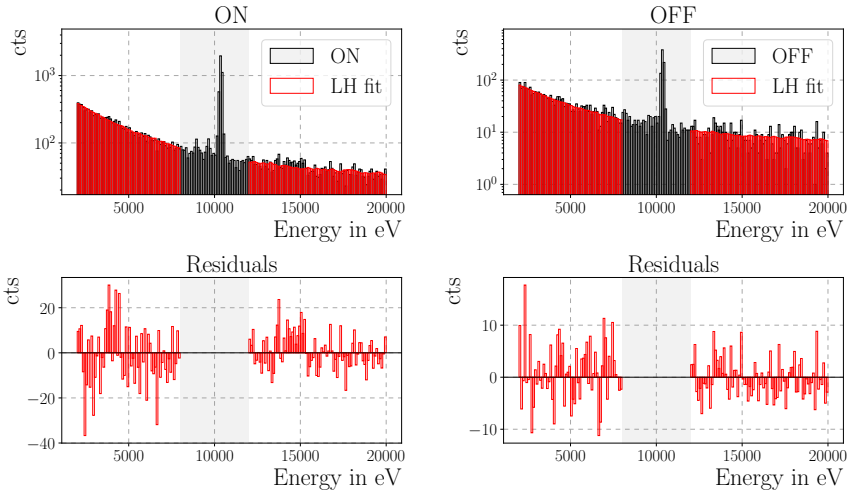

Figure D.1.: Best-fit result of CONUS-2 in Run-5 for the H_0 hypothesis assuming zero millicharge. On the left side, the reactor ON spectrum (top) is shown with respective residuals of (data - fit) (bottom), whereas the OFF spectrum is shown on the right side. In both cases, the data (black) is shown with the corresponding likelihood fit (red). The grey shaded area is excluded from the fit due to the activation lines of the germanium.

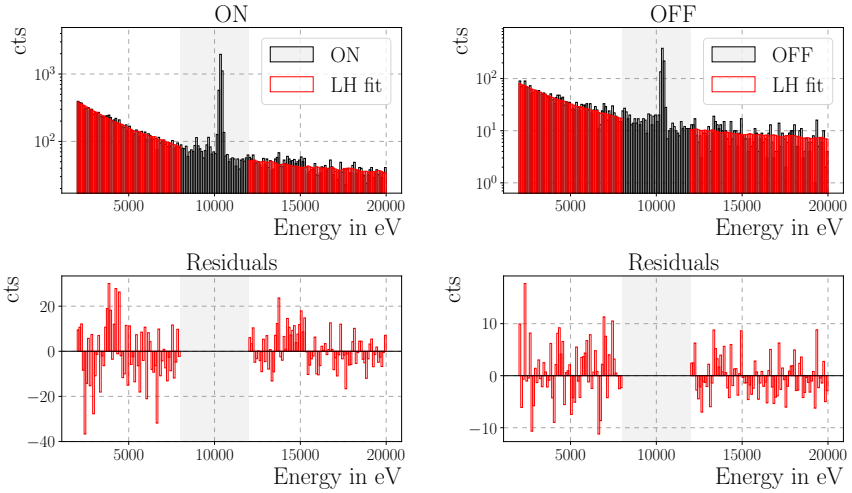

Figure D.2.: Best-fit result of CONUS-2 in Run-5 for the H_1 hypothesis with free millicharge parameter. On the left side, the reactor ON spectrum (top) is shown with respective residuals of (data - fit) (bottom), whereas the OFF spectrum is shown on the right side. In both cases, the data (black) is shown with the corresponding likelihood fit (red). The grey shaded area is excluded from the fit due to the activation lines of the germanium. For the best-fit case, no additional events due to a non-zero millicharge are found.

Table D.1.: Correlation matrix of the likelihood parameters for CONUS-2 Run-5 for the millicharge investigation. The color of the cells indicates the strength of the correlation, where red is positively correlated and blue is negatively correlated.

	$\lvert q_\nu \rvert$	ϕ_{reduced}	m	dE	c_{eff}	$b_{\text{add.ON}}$	b_{mc}	p_1	p_2	p_3
$q_\nu\rvert$	1	0	0	0	0	0	0	0	0	0
ϕ_{reduced}	0	1	0	0	0	0	0	0	0	0
m	0	0	1	0	0	0	0	0	0	0
dE	0	0	0	1	0	0	0	0	0	0
c_{eff}	0	0	0	0	1	0	-0.274	0	0	0
$b_{\text{add.ON}}$	0	0	0	0	0	1	-0.742	0	0	0
b_{mc}	0	0	0	0	-0.274	-0.742	1	0	0.337	0
p_1	0	0	0	0	0	0	0	1	0.110	-0.965
p_2	0	0	0	0	0	0	0.337	0.110	1	0.122
p_3	0	0	0	0	0	0	0	-0.965	0.122	1

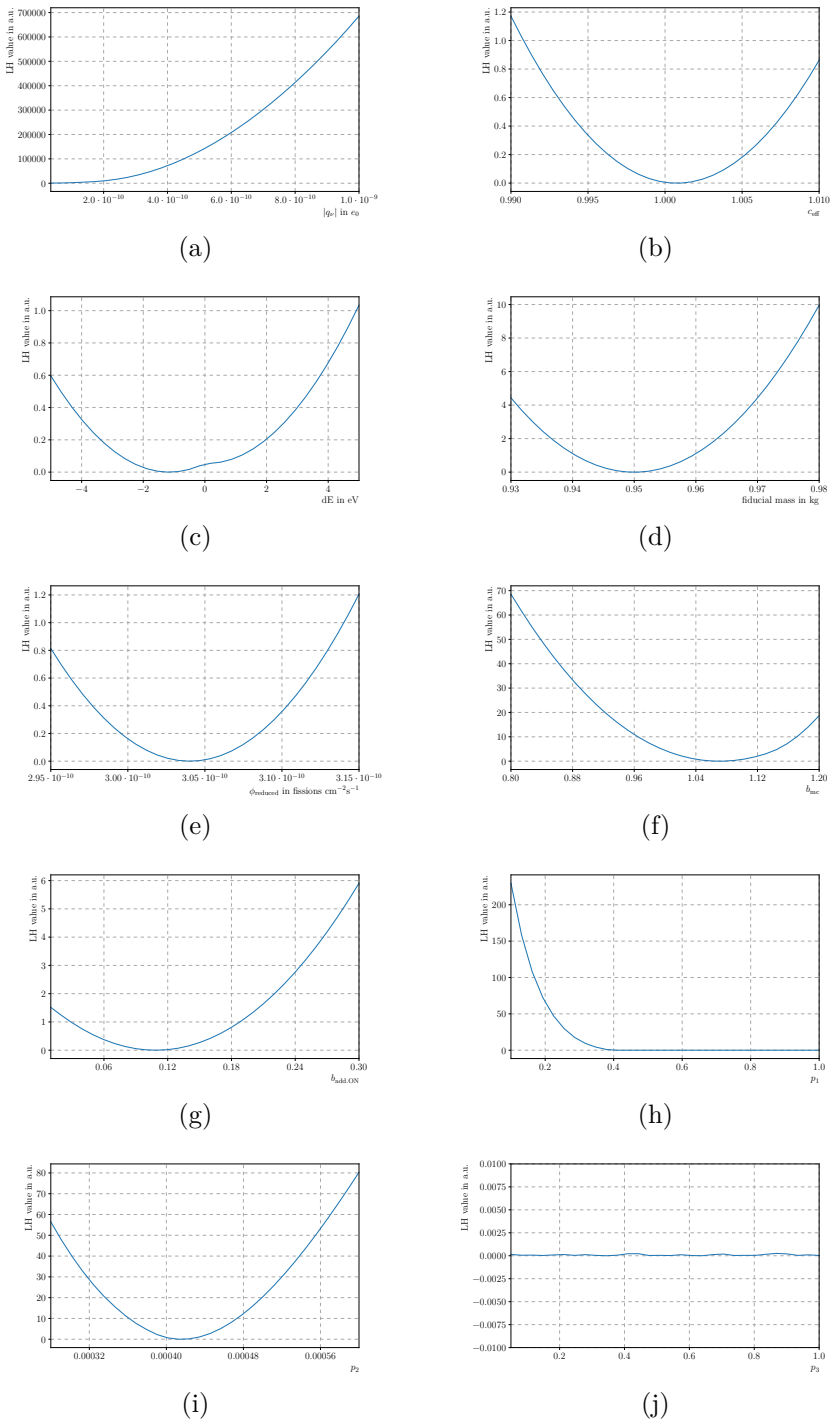

Figure D.3.: 1D profiles of all likelihood fit parameters for CONUS-2 in Run-5 for the millicharge investigation. The respective parameter is scanned over the whole parameter range, while all other parameters are minimized. The scanned parameters are the NMC $|q_\nu|$ (a), the efficiency c_{eff} (b), the energy scale uncertainty dE (c), the fiducial mass m (d), the reduced flux ϕ_{reduced} (e), the background normalization b_{mc} (f), the additional ON component $b_{\text{add.ON}}$ (g) and the three parameters of the leakage test component (h)-(j). On the y-axis, the likelihood value in a.u. is shown.

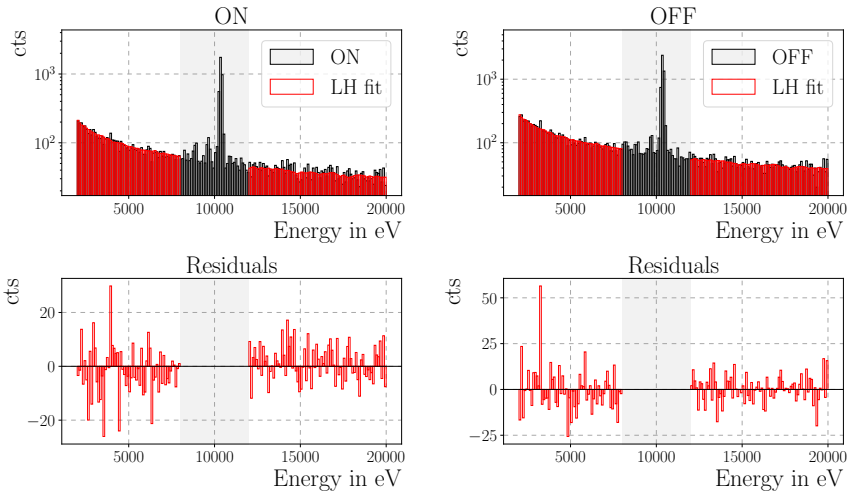

Figure D.4.: Best-fit result of CONUS-4 in Run-5 for the H_0 hypothesis assuming zero millicharge. On the left side, the reactor ON spectrum (top) is shown with respective residuals of (data - fit) (bottom), whereas the OFF spectrum is shown on the right side. In both cases, the data (black) is shown with the corresponding likelihood fit (red). The grey shaded area is excluded from the fit due to the activation lines of the germanium.

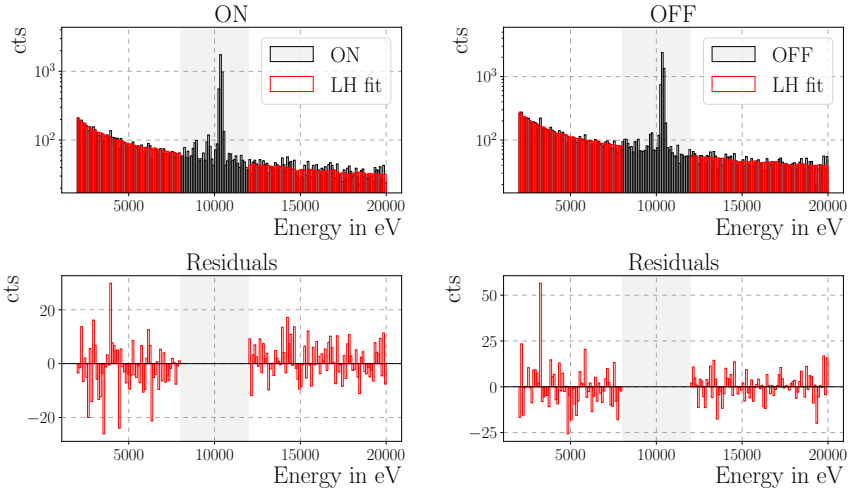

Figure D.5.: Best-fit result of CONUS-4 in Run-5 for the H_1 hypothesis with free millicharge parameter. On the left side, the reactor ON spectrum (top) is shown with respective residuals of (data - fit) (bottom), whereas the OFF spectrum is shown on the right side. In both cases, the data (black) is shown with the corresponding likelihood fit (red). The grey shaded area is excluded from the fit due to the activation lines of the germanium. For the best-fit case, no additional events due to a non-zero millicharge are found.

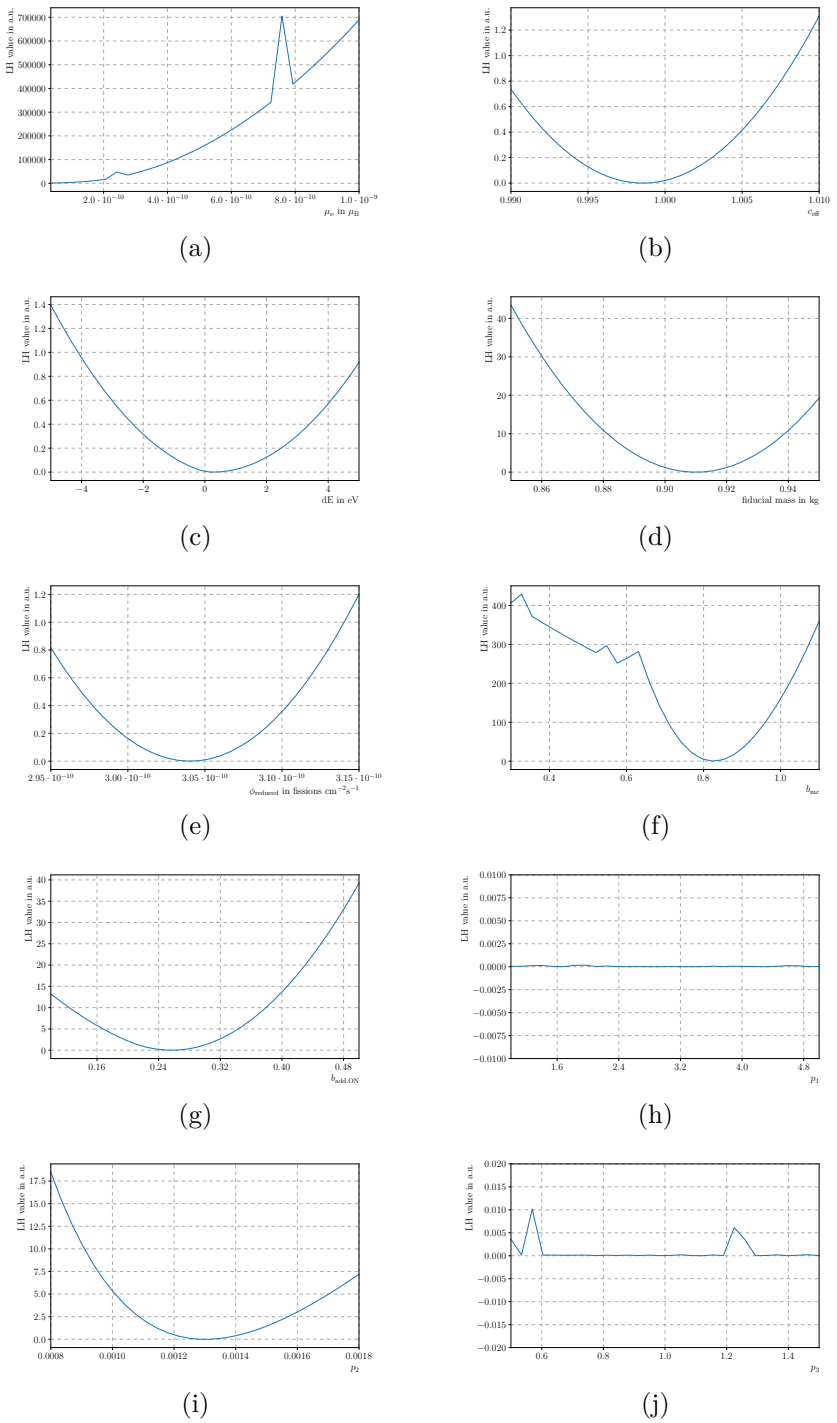

Figure D.6.: 1D profiles of all likelihood fit parameters for CONUS-4 in Run-5 for the millicharge investigation. The respective parameter is scanned over the whole parameter range, while all other parameters are minimized. The scanned parameters are the NMC $|q_\nu|$ (a), the efficiency c_{eff} (b), the energy scale uncertainty dE (c), the fiducial mass m (d), the reduced flux ϕ_{reduced} (e), the background normalization b_{mc} (f), the additional ON component $b_{\text{add.ON}}$ (g) and the three parameters of the leakage test component (h)-(j). On the y-axis, the likelihood value in a.u. is shown.

Table D.2.: Correlation matrix of the likelihood parameters for CONUS-4 Run-5 for the millicharge investigation. The color of the cells indicates the strength of the correlation, where red is positively correlated and blue is negatively correlated.

	$\lvert q_\nu \rvert$	ϕ_{reduced}	m	dE	c_{eff}	$b_{\text{add.ON}}$	b_{mc}	p_1	p_2	p_3
$q_\nu\rvert$	1	0	0	0	0	0	0	0	0	0
ϕ_{reduced}	0	1	0	0	0	0	0	0	0	0
m	0	0	1	0	0	0	0	0	0	0
dE	0	0	0	1	0	0	0	0	0	0
c_{eff}	0	0	0	0	1	0	-0.654	0	0	0
$b_{\text{add.ON}}$	0	0	0	0	0	1	−0.406	0	0	0
b_{mc}	0	0	0	0	-0.654	−0.406	1	0	0.243	0
p_1	0	0	0	0	0	0	0	1	0.169	-0.918
p_2	0	0	0	0	0	0	0.243	0.169	1	0.225
p_3	0	0	0	0	0	0	0	-0.918	0.225	1

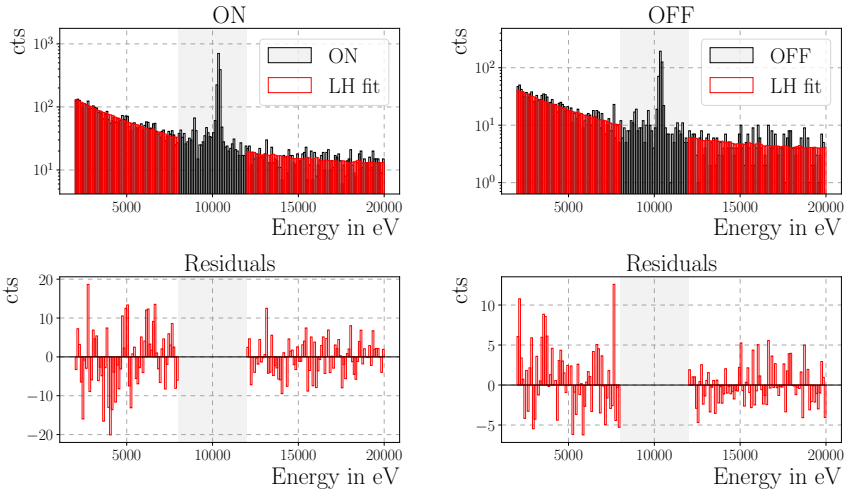

Figure D.7.: Best-fit result of CONUS-1 in Run-4 for the H_0 hypothesis assuming zero millicharge. On the left side, the reactor ON spectrum (top) is shown with respective residuals of (data - fit) (bottom), whereas the OFF spectrum is shown on the right side. In both cases, the data (black) is shown with the corresponding likelihood fit (red). The grey shaded area is excluded from the fit due to the activation lines of the germanium.

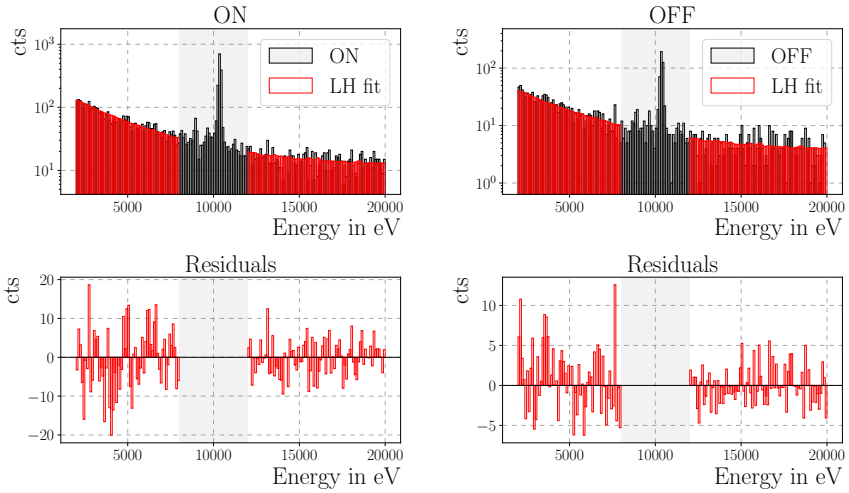

Figure D.8.: Best-fit result of CONUS-1 in Run-4 for the H_1 hypothesis with free millicharge parameter. On the left side, the reactor ON spectrum (top) is shown with respective residuals of (data - fit) (bottom), whereas the OFF spectrum is shown on the right side. In both cases, the data (black) is shown with the corresponding likelihood fit (red). The grey shaded area is excluded from the fit due to the activation lines of the germanium. For the best-fit case, no additional events due to a non-zero millicharge are found.

Table D.3.: Correlation matrix of the likelihood parameters for CONUS-1 Run-4 for the millicharge investigation. The color of the cells indicates the strength of the correlation where red is positively correlated and blue is negatively correlated.

	$\lvert q_\nu \rvert$	ϕ_{reduced}	m	dE	c_{eff}	b_{mc}	p_1	p_2	p_3	
$q_\nu\rvert$	1	0	0	0	0	0.649	0.595	0.854	0.593	
ϕ_{reduced}	0	1	0	0	0	0	0	0	0	
m	0	0	1	0	0	0	0	0	0	
dE	0	0	0	1	0	0	0	0	0	
c_{eff}	0	0	0	0	0	1	-0.250	0	0.072	0
b_{mc}	0.649	0	0	0	-0.250	1	0.107	0.488	0.105	
p_1	0.595	0	0	0	0	0.107	1	0.747	0.534	
p_2	0.854	0	0	0	0.072	0.488	0.747	1	0.745	
p_3	0.593	0	0	0	0	0.105	0.534	0.745	1	

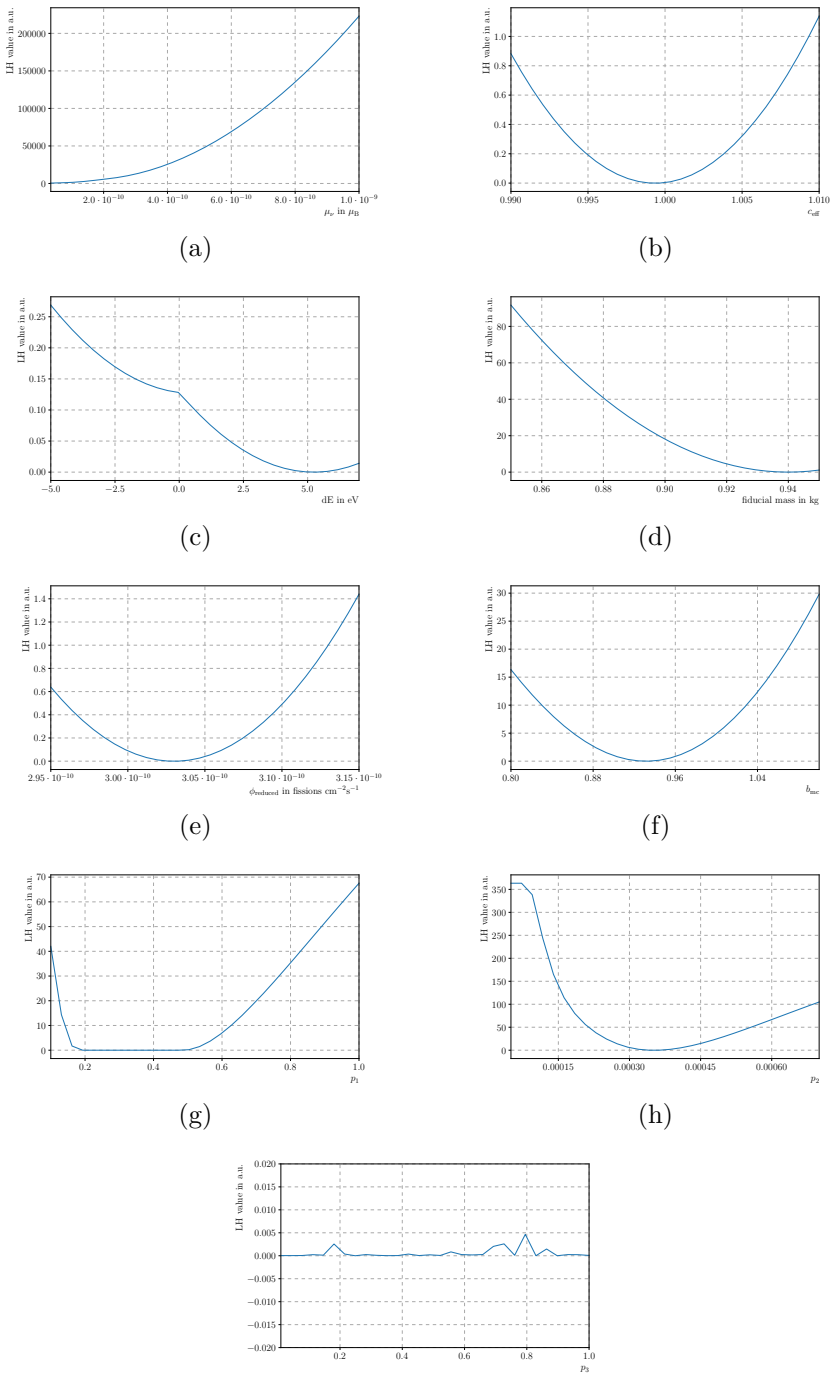

Figure D.9.: 1D profiles of all likelihood fit parameters for CONUS-1 in Run-4 for the millicharge investigation. The respective parameter is scanned over the whole parameter range, while all other parameters are minimized. The scanned parameters are the NMC $|q_\nu|$ (a), the efficiency c_{eff} (b), the energy scale uncertainty dE (c), the fiducial mass m (d), the reduced flux ϕ_{reduced} (e), the background normalization b_{mc} (f) and the three parameters of the leakage test component (g)-(i). On the y-axis, the likelihood value in a.u. is shown.

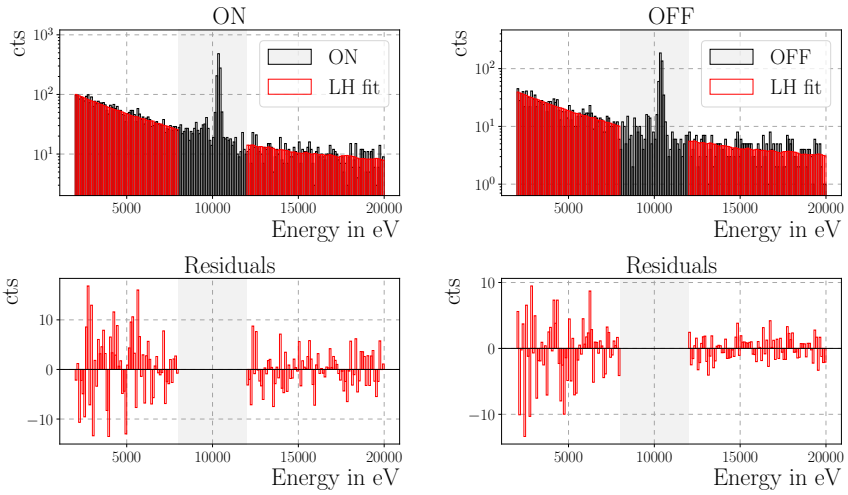

Figure D.10.: Best-fit result of CONUS-2 in Run-4 for the H_0 hypothesis assuming zero millicharge. On the left side, the reactor ON spectrum (top) is shown with respective residuals of (data - fit) (bottom), whereas the OFF spectrum is shown on the right side. In both cases, the data (black) is shown with the corresponding likelihood fit (red). The grey shaded area is excluded from the fit due to the activation lines of the germanium.

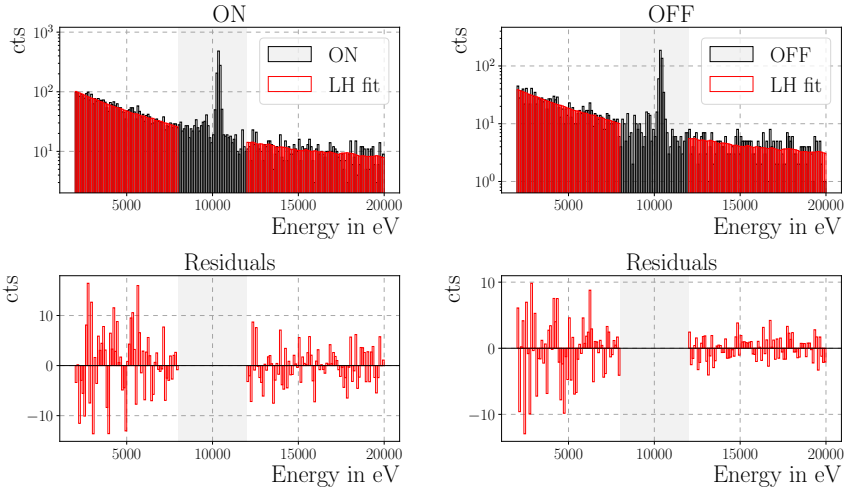

Figure D.11.: Best-fit result of CONUS-2 in Run-4 for the H_1 hypothesis with free millicharge parameter. On the left side, the reactor ON spectrum (top) is shown with respective residuals of (data - fit) (bottom), whereas the OFF spectrum is shown on the right side. In both cases, the data (black) is shown with the corresponding likelihood fit (red). The grey shaded area is excluded from the fit due to the activation lines of the germanium. For the best-fit case, a small but not significant millicharge is found.

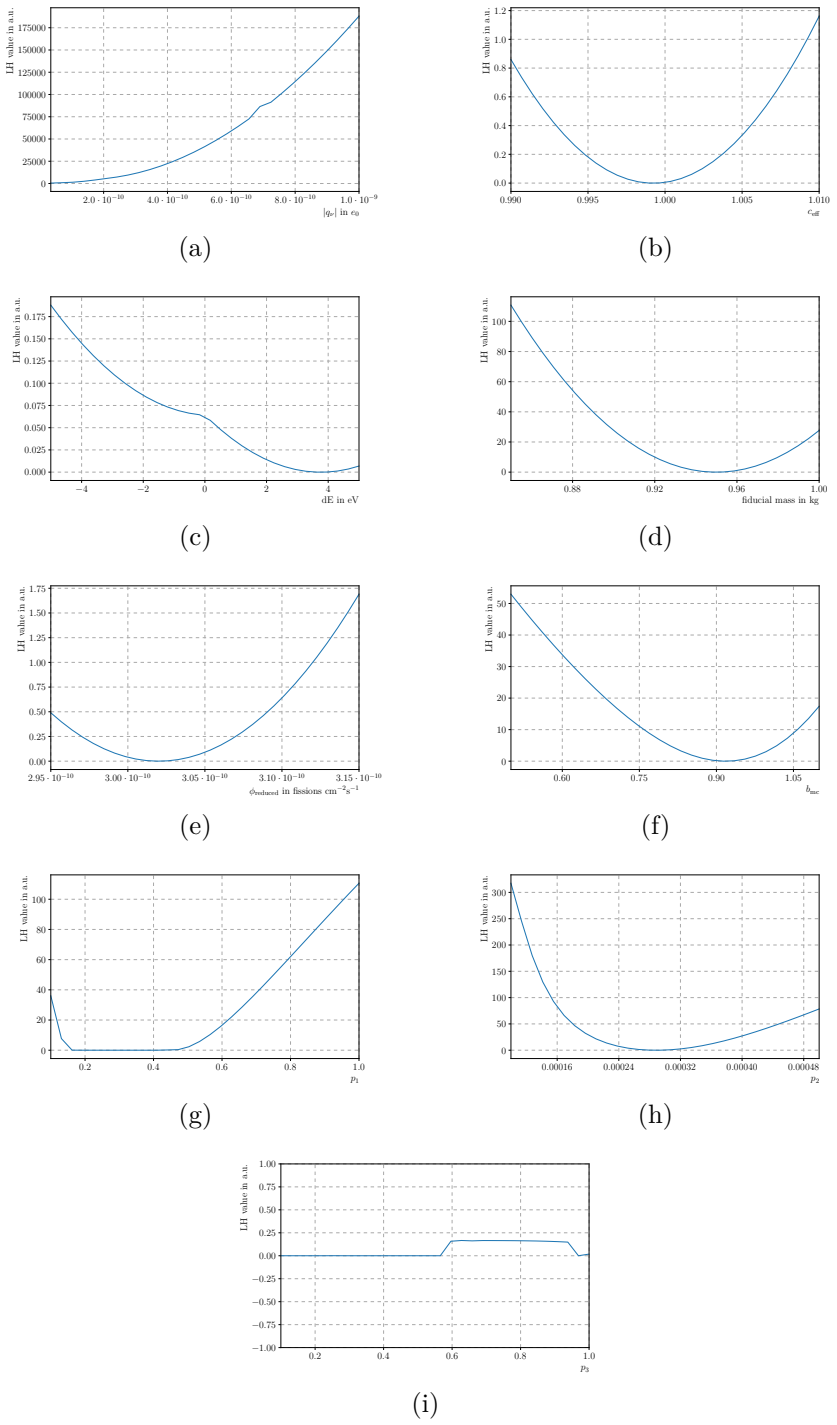

Figure D.12.: 1D profiles of all likelihood fit parameters for CONUS-2 in Run-4 for the millicharge investigation. The respective parameter is scanned over the whole parameter range, while all other parameters are minimized. The scanned parameters are the NMC $|q_\nu|$ (a), the efficiency c_{eff} (b), the energy scale uncertainty dE (c), the fiducial mass m (d), the reduced flux ϕ_{reduced} (e), the background normalization b_{mc} (f) and the three parameters of the leakage test component (g)-(i). On the y-axis, the likelihood value in a.u. is shown.

Table D.4.: Correlation matrix of the likelihood parameters for CONUS-2 Run-4 for the millicharge investigation. The color of the cells indicates the strength of the correlation, where red is positively correlated and blue is negatively correlated.

	$\lvert q_\nu \rvert$	ϕ_{reduced}	m	dE	c_{eff}	b_{mc}	p_1	p_2	p_3	
$q_\nu\rvert$	1	0	0	0	0	-0.236	-0.088	-0.347	-0.103	
ϕ_{reduced}	0	1	0	0	0	0	0	0	0	
m	0	0	1	0	0	0	0	0	0	
dE	0	0	0	1	0	0	0	0	0	
c_{eff}	0	0	0	0	0	1	-0.161	0	0	0
b_{mc}	-0.236	0	0	0	-0.161	1	0	0.684	0	
p_1	-0.088	0	0	0	0	0	1	0.099	-0.960	
p_2	-0.347	0	0	0	0	0.684	0.099	1	0.117	
p_3	-0.103	0	0	0	0	0	-0.960	0.117	1	

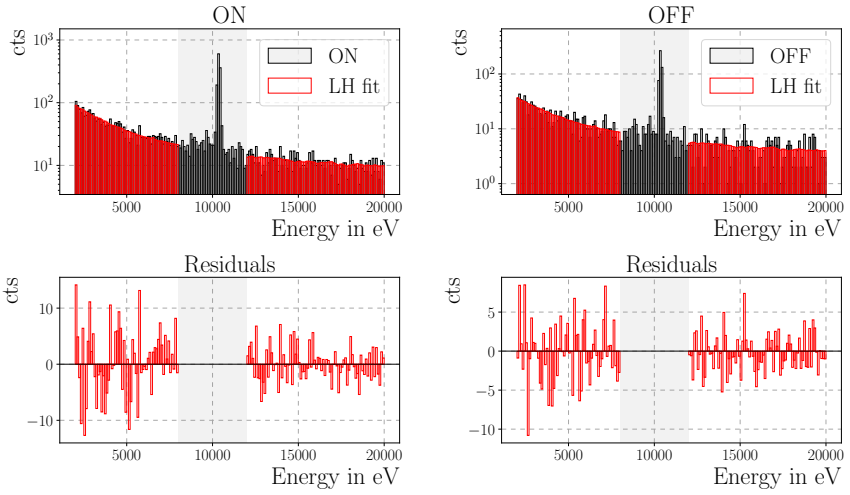

Figure D.13.: Best-fit result of CONUS-4 in Run-4 for the H_0 hypothesis assuming zero millicharge. On the left side, the reactor ON spectrum (top) is shown with respective residuals of (data - fit) (bottom), whereas the OFF spectrum is shown on the right side. In both cases, the data (black) is shown with the corresponding likelihood fit (red). The grey shaded area is excluded from the fit due to the activation lines of the germanium.

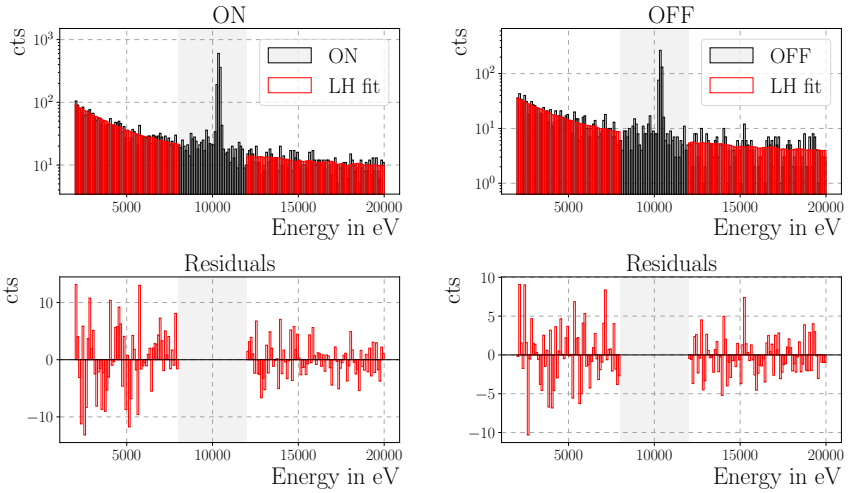

Figure D.14.: Best-fit result of CONUS-4 in Run-4 for the H_1 hypothesis with free millicharge parameter. On the left side, the reactor ON spectrum (top) is shown with respective residuals of (data - fit) (bottom), whereas the OFF spectrum is shown on the right side. In both cases, the data (black) is shown with the corresponding likelihood fit (red). The grey shaded area is excluded from the fit due to the activation lines of the germanium. For the best-fit case, a small but not significant millicharge is found.

Table D.5.: Correlation matrix of the likelihood parameters for CONUS-4 Run-4 for the millicharge investigation. The color of the cells indicates the strength of the correlation, where red is positively correlated and blue is negatively correlated.

	$\lvert q_\nu \rvert$	ϕ_{reduced}	m	dE	c_{eff}	b_{mc}	p_1	p_2	p_3	
$q_\nu\rvert$	1	0	0	0	0	-0.216	-0.061	-0.070	-0.080	
ϕ_{reduced}	0	1	0	0	0	0	0	0	0	
m	0	0	1	0	0	0	0	0	0	
dE	0	0	0	1	0	0	0	0	0	
c_{eff}	0	0	0	0	0	1	-0.315	0	0	0
b_{mc}	-0.216	0	0	0	-0.315	1	0	0.525	0.067	
p_1	-0.061	0	0	0	0	0	1	0.126	-0.943	
p_2	-0.070	0	0	0	0	0.525	0.126	1	0.165	
p_3	-0.080	0	0	0	0	0.067	-0.943	0.165	1	

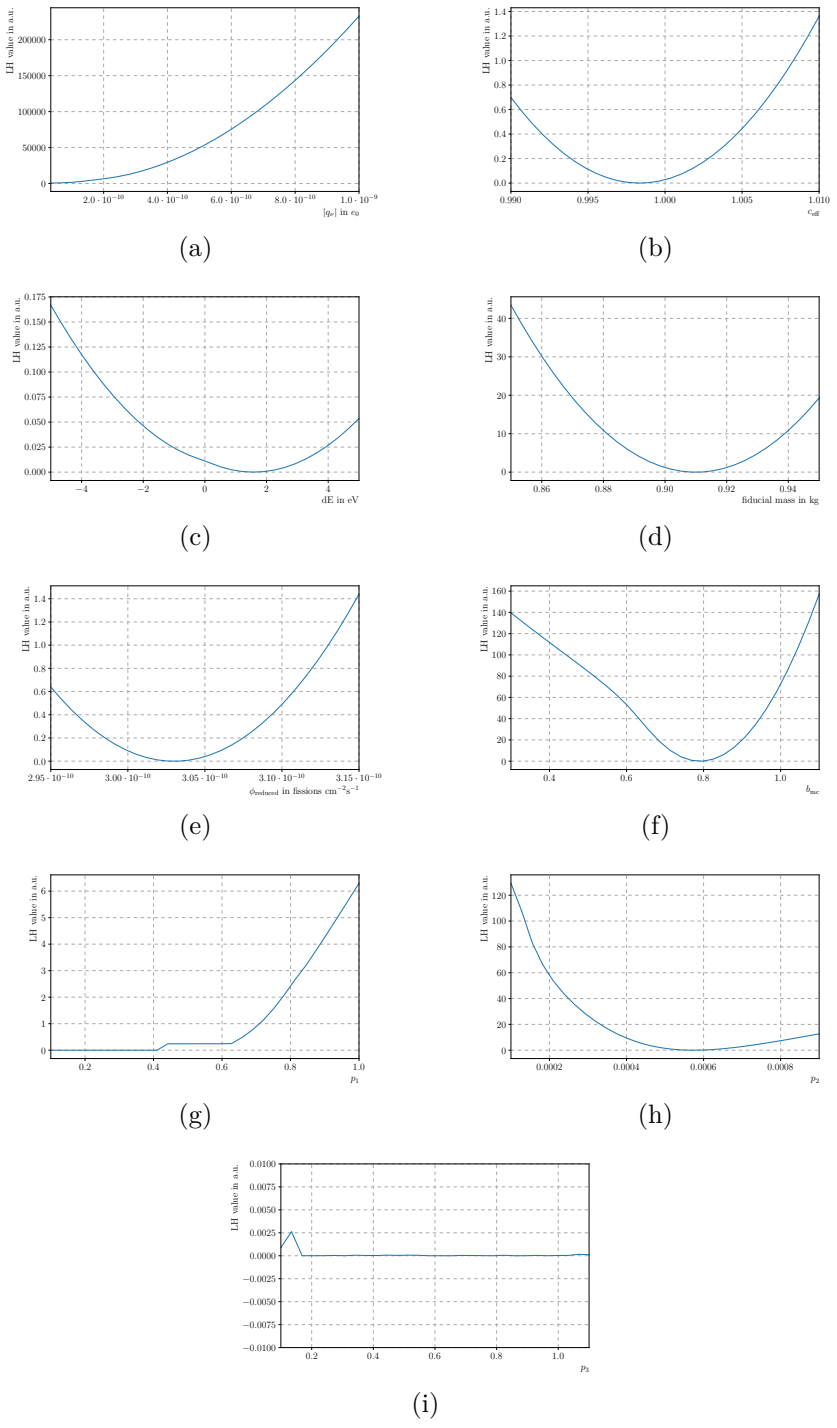

Figure D.15.: 1D profiles of all likelihood fit parameters for CONUS-4 in Run-4 for the millicharge investigation. The respective parameter is scanned over the whole parameter range, while all other parameters are minimized. The scanned parameters are the NMC $|q_\nu|$ (a), the efficiency c_{eff} (b), the energy scale uncertainty dE (c), the fiducial mass m (d), the reduced flux ϕ_{reduced} (e), the background normalization b_{mc} (f) and the three parameters of the leakage test component (g)-(i). On the y-axis, the likelihood value in a.u. is shown.

E. Simulated Detector Potentials

In the following the simulated electric and weighting potentials of CONUS-2 to CONUS-5 are shown. Due to different impurity concentrations and depletion voltages, the formation of the electric field and the weighting potential are individual for each detector.

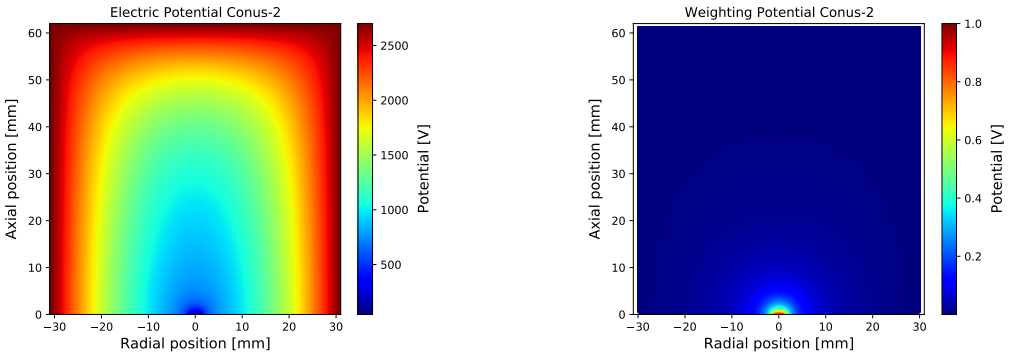

(a) (b)

Figure E.1.: Simulated electric (a) and weighting (b) potentials for the CONUS-2 detector.

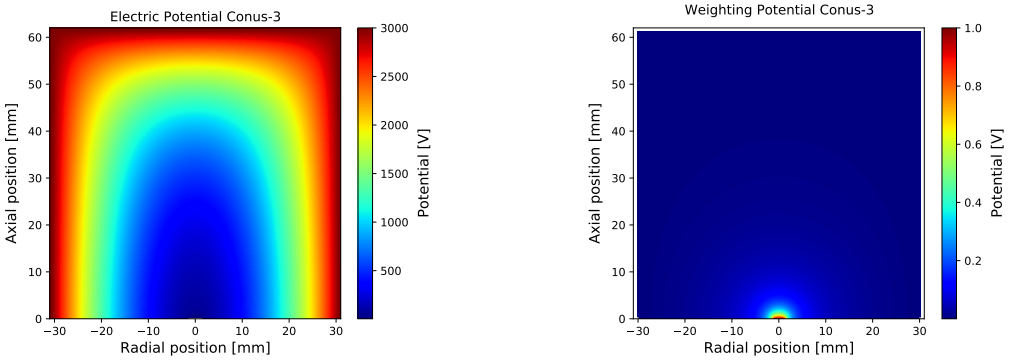

(a) (b)

Figure E.2.: Simulated electric (a) and weighting (b) potentials for the CONUS-3 detector.

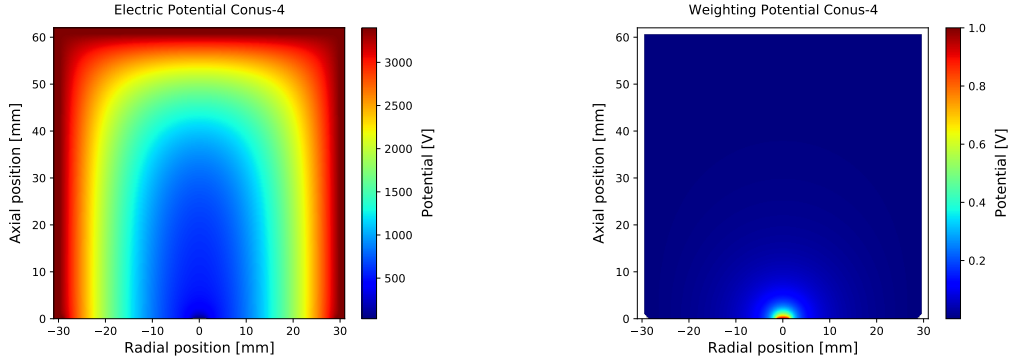

(a) (b)

Figure E.3.: Simulated electric (a) and weighting (b) potentials for the CONUS-4 detector.

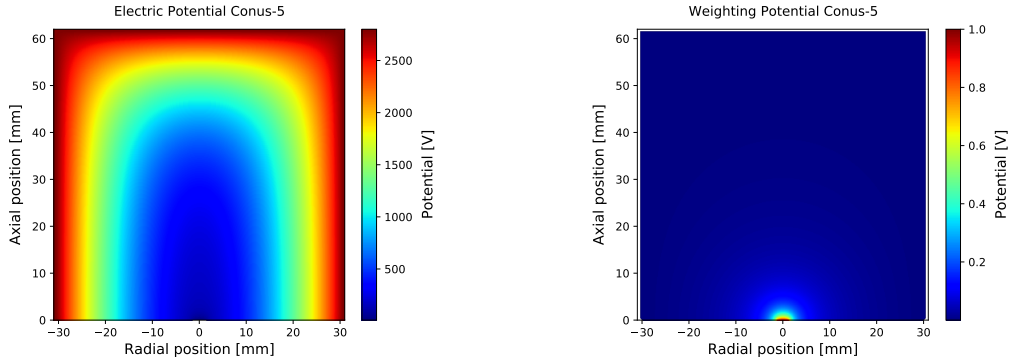

(a) (b)

Figure E.4.: Simulated electric (a) and weighting (b) potentials for the CONUS-5 detector.

APPENDIX

F. Calibration for the Detector Simulation

For the calibration of the simulation from arbitrary units to ADC channels calibration coefficients are needed. They are obtained by the following calibration lines for CONUS-2 to CONUS-5. Here, the maximum amplitude of background FP is plotted against the energy.

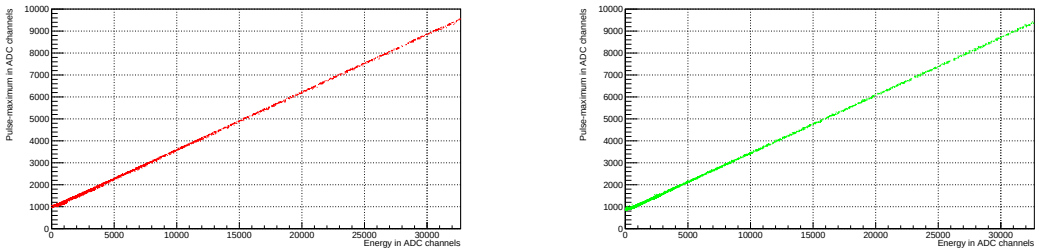

(a) (b)

Figure F.1.: Simulation calibration lines for the CONUS-2 (a) and CONUS-3 (b) detectors.

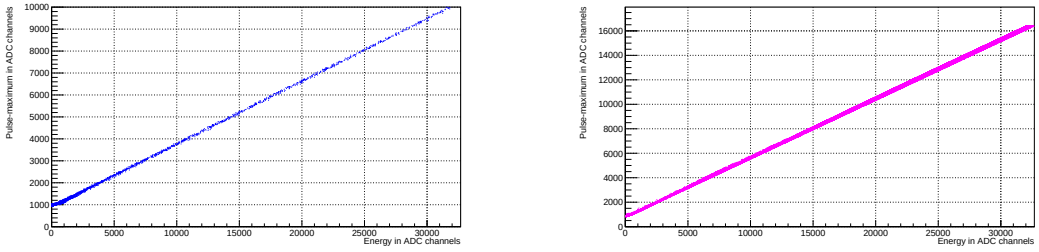

(a) (b)

Figure F.2.: Simulation calibration lines for the CONUS-4 (a) and CONUS-5 (b) detectors.

G. Noise Templates

Noise templates generated by the 'Noise Generator' for the CONUS-2 to CONUS-5 detectors. Measured noise samples are processed and the mean frequencies and the standard deviation are calculated. The calculated frequencies are varied around the standard deviation and individual noise templates are generated.

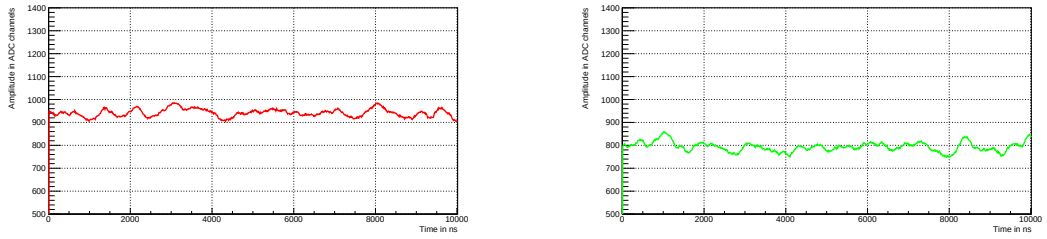

(a) (b)

Figure G.1.: Generated noise template for the CONUS-2 (a) and CONUS-3 (b) detectors.

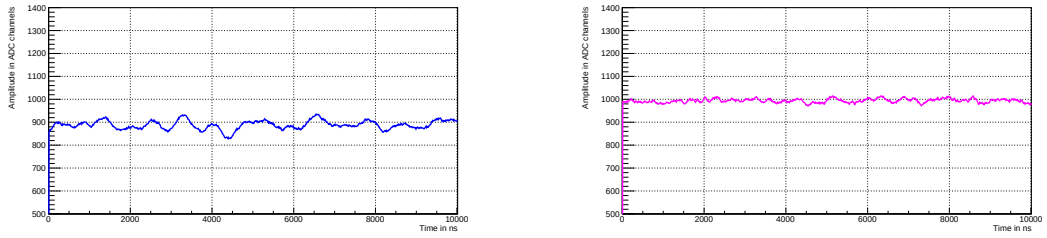

(a) (b)

Figure G.2.: Generated noise template for the CONUS-4 and CONUS-5 detectors.

H. Simulated and Measured Pulses

In the following, the simulated pulses of CONUS-2 to CONUS-5 are compared to the measured ones. The comparison is conducted for events of 500 eV, 1 keV, 10 keV and 25 keV. Furthermore, the parameters of the pulses fitted by Equation 4.10 are summarized for simulation and measurement.

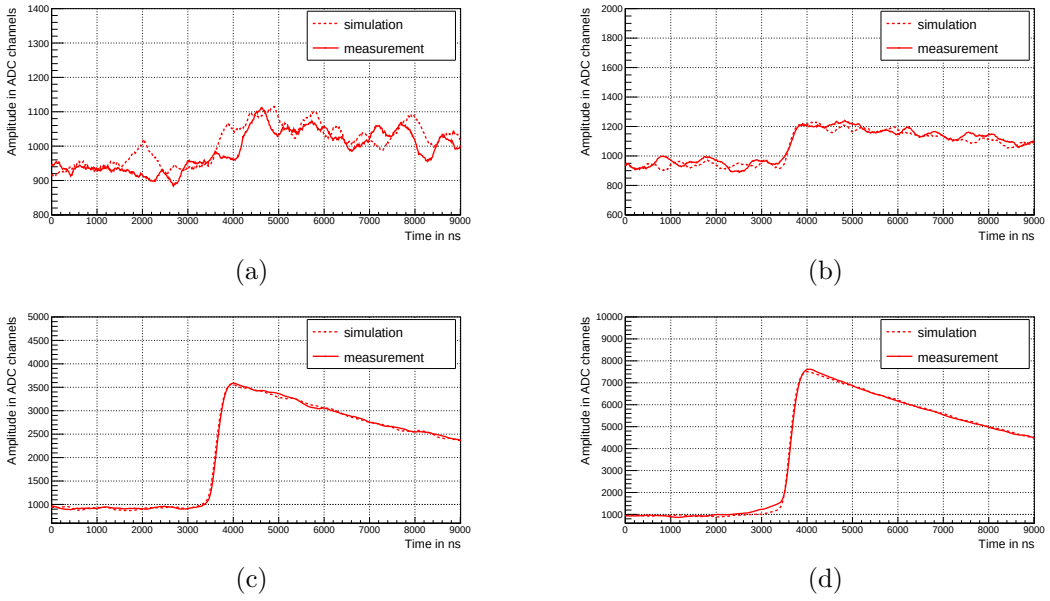

Figure H.1.: Comparison between simulated and measured pulses for the CONUS-2 detector at 500 eV (a), 1 keV (b), 10 keV (c) and 25 keV (d). The simulated pulse (dashed) is shifted in time to match the rise of the measured pulse (solid).

Table H.1.: Fit parameters of measured and simulated pulses for the CONUS-2 detector. The constant of the exponential decay τ_c is fixed in the fit to 0.000131 ns for measurement and simulation as well.

Energy in keV		A_0 in ADC channels	t_0 in ns	τ in ns	τ_c in ns	P_0 in ADC channels
0.5	measurement	72.48 ± 1.57	4074.17 ± 32.82	368.02 ± 68.51	0.000131	929.82 ± 1.67
	simulation	72.52 ± 1.22	3749.32 ± 17.93	261.73 ± 31.44	0.000131	946.40 ± 1.31
1	measurement	147.82 ± 1.14	3654.48 ± 5.96	181.58 ± 11.78	0.000131	947.96 ± 1.25
	simulation	148.69 ± 0.81	3629.94 ± 3.33	113.06 ± 5.44	0.000131	934.48 ± 0.90
10	measurement	1429.93 ± 1.30	3660.08 ± 0.68	166.49 ± 1.23	0.000131	926.24 ± 1.43
	simulation	1429.75 ± 1.56	3639.97 ± 0.84	174.42 ± 1.54	0.000131	922.87 ± 1.72
25	measurement	3507.77 ± 3.75	3655.66 ± 0.83	183.04 ± 1.58	0.000131	1003.5 ± 4.12
	simulation	3534.15 ± 2.88	3642.16 ± 0.62	171.99 ± 1.14	0.000131	964.69 ± 3.17

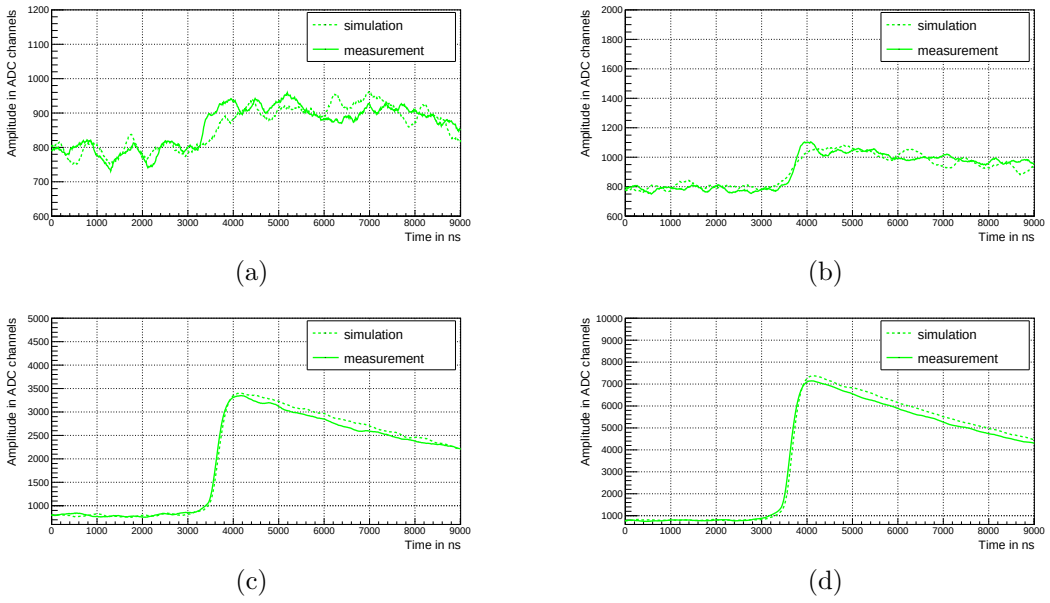

Figure H.2.: Comparison between simulated and measured pulses for the CONUS-3 detector at 500 eV (a), 1 keV (b), 10 keV (c) and 25 keV (d). The simulated pulse (dashed) is shifted in time to match the rise of the measured pulse (solid).

Table H.2.: Fit parameters of measured and simulated pulses for the CONUS-3 detector. The constant of the exponential decay τ_c is fixed in the fit to 0.000125 ns for measurement and simulation as well.

Energy in keV		A_0 in ADC channels	t_0 in ns	τ in ns	τ_c in ns	P_0 in ADC channels
0.5	measurement	81.47 ± 1.11	3439.44 ± 12.72	287.68 ± 29.20	0.000125	789.28 ± 1.21
	simulation	89.52 ± 2.07	4009.87 ± 36.22	1011.76 ± 78.92	0.000125	784.25 ± 1.92
1	measurement	151.59 ± 0.85	3712.49 ± 3.83	124.25 ± 6.34	0.000125	785.73 ± 0.96
	simulation	141.53 ± 1.17	3715.57 ± 8.08	285.16 ± 13.64	0.000125	793.89 ± 1.29
10	measurement	1355.48 ± 1.29	3655.53 ± 0.76	192.44 ± 1.25	0.000125	804.78 ± 1.44
	simulation	1418.87 ± 1.23	3699.62 ± 0.72	205.06 ± 1.35	0.000125	796.81 ± 1.36
25	measurement	3399.7 ± 1.87	3650.81 ± 0.45	194.92 ± 0.83	0.000125	800.56 ± 2.08
	simulation	3542.89 ± 2.04	3700.49 ± 0.47	192.98 ± 0.86	0.000125	811.40 ± 2.27

Table H.3.: Fit parameters of measured and simulated pulses for the CONUS-4 detector. The constant of the exponential decay τ_c is fixed in the fit to 0.000132 ns for measurement and simulation as well.

Energy in keV		A_0 in ADC channels	t_0 in ns	τ in ns	τ_c in ns	P_0 in ADC channels
0.5	measurement	78.39 ± 1.17	3149.62 ± 10.63	144.66 ± 16.36	0.000132	900.76 ± 1.32
	simulation	71.85 ± 0.99	3729.11 ± 11.08	190.86 ± 19.93	0.000132	899.62 ± 1.08
1	measurement	176.95 ± 1.23	3675.82 ± 4.86	138.76 ± 8.08	0.000132	887.25 ± 1.37
	simulation	143.65 ± 0.83	3761.53 ± 3.67	107.01 ± 5.16	0.000132	899.14 ± 0.92
10	measurement	1451.21 ± 2.22	3667.65 ± 1.12	153.09 ± 1.82	0.000132	905.18 ± 2.45
	simulation	1417.98 ± 1.95	3737.97 ± 1.04	164.31 ± 1.71	0.000132	901.42 ± 2.14
25	measurement	3621.91 ± 5.05	3673.10 ± 1.00	148.53 ± 1.61	0.000132	901.41 ± 5.58
	simulation	3549.14 ± 4.46	3734.80 ± 0.94	162.82 ± 1.58	0.000132	904.79 ± 4.89

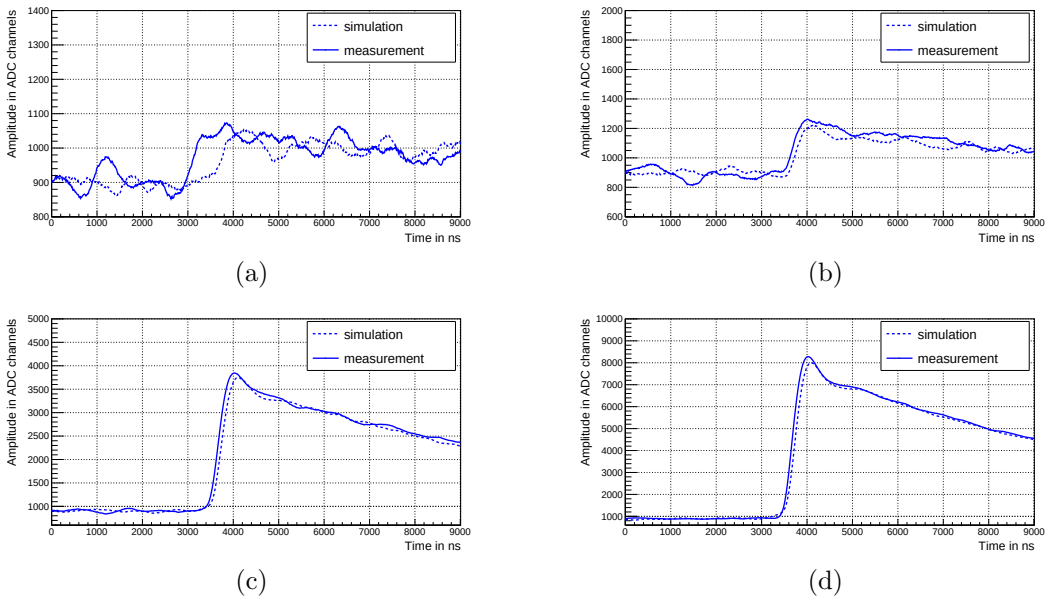

Figure H.3.: Comparison between simulated and measured pulses for the CONUS-4 detector at 500 eV (a), 1 keV (b), 10 keV (c) and 25 keV (d). The simulated pulse (dashed) is shifted in time to match the rise of the measured pulse (solid).

I. Ambient Temperature Correlation for CONUS+ Detectors

In the following, the detector rate, cryocooler power, and room temperature for the second and third temperature test are shown. In test 2, the chiller temperature was set to 10°C and the temperature in the tent was heated up to 40°C. In test 3 the chiller temperature was set to 18°C. Furthermore, the correlation plots for test 2 and test 3 are shown and the corresponding correlation coefficients and fit parameters are given. Additionally, the rate, cryocooler power, and room temperature during the cooling test with a chiller temperature of 18°C is shown in Figure I.7.

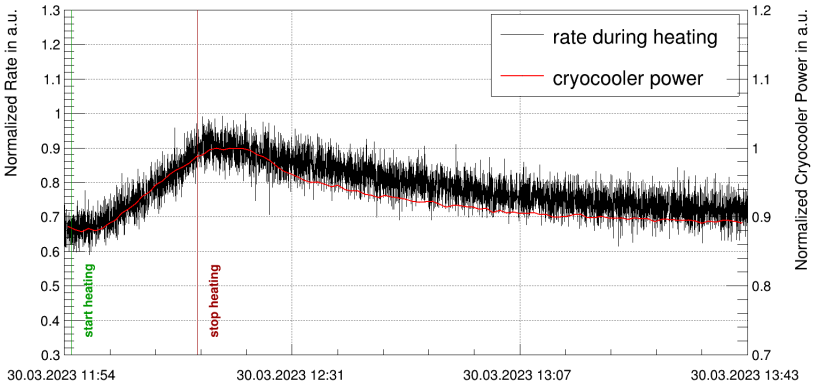

Figure I.2.: Normalized detector rate (black) and normalized cryocooler power (red) plotted over time for the second test with a chiller temperature of 10 °C. The time of start and stop of the heating is also marked.

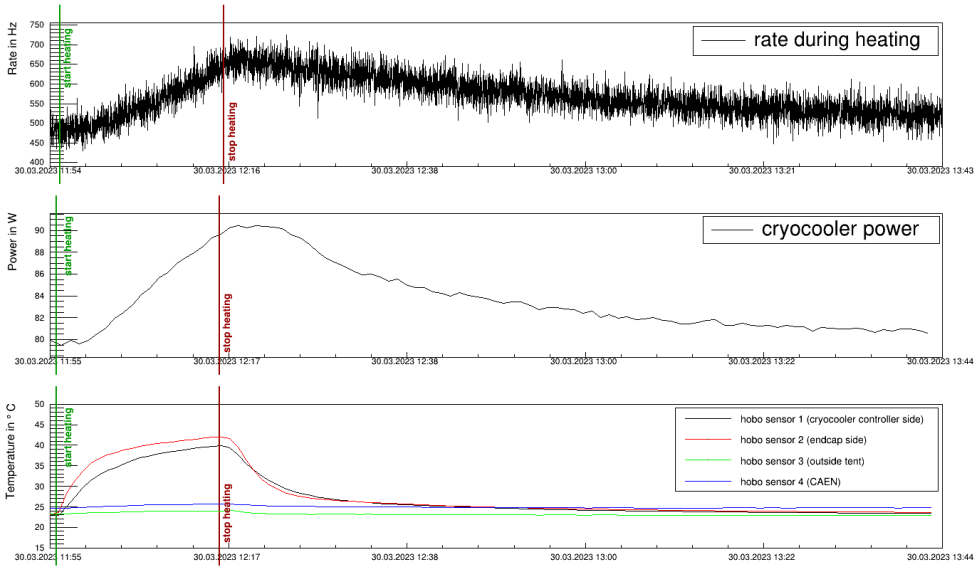

(a)

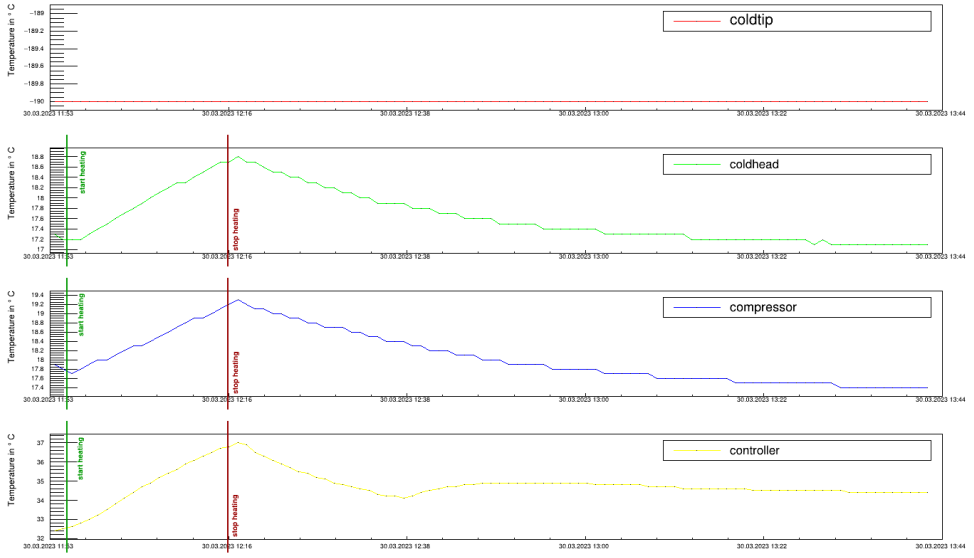

(b)

Figure I.1.: Rate, cryocooler properties and room temperature for the second test with a chiller temperature of 10 °C. The temperature in the tent was heated up to 40 °C and the detector rate (top), cryocooler power (middle), and temperature (bottom) were recorded over time (a). Additionally, the cryocooler properties such as the coldtip temperature (red), the coldhead temperature (green), the compressor temperature (blue), and the controller temperature (yellow) are also recorded over time (b). The time of start and stop of the heating is also marked.

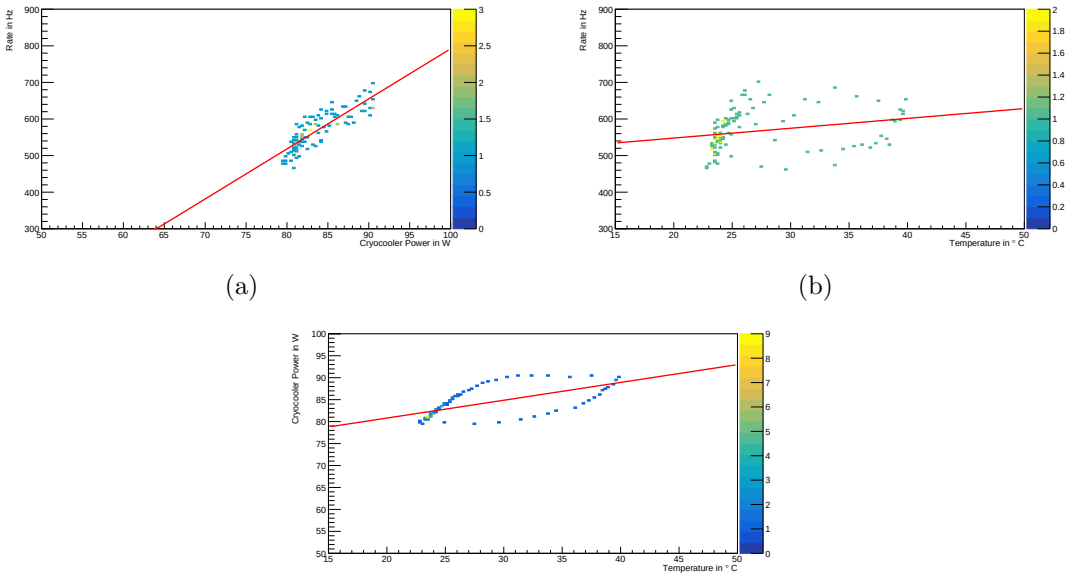

(a) (b)

(c)

Figure I.3.: Correlation between detector rate and cryocooler power (a), detector rate and temperature (b), and cryocooler power and temperature (c) for the second test. Here, the chiller temperature was set to 10 °C, and the room temperature was heated to 40 °C. The correlation coefficients are $\mathrm{cor}(R, P) = 0.84$, $\mathrm{cor}(R, T) = 0.24$ and $\mathrm{cor}(P, T) = 0.67$. A linear fit is indicated by the red lines.

Table I.1.: Correlation coefficients of rate and cryocooler power or temperature and of cryocooler power and temperature for the second test. The parameters of a linear fit for the correlation of rate, cryocooler power, and temperature are additionally given. The values were fitted by the function $f(x) = m \cdot x + c$.

Parameters	$\mathrm{cor}(X, Y)$	m	c
Rate - Cryocooler power	0.84	$13.68 \pm 0.90\ \frac{\mathrm{Hz}}{\mathrm{W}}$	$-576.01 \pm 75.51\ \mathrm{Hz}$
Rate - Temperature	0.24	$2.69 \pm 0.99\ \frac{\mathrm{Hz}}{^\circ\mathrm{C}}$	$494.08 \pm 27.48\ \mathrm{Hz}$
Cryocooler power - Temperature	0.67	$0.40 \pm 0.05\ \frac{\mathrm{W}}{^\circ\mathrm{C}}$	$72.69 \pm 1.41\ \mathrm{W}$

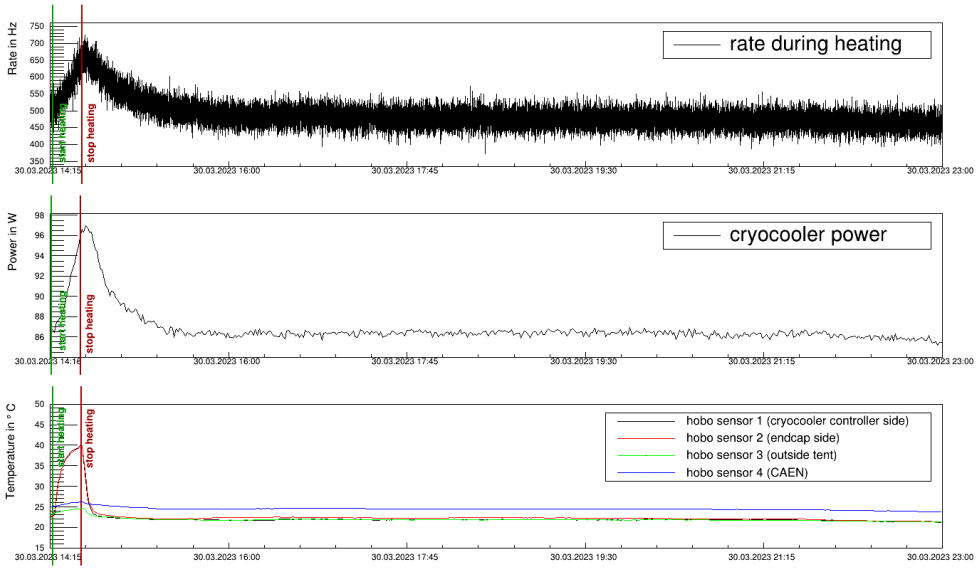

(a)

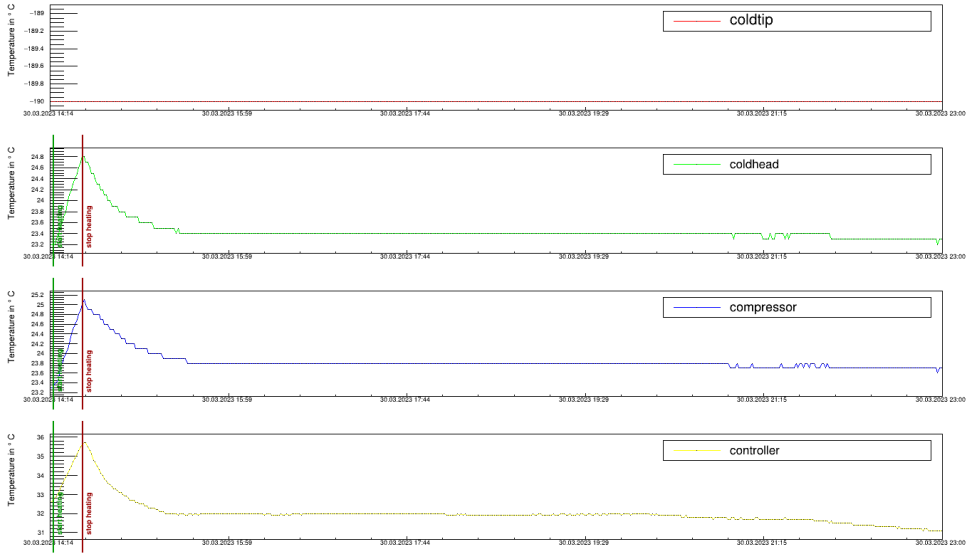

(b)

Figure I.4.: Rate, cryocooler properties and room temperature for the third test with a chiller temperature of 18 °C. The temperature in the tent was heated up to 40 °C, and the detector rate (top), cryocooler power (middle), and temperature (bottom) were recorded over time (a). Additionally, the cryocooler properties such as the coldtip temperature (red), the coldhead temperature (green), the compressor temperature (blue), and the controller temperature (yellow) are also recorded over time (b). The time of start and stop of the heating is marked also.

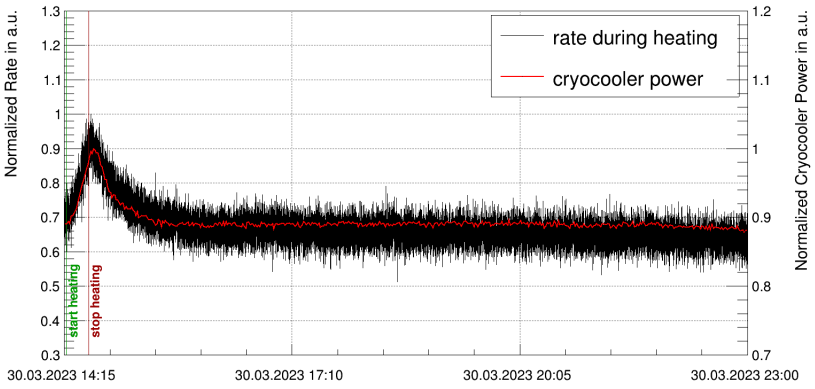

Figure I.5.: Normalized detector rate (black) and normalized cryocooler power (red) plotted over time for the third test with a chiller temperature of 18 °C. The time of start and stop of the heating is also marked.

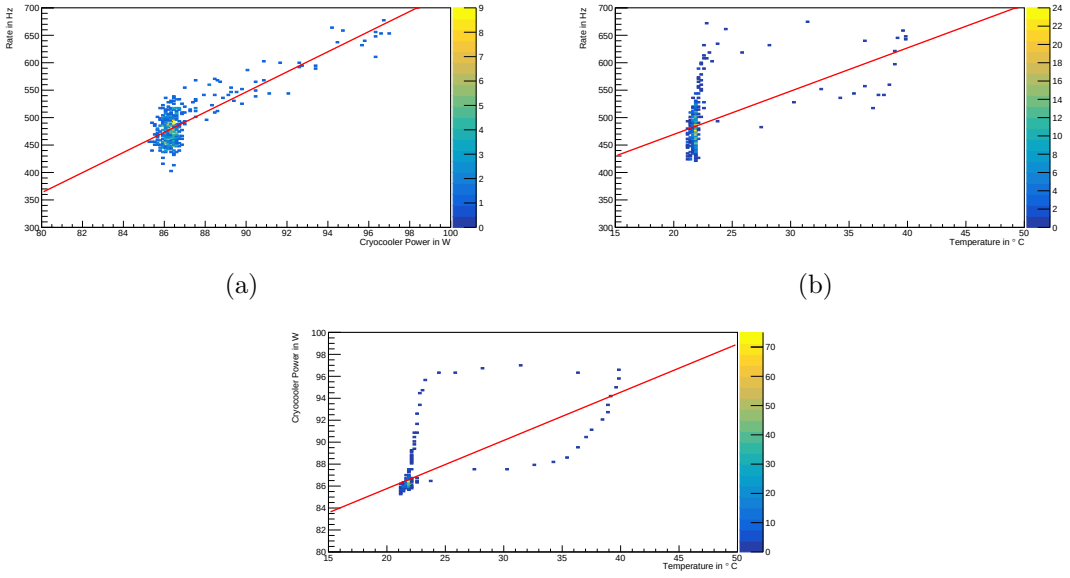

(a) (b)

(c)

Figure I.6.: Correlation between detector rate and cryocooler power (a), detector rate and temperature (b), and cryocooler power and temperature (c) for the third test. Here, the chiller temperature was set to 18 °C, and the room temperature was heated to 40 °C. The correlation coefficients are $\mathrm{cor}(R, P) = 0.81$, $\mathrm{cor}(R, T) = 0.52$ and $\mathrm{cor}(P, T) = 0.67$. A linear fit is indicated by the red lines.

Table I.2.: Correlation coefficients of rate and cryocooler power or temperature and of cryocooler power and temperature for the third test. The parameters of a linear fit for the correlation of rate, cryocooler power, and temperature are additionally given. The values were fitted by the function $f(x) = m \cdot x + c$.

Parameters	$\mathrm{cor}(X, Y)$	m	c
Rate - Cryocooler power	0.81	$18.35 \pm 0.82\ \frac{\mathrm{Hz}}{\mathrm{W}}$	$-1104.89 \pm 71.23\,\mathrm{Hz}$
Rate - Temperature	0.52	$7.88 \pm 1.00\ \frac{\mathrm{Hz}}{^\circ\mathrm{C}}$	$311.78 \pm 22.55\,\mathrm{Hz}$
Cryocooler power - Temperature	0.67	$0.44 \pm 0.05\ \frac{\mathrm{W}}{^\circ\mathrm{C}}$	$76.99 \pm 1.16\,\mathrm{W}$

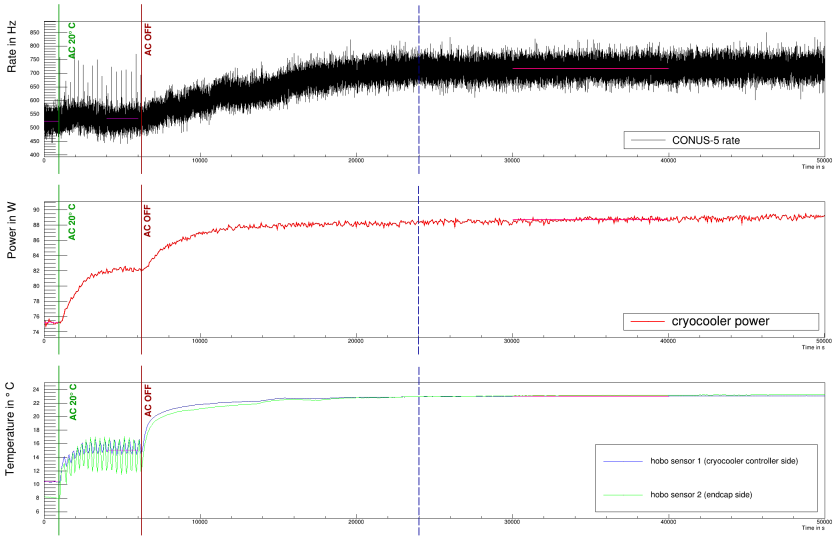

Figure I.7.: Detector rate (black), cryocooler power (red) and air temperature (blue) during the cooling test with chiller temperature 18 °C. The steps of increasing the AC temperature are marked in green.

J. List of Additional Tools

In the following, additional tools used for the analysis conducted in this thesis, as well as tools used for the preparation of this document are listed.

- The main part of the analysis, including work described in Chapters 4 and 5, is done in C++ with ROOT [75].
- The remaining part of the analysis, i.e. Chapter 3, is done in Python3.10.
- The analysis regarding neutrino electromagnetic properties is done with the analysis framework of the CONUS collaboration developed by T. Rink and T. Hugle, which is described in [43, 34].
- Additionally, the MPIK cluster was used for computing results of this work.
- Final language revision of this document was done using Grammarly.

Acknowledgements

With these last lines, I would like to thank everyone who supported me on the difficult journey to get to where I am now. First of all, I would like to thank Prof. Dr. Dr. h.c. Manfred Lindner that he gave me the great opportunity to do my PhD at MPIK and that he considered me suitable even when others did not. The friendly, open and never dismissive environment in his department gave me back my self-confidence and the belief in my skills.
Moreover, I want to thank PD Dr. Christian Buck and PD Dr. Theresa Marrodán Undagoitia for being my co-supervisors. They always supported me and gave me good advice when I needed it. During all the stressful times, it's reassuring to know that someone will take professional care of your concerns no matter what.
Many thanks also to JProf. Dr. Loredana Gastaldo for taking on the role of the second referee for this thesis.
A special thank goes to Dr. Thomas Rink, Dr. Werner Maneschg and again to PD Dr. Christian Buck for the final proof-reading of my thesis. I'm so grateful to you, as I never expected you to put so much work and detail into it. And also again a gigantic thank you to Dr. Thomas Rink for the great training and assistance in data analysis and for answering every question, no matter how stupid it was. At this point, I would also like to emphasize the greatness of the people in the CONUS collaboration. You are the best colleagues one can imagine and I really enjoyed working with you. Even though we are only a small team, we have achieved great things so far and I'm lucky to be a part of it. You all made the hard time of my PhD as pleasant as possible for me, with lots of laughter and sometimes a little bit of gossip. Many thanks to all of you, especially to my office mate Dr. Edgar Sanchez Garcia, who finally took away my fear of speaking English.
Zu guter Letzt möchte ich meinen Liebsten danken. Meinen Eltern und meiner Schwester, die mich immer unterstützt haben und mir mein Studium erst ermöglichen konnten. Vielen Dank euch für alles, ich wäre nicht so weit gekommen ohne euch. Meine tiefste Dankbarkeit geht an meinen wunderbaren Partner Johannes. Es tut mir Leid, dass du in den letzten Jahren so viel Gejammer von mir ertragen musstest. Ohne deine liebevolle Unterstützung und Ermunterung hätte ich es nicht geschafft. Ich liebe dich. Zusammen seid ihr die beste Familie, die man sich nur wünschen kann.

List of Publications

The results presented in this thesis are based on work done by the author in collaboration with others in the context of the CONUS experiment. This list contains the work published by the CONUS collaboration with the participation of the author. Publications containing the contents of this thesis are still in preparation and have not been published at the time of the submission of this thesis. Relevant documents are listed below.

- H. Bonet et al. First Upper Limits on Neutrino Electromagnetic Properties from the CONUS Experiment. *Eur. Phys. J. C*, 82(813), 2022. doi: 10.1140/epjc/s10052-022-10722-1.
- H. Bonet et al. Full Background Decomposition of the CONUS Experiment. *Eur. Phys. J. C*, 83(195), 2023. doi: 10.1140/epjc/s10052-023-11240-4.
- H. Bonet et al. Pulse Shape Discrimination for the CONUS Experiment in the keV and sub-keV Regime. *Eur. Phys. J. C*, 84(139), 2024. doi: 10.1140/epjc/s10052-024-12470-w.
- N. Ackermann et al. Final CONUS Results on Coherent Elastic Neutrino Nucleus Scattering at the Brokdorf Reactor, 2024. arXiv: 2401.07684.
- N. Ackermann et al. The CONUS+ Experiment (in preparation)
- CONUS publication on neutrino electromagnetic properties (in preparation, including results of this thesis)
- CONUS publication on optimization of Ge spectrometers for data collection at low energies (in preparation, including results of this thesis)

Bibliography

[1] W. Pauli. *Fünf Arbeiten zum Ausschließungsprinzip und zum Neutrino, Texte zur Forschung.* Wissenschaftliche Buchgesellschaft Darmstadt, 27. edition, 1977.

[2] S. Fukuda et al. Determination of Solar Neutrino Oscillation Parameters Using 1496 Days of Super-Kamiokande-I Data. *Physics Letters B*, 539(3):179–187, 2002. doi:10.1016/S0370-2693(02)02090-7.

[3] Q. R. Ahmad et al. Measurement of the Rate of $\nu_e + d \rightarrow p + p + e^-$ Interactions Produced by ^8B Solar Neutrinos at the Sudbury Neutrino Observatory. *Phys. Rev. Lett.*, 87:071301, 2001. doi:10.1103/PhysRevLett.87.071301.

[4] F. Reines et al. Detection of the Free Antineutrino. *Phys. Rev.*, 117:159–173, 1960. doi:10.1103/PhysRev.117.159.

[5] Y. Suzuki. The Super-Kamiokande Experiment. *Eur. Phys. J. C*, 79:298, 2019. doi:10.1140/epjc/s10052-019-6796-2.

[6] G. Alimonti et al. The Borexino Detector at the Laboratori Nazionali del Gran Sasso. *Nuclear Instruments and Methods in Physics Research Section A: Accelerators, Spectrometers, Detectors and Associated Equipment*, 600(3):568–593, 2009. doi:10.1016/j.nima.2008.11.076.

[7] D. Z. Freedman. Coherent Effects of a Weak Neutral Current. *Phys. Rev. D*, 9(5):1389–1392, 1974. doi:10.1103/PhysRevD.9.1389.

[8] B. Scholz. *First Observations of Coherent Elastic Neutrino-Nucleus Scattering.* Springer Nature Switzerland, 1. edition, 2018. doi:10.1007/978-3-319-99747-6.

[9] D. Akimov et al. Observation of Coherent Elastic Neutrino-Nucleus Scattering. *Science*, 357(6356):1123–1126, 2017. doi:10.1126/science.aao0990.

[10] K. Scholberg. Observation of Coherent Elastic Neutrino-Nucleus Scattering by COHERENT, 2018. arXiv:1801.05546.

[11] D. Z. Freedman, D. N. Schramm, and D. L. Tubbs. The Weak Neutral Current and its Effects in Stellar Collapse. *Annual Review of Nuclear Science*, 27(1):167–207, 1977. doi:10.1146/annurev.ns.27.120177.001123.

[12] CODATA. Weak Mixing Angle. [online]. Website, 2023. https://physics.nist.gov/cgi-bin/cuu/Value?sin2th [accessed: 17.05.2023].

[13] A. Drukier and L. Stodolsky. Principles and Applications of a Neutral-Current Detector for Neutrino Physics and Astronomy. *Phys. Rev. D*, 30:2295–2309, Dec 1984. doi:10.1103/PhysRevD.30.2295.

[14] P. Vogel and J. F. Beacom. Angular Distribution of Neutron Inverse Beta Decay, $\overline{\nu}_e + \vec{p} \; e^+ + n$. *Phys. Rev. D*, 60:053003, Jul 1999. doi:10.1103/PhysRevD.60.053003.

[15] J. A. Formaggio and G. P. Zeller. From eV to EeV: Neutrino Cross Sections Across Energy Scales. *Rev. Mod. Phys.*, 84:1307–1341, Sep 2012. doi:10.1103/RevModPhys.84.1307.

[16] M. Lindner, W. Rodejohann, and XJ. Xu. Coherent Neutrino-Nucleus Scattering and New Neutrino Interactions. *J. High Energ. Phys*, 97, 2017. doi:/10.1007/JHEP03(2017)097.

[17] M. Abdullah et al. Coherent Elastic Neutrino-Nucleus Scattering: Terrestrial and Astrophysical Applications, 2022. arXiv:2203.07361.

[18] A. Aguilar-Arevalo et al. Exploring Low-Energy Neutrino Physics with the Coherent Neutrino Nucleus Interaction Experiment. *Phys. Rev. D*, 100:092005, Nov 2019. doi:10.1103/PhysRevD.100.092005.

[19] I. Alekseev et al. First Results of the νGeN Experiment on Coherent Elastic Neutrino-Nucleus Scattering. *Phys. Rev. D*, 106:L051101, Sep 2022. doi:10.1103/PhysRevD.106.L051101.

[20] G. Angloher et al. Exploring CEνNS with NUCLEUS at the Chooz Nuclear Power Plant. *Eur. Phys. J. C*, 79:1018, 2019. doi:10.1140/epjc/s10052-019-7454-4.

[21] C. Augier et al. Ricochet Progress and Status. *J. Low Temp. Phys.*, 212:127–137, 2023. doi:10.1007/s10909-023-02971-5.

[22] PreussenElektra GmbH Kernkraftwerk Brokdorf. Informationen zum Kraftwert - Kernkraftwerk Brokdorf [online]. Website, 2020. https://www.preussenelektra.de/content/dam/revu-global/preussenelektra/documents/UnsereKraftwerke/Brokdorf/PEL_Standortbr_KBR_2020_rz_web.pdf [accessed: 20.11.2023].

[23] H. Bonet et al. Constraints on Elastic Neutrino Nucleus Scattering in the Fully Coherent Regime from the CONUS Experiment. *Phys. Rev. Lett.*, 126:041804, Jan 2021. doi:10.1103/PhysRevLett.126.041804.

[24] H. Bonet et al. Novel Constraints on Neutrino Physics Beyond the Standard Model from the CONUS Experiment. *J. High Energ. Phys.*, 85, 2022. doi:10.1007/JHEP05(2022)085.

[25] H. Bonet et al. Large-Size sub-keV Sensitive Germanium Detectors for the CONUS Experiment. *Eur. Phys. J. C*, 81(3):267, 2021. doi:10.1140/epjc/s10052-021-09038-3.

[26] G. Heusser et al. GIOVE: a New Detector Setup for High Sensitivity Germanium Spectroscopy at Shallow Depth. *Eur. Phys. J. C*, 75:531, 2017. doi:10.1140/epjc/s10052-015-3704-2.

[27] H. Bonet et al. Full Background Decomposition of the CONUS Experiment. *Eur. Phys. J. C*, 83(195), 2023. doi:10.1140/epjc/s10052-023-11240-4.

[28] J. Hakenmüller et al. Neutron-Induced Background in the CONUS Experiment. *Eur. Phys. J. C*, 79(8):699, 2019. doi:10.1140/epjc/s10052-019-7160-2.

[29] Mirion Technologies. Lynx Digital Signal Analyzer, Data Sheet. [online]. Website, 2023. https://mirionprodstorage.blob.core.windows.net/prod-20220822/cms4_mirion/files/pdf/spec-sheets/ops-509_lynx_dsa_spec_rebrand_5.pdf [accessed: 20.11.2023].

[30] CAEN. V1782 Octal Digital Multi Channel Analyzer [online]. Website, 2024. https://www.caen.it/products/v1782/ [accessed: 20.03.2024].

[31] N. Ackermann et al. Final CONUS Results on Coherent Elastic Neutrino Nucleus Scattering at the Brokdorf Reactor, 2024. arXiv:2401.07684.

[32] A. Bonhomme et al. Direct Measurement of the Ionization Quenching Factor of Nuclear Recoils in Germanium in the keV Energy Range. *Eur. Phys. J. C*, 82:815, 2022. doi:10.1140/epjc/s10052-022-10768-1.

[33] W. Maneschg. Recent Results from the CONUS Experiment, 2023. Talk at Magnificent CEvNS 2023 https://indico.cern.ch/event/1215362/contributions/5300024/attachments/2615794/4521004/M7_2023_conus_maneschg.pdf [accessed: 21.11.2023].

[34] H. Bonet et al. First Upper Limits on Neutrino Electromagnetic Properties from the CONUS Experiment. *Eur. Phys. J. C*, 82(813), 2022. doi:10.1140/epjc/s10052-022-10722-1.

[35] J. Lindhard, V. Nielsen, M. Scharff, and P. Thomsen. Integral Equations Governing Radiation Effects. *Mat. Fys. Medd. Dan. Vid. Selsk.*, 33(10), 1963.

[36] J. Lindhard. Influence of Crystal Lattice on Motion of Energetic Charged Particles. *Mat. Fys. Medd. Dan. Vid. Selsk.*, 34(14), 1965.

[37] E. Sanchez Garcia. The CONUS+ Experiment, 2023. Talk at Magnificent CEvNS 2023 https://indico.cern.ch/event/1215362/contributions/5300030/attachments/2617265/4524120/CONUS+_Magnificent_v2.pdf [accessed: 02.04.2024].

[38] K. Zuber. *Neutrino Physics*. CRC Press, 3. edition, 2020. doi:10.1201/9781315195612.

[39] C. Giunti and A. Studenikin. Neutrino Electromagnetic Interactions: A Window to New Physics. *Rev. Mod. Phys.*, 87:531–591, 2015. doi:10.1103/RevModPhys.87.531.

[40] M. Sajjad Athar et al. Status and Perspectives of Neutrino Physics. *Progress in Particle and Nuclear Physics*, 124:103947, 2022. doi:10.1016/j.ppnp.2022.103947.

[41] A. Studenikin. Status and Perspectives of Neutrino Magnetic Moments. *Journal of Physics: Conference Series*, 718(6):062076, 2016. doi:10.1088/1742-6596/718/6/062076.

[42] A. Studenikin. Overview on Neutrino Electromagnetic Properties. *Journal of Physics: Conference Series*, 1342(1):012047, 2020. doi:10.1088/1742-6596/1342/1/012047.

[43] T. Rink. *Investigating Neutrino Physics Within and Beyond the Standard Model Using CONUS Experimental Data*. PhD thesis, Ruprecht-Karls-Universität, Heidelberg, 2022. doi:10.11588/heidok.00031274.

[44] M. Fukugita and T. Yanagida. *Physics of Neutrinos and Application to Astrophysics*. Springer Berlin, Heidelberg, 1. edition, 2003. doi:10.1007/978-3-662-05119-1.

[45] K. S. Babu, S. Jana, and M. Lindner. Large Neutrino Magnetic Moments in the Light of Recent Experiments. *J. High Energ. Phys.*, 40, 2020. doi:10.1007/JHEP10(2020)040.

[46] M. Lindner, B. Radovčić, and J. Welter. Revisiting Large Neutrino Magnetic Moments. *J. High Energ. Phys.*, 139, 2017. doi:10.1007/JHEP07(2017)139.

[47] E. Aprile et al. Search for New Physics in Electronic Recoil Data from XENONnT. *Phys. Rev. Lett.*, 129:161805, 2022. doi:10.1103/PhysRevLett.129.161805.

[48] A. Beda et al. The Results of Search for the Neutrino Magnetic Moment in GEMMA Experiment. *Advances in High Energy Physics*, 2012, 2012. doi:10.1155/2012/350150.

[49] A. Beda et al. GEMMA Experiment: The Results of Neutrino Magnetic Moment Search. *Phys. Part. Nuclei Lett.*, 10:139–143, 2013. doi:10.1134/S1547477113020027.

[50] G. Raffelt. New Bound on Neutrino Dipole Moments from Globular-Cluster Stars. *Phys. Rev. Lett.*, 64:2856–2858, 1990. doi:10.1103/PhysRevLett.64.2856.

[51] J. Aalbers et al. Search for New Physics in Low-Energy Electron Recoils from the First LZ Exposure. *Phys. Rev. D*, 108:072006, 2023. doi:10.1103/PhysRevD.108.072006.

[52] M. Corona et al. New Constraint on Neutrino Magnetic Moment and Neutrino Millicharge from LUX-ZEPLIN Dark Matter Search Results. *Phys. Rev. D*, 107:053001, 2023. doi:10.1103/PhysRevD.107.053001.

[53] A. Studenikin. New Bounds on Neutrino Electric Millicharge from Limits on Neutrino Magnetic Moment. *EPL*, 107:21001, 2014. doi:10.1209/0295-5075/107/21001.

[54] A. Studenikin and I. Tokarev. Millicharged neutrino with anomalous magnetic moment in rotating magnetized matter. *Nuclear Physics B*, 884:396–407, 2014. doi:10.1016/j.nuclphysb.2014.04.026.

[55] G. Cowan. *Statistical Data Analysis*. Oxford University Press, 3. edition, 1998.

[56] L. Lista. *Statistical Methods for Data Analysis in Particle Physics*. Springer Cham, 2. edition, 2017. doi:10.1007/978-3-319-62840-0.

[57] W. Metzger. *Statistical Methods in Data Analysis*. Nijmegen Univ. Fys. Lab., 2010. https://web2.ba.infn.it/~pompili/teaching/data_analysis_lab/metzger_ediz2010.pdf [accessed: 19.02.2024].

[58] G. Bohm and G. Zech. *Introduction to Statistics and Data Analysis for Physicists*. Verlag Deutsches Elektronen-Synchrotron, 3. edition, 2017. doi:10.3204/PUBDB-2017-08987.

[59] C. Pruneau. *Data Analysis Techniques for Physical Scientists*. Cambridge University Press, 2017. doi:10.1017/9781108241922.

[60] G. Cowan et al. Asymptotic Formulae for Likelihood-Based Tests of New Physics. *Eur. Phys. J. C*, 71:1554, 2011. doi:10.1140/epjc/s10052-011-1554-0.

[61] J. Hakenmüller. *Looking for Coherent Elastic Neutrino Nucleus Scattering with the CONUS Experiment* . PhD thesis, Ruprecht-Karls-Universität, Heidelberg, 2020. doi:10.11588/heidok.00029165.

[62] G. Gilmore. *Practical Gamma-Ray Spectrometry*. John Wiley & Sons, Ltd, 2. edition, 2008. doi:10.1002/9780470861981.

[63] G. Lutz. *Semiconductor Radiation Detectors*. Springer Berlin, Heidelberg, 1. edition, 2007. doi:10.1007/978-3-540-71679-2.

[64] H. Bonet et al. Pulse Shape Discrimination for the CONUS Experiment in the keV and sub-keV Regime. *Eur. Phys. J. C*, 84(139), 2024. doi:10.1140/epjc/s10052-024-12470-w.

[65] J. Henrichs. Development of a Pulse Shape Analysis for the CONUS Experiment. Master's thesis, Ruprecht-Karls-Universität, Heidelberg, 2021. https://hdl.handle.net/21.11116/0000-0009-C7E1-8.

[66] J. Stauber. Pulse Shape Discrimination for the CONUS Experiment in the sub-keV Regime. Master's thesis, Ruprecht-Karls-Universität, Heidelberg, 2022. https://hdl.handle.net/21.11116/0000-000A-EBAC-C.

[67] M. Boswell et al. MaGe - A Geant4-Based Monte Carlo Application Framework for Low-Background Germanium Experiments. *IEEE Transactions on Nuclear Science*, 58(3):1212–1220, 2011. doi:10.1109/TNS.2011.2144619.

[68] D. Radford. Siggen Simulation Software Package. Website, 2014. https://github.com/radforddc/icpc_siggen [accessed: 07.09.2021].

[69] D. Radford. MAJORANA siggen. Conference, 2015. Final Symposium of the Sino-German GDT Cooperation, https://indico.mpp.mpg.de/event/3121/contributions/6645/attachments/5433/5982/radford_Ge_workshop_Oct2015_Bb.pdf.

[70] S. Agostinelli et al. Geant4 — A Simulation Toolkit. *Nuclear Instruments and Methods in Physics Research Section A: Accelerators, Spectrometers, Detectors and Associated Equipment*, 506(3):250–303, 2003. doi:10.1016/S0168-9002(03)01368-8.

[71] D. Lenz. *Pulse Shapes and Surface Effects in Segmented Germanium Detectors.* PhD thesis, Technische Universität München, 2010.

[72] S. Mertens et al. Characterization of High Purity Germanium Point Contact Detectors with Low Net Impurity Concentration. *Nuclear Instruments and Methods in Physics Research Section A: Accelerators, Spectrometers, Detectors and Associated Equipment*, 921:81–88, 2019. doi:10.1016/j.nima.2018.09.012.

[73] J. Li, J. Liu, and K. Kooi. HPGe Detector Field Calculation Methods Demonstrated with an Educational Program, GeFiCa. *Eur. Phys. J. C*, 80:230, 2020. doi:10.1140/epjc/s10052-020-7786-0.

[74] Z. He. Review of the Shockley–Ramo Theorem and its Application in Semiconductor Gamma-Ray Detectors. *Nuclear Instruments and Methods in Physics Research Section A: Accelerators, Spectrometers, Detectors and Associated Equipment*, 463(1):250–267, 2001. doi:https://doi.org/10.1016/S0168-9002(01)00223-6.

[75] R. Brun and F. Rademakers. ROOT — An Object Oriented Data Analysis Framework. *Nuclear Instruments and Methods in Physics Research Section A: Accelerators, Spectrometers, Detectors and Associated Equipment*, 389(1):81–86, 1997. New Computing Techniques in Physics Research V. doi:10.1016/S0168-9002(97)00048-X.

[76] M. Schlarb. *Simulation and Real-Time Analysis of Pulse Shapes from Segmented HPGe-Detectors*. PhD thesis, Technische Universität München, 2009.

[77] A. Jany et al. Fabrication, Characterization and Analysis of a Prototype High Purity Germanium Detector for ^{76}Ge-based Neutrinoless Double Beta Decay Experiments. *Eur. Phys. J. C*, 81:38, 2021. doi:10.1140/epjc/s10052-020-08781-3.

[78] T. Comellato, M. Agostini, and S. Schönert. Charge-Carrier Collective Motion in Germanium Detectors for $\beta\beta$-Decay Searches. *Eur. Phys. J. C*, 81:76, 2021. doi:10.1140/epjc/s10052-021-08889-0.

[79] B. Shanks and C. O'Shaughnessy. Waveform Simulation for Pulse-Shape-Analysis Validation in the MAJORANA DEMONSTRATOR. TUNL LII Progress Report 1 September 2012 – 30 November 2013, 2013. https://tunl.duke.edu/sites/tunl.duke.edu/files/file-attachments/2012-13.pdf.

[80] P. Barbeau, J. Collar, and O. Tench. Large-Mass Ultralow Noise Germanium Detectors: Performance and Applications in Neutrino and Astroparticle Physics. *Journal of Cosmology and Astroparticle Physics*, 2007(09):009, 2007. doi:10.1088/1475-7516/2007/09/009.

[81] M. Salathe. *Study on Modified Point Contact Germanium Detectors for Low Background Applications*. PhD thesis, Ruprecht-Karls-Universität, Heidelberg, 2015. doi:10.11588/heidok.00019889.

[82] G. Knoll. *Radiation Detection and Measurement*. John Wiley & Sons, Ltd, 4. edition, 2010.

[83] P. Luke et al. Low Capacitance Large Volume Shaped-Field Germanium Detector. *IEEE Transactions on Nuclear Science*, 36(1):926–930, 1989. doi:10.1109/23.34577.

[84] E. van der Meeren. Prototyping a Mobile CEνNS Detection Setup for CONUS. Master's thesis, Ruprecht-Karls-Universität, Heidelberg, 2020.

[85] Kistler Instrumente AG. Miniature PiezoBeam Accelerometer, Data Sheet. [online]. Website, 2023. https://nanosatlab.upc.edu/en/shared/documents/accelerometer_datasheet_2.pdf [accessed: 25.10.2023].

[86] Kistler Instrumente AG. Kistler LabAmp, Data Sheet. [online]. Website, 2023. https://kistler.cdn.celum.cloud/SAPCommerce_Download_original/003-146e.pdf [accessed: 25.10.2023].

[87] E. Weisstein. Statistical Correlation, MathWorld - A Wolfram Web Resource. [online]. Website, 2023. https://mathworld.wolfram.com/StatisticalCorrelation.html [accessed: 06.11.2023].